

SYNTHESIS OF MULTI-METALLIC CATALYSTS FOR FUEL CELL APPLICATIONS

by Sivapregasen Naidoo



A dissertation submitted in partial fulfillment of the requirements for the degree of
Doctor of Philosophy in the Department of Chemistry, University of the Western Cape,
Cape Town, Western Cape, South Africa

Supervisor: Dr Guntars Vaivars

April, 2008

Abstract

The direct methanol fuel cell or DMFC is emerging as a promising alternative energy source for many applications. Developed and developing countries, through research, are fast seeking a cheap and stable supply of energy for an ever-increasing number of energy-consuming portable devices. The research focus is to have DMFCs meet this need at an affordable cost is problematic. There are means and ways of making this a reality as the DMFC is found to be complementary to secondary batteries when used as a trickle charger, full charger, or in some other hybrid fuel cell combination. The core functioning component is a catalyst containing MEA, where when pure platinum is used, carbon monoxide is the thermodynamic sink and poisons by preventing further reactions at catalytic sites decreasing the life span of the catalyst if the CO is not removed. Research has shown that the bi-functional mechanism of a platinum-ruthenium catalyst is best because methanol dehydrogenates best on platinum and water dehydrogenation is best facilitated on ruthenium. It is also evident that the addition of other metals to that of PtRu/C can make the catalyst more effective and increase the life span even further. In addition to this, my research has attempted to reduce catalyst cost for DMFCs by developing a low-cost manufacturing technique for catalysts, identify potential non-noble metal catalytic systems and develop a basic process to combine various non-noble, less expensive metallic systems to form binary, ternary and quaternary catalysts.

The initial research focused on the identification of a suitable Pt/C preparation method, and characterization of the resulting catalysts by electrochemical methods (including

cyclic voltammetry), elemental analysis (by EDS), and morphological characterization (by TEM).

Once the preparation method for Pt/C had been established, binary (Pt–M/C), ternary (Pt–M₁M₂ /C) and quaternary (Pt–M₁M₂M₃ /C) catalysts were prepared by modifying the initial Pt/C preparation method. These multi-metallic catalysts primarily function in preventing CO poisoning and allowing MeOH oxidation at the anode. To determine the effectiveness of the in-house multi-metallic catalysts the catalysts were then compared to the commercially available bench mark JM commercially available catalyst. Cyclic voltammetric and chronoamperometric analysis revealed that the in-house catalysts electrochemical catalytic activity were similar to that of the commercially available catalysts. The Fuel application testing revealed similar trends to that of the EC activity at 0,5V (Ag/AgCl) test results, with the quaternary catalyst proving to be the most active anode catalyst producing the highest power density. The quaternary catalysts proved to be superior with its increased mass activity and high surface area (80% of the catalytic particles < 3nm).

DEDICATION

I dedicate this thesis to my family, my wife Qiling and to my daughter Livashni.



DECLARATION

I declare that “Synthesis of Multi-metallic Catalysts for Fuel Cell Application” is my own work, that it has not been submitted for any degree or examination at any other university, and that all the sources I have used or quoted have been indicated and acknowledged by complete references. If there are mention of unreferenced data this was not intentional but merely an oversight.

Sivapregasen Naidoo



LIST OF ABBREVIATIONS

DMFC	Direct Methanol Fuel Cell
FC	Fuel Cell
GDL	Gas Diffusion Layer
MEA	Membrane Electrode Assembly
PEMFC	Proton Exchange Membrane Fuel Cell
SEM	Scanning Electron Microscopy
TEM	Transition Electron Microscopy
XRD	X-ray Diffraction
CA	Chronoamperometry
CV	Cyclic Voltammetry
ECA	Electrochemical Activity
ST	Sonication time
RA	Reducing agent
F	40% Formaldehyde
SBH	NaBH ₄
MWCNT	Multiwalled carbon nanotubes
D	Deposition
ID	Individual deposition
SD	Simultaneous deposition
N/A	Not available
(fcc)	Face centered cubic
APS	Average catalyst particle size
EC	Electrochemical

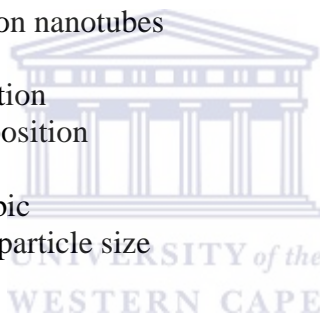


TABLE OF CONTENTS

	Page
DECLARATION	i
AKNOWLEDGMENTS	ii
ABSTRACT	iii
TABLE OF CONTENTS	v
LIST OF FIGURES	viii
LIST OF TABLES	xi
LIST OF ABBREVIATIONS	xii
CHAPTER 1: INTRODUCTION	1
1.1 Background	1
1.2 Existing Problems with Current Fuel Cell Technologies	2
1.3 Key Objectives In Respect Of Future Research	2
1.4 Research Approach Pursued in This Project	3
1.5 Structure of Thesis	3
CHAPTER 2: LITERATURE REVIEW	4
2.1 INTRODUCTION	4
2.1.1 Background	4
2.1.2 Low Temperature Fuel Cells	5
2.1.3 Principle of the H ₂ -PEMFC	6
2.1.4 Principle of the DMFC	7
2.1.5 Advantages and Disadvantages of DMFCs	10
2.1.6 Hydrogen versus Methanol as a Fuel	11
2.1.7 Other Fuel sources available for Low Temperature Fuel Cells	14
2.2 PRECURSORS AND SUPPORTS	17
2.2.1 Platinum salt precursors - Chloroplatinic Acid (H ₂ PtCl ₄ : 6H ₂ O)	17
2.2.2 Types of Carbon Supports	19
2.2.3 Surface Chemistry of Carbon Black	21
2.2.4 Electrical Conductivity of Conductive Carbon Blacks	21
2.2.5 Effects of Carbon Pretreatment for Oxygen Reduction	22
2.2.6 Carbon Nano-Tubes	24
2.2.7 Characterization of Carbon Supports	27

Table of Contents

2.3 ANODE CATALYST - METHANOL OXIDATION.....	28
2.3.1 Anode Catalyst - Methanol Oxidation.....	28
2.3.2 XRD Analysis of Pt Catalysts.....	31
2.3.3 TEM analysis.....	32
2.3.4 Cyclic voltammetry (CV) analysis.....	32
3.3.4.1 Kinetics of the hydrogen oxidation at Pt/C catalysts.....	33
2.3.5 Citrate reduction of platinum.....	36
2.3.6 Typical Physico and Electrochemical Characterization of a Multi-metallic catalyst.....	41
2.3.6.1 Physicochemical characterization of a Binary catalyst.....	44
2.3.6.2 Electrochemical characterization of a Binary catalyst.....	45
CHAPTER 3: EXPERIMENTAL.....	47
3.1 TEM.....	47
3.2 XRD.....	48
3.3 SEM-EDS.....	51
3.4 ELECTROCHEMICAL ANALYSIS BY CV AND CA.....	52
3.5 METHOD DEVELOPMENT.....	57
CHAPTER 4: MONO-METALLIC CATALYSTS.....	66
4.1 Objectives.....	66
4.2 Introduction.....	66
4.3 Synthesis Parameters.....	68
4.4 Results and Discussion.....	71
4.4.1 Structural Characterization by XRD.....	71
4.4.2 Morphological Characterization by TEM.....	75
4.4.3 Elemental Analysis by SEM-EDS.....	83
4.4.4 Electrochemical Analysis by CV and CA.....	84
CHAPTER 5: BI-METALLIC CATALYSTS.....	106
5.1 Objectives.....	106
5.2 Introduction.....	106
5.3 Synthesis Parameters.....	108
5.4 Results and Discussion.....	110

Table of Contents

5.4.1	Structural Characterization by XRD	110
5.4.2	Morphological Characterization by TEM	113
5.4.3	Elemental Analysis by SEM-EDS	119
5.4.4	Electrochemical Analysis by CV and CA	120
CHAPTER 6: TERNARY CATALYSTS		133
6.1	Objectives	133
6.2	Introduction	133
6.3	Synthesis Parameters	135
6.4	Results and Discussion	137
6.4.1	Structural Characterization by XRD	137
6.4.2	Morphological Characterization by TEM	140
6.4.3	Elemental Analysis by SEM-EDS	144
6.4.4	Electrochemical Analysis by CV and CA	146
CHAPTER 7: QUATERNARY CATALYSTS		157
7.1	Objectives	157
7.2	Introduction	157
7.3	Synthesis Parameters	160
7.4	Results and Discussion	164
7.4.1	Structural Characterization by XRD	164
7.4.2	Morphological Characterization by TEM	167
7.4.3	Elemental Analysis by SEM-EDS	173
7.4.4	Electrochemical Analysis by CV and CA	175
CHAPTER 8: FUEL CELL APPLICATION AND TESTING		191
8.1	Objectives	191
8.2	Introduction	191
8.3	Synthesis Parameters and MEA Formation	208
8.4	Results and Discussion	215
CHAPTER 9: CONCLUSIONS AND RECOMMENDATIONS FOR FUTURE RESEARCH		225
CHAPTER 10: REFERENCES		233

Figure 2.1	Low Temperature Fuel Cell Components	9
Figure 2.2	Principal of H ₂ -PEMFC.....	9
Figure 2.3	Principal of DMFC.....	9
Figure 2.2.1.1	Chloroplatinic Acid – hydrated.....	17
Figure 2.2.1.6.1	Multiwalled carbon nanotubes	24
Figure 2.2.1.6.2	TEM images of Multiwalled carbon nanotubes.....	25
Figure 2.2.1.6.3	Carbon Nanotube Tips for Atomic Force Microscopy	26
Figure 2.3.4.1.1	Hydrogen desorption peak area in the CV curves of Pt/C catalysts... ..	35
Figure 2.3.4.1.2	Current vs. potential curves of the electrocatalytic oxidation of H ₂ ...	35
Figure 2.3.4.1.3	Plots of $E-\log [(IL -I)/IL]$ and $E-\log [IL \times I/(IL -I)]$	36
Figure 3.1.4.1	Schematic of Electrochemical Testing Unit	52
Figure 3.1.4.1.1	(a) CV of the GCE and (b) sample loss after multiple scans	54
Figure 3.1.4.1.2	(a) CV of catalyst D3 and (b) sample loss after multiple scans	54
Figure 4.4.1.1	XRD of catalysts (a) A1, A2 and JM and (b) A3, A4 and JM	71
Figure 4.4.1.2	XRD of catalysts (a) A5, A6 and JM and (b) A7, JM40% and JM20% Pt	72
Figure 4.4.1.3	XRD of catalysts (a) A8, JM 20% and JM 40% (b) A9, A10 and JM20%Pt.....	73
Figure 4.4.2.1	TEM images of catalysts (a) A1, (b) A2, (c) A3, (d) A4	76
Figure 4.4.2.2	Particle size distribution of catalysts (a) A1, (b) A2, (c) A3, (d) A4 ...	76
Figure 4.4.2.3	TEM images of catalysts (a) A5, (b) A6, (c) A7, (d) A8	79
Figure 4.4.2.4	Particle size distribution of catalysts (a) A5, (b) A6, (c) A7, (d) A8 ...	79
Figure 4.4.2.5	TEM images of catalysts (a) A9, (b) A10	80
Figure 4.4.2.6	Particle size distribution of catalysts (a) A9 and (b) A10	81
Figure 4.4.4.1	CV of catalyst A1 at 1,0V vs. Ag/AgCl	86
Figure 4.4.4.2	CV of catalyst A1R1 at 1,0V vs. Ag/AgCl	87
Figure 4.4.4.3	CV of catalyst A1R2 at 1,0V vs. Ag/AgCl	87
Figure 4.4.4.4	CV of catalyst A2 at 0,6V vs. Ag/AgCl	88
Figure 4.4.4.5	CV of catalyst A3 at 1,0V vs. Ag/AgCl	89
Figure 4.4.4.6	CV of catalyst A4, 1,0V vs. Ag/AgCl	90
Figure 4.4.4.7	CV of catalyst A5 at 1,0V vs. Ag/AgCl	91
Figure 4.4.4.8	CV of catalyst A6 at 1,0V vs. Ag/AgCl	92
Figure 4.4.4.9	CV of catalyst, A7 at 1,0V vs. Ag/AgCl	93
Figure 4.4.4.10	CV of catalyst, A8, and JM 20% at 0,6V Vs Ag/AgCl	95
Figure 4.4.4.11	CV of catalyst, A9 at 1,0V vs. Ag/AgCl	96
Figure 4.4.4.12	CV of catalyst A10 at 1,0V vs. Ag/AgCl	96
Figure 5.4.1.1	XRD of catalysts B1, B2 and JM.....	110
Figure 5.4.1.2	XRD of catalysts B3 and JM.....	111
Figure 5.4.1.3	XRD of catalysts B4, B5 and JM.....	112
Figure 5.4.2.1	TEM images of catalysts (a) B1, (b) B2, (c) B3, (d) B4.....	115
Figure 5.4.2.2	Particle size distribution of catalysts (a) B1, (b) B2, (c) B3, (d) B4.....	115
Figure 5.4.2.2	Catalyst B5 (a) TEM image and (b) Particle size distribution.....	117
Figure 5.4.4.1	CV of catalyst B1 at 0,6V vs. Ag/AgCl.....	120

Figure 5.4.4.2 CV of catalyst B2 at 0,6V vs. Ag/AgCl.....	122
Figure 5.4.4.3 CV of catalyst B3 at 1,0V vs. Ag/AgCl.....	123
Figure 5.4.4.4 CV of catalyst B4 at 1,0V vs. Ag/AgCl.....	124
Figure 5.4.4.5 CV of catalyst B5 at 1,0V vs. Ag/AgCl.....	125
Figure 5.4.4.6 CV of catalyst JM Pt-Ru at 1,0V vs. Ag/AgCl.....	126
Figure 5.4.4.7 CA of catalyst B5 at 0,3V vs. Ag/AgCl (1800 sec.).....	127
Figure 6.4.1.1 XRD of catalysts (a) C1, C2 and JM.....	137
Figure 6.4.1.2 XRD of catalysts (a) C3, C4 and JM.....	138
Figure 6.4.2.1 TEM images of catalysts (a) C1, (b) C2, (c) C3, (d) C4.....	141
Figure 6.4.2.2 Particle size distribution of catalysts (a) C1, (b) C2, (c) C3, (d) C4.....	141
Figure 6.4.2.3 Catalyst C5 (a) TEM image and (b) Particle size distribution.....	142
Figure 6.4.4.1 CV of catalyst C1 at 1,0V s.Ag/AgCl.....	147
Figure 6.4.4.2 CV of catalyst C2 at 1,0V vs. g/AgCl.....	148
Figure 6.4.4.3 CV of catalyst C3 at 1,0V vs. g/AgCl.....	149
Figure 6.4.4.4 CV of catalyst C4 at 1,0V vs. g/AgCl.....	150
Figure 6.4.4.5 CV of catalyst C5 at 1,0V vs. g/AgCl.....	152
Figure 6.4.4.6 CA of catalyst C5 and JM at 0,3V s.Ag/AgCl.....	153
Figure 7.4.1.1 XRD of catalysts D1, D2 and JM.....	164
Figure 7.4.1.2 XRD of catalysts D5, D3 and JM.....	165
Figure 7.4.1.3 XRD of catalysts D4, D6 and JM.....	166
Figure 7.4.2.1 TEM images of catalysts (a) D1, (b) D2, (c) D3, (d) D4.....	169
Figure 7.4.2.2 Particle size distribution of catalysts (a) D1, (b) D2, (c) D3, (d) 4.....	169
Figure 7.4.2.3 TEM images of catalysts (a) D5, (b) D6, (c) D7.....	171
Figure 7.4.2.4 Particle size distribution of catalysts (a) D5, (b) D5, (c) D7.....	171
Figure 7.4.4.1 CV of catalyst D1 at 1,0V vs. g/AgCl.....	176
Figure 7.4.4.2 CV of catalyst D2 at 1,0V vs. g/AgCl.....	177
Figure 7.4.4.3 CV of catalyst D3 at 1,0V vs. g/AgCl.....	180
Figure 7.4.4.4 CV of catalyst D4 at 1,0V vs. g/AgCl.....	181
Figure 7.4.4.5 CV of catalyst D5 at 1,0V vs. g/AgCl.....	182
Figure 7.4.4.6 CV of catalyst D6 at 1,0V vs. g/AgCl.....	184
Figure 7.4.4.7 CV of catalyst D7 at 0.6V vs. g/AgCl.....	186
Figure 7.4.4.8 CA of catalyst D7 at 0.3V vs. g/AgCl.....	187
Figure 8.1.1 Solvent use in CI preparation, blue: IPA and pink: Butyl Acetate.....	216

List of Figures	Page
Figure 8.2.1 Effect of hot pressing time on power density curves of MEAs fabricated at 1500psi and 100°C.....	219
Figure 8.2.2 Effect of hot pressing pressure on power density curves of MEAs fabricated at 100°C.....	219
Figure 8.2.3 Optimization of hot-pressing temperature on polarization of MEAs fabricated under 1000 psi for 2 min.....	220
Figure 8.2.3.1 The effect on current density using different cathode feeds.....	222
Figure 8.2.3.2 Influence of air cathode pressure on cell performance at 80°C, Nafion 117 as the membrane.....	222
Figure 8.3.1 Polarization curves for in-house and commercial catalyst containing MEAs at 80°C under atmospheric pressure.....	224



List of Tables	Page
Table 2.1	List of Fuel Cell Systems.....5
Table 2.2	Specific gravimetric and volumetric energy densities of selected fuels and comparison with batteries.....12
Table 2.3	Physical properties of hydrogen, methanol and petrol relevant To accident Safety..... 13
Table 2.2.1.7	Porous Properties of Carbon Supports.....28
Table 3.1.1.1	LEO 912 OMEGA transmission electron microscope operational Parameters.....48
Table 3.1.3.1	Table 3.1.3.1 Hitachi X-650 SEM operational parameters.....51
Table 3.1.4.1	Standard Operating Parameters for CV and CA analysis.....52
Table 3.1.4.2	List of reagents, supports and gases used for catalyst preparation.....56
Table 4.2.1	Summary of the synthesis parameters69
Table 4.4.3.1	Results of the elemental analysis by EDS.....83
Table 4.4.4	Comparing the Electrochemical Activity by CV Analysis85
Table 4.5.1	Summary table comparing the different reducing agents and Temperatures.....99
Table 4.5.2	Summary table using Formaldehyde as the reducing agent100
Table 5.3.1	Summary of the synthesis parameters108
Table 5.4.2.1	Catalysts APSD and depositing sequence113
Table 5.4.3.1	Results of the elemental analysis by EDS.....119
Table 5.4.4.1	Comparing the Electrochemical Activity by CV Analysis120
Table 5.5.1	Summary table comparing the different reducing agents and temperatures and EC activities of the bimetallic catalysts.....128
Table 6.3.1	Summary of the synthesis parameters.....135
Table 6.4.2.1	Catalyst APSD and depositing sequence.....140
Table 6.4.3.1	Results of the elemental analysis by EDS.....144
Table 6.4.4.1	Comparing Catalyst Electrochemical Activity by CV Analysis..... 146
Table 6.5.1.1	Summary table comparing the different supports, reduction temperatures, particle size and EC activities of the ternary catalysts.....155
Table 7.2.1	Summary of the synthesis parameters.....161
Table 7.4.2.1	Catalyst APSD and deposition sequence.....168
Table 7.4.3.1	Results of the elemental analysis by EDS.....173
Table 7.4.4.1	Comparing Catalyst Electrochemical Activity by CV Analysis.....175
Table 7.5.1	Summary table comparing the different reducing agents and Temperatures and EC activities of the quaternary catalysts.....189
Table 8.2.2.1	Physical properties of the single solvents used for inks preparation.....193
Table 8.2.2.2	Experimental values of dielectric constants and viscosity obtained for binary and ternary mixtures of solvents with glycerine.....194
Table 8.2.3	Anode activity. EAS area and Pt percentage of prepared MEAs.....201
Table 8.2.4	Process parameters and resulting Pt loadings.....201

CHAPTER 1

INTRODUCTION

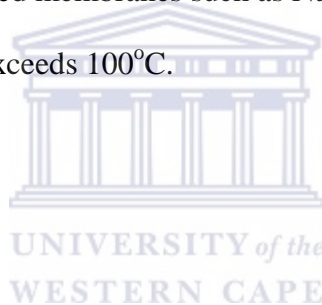
1.1 BACKGROUND

The direct methanol fuel cell or DMFC is emerging as a future winner in many applications. The DMFC is an important subset of the proton exchange membrane (PEM) fuel cell technology. DMFC emergence is especially viable in the portable device sector. Commercialization is driven by consumer demand and desire for a superior power source that can operate alone or as a supplement or synergist with existing advanced battery technologies. The innovation driver for DMFC development is the need, want, and desire for sustainable energy sources. Every developed country in the world wants a cheap and stable supply of energy for an ever-increasing number of energy-consuming portable devices. How to have DMFCs meet this need at an affordable cost is problematic. A new reality is emerging as the DMFC is found to be complementary to secondary batteries when used as a trickle charger, full charger, or in some other hybrid fuel cell combination. With pure platinum, carbon monoxide is the thermodynamic sink and will poison the surface if not removed. Research has shown that the bi-functional mechanism of a platinum-ruthenium catalyst is best because methanol dehydrogenates best on platinum and water dehydrogenation is best facilitated on ruthenium. It is the anode catalyst that provides the foundation for converting the chemical energy of the fuel into electrical energy. Platinum (Pt) is the best anode for hydrogen oxidation, but in the presence of methanol CO, formed as a reaction intermediate, irreversibly absorbs to the

Pt surface rapidly lowering its activity. Pt/Ru bifunctional catalysts are presently the most active for methanol oxidation, with ruthenium (Ru) believed to serve the role of removing the absorbed carbon monoxide as carbon dioxide gas.

1.2 EXISTING PROBLEMS WITH CURRENT FUEL CELL TECHNOLOGIES

- Platinum is very expensive and has a negative influence on pricing resulting in high cost fuel cells not affordable to the public.
- Catalyst poisoning and reduced cell potential.
- Low temperature designed membranes such as Nafion[®] dehydrate as the temperature nears and exceeds 100°C.



1.3 KEY OBJECTIVES IN RESPECT OF FUTURE RESEARCH

- Reduce catalyst cost for DMFCs.
- Develop a low-cost manufacturing technique for catalysts.
- Identify potential non-noble metal catalytic systems.
- Develop a basic process to combine various non-noble metals to form binary, ternary and quaternary catalysts

1.4 RESEARCH APPROACH PERSUED IN THIS PROJECT

The initial research focused on the identification of a suitable Pt/C preparation method, and characterization of the resulting catalysts by electrochemical methods (including cyclic voltammetry), elemental analysis (by EDS), and morphological characterization (by TEM).

Once the preparation method had been established, binary, ternary and quaternary catalysts preventing CO poisoning and allowing MeOH oxidation at the anode were prepared by modifying the preparation method.

These catalysts were then compared to the commercially available catalyst.

1.5 STRUCTURE OF THESIS

- 
- Chapter 2: Introduction to fuel cells and literature review. Presents a theoretical overview of research, undertaken to date.
 - Chapter 3: Experimental. Outlines the methods employed when producing, and the principles supporting the characterization techniques when testing the catalysts.
 - Chapter 4: Mono-metallic platinum-based catalysts.
 - Chapter 5: Binary platinum-based catalysts.
 - Chapter 6: Ternary platinum-based catalysts.
 - Chapter 7: Quaternary platinum-based catalysts.
 - Chapter 8: Fuel Cell Application and Testing
 - Chapter 9: Conclusions and recommendations for future research
 - Chapter 10: References

CHAPTER 2: LITERATURE REVIEW

2.1 INTRODUCTION

2.1.1 Background

The criteria that are going to influence the evolution of the world energy system in the present century are complex. The most important new factor is the need to preserve the environment, both locally and globally, through the use of new technologies and sustainable use of existing resources.

The Kyoto protocol, which places a limit on greenhouse gas emissions (mainly CO₂) from the industrialized countries, is a turning point in the global energy chain. On the other hand, the 2005 fuel specifications to control automotive exhaust gas emission obligate fuel producers to look for different ways of making clean fuel. Automotive makers are also obligated to look for alternative technology to the internal combustion engine. E.S. Goodstein has suggested that the interest in studies on energy sources alternative to fossil fuels is linked both to the reduction of their availability and the increasing environmental impact caused by their use [1]. In the energy field, an important cause of pollutant emissions is linked to ground transportation. In the last 40 years, some economic, social and cultural changes have encouraged a wide proliferation of vehicles. For example, in Europe, private cars have increased from 232 to 435 per 1000 inhabitants in the period 1971-1995 [2].

Fuel cells are alternative power sources that can meet global emission regulations and clean production of energy and power. Although fuel cells have been used since the 1960s for aerospace and military applications, cost was a strong impediment to terrestrial

applications. Five major types of fuel cells are available and are defined by their electrolyte. These include alkaline (AFCs), phosphoric acid (PAFCs), molten carbonate (MCFCs), solid oxide (SOFCs) and proton exchange membrane fuel cells (PEMFCs).

Table 2.1 summarizes some characteristics of these fuel cells. PEMFCs are the most attractive candidates for alternative automotive and stationary power sources due to their smaller size and much lower operating temperature compared to other fuel cell systems.

In this thesis, we only consider low temperature fuel cells, namely, the DMFC.

Table 2.1: Fuel cells systems [3, 4]

Type	Electrolyte	Charge carrier in the electrolyte	Temperature (°C)	Likely applications
Alkaline fuel cells (AFC)	aqueous KOH solution	OH^-	<100	Transportation, Space, Military Energy storage systems
Proton exchange membrane fuel cells (PEMFC)	proton exchange membrane	H^+	60-120	Transportation, Space, Military Energy storage systems
Phosphoric acid fuel cells (PAFC)	concentrated phosphoric acid	H^+	160-220	Combined heat and power for decentralised stationary power systems
Molten carbonate fuel cells (MCFC)	mixture of molten carbonates ($\text{Li}_2\text{CO}_3/\text{K}_2\text{CO}_3$)	CO_3^{2-}	600-650	Combined heat and power for decentralised stationary power systems and for transportation (trains, boats)
Solid oxide fuel cells (SOFC)	ceramic solid $\text{ZrO}_2(\text{Y}_2\text{O}_3)$	O_2^-	800-1000	Combined heat and power for decentralised stationary power systems and for transportation (trains, boats)

2.1.2 Low Temperature Fuel Cells

A fuel cell is an electrochemical system which converts chemical energy to electrical energy. A fuel cell differs from a battery in that fuels are continuously supplied and the products are continuously removed. There are two distinct fuels for low temperature fuel

cells: hydrogen as used in a H₂-PEMFC, and methanol as used in a DMFC. These fuel cells consist of six major parts: end plates, current collectors, flow channel blocks, gaskets, gas diffusion layers, and a membrane electrode assembly (MEA). Figure 2.1 shows the components of a low temperature fuel cell. The fuel cell principle enables a distinction between power and energy. The maximum power required determines the size of the fuel cell; the energy required determines the amount of fuel to be carried. The specific power (W.kg⁻¹) of the H₂-PEMFC is roughly twice that of the DMFC [5]. D.M. Bernardi et al. have found that because no mobile electrolyte is employed, corrosion problems in low temperature fuel cells are reduced and cell construction is simplified with few moving parts [6]. Also, fuel cells operate very quietly, therefore, reducing noise pollution [4].

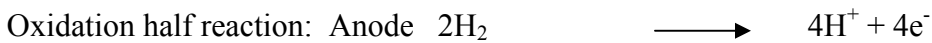
Since the proton exchange membrane used for the electrolyte is a solid phase, it does not penetrate deeply into the electrode as does a liquid one; therefore the reaction area is limited to the contact surface between the electrode and membrane [7]. The advantage of using solid electrolyte is that no electrolyte leakage will occur [8-9]. To meet the requirements of practical application a large number of single cells are assembled together to form a stack. The performance of a stack is different from that of a single cell. D. Chu et al. suggested that the stack has a much higher operating voltage, a greater power and better fuel-energy efficiency [10].

2.1.2.1 Principle of the H₂-PEMFC

H₂-PEMFCs have existed since the 1960s; in fact they were used in the Gemini aerospace program of the National Aeronautics and Space Administration (NASA) of the United

States. The MEA for H₂-PEMFCs consists of five components namely: a porous backing layer, an anode catalyst layer, a proton exchange membrane, a cathode catalyst layer, and a porous backing layer. Hydrogen is oxidized at the anode. The proton formed migrates through the membrane while the electrons flow through the external circuit. In the cathode reaction water is formed from oxygen, protons and electrons. Figure 2.2 shows the principle of the H₂-PEMFC.

The two half reactions for the H₂-PEMFC are as follows:



Cell reaction



2.1.4 Principle of the DMFC

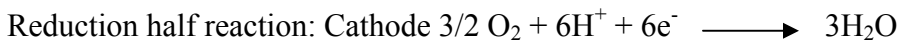
DMFC technology is relatively new compared to the H₂-PEMFC. However, the direct oxidation of methanol in a DMFC has been investigated over many years and some prototypes were built in the 1960s and early 1970s by the Shell Research Center in England [11, 12] and by Hitachi Research Laboratories in Japan [13, 14]. These studies were abandoned in the mid-1980s due to the low performance (25 mW.cm⁻² at best) resulting from the use of a liquid acid electrolyte [11, 15, 16]. An alkaline electrolyte was also used, but evolved CO₂ caused carbonation of the electrolyte resulting in decreased efficiency by reducing the electrolyte conductivity and de-polarizing the cathode [17, 18].

Chapter 2 - Literature Review

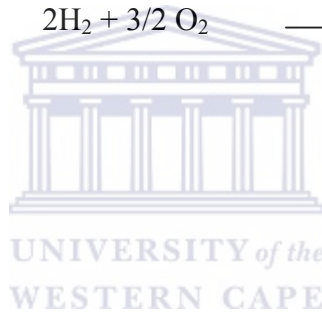
Currently all the research in DMFCs focuses on using solid proton exchange membranes as electrolyte, largely due to its proliferation in H₂-PEMFCs.

The structure of the DMFC is similar to the H₂-PEMFC. At the anode methanol is directly oxidized to carbon dioxide, and the reaction at the cathode is similar to the H₂-PEMFC. Figure 2.3 shows the structure of a DMFC.

The two main half reactions for the DMFC can be summarized as follows:



Cell reaction



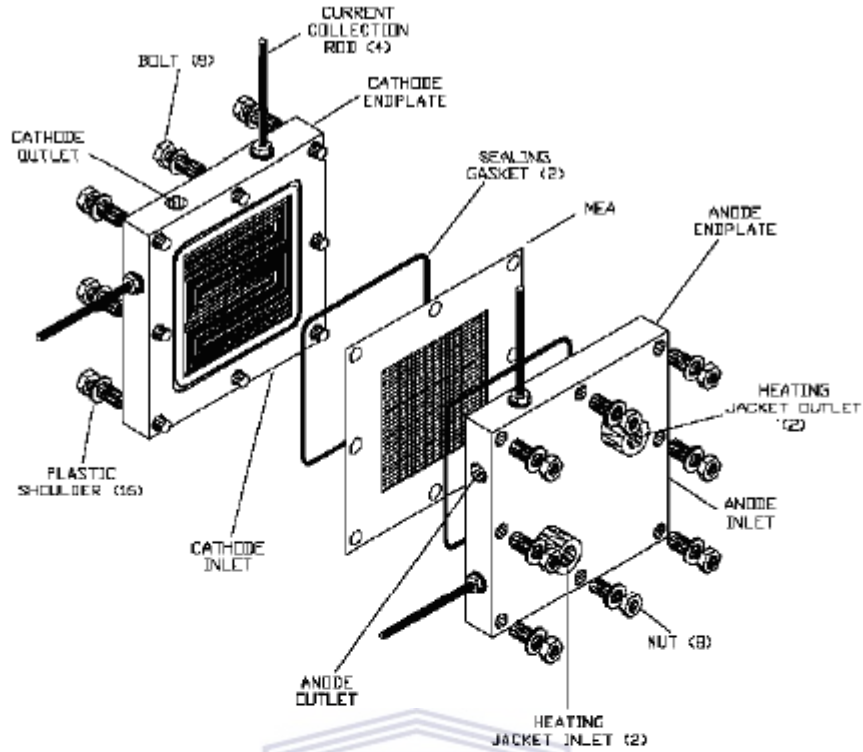


Figure 2.1: Low temperature fuel cell components.

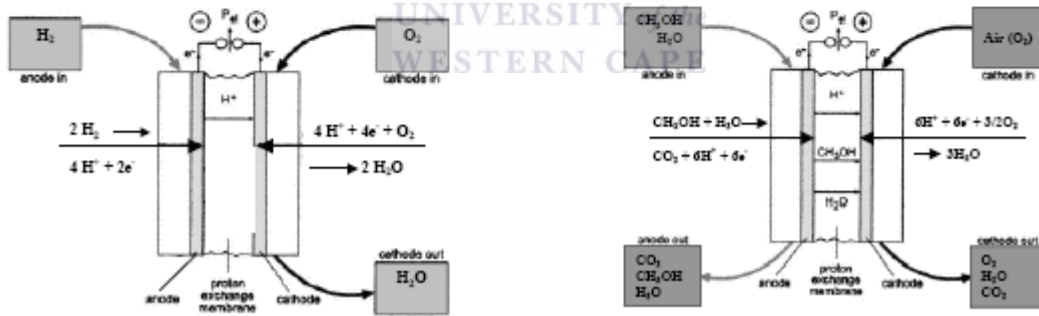


Figure 2.2: Principal of H₂-PEMFC.

Figure 2.3: Principal of DMFC.

2.1.5 Advantages and Disadvantages of DMFCs

The thermodynamic reversible potential for a DMFC is 1.21V at 25°C [20]. This value is comparable to that for a H₂-PEMFC, which is 1.23V [21-24]. In practice, a DMFC has a much lower open circuit voltage (OCV) [22] and electrochemical losses at both electrodes lead to a significant reduction in overall performance from the theoretical thermodynamic maximum [25].

Since methanol is used directly at the anode, and as a consequence, a DMFC requires less auxiliary equipment and is therefore a more simplified system compared to a H₂-PEMFC. Methanol is a liquid made from natural gas or renewable biomass sources, which is relatively cheap. Methanol is also easy to store, transport, and distribute, where advantage can be taken of the existing gasoline infrastructure. The anodic reaction is exothermic for both the H₂-PEMFC and the DMFC; heat management is a problem in H₂-PEMFC stacks whereas aqueous methanol acts as a coolant in DMFCs [26-29].

However, as the DMFC is still in its infancy, many problems need to be overcome to reach the commercialization stage. This includes the very sluggish methanol oxidation reaction, methanol crossover through the polymeric proton exchange membrane, CO₂ evolution at the anode [23, 25, 30-31], and cathode flooding [19, 32-34]. The methanol crossover through the polymer electrolyte leads to a mixed potential at the cathode, which results from the ORR and the methanol oxidation occurring simultaneously. This effect causes a negative potential shift at the cathode and a significant decrease of performance in the DMFC. Methanol crossover also causes fuel losses; it had been found that over 40% of methanol can be wasted in a DMFC across Nafion[®] membranes [35].

In a DMFC, cathode flooding, which typically occurs unless high cathode stoichiometries are used, can determine to a great extent overall cell performance [19, 32-34]. Water management in the DMFC is especially critical because anode water activity is near unity due to contact with liquid methanol solution [36]. Thus, unlike a H₂-PEMFC, no back-diffusive flux of water from cathode to anode will occur, and as a result, vaporization into dry cathode flow is the only pathway for removal of excess cathode-side water accumulation from electro-osmotic drag, ORR, and diffusion [36].

2.1.7 Hydrogen versus Methanol as a Fuel

There are many production processes possible for hydrogen. The current main industrial processes include Steam Methane Reforming (SMR) of natural gas, coal gasification and water electrolysis. These processes are well known and understood.

A major issue in the advancement of the H₂-PEMFC is that of hydrogen storage. Hydrogen storage can occur in one of the following forms: pressurized gas, cryogenic liquid, in absorbed form as metal hydrides, in absorbed form in carbon nanotubes, and as chemical storage in the form of a liquid fuel. Hydrogen compressed into a steel or reinforced plastic composite gas cylinder [37], can be achieved, but with considerable resultant size and weight penalty. Liquid hydrogen can be obtained by cooling hydrogen gas down to -253°C. The storage facility for liquid hydrogen must be very well insulated. Liquid hydrogen storage is an energy intensive process due to the high amount of energy needed to convert hydrogen to a liquid. Thus, liquid hydrogen is an inefficient choice [3]. It takes up to two hours to refuel tanks of three buses [38]. Hydrogen storage can also be in carbon nanotubes [39-43] and metal hydrides [37, 44-46]. A metal alloy exposed to hydrogen can form a metal hydride depending on the type of alloy. The release of

hydrogen usually involves the heating up of the metal hydride [3]. There have been a number of companies that have offered commercial hydride storage containers for many years, e.g. Ergenics Inc., Hydrogen Components Inc., Gesellschaft für Electrometallurgie, Japan Metals and Chemicals, Texaco Ovonic Hydrogen Systems L.L.C., HERA Hydrogen Storage Systems, etc. Chemical storage in liquid fuel form has the advantage of being able to utilize an already available infrastructure for fuel distribution to end-users [47]. On the other hand, an on-board fuel processor is necessary to convert liquid fuel to hydrogen [48]. A comparison of the specific energy densities of selected fuels and batteries is presented in Table 2.2.

Table 2.2: Specific gravimetric and volumetric energy densities of selected fuels and comparison with batteries [49]

	kW/kg	kWh/l
Diesel fuel	10,0	8,3
Gasoline	10,2	7,0
Ethanol	6,9	5,8
Methanol	5,0	4,2
Liquid H ₂	5,0	1,8
Compressed natural gas (CNG)(300 bar)	3,0	1,8
Pressurized hydrogen (300 bar)	1,1	0,4
Ti-Fe-hydride	0,4	1,2
Na/S batteries	0,12	0,13
Pb/PbO batteries	0,025	0,07

Methanol is produced from steam reformed natural gas and carbon dioxide using copper-based catalyst, and also from renewable biomass sources. Methanol is a leading candidate to provide the hydrogen necessary to power a fuel cell, especially in vehicular applications [48]. Methanol is currently used as a feed stock for a variety of widely used

organic chemicals, including formaldehyde, acetic acid, chloromethane, and methyl tert-butyl ether (MTBE).

Since 1965, methanol has been used in the United States as a fuel in certain vehicles (e.g. racing cars) either as pure methanol (M100) or as a gasoline-methanol mixture which consists of 15% gasoline and 85% methanol (M85). Nearly 15,000 methanol vehicles have been operating for nearly a decade now in California, New York and elsewhere in the United States. These methanol vehicles are supported by a fueling infrastructure of 100 methanol fueling stations in California alone and many more across the United States. A recent study by EA Engineering, Science, and Technology, Inc., shows that the capital cost of increasing the throughput of an existing gasoline station by adding methanol storage and methanol compatible piping and dispenser was about US\$ 62,400 [30]. Table 2.3 outlines a number of important properties of hydrogen, methanol and petrol relevant to the assessment of safety in case of an accident [51].

Table 2.3: Physical properties of hydrogen, methanol and petrol relevant to accident safety [51]

	Hydrogen	Methanol	Petrol
Molecular weight	2,016	32,04	107
Liquid density (g.ml ⁻¹)	71(LH ₂) 0,0013(GH ₂)	791	917,86
Vapor density relative to air (=1)	14 x lighter	1,1 x heavier	2-5 x heavier
Volatility (RVP-psi)		4,6-5,3	9-15
Boiling point (K)	20,27	338	310,94 - 477,6
Minimum ignition energy (m.J)	0,14	0,02	0,024
Diffusion coefficient (cm ² s ⁻¹)	0,61	0,0042	0,05
Flammability limits (vol.%)	4-75	6-36,5	1-7,6
Explosive limits (vol.%)	18,3-59,0	6-36	1,1-3,3
Fraction of heat in radiative form	17-25	17	30-42
Flame temperature in air (K)	2318	-	2470

2.1.7 Other Fuel for Low Temperature Fuel Cells

The question of whether customers will be fuelling their vehicles directly with hydrogen or via the hydrogen-rich carrier (e.g. methanol, ethanol, gasoline, diesel, etc.) still seems to be unanswered. This is a very important issue not just from a refueling infrastructure perspective but also from the public's perception and from the gearing-up of production, and developing guidelines for dealing with safety issues that will need to be put in place for the new fuel [51].

In principle, any type of liquid fuel may be employed as a hydrogen source, e.g. gasoline, diesel, methanol, ethanol, etc. Methanol can be reformed to hydrogen by different processes including steam reforming [52-59], partial oxidation [60-62] and autothermal reforming [63-66].

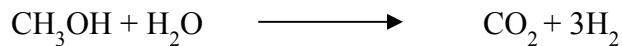
Steam reforming of methanol occurs by two different pathways [56-57]. The first one involves the decomposition of methanol into CO and H₂ through the following reaction:



followed by a water gas shift reaction:



The second mechanism for methanol steam reforming consists of the reaction of water and methanol to CO₂ and hydrogen:



which can be followed by a reverse shift reaction to establish the thermodynamic equilibrium:



Methanol steam reforming is endothermic and therefore requires that external heat, typically 300°C, is supplied. Steam reforming of methanol is usually catalyzed over Cu/ZnO-type catalyst and can be performed in fixed-bed reactors [58].

Methanol powered cars would consume less energy than diesel or gasoline powered cars. Furthermore, the overall emissions from the system are 90% less than from conventional vehicles [67].

Among other candidate liquid fuels, ethanol is a particular case, since it can easily be produced in great quantity by the fermentation of sugar-containing raw materials. In addition, in some countries (e.g. Brazil) ethanol is already distributed in gas stations for use in conventional cars with internal combustion engines.

Hydrogen is produced from ethanol in a process unit consisting of either a steam reformer (SR) or a partial oxidation (POX) reactor in series with a water-gas shift (WGS) reactor and a reactor for selective oxidation (SOX) of CO. Product gas from the reformer or the POX reactor, which operates at an exit temperature higher than 677°C, contains a mixture of H₂, CO, CO₂, CH₄ and H₂O. After cooling, this stream enters the WGS reactor, where a large fraction of CO reacts with H₂O towards CO₂ and H₂ at a temperature of 200°C. The product gas of the WGS reactor contains 0.1-1.5% of residual CO and enters the SOX reactor, where CO is totally oxidized - with the addition of a small amount of air - to CO₂ with residual CO being less than 10 ppm. The CO-free, hydrogen rich stream is then fed to the H₂-PEMFC [88].

Hydrogen can also be obtained from diesel fuel by a reforming process with an efficient overall cell design. A diesel fuel infrastructure is already in place; therefore the associated start-up cost of fueling with diesel would be significantly less than for

methanol-fueled systems. Diesel also has a much higher potential energy density than methanol. However, diesel fuel reforming is more complicated and requires much higher temperatures [69]. The tailpipe emission of hydrogen-fuelled fuel cell vehicles, in terms of the normally monitored pollutants, is zero, since the cell produces only water and heat. However, when a reformed hydrogen is used, the reforming process produces some pollutants; therefore, the principle of zero pollution is compromised. Direct fuel utilization will therefore be of interest. Besides methanol, other alcohols, particularly those coming from biomass resources, are being considered as alternative fuels. Ethanol as an attractive fuel for electric vehicles was investigated in direct ethanol fuel cells [15, 70-72]. However, multimetallic catalysts are necessary to orientate the oxidation reaction selectively in the direction of complete combustion to carbon dioxide [15]. The reaction mechanisms of anodic oxidation of ethanol are more difficult to elucidate than methanol oxidation, since the number of electrons exchanged greatly increases (12 electrons per ethanol molecule versus 6 electrons for methanol), and many adsorbed intermediates and products are involved [15]. However, a direct ethanol fuel cell was investigated by Aricò et al. [73] using a high temperature membrane (Nafion[®] / Silica), and also by Wang et al. [74] using a phosphoric acid doped polybenzimidazol (PBI) membrane.

Other fuels that were investigated for direct fuel cells included ethylene glycol [75-77], glycerol [78], propanol [15, 74, 79-83], propane [84-85], trimethoxy methane, [86], and dimethyl ether (DME) [87].

2.2 SUPPORTS AND PRECURSORS

2.2.1 Platinum salt precursors - Chloroplatinic Acid $H_2PtCl_4 \cdot 6H_2O$

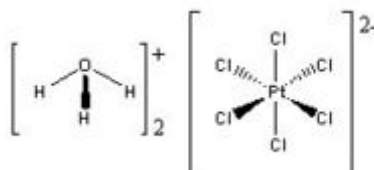


Fig. 2.2.1.1 Chloroplatinic Acid – hydrated

Various chemical routes are available for the synthesis of Pt-Ru catalyst. A common method is the reduction of metal chloride salts, but this preparation technique leads to significant amounts of chloride poisoning currently the most widely used chemical preparation technique is based on the oxidation and subsequent reduction of metal sulphite salts, which can be prepared from chloride metal salts [142, 186]. Recently, the Bönemann method was used to synthesize colloidal precursors for carbon supported and unsupported Pt-Ru catalysts by the Bönemann group [187-192] and subsequently by other groups [181, 193]. Furthermore, metal-oxide modified Pt-Ru catalyst was recently prepared [194]. A new method was also proposed by Dickinson et al. [195], where the catalyst is produced from carbonyl metal complexes by deposition of the precursors on carbon in high boiling-point solvent.

The chloroplatinic acid compound itself is very stable, but hygroscopic and handled with care avoiding acids, basis, light and water. Chloroplatinic acid I is produced by dissolving platinum metal sponge in a 1:3 (v:v) solution of nitric and hydrochloric acids called aqua regia [196]. This reaction produces a mixture of chloroplatinous acid (H_2

PtCl₄) and nitrosoplatinum chloride ([NO]₂ PtCl₄). The nitrosoplatinic chloride is removed by repeatedly extracting and evaporating HCl from the solid mixture produced in the reaction with platinum in aqua regia. The remaining chloroplatinous acid is then oxidized to chloroplatinic acid by saturating the solution with chlorine and heating to remove any excess HCl [199]. The resulting chloroplatinic acid is brownish-red [196]. Alternatively, the nitric acid in aqua regia can be replaced with a 30% solution of hydrogen peroxide. However, this preparation requires the use of finely divided platinum powder known as platinum black. This approach avoids the formation of the nitrosoplatinic chloride and the use of chlorine gas in the traditional synthesis [199]. Like many platinum compounds, chloroplatinic acid is used in catalysis. This compound was first used by John Speier and his colleagues to catalyze the reaction of silyl hydrides with olefins [198]. Typical of his reactions Speier used isopropanol solutions containing trichlorosilane (SiHCl₃), and methyldichlorosilane (CH₃SiCl₂), with pentenes. Speier found that chloroplatinic acid avoided polymerization, a problem that plagued attempts of hydrosilylation.

Much speculation has surrounded the actual site of catalysis in chloroplatinic acid. Speier himself proposed that catalysis centered on the platinate ion [202], and possibly involved an oxidative addition reductive elimination process with the olefinic substrate. This process seems plausible since the chlorine ligands are easily removable. However, more recent evidence has suggested that catalysis with chloroplatinic acid involves low valent platinum. The II and IV oxidation states of platinum could not be sufficient the

highly catalytic nature of the reactions observed. Instead Lewis and his co-workers have suggested a mechanism involving Pt^0 with olefins as ligands [203].

2.2.2 Carbon Supports

There has been continuing effort to increase the efficiency of carbon-supported Pt and Pt alloys, which are the most important electrocatalysts for the reactions of interest in fuel cell technology. One possibility to enhance the activity of the catalyst is to increase its surface area by dispersing it on a proper support. The importance of the supporting material for the functioning of the catalysts is well recognized. It has to offer a highly developed surface combined with excellent electronic conductivity and corrosion resistance. Most often the increase in surface area is achieved by deposition of nano-sized catalyst particles on carbon supports [204-206]. Until now, the microporous carbon blacks, such as Vulcan XC-72 or Ketjen Black have been most frequently used as supports of the electrocatalysts. Recently, carbon aerogels and carbon cryogels prepared by sol-gel polycondensation of resorcinol and formaldehyde [207-215] have been attractive as new supports of electrocatalyst for the fuel cell. Carbon aerogels and cryogels are a special class of carbon materials with many common characteristics, such as a tortuous open-cell structure, ultrafine particle and pore size, and high specific surface area ($400\text{--}1000\text{m}^2\text{ g}^{-1}$). Their unique microstructure originates from their wet-chemical preparation by the solution sol-gel method and subsequent solvent removal via supercritical or freeze-drying. These novel carbon materials thus offer interesting opportunities for preparation of nano-composite electrocatalysts. Although carbon

aerogels possess superior porous properties, their commercial applicability is quite limited mainly due to their high cost of production. Supercritical drying is thought to be the most costly process during production of carbon gels. It has been shown that mesoporous carbon could be obtained even when more economical drying methods, such as freeze-drying [216-230] are used instead of supercritical drying. Pt catalysts prepared using the modified polyol synthesis method on the novel carbon cryogel support and commercial Vulcan XC-72 were used in order to investigate the effect of the physical structure of the support (porosity and surface area) on the size distribution and dispersion of Pt catalyst particles so as, consequently on catalytic activity for the hydrogen oxidation reaction. In this study, we also report a simple procedure for the preparation of Pt catalysts based on the polyol synthesis method. This method is a very efficient way to prepare noble metal nanoclusters with very small particle size and very narrow particle size distribution. The synthesis procedure given by Zhou et al. [231] was modified and used for catalyst preparation. Many investigations have since been performed to study the influence of the specific surface area of carbon black supports on the fundamental properties of Pt/C catalyst, such as the mean metal particle size and particle size distribution and their dispersion, when comparing two kinds of carbon black, such as: (A) carbon cryogel synthesized by sol-gel polycondensation and freeze-drying, with a specific surface area (BET) of $517\text{m}^2\cdot\text{g}^{-1}$ (the preparation procedure was thoroughly described previously in Ref. [220] and (B) commercial Vulcan XC-72 (Cabot International) with a specific surface area (BET) of $180\text{m}^2\cdot\text{g}^{-1}$. The prepared catalysts were denoted as Pt/C (cryogel) and Pt/C (XC-72), respectively.

2.2.3 Surface Chemistry of Carbon Black

All carbon blacks have chemisorbed oxygen complexes (i.e. carboxylic, quinonic, lactonic, phenolic groups and others) on their surfaces to varying degrees depending on the conditions of manufacture. These surface oxygen groups are collectively referred to as volatile content. Electrode preparations for fuel cell applications involves the technique of spraying the ink preparations of binder i.e. Nafion and Nano-sized metallic particles onto gas diffusible carbon cloth. The inks industries prefer grades of carbon black that acid oxidized. Acid is sprayed in high temperature dryers during the manufacturing process to change the inherent surface chemistry of the black. The amount of chemically bonded oxygen is increased to enhance the surface performance characteristics. UV protection, infrared absorption and heat protection are important in robust applications such as fuel cell electrodes that are exposed to changing temperatures, oxidation and catalytically enhanced reactions. Carbon black protects products from UV light because of its ability to absorb and dissipate light rays. UV rays are harmful because the cause product breakdown, making UV protection especially important in inks when used in the presence of light.

2.2.4 Electrical Conductivity of Conductive Carbon Blacks

The electrical conductivity of conductive carbon blacks is related to their surface properties. For small surface area conductive blacks, a good correlation between the conductivity and the graphitic character of the surface exists. This correlation could also be extended to other types of blacks, confirming the determining influence of the surface graphitic character on the conductivity. Other properties such as the chemical nature of

oxygen- and sulphur-containing surface groups have only a very limited influence on the conductivity. The graphitic character can be characterized by three different techniques. However, it should be recognized that, in fact, each of these techniques measures a different property related to the graphitic character: (i) the homogeneity of the electronic environment of the carbon atoms on the surface (XPS, FWHM of the C_{1s} peak), (ii) dimensions of the graphene layers on the surface (ratio of the SIMS C_2H^-/C_2^- peaks), and (iii) homogeneity of the surface topology (low pressure nitrogen adsorption). This explains the differences in the correlations of these parameters with conductivity. For example, for the SIMS parameter a good correlation was found for all types of blacks with the exception of high surface area conductive blacks, whereas for the XPS parameter this was the case for all blacks, except the thermal black.

2.2.5 Effects of Carbon Pretreatment for Oxygen Reduction

The activity and durability tests of carbon-based gas diffusion electrodes strongly depend on the mode of thermal, chemical and physical pretreatment of the carbon blacks. The pretreatment steps in turn influence the surface and physicochemical properties of the carbons to be selectively applied for the ORR in alkaline electrolyte. The ageing rate could be ascribed to the disruption of the three phase boundary i.e. when electrolyte penetration and inaccessibility of oxygen in the porous system of the electrodes become dominant. Furthermore, carbonate precipitation in the porous system significantly enhances the “flooding” of the electrode and suppresses the hydroxide concentration as well as interferes with the electrode kinetics affecting the durability and activity of the gas diffusion electrodes. Based on the results obtained in this literature study, the

following conclusions could be deduced from the effects of pretreatment on the physicochemical changes of the carbon black materials as well as on their electrochemical activity and stability for the ORR:

- High weight loss is observed when carbon blacks are pretreated at high temperatures in the presence of CO₂, which might be ascribed to the loss of the volatile or oxygen containing groups. The more the volatile content, the larger is the loss of weight.
- High pH changes are encountered for all samples of Vulcan XC-72, when heat-treated at both 600 and 900 °C in the presence of hydrogen gas, while the same was observed at both temperatures when samples of Ketjenblack EC are treated with CO₂.
- Increased BET-surface areas have been measured for Vulcan XC-72 when heat-treated at 900 °C in the presence of CO₂, while the same was observed for Ketjenblack EC at the same temperature but in a nitrogen atmosphere.

Although no clear distinction can be drawn on the relationship between the electrochemical activity towards ORR and the characterization of the carbon blacks, the potentials at 50 mA.cm⁻² show that increased temperature treatment has more significant effect on improved electrode performance than low temperature treatment.

High temperature treatment and high BET-surface area carbon blacks have shown increased stability for the gas diffusion electrodes in the alkaline media. An overall increase in stability was noted for carbon blacks treated with formic acid when compared to the corresponding untreated, gas or fluoric acid treatments. The wettability as well as the decay rate for the formic acid-treated electrodes is less pronounced. Further studies

on the role of gases and high temperature on some selected samples, which have shown enhanced activities and stability, are to be carried out in future research in order to characterize and determine reactivity, porosity, textural and chemical properties both before and after electrochemical tests of the carbons.

2.2.6 Carbon Nano-Tubes

"Conceptually, single-wall carbon nanotubes (SWCNTs) can be considered to be formed by the rolling of a single layer of graphite (called a graphene layer) into a seamless cylinder. A multi-wall carbon nanotube (MWCNT) can similarly be considered to be a coaxial assembly of cylinders of SWCNTs, like a Russian doll, one within another; the separation between tubes is about equal to that between the layers in natural graphite. Hence, nanotubes are one-dimensional objects with a well-defined direction along the nanotube axis that is analogous to the in-plane directions of graphite."
—M. S. Dresselhaus, Department of Physics and the Department of Electrical Engineering and Computer Science, Massachusetts Institute of Technology

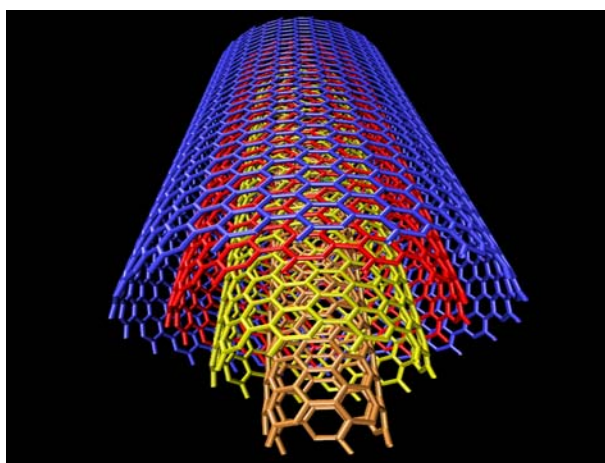


Fig. 2.2.1.6.1 Multiwalled carbon nanotubes

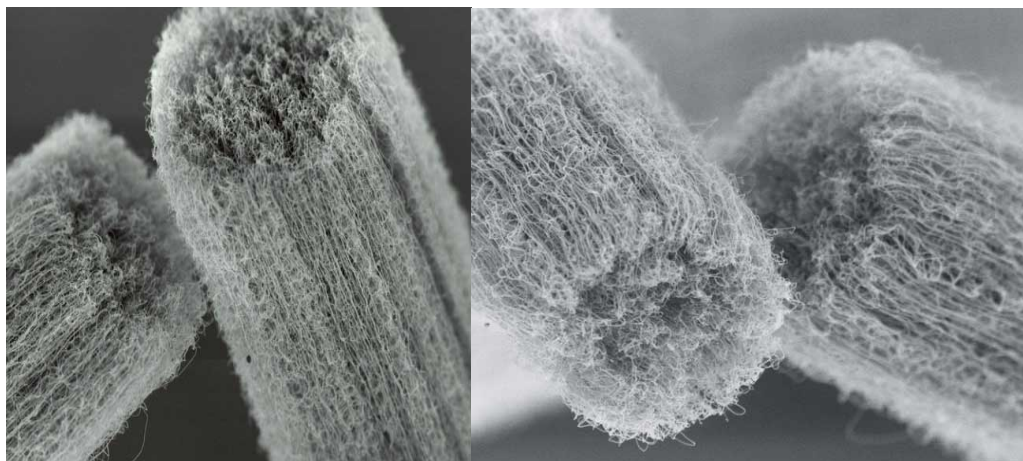
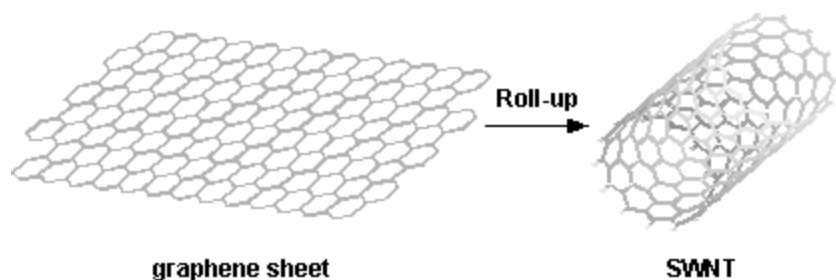


Fig. 2.2.1.6.2 TEM images of Multiwalled carbon nanotubes

A commonly mentioned non-carbon variety is made of boron nitride, another is silicon. These noncarbon nanotubes are most often referred to as *nanowires*. The dimensions are variable (down to 0.4 nm in diameter) and one can also get nanotubes within nanotubes, leading to a distinction between multi-walled and single-walled nanotubes. Apart from a remarkable tensile strength, nanotubes exhibit varying electrical properties (depending on the way the graphite structure spirals around the tube, and other factors, such as doping), and can be superconducting, insulating, semiconducting or conducting (metallic). [CMP]

Nanotubes can be either electrically conductive or semiconductive, depending on their helicity, leading to nanoscale wires and electrical components. These one-dimensional fibres exhibit electrical conductivity as high as copper, thermal conductivity as high as diamond, strength 100 times greater than steel at one sixth the weight, and high strain to failure. A nanotube's chiral angle--the angle between the axis of its hexagonal pattern and the axis of the tube--determines whether the tube is metallic or semiconducting. A graphene sheet can be rolled more than one way, producing different types of carbon nanotubes. The three main types are armchair, zig-zag, and chiral.



Copyright Professor Charles M. Lieber Group

Fig. 2.2.1.6.3 Carbon Nanotube Tips for Atomic Force Microscopy

Carbon nanotubes possess many unique properties which make them ideal AFM probes. Their high aspect ratio provides faithful imaging of deep trenches, while good resolution is retained due to their nanometer-scale diameter. These geometrical factors also lead to reduced tip-sample adhesion, which allows gentler imaging. Nanotubes elastically buckle rather than break when deformed, which results in highly robust probes. They are electrically conductive, which allows their use in STM and EFM (electric force microscopy), and they can be modified at their ends with specific chemical or biological groups for high resolution functional imaging. CNTs exhibit extraordinary mechanical properties: the Young's modulus is over 1 Tera Pascal. It is as stiff as diamond. The estimated tensile strength is 200 Giga Pascal. These properties are ideal for reinforced composites and nanoelectromechanical systems (NEMS). Carbon Nanotube Transistors exploit the fact that nm-scale nanotubes (NT) are ready-made molecular wires and can be rendered into a conducting, semiconducting or insulating state, which make them valuable for future nanocomputer design. Carbon nanotubes are presently quite popular for their prospective electrical, thermal and even selective-chemistry applications.

Many potential applications have been proposed for carbon nanotubes, including conductive and high-strength composites; energy storage and energy conversion devices; sensors; field emission displays and radiation sources; hydrogen storage media; and

nanometer-sized semiconductor devices, probes, and interconnects. Some of these applications are now realized in products. Others are demonstrated in early to advanced devices, and one, hydrogen storage, is clouded by controversy. Nanotube cost, polydispersity in nanotube type, and limitations in processing and assembly methods are important barriers for some applications of single-walled nanotubes. Carbon Nanotubes—the Route Toward Applications Ray H. Baughman, Anvar A. Zakhidov and Walt A. de Heer.

2.2.7 Characterization of Carbon Supports

Specific surface areas of different carbon black supports were determined from nitrogen adsorption isotherms, before and after addition of nano-sized Pt particles. All supports are characterized by quite similar nitrogen adsorption isotherms with a hysteresis loop in the desorption branch indicative of a significant mesoporosity. Specific surface areas calculated from the BET equation, S_{BET} , are listed in the [table below](#). The mesoporous surface area of the carbon cryogel sample decreases with addition of nano-sized Pt particles, while the micropore volume and mesoporous surface area of XC-72 sharply decrease with addition of Pt particles.

Table 2.2.1.7: Porous Properties of Carbon Supports

Sample					
Pt/C (cryogel) + 20wt.% Pt			Pt/C (XC-72) + 20wt.% Pt		
S_{BET} (m^2g^{-1})	S_{meso} (m^2g^{-1})	V_{micro} (cm^3g^{-1})	S_{BET} (m^2g^{-1})	S_{meso} (m^2g^{-1})	V_{micro} (cm^3g^{-1})
573	258	0,15	180	77	0,05
517	234	0,13	91	15	0,03

The specific surface area of Vulcan XC-72 determined in this experiment is lower than the value ($273\text{m}^2\text{g}^{-1}$) declared by the manufacturer.

2.3 ANODE CATALYST - METHANOL OXIDATION

2.3.1 Anode Catalyst - Methanol Oxidation

Methanol oxidation has been extensively studied for the last three decades. Very few electrode materials are capable of methanol oxidation - only platinum and platinum-based catalysts have been found to display the necessary reactivity and stability in the acidic environment of the DMFC, and almost all mechanistic studies have concentrated on these materials [29, 88].

Methanol oxidation and its mechanisms in different catalyst systems under well-characterized conditions have been reviewed [16, 21, 28, 88-101]. Methanol oxidation can be summarized in terms of two basic functionalities: (a) Electrosorption of methanol

onto the substrate and (b) Addition of oxygen to adsorbed carbon-containing intermediates to generate CO_2 [88].

Morphology appears to play a major role in the electro-activity of platinum [102], with roughened platinum showing much higher activity [103]. Methanol adsorption is inhibited, in general, by the adsorption of anions: chloride ions strongly inhibit methanol oxidation at platinum, while bromide and iodide ions entirely arrest the process [104]. Adsorbed phosphate ions also inhibits the rate of methanol oxidation [105].

The influence of particle size on methanol oxidation has been investigated by numerous authors [106-114]. However, there is considerable controversy over whether there exists a “size effect” in methanol oxidation. Some authors have observed a decrease in activity with decreasing particle size for particles with diameter less than 5 nm [106-115]. Earlier data from Shell suggested that there was a pronounced size effect, with an optimal Pt cluster diameter of ca. 3 nm [109, 110] and the Oxford group suggested an optimal diameter of ca. 2 nm [111-113]. However, Watanabe et al. [114] do not find any evidence for size effects, even for particles as small as 1.4 nm. The methods of electro-catalyst preparation and their subsequent treatment in reducing atmospheres differ considerably in the various studies relating to the particle size effect [115, 116].

It was first shown by Electrochemically Modulated Infrared Reflectance Spectroscopy (EMIRS) that the main poisoning species formed during the chemisorption and oxidation of methanol on a platinum electrode is CO, either linearly bonded or bridge bonded to the surface [117]. The coverage by linearly bonded CO can reach 90% on a pure platinum

electrode, so that most of the active sites are blocked [15]. Such results were widely confirmed [76, 89, 118-127].

Platinum itself, though widely studied as an electro-catalyst for methanol oxidation, is not sufficiently active, and there has been an intensive search for other active materials - in particular, materials that might be able to combine with platinum as promoter by facilitating the oxidation of the chemisorbed CO [88].

Pt promotion can be obtained by using surface ad-atoms deposited on the platinum surface, such as Au [128], Sn [129-133], Ru [133-135], Pb [133, 136] and Bi [131, 133, 137]. Also Pt promotion can be effected by alloying platinum with different metals, where the second metal forms a surface oxide in the potential range for methanol oxidation [88, 138]. Such alloys are Pt-Sn [129, 133, 139-141], Pt-Os and Pt-Ir [142], Pt-Pd [143] and Pt-Ru [130, 140, 142, 144-155]. WO_3 as a promoter for Pt was also investigated [156-164]. Electrodeposited Mo on Pt has also been reported [165-166]. The combination of Pt with a base-metal oxide as promoter (e.g. Nb, Zr and Ta) has been reported by Hamnett et al. [156].

The methanol electro-oxidation activity of the Pt-Ru was found to be the highest of the binary Pt-based alloys [46, 49, 167-170]. Studies on Pt-Ru suggested that the reaction occurs by the dissociative adsorption of methanol on platinum sites to form a strongly adsorbed intermediate, CO. In parallel, at higher levels of polarization, water adsorbs and dissociates on Ru sites to provide a hydroxylic species that subsequently oxidizes the CO.

The dissociation of water on Ru occurs at lower potentials than on Pt, resulting in the enhanced activity for Pt-Ru over pure Pt [171-174].

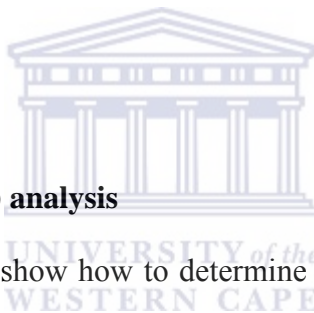
Given the effectiveness of binary alloy formation, particularly with Pt-Ru, attention has turned to ternary alloys. The Pt-Ru-Sn system was explored [175, 176] but it was found that alloying Pt-Ru with tin tends to expel the Ru leading to no advantage [186-195]. Other ternary systems reported were Pt-Ru-Os [177-179] and Pt-Ru-W [180, 181]. Quaternary systems were also explored, including Pt-Ru-Os-Ir [178], Pt-Ru-Mo-W [182] and Pt-Ru-Sn-W [183-185].

2.3.2 XRD Characterization Analysis of a typical 20 wt. % Pt/C catalyst

The characteristic diffraction peaks of the face centered cubic (fcc) Pt demonstrate that a successful reduction of Pt precursor to metallic form has been achieved. The peak of $2\theta = 42.4$, corresponds to hexagonal graphite structure (1 0 0) and suggests that carbon support has a good graphite characteristic locally. The diffraction peaks at about 39° and 46° are due to the Pt(1 1 1), and (2 0 0) plane, respectively, which represents the typical character of a crystalline Pt face, that is fcc. There are no distinct reflection peaks in the spectra, in the investigated 2θ range other than those of the three peaks mentioned above, indicating that most of the in-house-supported Pt catalysts have prevailed Pt (fcc) crystal structure [204-209].

2.3.3 TEM analysis

From the low-magnification TEM micrographs, it is found that metal particles of all supported Pt catalysts are very uniform. However, at this magnification, there is little apparent difference between investigated catalysts. A typical TEM image of in-house Pt/C catalysts and Pt particle size distribution with a mean particle size of about 2.65 nm has a narrow particle size distribution on carbon support. In comparison, the mean particle size or the particle size distribution of Pt on Vulcan XC-72 or MWCNT carbon support is higher and becomes wider and has mean size of 3.4 nm depending on the reduction method utilized for the catalyst preparation. The histograms of Pt particle size distribution of Pt/C catalysts are based on measurements of over 300 individual Pt particles [208, 214, 215-217].



2.3.4 Cyclic voltammetry (CV) analysis

Here a typical CV was used to show how to determine the electrochemical surface area and to elucidate the adsorption properties of the catalysts. The CV was performed in 0,5 mol.dm⁻³ HClO₄ for a Pt/C catalyst. The electrochemically active surface area of the catalysts was calculated from the charge associated with the anodic desorption peak of hydrogen. The base line was taken by extrapolation of the double-layer region of the voltammogram. The electrochemically active surface area of the catalysts (*S_{esa}*) was calculated from the measured charges assuming 210μC.cm⁻² as a charge of full coverage.

The total surface area can also be calculated using the following equation:

$$S_{\text{tot}} = \frac{6 \times 10^3}{Pd} \quad (1)$$

where d is the mean Pt particle size in nm (from TEM results) and ρ is the density of Pt metal (21.4 g.cm^{-3}). Then the Pt utilization efficiency for RDE can be calculated, using the following equation:

$Pt_{u.e.} = S_{easa}/S_{tot}$ (S_{easa} is the electrochemical active surface area). Taking into account the results obtained from BET, TEM and cyclic voltammetry analysis one can conclude that the size of Pt particles decreases with an increase in the specific surface area of the carbon support [204-211].

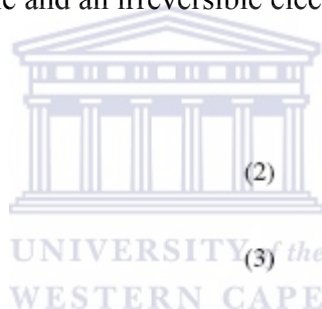
2.3.4.1 Kinetics of the hydrogen oxidation at Pt/C catalysts

Kinetic equations for a reversible and an irreversible electrochemical reaction [21],

respectively, can be given as:

$$E = E_1^0 - \frac{2.303RT}{nF} \log \left(\frac{I_L - I}{I_L} \right) \quad (2)$$

$$E = E_2^0 + \frac{2.303RT}{\alpha nF} \log \left(\frac{I_L \cdot I}{I_L - I} \right) \quad (3)$$



where E_1^0 and E_2^0 are current independent constants, and α is the charge transfer coefficient. Eq. (2) is used to obtain the mass transport corrected Tafel diagrams if the reaction is assumed reversible, while Eq. (3) is employed to obtain mass transport corrected Tafel diagrams if the reaction is irreversible. If one or the other condition is satisfied, according to Eqs. (2) or (3), the plots should be linear with the points independent of the rotation rate. It is clearly seen in Fig. 3.3.4.1.2 that linear plots independent of rotation speed are obtained when reversible kinetics are assumed. The slopes of the linear plot very close to the theoretical value of 29 mVdec^{-1} . However, there is no agreement with the prediction of Eq. (3). In this case the linear relationship of E -log

$[(I_L \times J)/(I_L - J)]$ is also established in the potential range, where the correction for the backward reaction is not necessary, but liner plots depend on rotation speed and the slopes are limited to 30–35mV.dec⁻¹, that is only half of the predicted value of 58mV.dec⁻¹. Therefore, most reasonable assumption that the hydrogen oxidation reaction for both investigated Pt/C catalysts is electrochemically reversible seems to be experimentally supported. It is not practicle to determine the exchange currents (I^0) simply by extrapolating the Tafel lines to the reversible potential due to the absence of a well-defined Tafel region. The exchange current is estimated from the slope of the linear polarization response and after correction for diffusion, using the following equation:

$$\frac{\Delta E}{\Delta I} = \frac{RT}{nF} \left(\frac{1}{I_0} + \frac{1}{I_L} \right) \quad (4)$$

where $n = 2$ and I_L is the limiting current. This calculation assumes that the HOR and hydrogen evolution reaction (HER) follow the same reaction mechanism around the equilibrium potential. The calculated values and corresponding values of the exchange current densities were obtained by dividing the exchange current with the active surface area of Pt particles. These values have the same order of magnitude as those for the HOR in acidic solution at single crystal [225, 226] and polycrystalline [227] Pt determined by the RDE technique. The mechanism of the HOR has been extensively studied in acidic and base solutions. The chance of extracting two electrons directly from H₂ in a direct discharged reaction is usually considered low. However, the kinetic analysis shows that HOR takes place at Pt/C catalysts as a reversible two-electron direct discharged reaction.

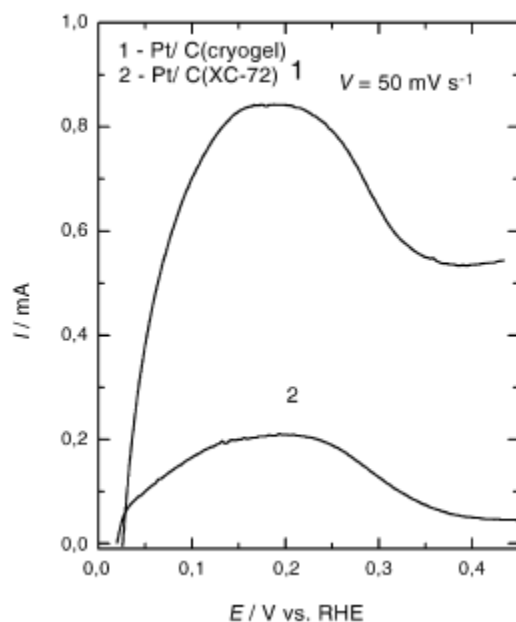


Fig. 2.3.4.1.1 Hydrogen desorption peak area in the CV curves of Pt/C catalysts.

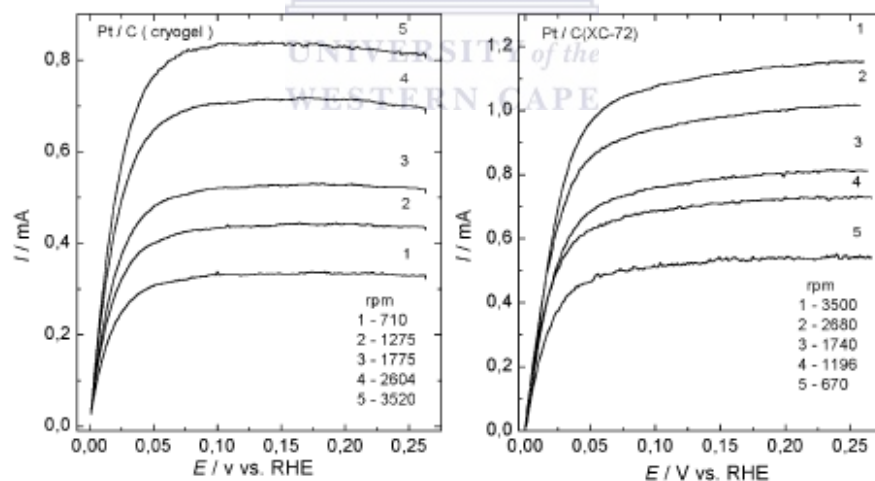


Fig. 2.3.4.1.2 Current vs. potential curves of the electrocatalytic oxidation of H_2 ($T = 293$ K, $v=2mVs^{-1}$) on RDE electrodes: Pt/C(cryogel) and Pt/C(XC-72) in 0.5 mol dm^{-3} $HClO_4$ solution under H_2 atmosphere.

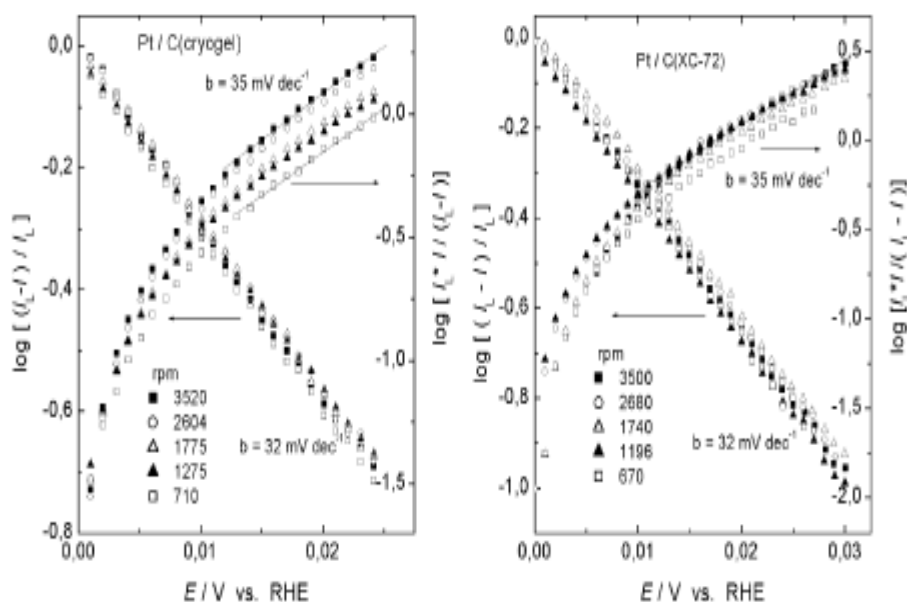


Fig. 2.3.4.1.3 Plots of $E-\log [(I_c - I)/I_c]$ and $E-\log [I_c \times I/(I_c - I)]$. Data taken from the RDE plots in Fig. 3.3.4.2: Pt/C(cryogel) and Pt/C(XC-72).

Finally, the specific activity of Pt/C catalysts for HOR is similar, despite the differences in the specific surface area of the Pt particle catalysts [218-225].

2.3.5 Citrate reduction of platinum

It was experimentally found that Pt^{4+} could not be reduced by citrate at room temperature even after a sufficiently long period of time. This finding is in some way expected as Turkevich and Kim had reported that the Pd^{2+} reduction by citrate was not feasible below 50°C [227]. Hence, the room temperature reduction of Pt^{4+} had to be assisted by NaBH_4 . The particles were smaller and more narrowly distributed due to the presence of citrate as a stabilizer during synthesis [228]. Varying the amount of citrate used from 1×10^{-4} to 4×10^{-4} mol ($\text{H}_2\text{Cyt}^-:\text{PtCl}_6^{2-} = 2:1$ to $\text{H}_2\text{Cyt}^-:\text{PtCl}_6^{2-} = 8:1$) had no apparent effect on the morphology, size, and size distribution of the particles. Cyclic voltammetry studies showed that all Pt-1 catalysts with the same Pt loading had the same activity and

therefore independent of the amount of citrate used in the synthesis. The dispersion of Pt on the carbon support was as high as that attainable by poly(N-vinyl-2-pyrrolidone) (PVP), which is generally considered as the most effective polymeric stabilizer for this purpose [238].

A number of papers have reported on the preparation of Pt hydrosols by the citrate reduction of chloroplatinic acid. Elevated temperature and prolonged heating are often required. The Pt hydrosols so prepared varied in size from 1.6 nm [248] and 2.0 nm [245] to 2.5 nm [244]. Particle size was reported to increase with increasing temperature, e.g. from 1.6 to 3.2 nm when the temperature was increased from 80 to 90 °C [248]. A stabilizer such as polyacrylate was often present to impart stability to the Pt hydrosol [244]. The synthesis of Pt hydrosol by citrate reduction was also carried out using microwave heating to substitute for conventional conductive heat transfer, but in the absence of a polymeric stabilizer. The energy efficient microwave heating was used to provide a homogenous reaction environment for the formation of more uniform Pt nanoparticles. All the particles in Pt-3 were in the range of 1.7–3.2 nm, with the majority of them at 2.2 nm. The particle size was significantly smaller than that of Pt-1 (4 nm) and the ETEK Pt/C catalyst (3.5 nm). As in the case of Pt-1, excess citrate used in the synthesis of Pt-3 did not bring about any decrease in the particle size. It was observed that the reduction of Pt⁴⁺ occurred in a few minutes after the reaction mixture was microwave heated to boiling temperature. However, to ensure the complete reduction of Pt⁴⁺ and a better dispersion of the Pt nanoparticles on the carbon support, the reaction was allowed to continue for 1 h. By comparison, the time taken to process the same batch of material by conductive heating would be about 3.5–4 h [244-249]. The particle size

obtained by microwave-assisted citrate reduction of Pt⁴⁺ (2.2 nm) was also smaller than that by microwave-assisted ethylene glycol reduction (3.5–4 nm) [11]. The XRD patterns of Pt-1 and Pt-3 catalysts show both catalysts have strong diffraction peaks at Bragg angles of 39.88, 46.38, 67.58 and 81.38 can be indexed to the (1 1 1), (2 0 0), (2 2 0) and (3 1 1) planes of face-centered cubic (fcc) platinum [249]. A volume-averaged particle size can be calculated from the Scherrer equation based on the Pt(2 2 0) peak.

$$L = \frac{0.9\lambda_{K\alpha 1}}{B_{2\theta}\cos\theta_{\max}}$$

$B_{2\theta}$ is the half where L is the average Pt particle size, λ_K the wavelength of the incident X-ray (Cu K α 1 = 1.5406 Å), $2\theta_{\max}$ the Bragg angle for peak maximum and width at peak maximum [250]. The average Pt particle sizes in Pt-1 and Pt-3 calculated this way were 4.8 and 2.5 nm, respectively, and agreed well with the TEM measurements.

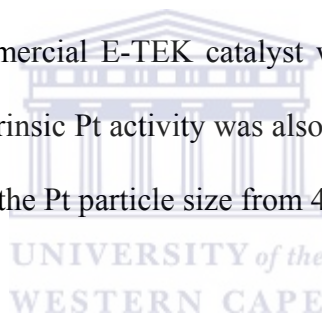
The current density was normalized by the geometrical area of the working electrode to indicate the catalyst mass activity. The Pt loadings for Pt-3 and Pt-4 were approximately 20 wt.% according to EDX. The voltammetric features are typical of methanol oxidation catalyzed by Pt [251]. The forward anodic peak at ca. 0.65 V was methanol electro-oxidation on Pt. The reverse anodic peak at 0.45 V was methanol oxidation on reactivated oxidized Pt sites [235]. The anodic peak current density was higher in Pt-3, indicating that it was the better catalyst of the two. Hence, despite the lack of apparent difference between the geometrical attributes of the nano-particles (size, shape and distribution), excess citrate used in the catalyst preparation did affect the catalytic activity in a negative way. This is different from the case of Pt-1, where excess citrate had little influence on the catalyst activity. In stark contrast to a previous study where thermal post-treatment

(400°C in N₂) was applied to Pt/C catalysts prepared by the NaBH₄ reduction of H₂PtCl₆ in the presence of citric acid under alkaline conditions [228], the catalysts in this study were not thermally treated in order to prevent particle sintering at high temperatures. In the preparation of Pt-1, the citrate functioned primarily as a stabilizer as it was unable to reduce Pt⁴⁺ under the low temperature experimental condition. In the preparation of Pt-3 and Pt-4, citrate was the reducing agent cum stabilizer. The adsorption of reaction products or reaction intermediates in citric acid oxidation [235-239] on the nano-particles could have contributed to the observed activity decrease with the increase in citrate presence in the preparation. Unfortunately, FTIR spectroscopy was unable to provide substantiating evidence for the adsorption of citrate or its oxidation products on the nanoparticles. This explanation can only be offered as a working hypothesis. The Pt loading in the three catalysts was kept at around 20 wt.% determined by EDX. Catalytic activity was evaluated by the anodic peak current density in the forward scan, and was found to increase in the following order: Pt-1 (33 mA.cm⁻² or 330 mA.mg⁻¹ Pt), ETEK-Pt (38 mA.cm⁻² or 380 mA.mg⁻¹ Pt) and Pt-3 (46 mA.cm⁻² or 460 mA.mg⁻¹ Pt). In theory, the specific surface area of Pt (m²/g) is inversely proportional to the particle size. Hence, the amount of metal required to provide the same surface area is halved when the particle size decreases by 50% [252]. In the current case, the peak current density increased with the decrease in Pt particle size but not reciprocally. Therefore, the mass activity difference between these three catalysts was not purely due to the difference in their surface areas and the quantum size effect of small nano-particles could be at work [253]. Although mass activity is a good indicator to measure the effectiveness of metal utilization in a catalyst, specific activity, which uses the electrochemically active surface

area (ECSA) for the normalization of measured currents, is a more useful measure of the intrinsic activity of Pt [232]. The electrochemically active surface area of Pt is often estimated from the charge associated with hydrogen adsorption on Pt [229]. Multiple hydrogen adsorption/desorption peaks with different intensities were obtained in the region -0.2 to 0.1 V for all the catalysts. This can be used to indicate the presence of well-developed Pt crystal faces [229, 254]. Besides the difference in electrochemically active surface areas due to the different particle size, the surface Pt oxide reduction peak also shifted progressively negative with the decrease in particle size as a result of the increase in the OH adsorption strength, which was shown by an earlier in situ XAS investigation [255]. This size dependence effect is consistent with previous reports [256, 257]. Although the mass activity increased with decreasing particle size, the specific activity showed the opposite trend, which is similar to the conclusion of others [256, 258]. The size effect on the intrinsic Pt activity could be caused by the restricted diffusion of reaction intermediates (e.g. CO_{ads}) on small particles [256]. On the other hand, it has been suggested that maximum electrochemically active surface area exists in Pt particles about 2 nm in size, subsequently producing the best observed mass activity [243]. The high mass activity and low intrinsic Pt activity of Pt-3 may be rationalized on the same basis. For practical applications as a catalyst, the more important activity indicator is the mass activity since it reflects noble metal utilization. Although unable to establish the extent of citrate remnants' presence on the catalyst surface that might interfere with the intrinsic activity of Pt (the adversarial effects were implicated in the comparison between Pt-3 and Pt-4), the mass activity of Pt-3 still surpassed that of a commercial catalyst of the same Pt loading. The citrate-route of low temperature synthesis is currently being

extended to the preparation of PtRu catalysts, which are known to be more CO tolerant in low temperature DMFC applications.

Carbon-supported Pt nano-particles were prepared by relatively low temperature chemical reduction methods: NaBH₄ reduction of H₂PtCl₆ with and without citrate and the citrate reduction of H₂PtCl₆ by microwave heating (under reflux). The addition of citrate definitely contributed to smaller particle size and narrower size distribution, particularly for the microwave-assisted synthesis. Excess citrate was not adversarial to catalytic activity in the NaBH₄ reduction of H₂PtCl₆, but was a concern in the microwave-assisted reduction of H₂PtCl₆. It was shown experimentally that the Pt/C catalyst synthesized with H₂Cyt⁻:PtCl₆²⁻ = 5:1 by microwave had the best mass activity, even surpassing that of a commercial E-TEK catalyst with the same metal loading. In addition, a size effect on the intrinsic Pt activity was also detected: the specific activity of Pt decreased with a decrease in the Pt particle size from 4.0 to 2.2 nm.



2.3.6 Typical Physico and Electrochemical Characterization of a Multi-metallic catalyst

Direct methanol fuel cells (DMFCs) are attracting much attention as one of the most promising options to solve the future energy problem because of their high energy conversion efficiency, low pollutant emission, low operating temperature, and simplicity of handling and processing of liquid fuel [259-260]. Electro-catalysts with higher activity for methanol oxidation at room temperature are critically needed to enhance DMFCs' performance for commercial applications. Pt has been demonstrated to be the most active electro-catalyst for the oxidation of small organic molecules including methanol. A well-known problem associated with the utilization of pure platinum is that it experiences

surface poisoning by strongly adsorbed CO, a byproduct in methanol electro-oxidation at low temperatures, which inhibits the hydrogen oxidation reaction [261]. Many researches indicate that the alloying of Pt with other transition metals enhances significantly the electro-catalytic activities and poison tolerance of Pt on the basis of a bi-functional mechanism, an electronic effect, or an ensemble effect [262–264]. Currently, the benchmark anode catalyst for DMFC is PtRu, because it demonstrates significant activity for methanol oxidation as well as the dehydrogenation of water which is critical for the removal of adsorbed CO species [265–268], but it is still not good enough for commercial applications due to its prohibitively high cost and limited supply. As a result, the discovery of non-precious metal alternatives to the Pt-Ru catalysts would greatly facilitate the commercialization of the methanol-based fuel cell systems. Pt-Fe alloys have been found to be excellent CO-tolerant anode catalysts as well as Pt-Ru, Pt-Co, Pt-Ni, or Pt-Mo based on the proposed mechanism for the CO tolerance, i.e., the lowered electron density of the 5d orbital of Pt decreases an electron back-donation from the Pt 5d orbital to the 2p* orbital of CO, and consequently suppresses CO-Pt bonding, resulting in the lowered CO coverage [269–273]. The studies conducted on Pt-Fe alloy as a cathode catalyst suggest that it contains a higher proportion of platinum active sites with a distinctly different nearest neighbour environment in relation to the non-alloyed Pt sample [274–277], however, the preparation and electro-catalysis of Pt-Fe alloy as an anodic one are lacking in the literature. Among the possible supports, carbon black has been widely used as an electrode, which disperses catalyst nano-particles [278–281]. But carbon nano-tubes (CNTs), as a new form of carbon, have been considered as new supports for metal catalysts due to their small size, high chemical stability and large

surface-to-volume ratio [282-283]. Catalytic nano-particles on the external CNT walls make easier contact with the reactant than those trapped in the pores of the carbon black electrode. Multi-walled carbon nano-tubes (MWNTS) as potential supports in heterogeneous catalysts have been studied due to their unique electronic and structural characteristics [284-285]. It has been found that MWNTs exhibit better performance in DMFCs when compared to carbon black (XC-72) [286-287] under identical conditions for catalysts preparation and cell performance test. As part of an ongoing investigation into new synthetic strategies for preparing metal alloy/carbon nano-composites exhibiting high performance as DMFC anode catalysts, a novel synthetic route to preparing well-dispersed catalytic nanoparticles on CNTs with a narrow particle size distribution. The MWNTS were first subjected to oxidation pretreatment [288] to remove impurities and generate sufficient amounts of functional groups on the surfaces. Then Pt-Fe alloy particles were deposited on the surface-oxidized MWNTs by a spray-cooling reduction method using NaBH_4 . TEM, EDS, ICP and XRD were carried out to characterize the Pt-Fe/ MWNTs nanocomposites. The electrocatalytic activity toward the oxidation of methanol was studied by cyclic voltammetry (CV) and chronoamperometry (CA). Its catalytic performance was compared with that of Pt/MWNTs synthesized with the same method. It is well known that the particle size and the distribution of Pt-based catalysts are key factors that determine their catalytic activity and cell performance for DMFCs. To produce nano-particles with a narrow particle size distribution, a solution of NaBH_4 was added to the catalyst precursor solution by a spraying method under constant stirring. NaBH_4 solution carried by nitrogen was sprayed uniformly onto the whole surface of the catalyst precursor solution, and then dissolved into the solution (in ice-bath) with stirring.

Here DMF(Dimethylformamide) was adopted as an assistant solvent, which is excellent to wet CNTs, moreover, it can be easily eliminated by washing. This method offers a homogeneous approach to the reduction of Pt^{4+} and Fe^{3+} , for well dispersed catalytic nano-particles on CNTs with a narrow particle size distribution.

2.3.6.1 Physicochemical characterization of a Binary catalyst

Pt–Fe alloy nanoparticles are distributed on tube walls uniformly, they do not aggregate with each other to form larger clusters, and are roughly spherical in shape. It is found that the Pt–Fe particles have a relatively narrow particle size distribution of 1–3 nm, the average particle size being 1.9 nm. The EDS spectrum of the Pt–Fe/MWNTs indicates Pt: Fe = 1:1.04 (a.t.), ICP analysis confirmed the exact Pt and Fe content in the composites at Pt: 25.6 wt% and Fe: 6.8 wt%; with a platinum to iron mole ratio of 1.08, which agrees well with the composition in the starting mixture. Therefore, the spray-cooling reduction method resulted in the production of highly dispersed Pt–Fe nanoparticles with a narrow particle size distribution. In order to obtain information on the average particle size and the Pt–Fe alloy effect, the Pt–Fe/MWNT nano-composites were characterized by XRD. The patterns presented the diffraction pattern of the as-prepared Pt/MWNTs catalyst used as a comparison. No Fe^0 or Fe_2O_3 peaks are observed in the XRD pattern of the Pt–Fe/MWNTs sample, indicating the absence of segregated metallic Fe phases. XRD analysis of the Pt–Fe/MWNTs nano-composite confirms the crystallinity of the Pt–Fe nano-particles as evidenced by the presence of peaks around 40.5° , 46.4° and 67.9° . These peaks are assigned to Pt-(1 1 1), (2 0 0), and (2 2 0), respectively [289]. Compared to that obtained from a non-alloyed Pt/MWNTs sample, the shift of the Pt (1 1 1) peak position to a higher 2θ angle by about half a degree could be indexed to a tetragonal crystal

structure with lattice constant $a = 3.895 \text{ \AA}$, $c = 3.820 \text{ \AA}$. As reported in the literature, the lattice parameters for Pt–Fe (1:1) alloy are $a = 3.852 \text{ \AA}$, $c = 3.713 \text{ \AA}$ [276], where the difference would indicate that part of the Fe remains as non-alloyed nanoparticles. This interpretation is in accordance with the EDS and ICP data showing that, on average, Pt:Fe is 1:1. The broad diffraction peaks for the Pt–Fe/MWNTs nano-composites reflect the smaller average size of the Pt–Fe particles. Although this result is not consistent with Ref. [274], it may be attributed to detail differences in the synthesis conditions. The average particle size of Pt–Fe alloy is 1.6 nm calculated by the Debye–Scherrer equation from the peak that matches the Pt (2 2 0) characteristic [290], which is in good agreement with the TEM measurement.

2.3.6.2 Electrochemical characterization of a Binary catalyst

After performing several cycles, the peak position and current intensities remained constant. During the forward scan, the current increases rapidly until a current peak is seen. After reversing the potential, a reactivation is observed on both electrodes. The peak at around 0.68 V is attributed to electro-oxidation of methanol in the forward scan, while the peak at around 0.47 V is due to the reactivation of Pt-oxides in the reverse scan [291]. Even though the general features of the voltammetric curves are somewhat similar, it is evident that the electrode composition has a significant influence on its behaviour towards methanol oxidation. The large methanol oxidation peak is about 0.689 V for catalyst a, but 0.677 V for catalyst b which shifted to a lower potential. Moreover, the oxidation current of the catalyst b is considerably higher than that of catalyst a. Therefore, the lower potential of the anodic peak which appeared in the forward scan and the higher peak current provide clear evidence for superior catalytic activity for methanol

electro-oxidation of catalyst b. These significant improvements in catalytic performance can be attributed to the addition of Fe which finally leads to the small average particle size and high utilization of Pt in the Pt–Fe/MWNTs catalyst. Pt–Fe/MWNTs electro-catalyst was prepared by a spray-cooling method and characterized using different techniques. The preliminary results indicated that the Pt–Fe alloy catalyst could significantly improve the electrode performance for methanol oxidation. Further optimization of the ratio between Pt and Fe can be expected to generate highly efficient catalyst for methanol electro-oxidation.



CHAPTER 3

3. EXPERIMENTAL

The catalysts were manufactured with certain properties to withstand the experimental conditions to which they would be subject, during testing. The characterization thereof was necessary to observe the changes in activity the catalysts underwent when subjected to conditions similar to those of a working fuel cell at intermediate temperatures. To obtain maximum activity at optimum conditions, the catalysts were observed using analytical techniques similar to that of their characterization.

The following physical and electrochemical methods were used:

- Transmission Electron Microscopy (TEM)
- X-ray Diffraction (XRD)
- Scanning Electron Microscopy (SEM/EDS)
- Electrochemical Cyclic Voltammetry and Chronoamperometry

3.1 Transmission Electron Microscopy

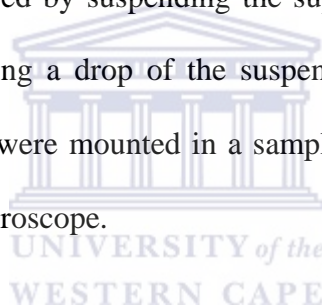
Transmission electron microscopy (TEM) is almost exclusively used in the investigation of average particle size, particle shape and particle size distribution of electrocatalysts. In this study, TEM was used to determine the aggregate morphology, particle size and the particle size distribution of the catalysts. All prepared samples were viewed and photographed using a LEO 912 OMEGA electron microscope at the University of Cape Town. The experimental parameters are given in Table 3.1.1.1.

Table 3.1.1.1 LEO 912 OMEGA transmission electron microscope operational parameters

Parameter	Setting
Accelerating voltage (kV)	200
Current (μA)	20
Condenser aperture	1
Objective aperture	3
Exposure time	3

Sample preparation

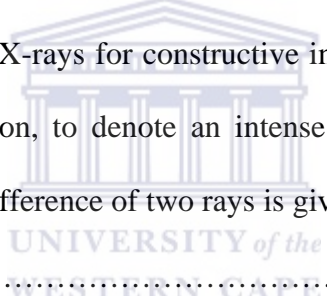
The TEM samples were prepared by suspending the supported Pt/C catalyst powder in methanol solution and depositing a drop of the suspension on a standard copper grid covered with carbon. Samples were mounted in a sample holder, which was introduced directly into the shaft of the microscope.



3.2 X-Ray Diffraction Analysis

A greater displacement is created where peaks or troughs coincide and a smaller displacement where peaks coincide with troughs. Classical electromagnetic theory states that the intensity of electromagnetic radiation is proportional to the square of the amplitude of the waves. Thus the regions of constructive and destructive interference, is displayed as areas of enhanced and diminished intensities. Diffraction is the interference phenomenon caused by an object in the path of the waves. A diffraction pattern results from the pattern of varying intensity caused by the interference. For the determination of structures of molecules and solids, the diffraction of waves by atoms and molecules is

used effectively for this purpose. X-rays are electromagnetic radiation with wavelengths below 100 nm. Bombarding a metal with high-energy electrons produces the radiation. The electrons slow down as they plunge into the metal and radiation is generated with a continuous range of wavelengths called Bremsstrahlung. Superimposed on the continuum are a few high-intensity sharp peaks. These peaks arise from an incoming electron colliding with an electron in the inner shell and ejects it, and an electron of higher energy drops into the vacancy, emitting the excess energy as an X-ray photon. The earliest approach to the analysis of diffraction patterns produced by crystals was to regard a lattice plane as a mirror, and to model a crystal as stacks of reflecting lattice planes of separation d . The model makes it easy to calculate the angle the crystal must make to the incoming beam of X-rays for constructive interference to occur. It has also given rise to the name reflection, to denote an intense spot arising from constructive interference. The path length difference of two rays is given by


$$AB + BC = 2d \sin \theta \dots\dots\dots \text{Equation 3.1}$$

where θ is the glancing angle. In numerous cases the glancing angles' path length difference is not an integral number of wavelengths, and the waves interfere destructively. But when the pathlength difference is an integral number of wavelengths ($AB + BC = n\lambda$), the reflected waves are in phase and interfere constructively. This should result in a bright reflection when the glancing angle satisfies the Bragg Law

$$n\lambda = 2d \sin \theta \dots\dots\dots \text{Equation 3.2}$$

Reflections with $n = 2$ is called second order, $n = 3$, third order, and so on the n th order reflection arising from the (nh, nk, nl) planes. First order is assumed. In more recent applications it is quite normal to absorb the n into d and to write the Bragg Law as

$$\lambda = 2d \sin \theta \dots\dots\dots \text{Equation 3.3}$$

The primary function of Bragg's Law is the determination of the spacing between layers in the lattice, because once the angle θ corresponding to a reflection has been determined, d may easily be established through calculation.

Laue's original powder method consisted of passing a broad-band beam of X-rays into a single crystal and recording the diffraction pattern photographically. The rationale was that a crystal would not be suitably orientated to serve as a diffraction grating for a single wavelength. Irrespective of its orientation, the Bragg law would be adhered to with respect to one of the wavelengths if several wavelengths were used. Peter Debye, Paul Scherrer and Albert Hull developed another technique. They used monochromatic radiation and a sample in a powder form. For powder samples few of the crystallites would be orientated to satisfy the Bragg law for each set of planes (hkl). For example, some of the crystallites will be positioned so that their (111) planes of spacing d_{111} result in a diffracted intensity at the glancing angle θ . The crystallites which have the glancing angle, lie at all possible angles around the incoming beam. The diffracted beams lie on a cone around the incoming beam of half angle, 2θ . The other crystallites would be positioned with different angles satisfying Bragg's law. These crystallites produce a cone of diffracted intensity with a different half angle. The underlying principle is that each set of (hkl) planes produces a diffraction cone, because some of the randomly orientated crystallites in the sample will possess the correct angle causing diffraction of the incident beam.

3.3 Energy dispersive spectroscopy (SEM-EDS)

The elemental composition of the catalysts was investigated using energy dispersive spectroscopic (EDS) emission analysis with a Hitachi X-650 SEM. Relative element concentrations were estimated using GENESIS software. Every sample was scanned five times to obtain the average wt.% of the metal. The operating parameters of the SEM are described in Table 3.1.3.1.

Table 3.1.3.1 Hitachi X-650 SEM operational parameters

Parameter	Setting
Accelerating voltage	25keV
Tilt Angle	0°
Aperture	0.4mm
Resolution	3nm
Working distance	15mm
Magnification	50k

Specimen preparation

The conductive powders of the catalytic samples were dispersed upon the carbon stick tabs and mounted on an aluminum stub holder. After that, the holder was loaded into the spectrometer.

3.4 Cyclic Voltammetry and Chronoamperometry; Testing catalyst activity

Cyclic voltammetry was used to determine the most active catalyst between 0,5 and 0,6V (vs. Ag/AgCl). The most active binary, ternary and quaternary catalysts were analyzed by chronoamperometry to determine if they possessed properties which could counter the CO poisoning effect, discussed earlier and in chapters 5, 6 and 7. Figure 3.1.4.1 illustrates the 3 electrode cell, autolab and processing unit system and alignment used for the cyclic voltammetry and chronoamperometry analysis.

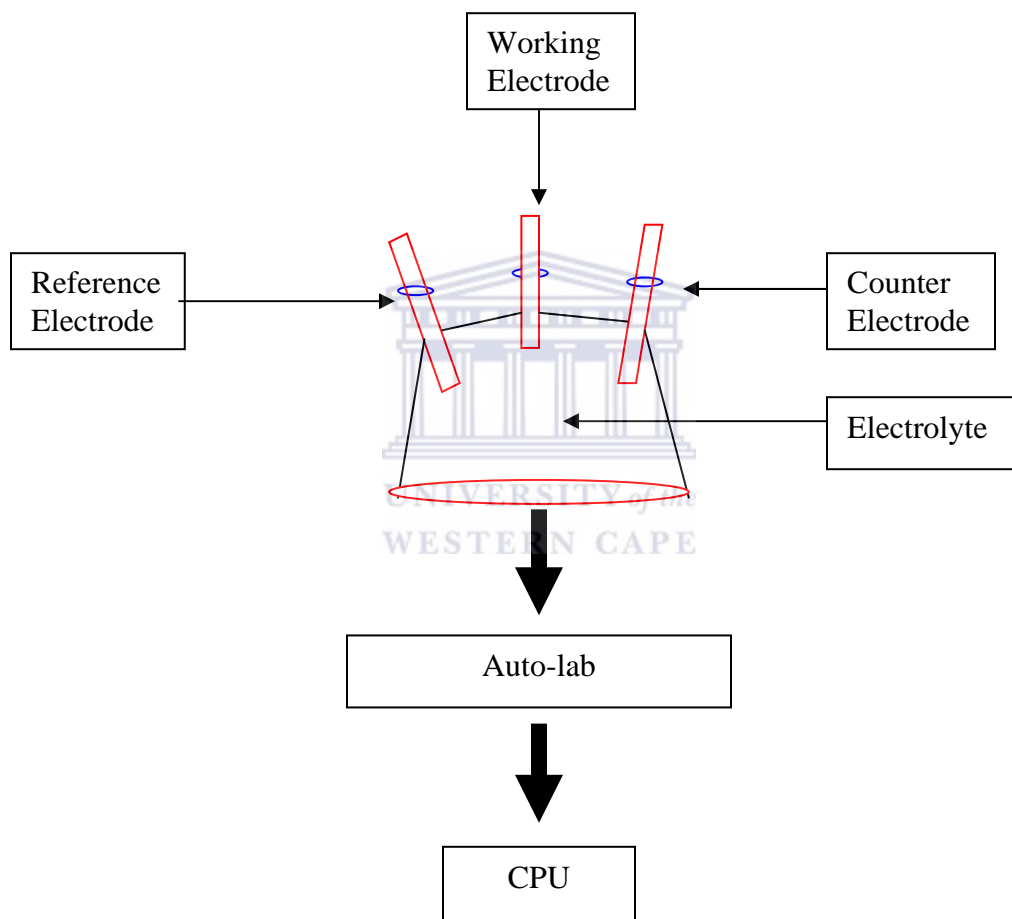
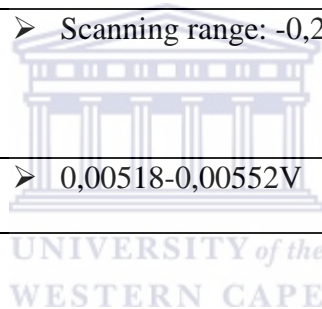


Fig. 3.1.4.1 Schematic of Electrochemical Testing Unit

Table 3.1.4.1 Standard Operating Parameters for CV and CA analysis.

Chapter 3 - Experimental

Electrolyte	<ul style="list-style-type: none">➤ Added 100ml 0,5M sulphuric acid to the cell. Degassed with nitrogen by saturation, while stirring, and then ran test run (base).
Methanol	<ul style="list-style-type: none">➤ Added 3,2ml methanol. Stirred for 15min.
Scan rate	<ul style="list-style-type: none">➤ 50mV Base run (0,5M sulphuric acid).➤ 20mV/s (0,5M sulphuric acid and 1M methanol).
Scan range	<ul style="list-style-type: none">➤ Scanning range: -0,2 to 1,0 V
Step potential	<ul style="list-style-type: none">➤ 0,00518-0,00552V



3.1.4.1 Electrode degradation and stability

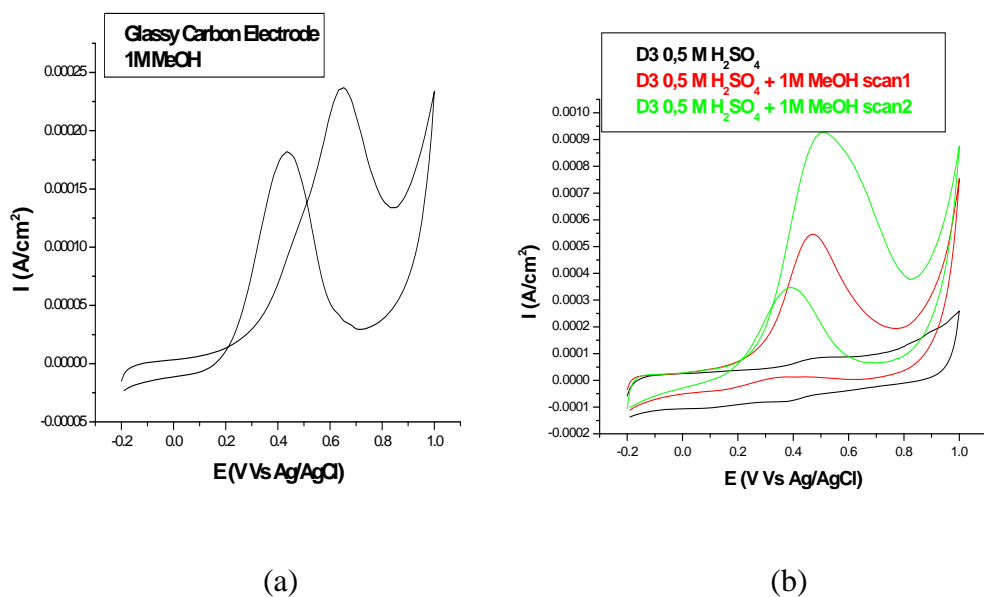


Fig. 3.1.4.1.1 (a) CV of the GCE and (b) sample loss after multiple scans

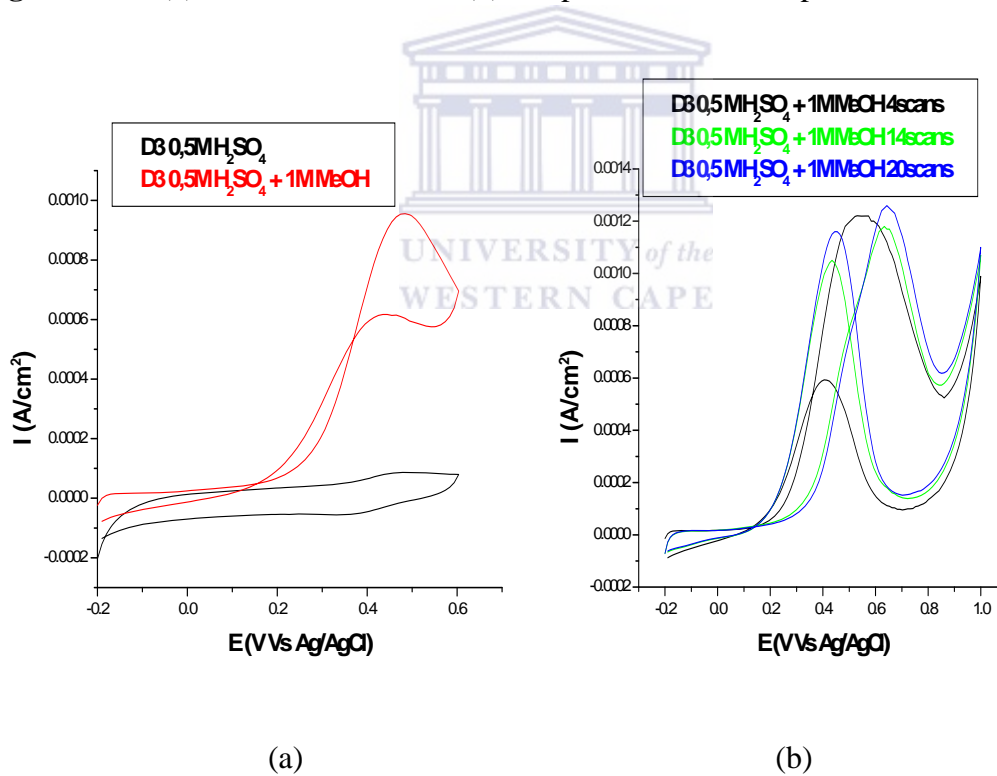


Fig. 3.1.4.1.2 (a) CV of catalyst D3 and (b) sample loss after multiple scans

The peak currents in the 0,42V and 0,5V regions increases as the number of scans are increased at a scan rate of 20mV/s. The forward scan methanol oxidation peaked at 0,5V after the 4th scan. The peak shifted to 0,65V after the 20th scan. The reverse peak remained in the 0,4-0,42V region. To prevent electrode degradation a gel electrode was formed using 5% Nafion solution with incomplete drying forming a glossy viscous gel, after approximately 3minutes with constant inspection.

MWCNT Gel-Electrode Preparation

1. Weigh 8mg sample.
2. Add 1,8ml DI water.
3. Add 150uL 5% Nafion and sonicate for 5inutes.
4. Place 10uL as a droplet on the exposed glassy carbon electrode.
5. Dry to gel state, be aware not to completely dry the ink droplet.

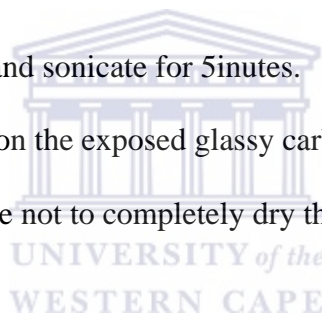


Table 3.1.4.2 List of reagents, supports and gases used for catalyst preparation

Reagent	Grade or Purity	Supplier	Catalysts
Chloroplatinic acid	99,9%	Alfa Aesar	All
Hydrochloric acid	99,9%	KIMIX	All
Potassium hydroxide	99,9%	KIMIX	All
Glacial acetic acid	99,9%	KIMIX	All
Water	DI	In-house	All
Iron chloride	99,9%	Alfa Aesar	B,C and D
Cobalt Hydroxide	99,9%	Alfa Aesar	C and D
Ruthenium chloride	99,9%	Alfa Aesar	All
Vulcan XC72	HP	Alfa Aesar	See synthesis parameter tables
MWCNT	HP	Alfa Aesar	See synthesis parameter tables
MWCNT	HP	Cheap Tubes	See synthesis parameter tables
Hydrogen	UHP	Afrox	A

HP (High purity); UHP (Ultra high purity); MWCNT (Multiwalled Carbon Nano-tubes)

3.5 METHOD DEVELOPMENT

3.5.1 Monometallic Catalysts

3.5.1.1 Catalysts A1,A1R1 and A1R2: 20% Pt on carbon (Vulcan):

The platinum on carbon was prepared using hydrogen (H_2) as the reducing agent.

Weighed 200mg Vulcan in a 250ml beaker.

1. Added approx. 10ml deionized water.
2. Allowed to sonicate for 5min, continuously submerging the particles, until a paste like suspension is formed.
3. Added additional 10-20ml deionized water.
4. Allowed to sonicate for 30min.
5. Added 84mg chloroplatinic acid in 150ml 0,5M HCl. This constitutes 20% Pt on 200mg carbon black.
6. The above solution was added drop wise to the 250ml beaker containing the carbon in paste like suspension.
7. Allowed to sonicate for further 15min.
8. NB: Repeat the sonication and stirring for approx. x6 for drying step as well.
9. Heated while stirring at 80 °C until dryness.
10. Ground dry powder in mortar and pestle.
11. Purged the ground sample in the furnace in the presence of H_2 (hydrogen) for approximately 1hours room temperature.
12. Placed in the furnace with H_2 (hydrogen) continuously flowing at 650 °C for 3 hours.
13. Allowed the sample to cool overnight in presence of H_2 .

Catalysts A1R1 and A1R2 were prepared using the same method, except reduction took place at 900 and 700°C respectively.

3.5.1.2 Catalyst A2: Preparation of 20% Pt on carbon (Vulcan) by Formic acid (FA) reduction.

1. 200mg Vulcan weighed in a 250ml beaker.
2. Added approx. 10ml deionized water.
3. Allowed to sonicate for 5min, continuously submerging the particles, until a paste like suspension is formed.
4. Added additional 10-20ml deionized water.
5. Allowed to sonicate for 30min.
6. Added 84mg chloroplatinic acid in 150ml 0,5M HCl. This constitutes 20% Pt on 200mg carbon black.
7. The above solution was added drop wise to the 250ml beaker containing the carbon in paste like suspension.
8. Allowed to sonicate for further 15min.
9. NB: Repeat the sonication and stirring for approx. 10x
10. Added 30ml formic acid drop wise using a burette, allowed to stir for 5hours at 22°C.
11. Sonication for ½ hour, filtered the solution with vacuum assistance, using Whatman no. 1 filter paper.
12. Washed the sample with 1L purified water.
13. Dried the powder at 80-100°C.

3.5.1.3 Catalyst A3: Preparation of 20% Pt on carbon (Vulcan) Formaldehyde

reduction

1. Weighed 200mg Vulcan in a 250ml beaker.
2. Added approx. 10ml deionized water.
3. Allowed to sonicate for 5min, continuously submerging the particles, until a paste like suspension was formed.
4. Added additional 10-20ml deionized water.
5. Allowed to sonicate for 30min.
6. Added 84mg chloroplatinic acid in 150ml 0,5M HCl.
7. The above solution was added drop wise to the 250ml beaker containing the carbon in paste like suspension.
8. Allowed to sonicate for further 15min.
9. NB: Repeat the sonication and stirring for approx. 10x
10. Added 50ml formaldehyde drop wise using a burette, allowed to stir overnight at room temperature.
11. Sonication for ½ hour, filtered the solution with vacuum assistance, using Whatman no. 1 filter paper.
12. Washed the sample with 1L purified water.
13. Dried the powder at 80-100°C.

3.5.1.4 Catalyst A4: Preparation of 20% Pt on carbon (Vulcan) Hydrogen purging the Solution (22°C).

1. Weighed 200mg Vulcan in a 250ml beaker.
2. Added approx. 10ml deionized water.
3. Allowed to sonicate for 5min, continuously submerging the particles, until a paste like suspension is formed.
4. Added additional 10-20ml deionized water.
5. Allowed to sonicate for 30min.
6. Added 84mg chloroplatinic acid in 150ml 0,5M HCl.
7. The above solution was added drop wise to the 250ml beaker containing the carbon in a paste like suspension.
8. Allowed to sonicate for further 15min. Purged the sample with H₂ for approximately 3 hours at room temperature (22°C).
9. Washed and filtered the sample.
10. Allowed the sample to dry overnight at 100°C.

3.5.1.5 Catalyst A5: Preparation of 20% Pt on Carbon nanotubes (CNT).

1. Weighed 200mg Vulcan in a 250ml beaker.
2. Added approx. 10ml de-ionized water.
3. Allowed to sonicate for 5min, continuously submerging the particles, until a paste like suspension was formed.
4. Added additional 10-20ml de-ionized water.
5. Allowed to sonicate for 30min.

6. Dissolved 84mg chloroplatinic acid in 0,5M HCl. The above solution was added drop wise to the 250ml beaker containing the carbon in paste like suspension.
7. Allowed to sonicate for further 15min.
8. Stirred for 3hours at 4°C.

9. Added Formic acid drop wise to the solution.
10. Continued stirring for an additional 2 hours 4°C .
11. Washed and filtered the sample.
12. Dried sample at 100°C.

3.5.1.6 Catalyst A6: Preparation of 20% Pt on carbon (Vulcan) using H₂ at 4°C.

1. Weighed 200mg Vulcan in a 250ml beaker.
2. Added approx. 10ml de-ionized water.
3. Allowed to sonicate for 5min, continuously submerging the particles, until a paste like suspension was formed.
4. Added additional 10-20ml de-ionized water.
5. Allowed to sonicate for 30min.
6. Dissolved 84mg chloroplatinic acid in 0,5M HCl. The above solution was added drop wise to the 250ml beaker containing the carbon in paste like suspension.
7. Allowed to sonicate for further 15min.
8. Stirred for 3hours at 4°C.

9. Bubbled H₂ into the solution.
10. Continued stirring for an additional 2 hours at 4°C .
11. Washed and filtered the sample.
12. Dried sample at 100°C.

3.5.1.7 Catalyst A7: Preparation of 20% Pt on carbon (4-80°C) Formaldehyde reduction.

1. Weighed 200mg Vulcan in a 250ml beaker.
2. Added approx. 10ml deionized water.
3. Allowed to sonicate for 5min, continuously submerging the particles, until a paste like suspension was formed.
4. Added additional 10-20ml deionized water.
5. Allowed to sonicate for 30min.
6. Added 84mg chloroplatinic acid in 150ml 0,5M HCl.
7. The above solution was added drop wise to the 250ml beaker containing the carbon in paste like suspension.
8. Allowed to sonicate for further 15min.
9. NB: Repeat the sonication and stirring for approx. 10x
10. Added 50ml formaldehyde drop wise using a burette, allowed to stir for 5hours at 4°C, followed by heating to 80°C to assist with filtration.
11. Sonication for ½ hour, filtered the solution with vacuum assistance, using Whatman no. 1 filter paper.

12. Washed the sample with 1L purified water.

13. Dried the powder at 80-100 °C.

3.5.1.8 Catalyst A8: Preparation of 20% Pt on carbon (4-80°C) Formaldehyde reduction.

1. Weighed 200mg Vulcan in a 250ml beaker.
2. Added approx. 10ml deionized water.
3. Allowed to sonicate for 5min, continuously submerging the particles, until a paste like suspension was formed.
4. Added additional 10-20ml deionized water.
5. Allowed to sonicate for 30min.
6. Added 84mg chloroplatinic acid in 150ml 0,5M HCl.
7. The above solution was added drop wise to the 250ml beaker containing the carbon in paste like suspension.
8. Allowed to sonicate for further 15min.
9. NB: Repeat the sonication and stirring for approx. 10x
10. Added 50ml formaldehyde drop wise using a burette, allowed to stir for 18hours at 4°C, followed by heating to 80°C to assist with filtration.

11. Sonication for ½ hour, filtered the solution with vacuum assistance, using Whatman no. 1 filter paper.
12. Washed the sample with 1L purified water.
13. Dried the powder at 80-100 °C.

3.5.1.9 Catalyst A9: Preparation of 20% Pt on carbon (4-80°C)

Formaldehyde reduction. (Decreased the sonication frequency)

1. Weighed 200mg Vulcan in a 250ml beaker.
2. Added approx. 10ml deionized water.
3. Allowed to sonicate for 5min, continuously submerging the particles, until a paste like suspension was formed.
4. Added additional 10-20ml deionized water.
5. Allowed to sonicate for 30min.
6. Added 84mg chloroplatinic acid in 150ml 0,5M HCl.
7. The above solution was added drop wise to the 250ml beaker containing the carbon in paste like suspension.
8. Allowed to sonicate for further 15min.
9. NB: Repeat the sonication and stirring for approx. 5x
10. Added 50ml formaldehyde drop wise using a burette, allowed stirring for 18hours at 4°C, followed by heating to 80°C to assist with filtration.

11. Sonication for ½ hour, filtered the solution with vacuum assistance, using Whatman no. 1 filter paper.
12. Washed the sample with 1L purified water.
13. Dried the powder at 80-100 °C.

3.5.1.10 Catalyst A10: 20% Platinum on Carbon nano-tubes

The production method is the same as that of A9, with CNT instead of Vulcan.



CHAPTER 4

MONOMETALLIC CATALYSTS

4.1 OBJECTIVES

- 4.1.1 To synthesize catalysts for methanol oxidation.
- 4.1.2 To synthesize catalysts with large electrochemically active surface areas.
- 4.1.3 To synthesize catalysts with similar electrochemical activity to JM catalysts.

4.2 INTRODUCTION

The physical and chemical properties of nano-particles of various elements are extremely sensitive to the number of atoms comprising the cluster when they contain less than a few dozen atoms. Furthermore, these variations in properties are often manifested in a non-linear fashion as the size of the cluster changes [293–299], and may be attributed to electronic and/or structural changes. The interaction of small clusters of atoms with the surface of a support may result in alteration of the electronic state of the cluster, depending on the nature of the support material [300]. There are various reports in the literature showing that as the Pt cluster size reduces to below 3–5 nm, electrochemical mass activity decreases [301, 302], however, large uncertainties exist due to the broad size distributions of most catalyst preparations analyzed in the literature. Direct measurement of the size-dependent properties of small Pt clusters with narrow size distribution would enable design of optimized electro-catalysts for PEM-FCs. Traditional bulk Pt/C electro-catalysts are typically prepared via impregnation or precipitation from solution phase of a Pt-salt onto a pre-formed carbon support, followed by thermal or chemical reduction of the Pt species to form clusters [303]. This yields Pt clusters spanning a range of sizes which are weakly attached to the carbon; stabilization of the

active metal species on the carbon surface is reliant on the presence of surface functional groups [304]. An alternative approach, electrostatic adsorption of Pt complex ions from solution onto a support [305,306], can lead to highly dispersed Pt clusters. Dispersions of Pt as high as 50% (≈ 2 nm) were reported for 9.4 wt.% Pt/carbon (XC-72) prepared by this method [307]. Well-defined Pt clusters of narrow size distribution down to below 1nm may be obtained in zeolite hosts under suitable conditions [308, 309]. Due to their poor electrical conductivity, however, zeolite-supported clusters are not suitable as electrocatalysts. Several recent publications have described the preparation of mesoporous [310–313] or microporous [314] pyrolytic carbons through templating by mesoporous or microporous hosts, respectively. In some cases these carbons have been used as substrates for Pt clusters in the fabrication of fuel cell catalysts, however, only relatively large Pt clusters [315], or ones with a broad size distribution [316], were achieved. In this chapter I have developed a hybridized approach for the preparation of Pt/C electro-catalysts: a series of synthetic methodologies were attempted whereby size-controlled Pt clusters are rendered electro-catalytically active through experimental trials using different temperatures, reducing agents and supports. The eventual formulation method of nano-structured catalysts described here is unique in the ability to control Pt cluster size.

4.3 SYNTHESIS PARAMETERS

Here the Pt/C catalysts will be prepared using various methods including heat treatment, reducing agents, and low temperature and combined reducing agents to produce nano-particle sized catalysts. This work will not include stabilizers or organic dispersants which require expensive and time-consuming post-synthesis treatments.

The reducing agents used were hydrogen, formaldehyde and formic acid. The temperatures at which the reduction processes were performed were selected after a series of temperature ranges were investigated. The temperatures ranged from 0 to 900°C. In table 4.2.1 only the parameters that showed trends and where further investigations were proving fruitful were recorded. In other words, there were a number of investigations and experiments performed that did not provide any convincing results and thus did not warrant any further investigation.

The temperature utilized were in the range of 400-900°C and 22-400°C, not mentioned here are the results of the intermediate parameter settings, e.g. Temperature ranges between 22-5°C; 22-400 °C and 400-650 °C. These trend determining results (TDR) were significant in producing and observing trends, but do not form part of the mentioned data. The TDR were interpreted and used to arrive at the mentioned data. The mentioned data are the most reflective of the experimental analysis.

For the formaldehyde and formic acid reduction methods, the pH (will not be discussed here) was controlled using various strong acids and bases.

Table 4.2.1 Summary of the synthesis parameters

Catalyst	%Metal Support	Synthesis Parameters				
		RT hrs	TP °C	RA	Vol. ml	Flow rate ml/min.
A1	<u>20%Pt</u> Vulcan	5	650	H ₂	150	3
A1R1	<u>20%Pt</u> Vulcan	5	900	H ₂	150	3
A1R2	<u>20%Pt</u> Vulcan	5	700	H ₂	150	3
A2	<u>20%Pt</u> Vulcan	5	22	FA	150	N/A
A3	<u>20%Pt</u> Vulcan	5	22	F	150	N/A
A4	<u>20%Pt</u> Vulcan	5	22	H ₂	150	3
A5	<u>20%Pt</u> Vulcan	5	4	FA	150	N/A
A6	<u>20%Pt</u> Vulcan	5	4	H ₂	150	3
A7	<u>20%Pt</u> Vulcan	5	4-80	F	150	N/A
A8	<u>20%Pt</u> Vulcan	18	4-80	F	150	N/A
A9	<u>20%Pt</u> Vulcan	18	4-80	F	150	N/A
A10	<u>20%Pt</u> MWNT	18	4-80	F	150	N/A
JM	<u>20%Pt</u> Vulcan	N/A	N/A	N/A	N/A	N/A

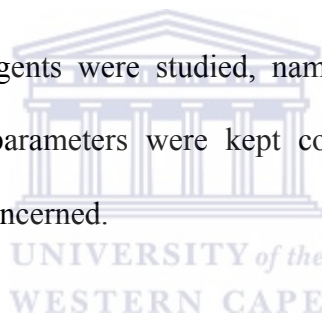
RA (Reducing agent); F (40% Formaldehyde); TP (Temperature programme);
H₂ (Hydrogen); RT (Reduction time); N/A (Not available)

Table 4.2.1 gives a summary of the catalysts identified as TDR and these catalysts will be characterized and their EC activity quantified. This will then enable a profile for each catalyst with regards to its synthesis route, character and EC activity. The most EC active synthesis route will be used to prepare multi-metallic platinum based

catalysts discussed in future chapters. The most active multi-metallic catalyst will then be used in an MEA (Membrane Electrode Assembly) and applied in a fuel cell. The fuel cell application will be an additional chapter (Chapter 8) that should be treated as outside the scope of the objectives for this thesis by the reader.

At high temperatures, as noted in table 4.2.1, the hydrogen reduction method was performed at 650, 700 and 900°C. In all three cases the flow rate of the hydrogen was kept constant at 3ml/minute. The reduction period was 5 hours and the support used was Vulcan.

At 22°C, three reducing agents were studied, namely hydrogen, formic acid and formaldehyde. The test parameters were kept constant, where the volume and precursor quantities were concerned.



At 4°C, three reducing agents were studied, namely hydrogen, formic acid and formaldehyde. The test parameters were kept constant, where the volume and precursor quantities were concerned. MWCNT will be introduced as an alternate support to Vulcan in an attempt to aid in the dispersion and increase EC activity by possibly being more electronically conductive.

4.4 RESULTS AND DISCUSSION

4.4.1 Structural Characterization by XRD

As mentioned previously the characteristic diffraction peaks of the face centered cubic (fcc) Pt demonstrate that a successful reduction of Pt precursor to metallic form has been achieved. The diffraction peaks at about 39° and 46° are due to the Pt(1 1 1), and (2 0 0) plane, respectively, which represents the typical character of a crystalline Pt face, that is fcc. This indicates that the in-house-supported Pt catalysts possess a Pt (fcc) crystal structure [204-209].

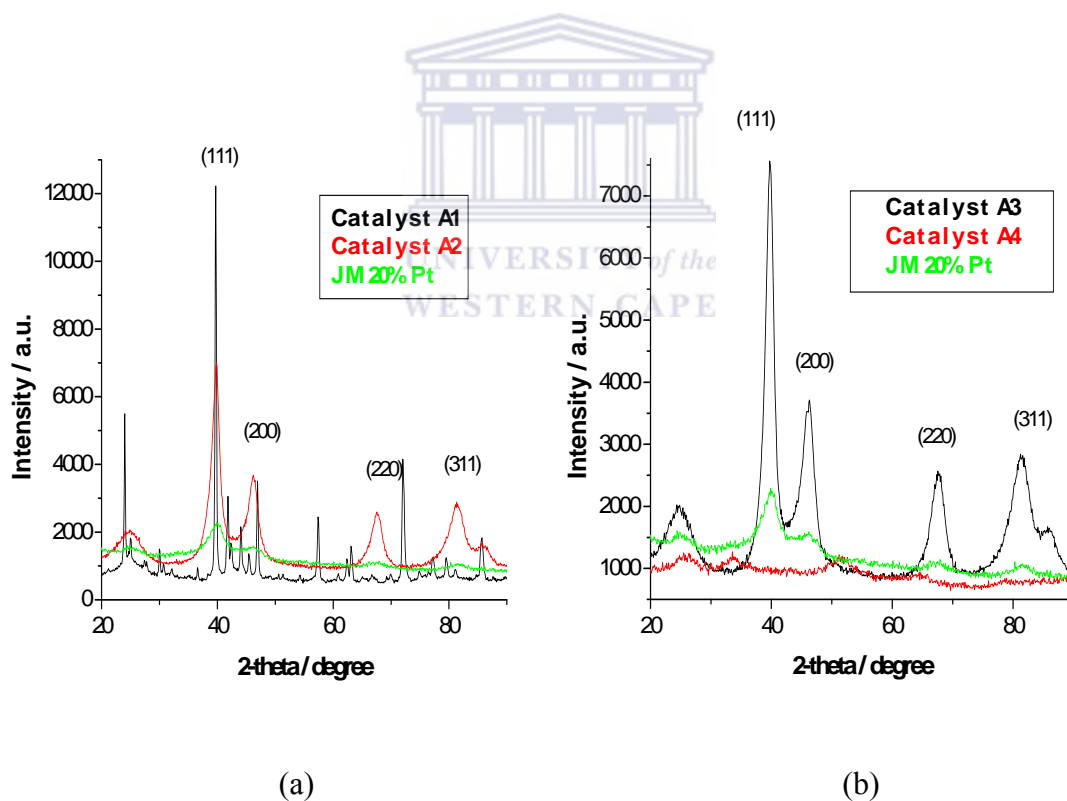


Fig. 4.4.1.1 XRD of catalysts (a) A1, A2 and JM and (b) A3, A4 and JM

In fig. 4.4.1.1 (a) the spectrum shows the formation of metallic particles synthesized by a high temperature reduction procedure and H_2 as the reducing agent referring to sample

A1, whereas sample A2 was synthesized at 22°C using formic acid as the reducing agent. Sample A2 has a similar XRD peak positioning profile to that of the JM catalyst. Sample A1 shows more peaks formed possibly stemming from the formation of different metal alloys, impurities on the support surface or disintegration of the support into smaller particles and composite formations at temperatures in excess of 600°C.

In fig. 4.4.1.1 (b) the spectrums show differences with regards to peak prominence and definition. As can be seen for sample A4 the peaks are not as clearly defined and non-alignment with the JM peak positioning indicates that there was little or no platinum reduction during this synthesis method. The lack or absence of platinum reduction or formation should adversely affect the catalyst electrochemical performance and this can be later confirmed by reviewing the relative EC activity.

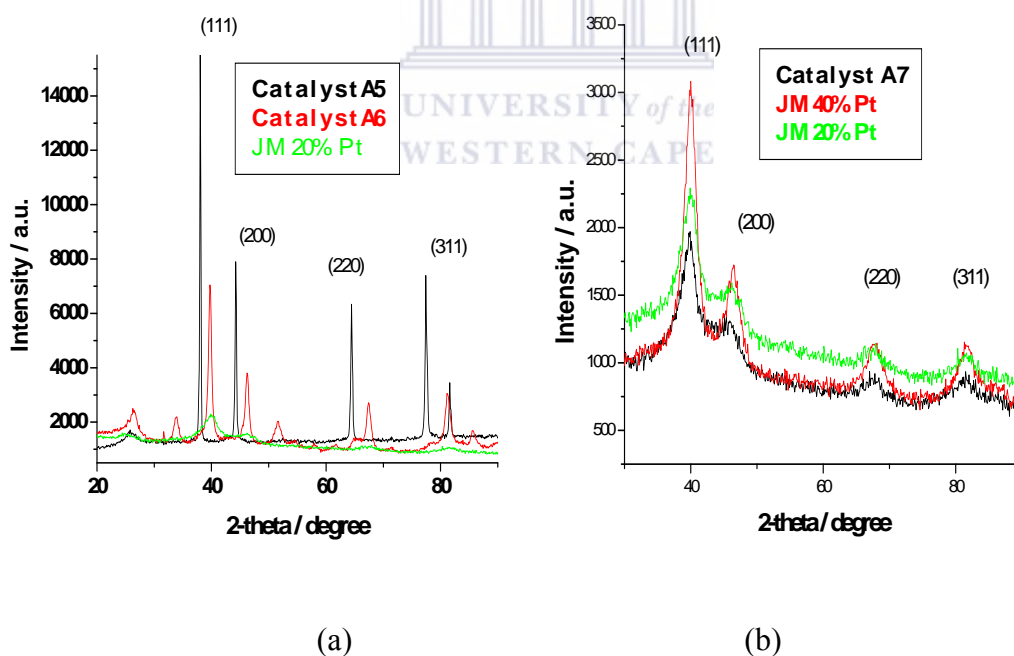


Fig. 4.4.1.2 XRD of catalysts (a) A5, A6 and JM and (b) A7, JM40% and JM20% Pt.

Samples A5 and A6, Fig. 4.4.1.2 (a), were synthesized in sub ambient temperatures, using formic acid and hydrogen respectively as reducing agents. The synthesis

parameters mentioned have favoured the utilization of hydrogen as a reducing agent in producing a catalyst with a similar XRD profile for A6 to that of JM. Once again, samples A5 - A6 – JM XRD spectrum profiling can be further supported by the EC later discussed in section 4.4.4, where XRD profiles with peak positioning similar to that of the JM catalyst produces EC activity higher than that of catalysts which do not show similarity in XRD spectra peak profiles.

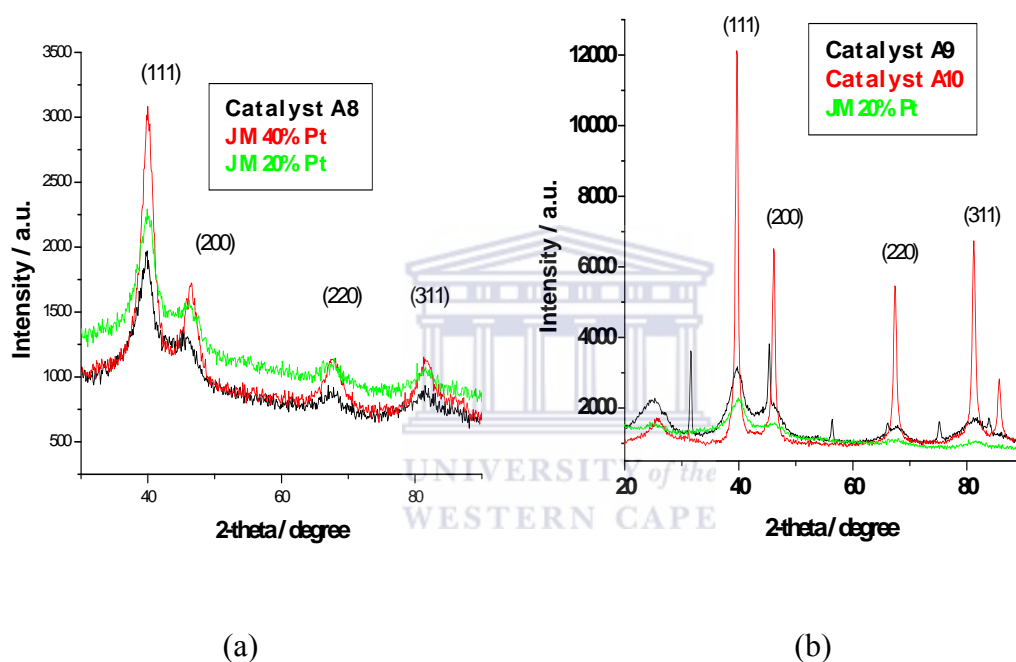
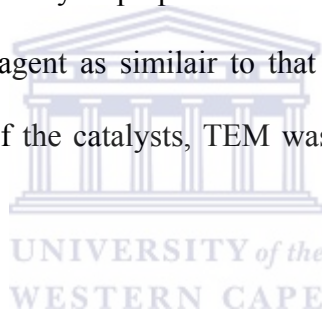


Fig. 4.4.1.3 XRD of catalysts (a) A8, JM 20% and JM 40% (b) A9, A10 and JM 20%Pt

Although the different reducing agents have managed to reduce platinum, the temperature at which the reaction took place played a critical role in the reduction process as well. These temperatures were explored and after studying the XRD, TEM, particles size and EC profiles, it was decided that the sub ambient temperature and formaldehyde reduction method be pursued further, producing samples A7 – A10, producing XRD profiles similar to that of the JM XRD spectrums, fig. 4.4.1.3. As mentioned earlier, a systematic approach was adopted in this research covering a wide range of parameters

and only the results producing trends significant to drawing conclusions and supporting further catalyst development is mentioned here. Temperatures ranging from below 5 to 900°C were explored as reducing temperatures. The sample or catalyst A7, Fig. 4.4.1.2 (b), produced at 5°C utilizing formaldehyde as the reducing agent, once again showed an XRD spectrum profile similar to that of JM. Samples A8 and A9 were produced by an identical methodology to confirm certain synthesis and test parameters. The EC activity for samples A8 and A9 were significantly higher than that of samples prepared with different synthesis parameters including temperatures ranging from above 400 to 900°C and using hydrogen as the reducing agent. The XRD spectrum, fig. Fig. 4.4.1.3, profiled once again the in-house active catalysts prepared at sub ambient temperatures and using formaldehyde as the reducing agent as similar to that of the JM catalyst. To further profile the physical character of the catalysts, TEM was used relate particle size to EC activity, 4.4.2.



4.4.2 Morphological Characterization by TEM

As previously noted, the TEM was performed on 4 different categories of catalysts. The first was the high temperature methods, 400 to 900°C, producing catalytic particles larger than the rest. The second category included catalytic particles produced at 22°C that were small enough to be EC active depending on the synthesis route ie. the type of reducing agent etc. thirdly, TEM was used to characterize nano-sized catalytic particles produced at sub ambient temperatures with a particle size distribution ranging ~ 80% < 3nm in diameter with exceptionally high EC performance comparable to the commercially available JM catalysts. Lastly the MWCNT was used support was used and

Although few particles dispersed evenly due to the intense sonication treatment provided during the hydrogen reduction, also present were areas where there is an absence of metal particles. This suggests that the reduction process was incomplete and poor dispersion characterized the early stages of the catalyst synthesis.

Large particles and agglomerations were formed during the synthesis of catalyst A6 particle sizes ranging from 40 to 70nm.

Approximately 80% of catalyst A7's particle diameters were > 3nm and 70% were less than 4nm in diameter.



4.4.2 Morphological Characterization by TEM Analysis

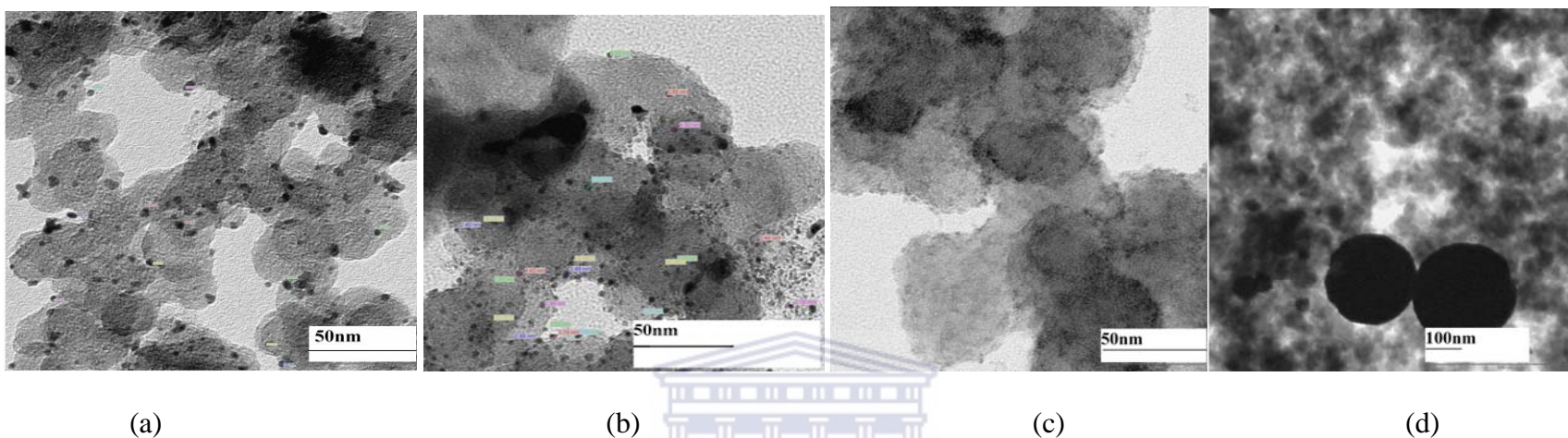


Fig. 4.4.2.1 TEM images of catalysts (a) A1, (b) A2, (c) A3, (d) A4

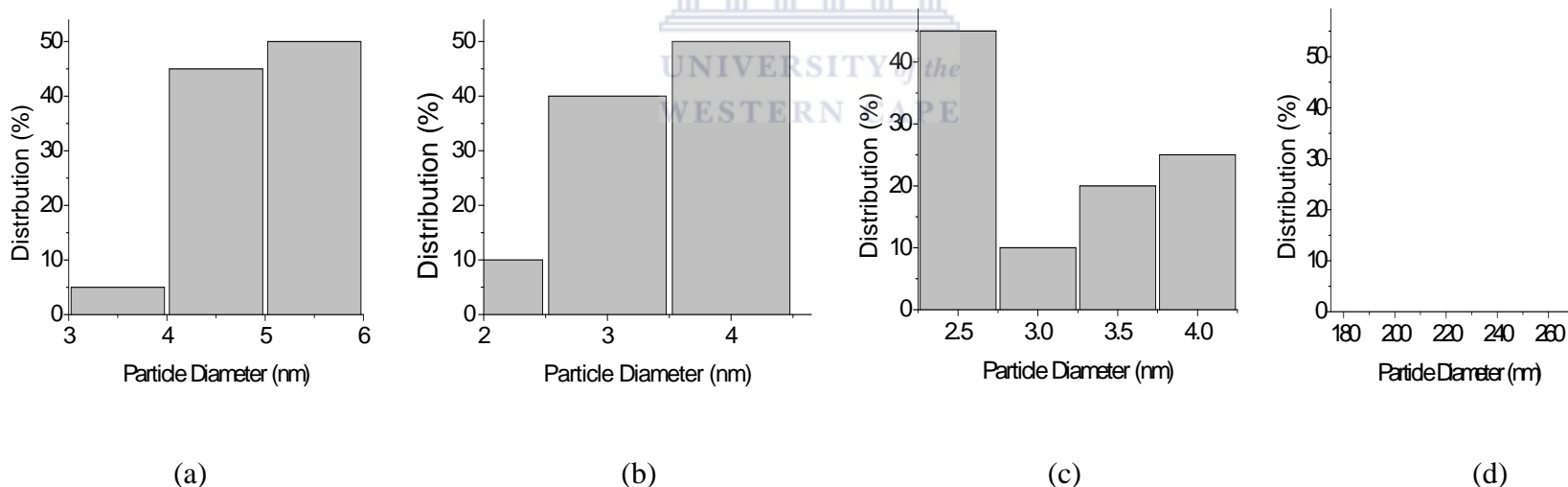


Fig. 4.4.2.2 Particle size distribution of catalysts (a) A1, (b) A2, (c) A3, (d) A4 (Catalyst A4 had low to no levels of reduction)

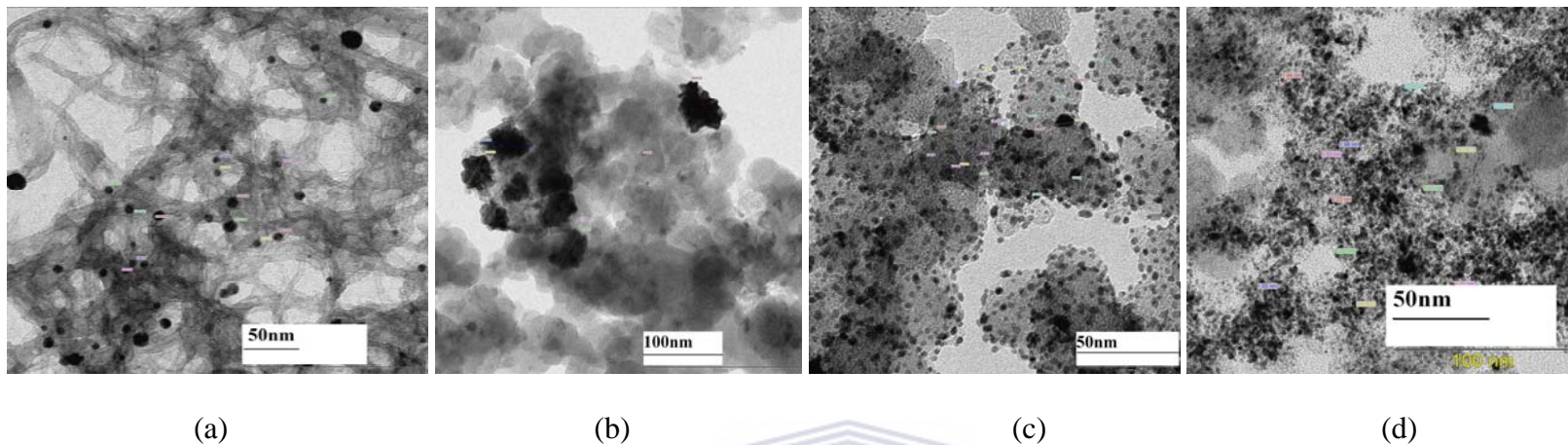


Fig. 4.4.2.3 TEM images of catalysts (a) A5, (b) A6, (c) A7, (d) A8

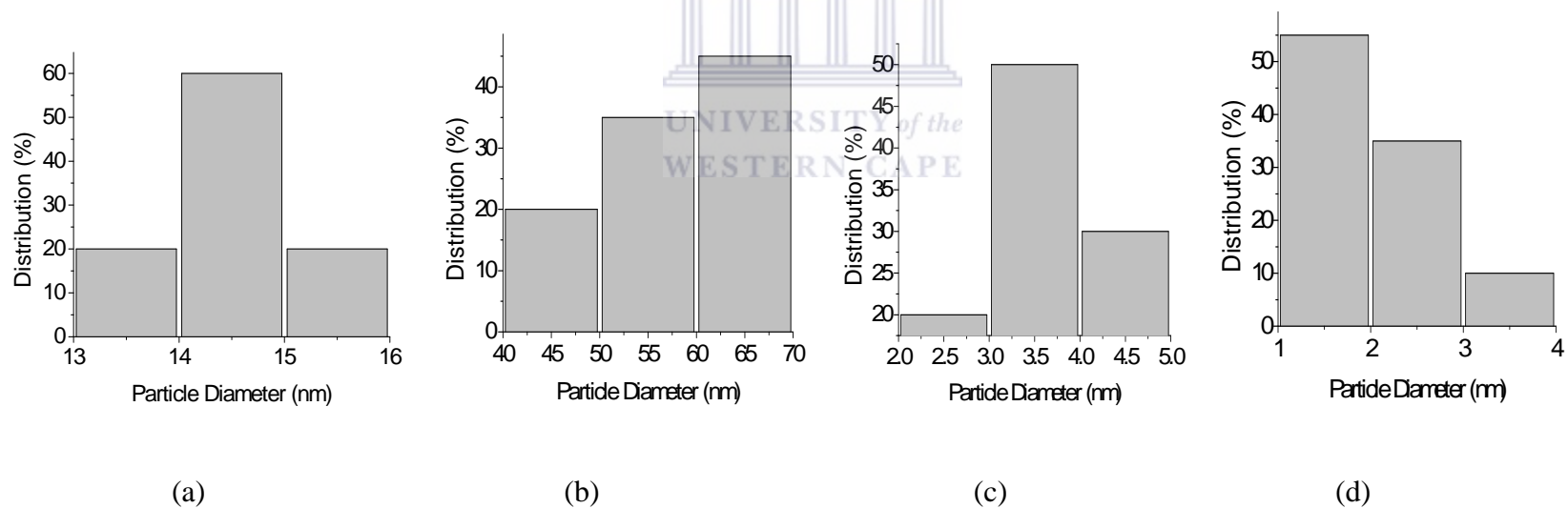


Fig. 4.4.2.4 Particle size distribution of catalysts (a) A5, (b) A6, (c) A7, (d) A8

Catalysts reduced at high temperatures were composed of particles with particle size distributions in the region of 50% < 3nm as can be seen in fig's. 4.4.2.1 (a) and 4.4.2.2 (a). The concentration of particle formation in a specific surface area is less than that formed at sub ambient temperatures. The formation of larger particles could be assigned to particle growth due to lack of dispersion during the metal formation process. The high temperature methods are limited with regards to the options for implementing dispersion techniques as the reduction takes place in a furnace where no physical or mechanical equipment at laboratory level can be installed to aid in particle dispersion without adding immensely to the cost factor. This analysis applied to samples A1, A1R1 and A1R2 prepared under similar conditions with different pretreatments, which had very little or no effect on the poor EC activity observed later.

Apart from increased dispersion, slowing down the particle growth rate was also attempted by exploring ambient and sub ambient temperatures at which reduction could take place.

Fig. 4.4.2.1 (b) shows the TEM particle dispersion image for catalysts A2, A3 and A4 synthesized using formic acid, formaldehyde and hydrogen respectively as the reducing agents and synthesis route performed at 22°C. In terms of particle size, distribution and relative EC activity, catalyst A2 showed the positive direct influence smaller particles and the resulting increased surface area have on the EC activity, although there is poor dispersion and formation of agglomerations of smaller particles (~30% <3.5 nm) in the region of 10nm, the EC activity at 0,6V (Vs. Ag/AgCl) was significantly higher than the

catalysts produced at high temperatures. There were further attempts to disperse the catalytic particles by using MWCNT supports were attempted and the resulting image observed for sample A5 Fig. 4.4.2.3 (a) shows an image with larger particles than anticipated. To make the MWCNT support more effective required a series of pretreatments to firstly remove impurities and secondly disperse the tubes themselves prior to the actual deposition of metallic particles. A more successful approach involving support pretreatments, precursor pretreatments and temperature ramping prior to deposition onto the MWCNT supports will be observed and reported in chapter 5, 6 and 7.





The poor dispersion was noted once again for sample A3, and highlighted the need to introduce effective dispersion methods while slowing down and controlling the particle growth rate. From the XRD and SEM it can be clearly seen that the method employed to synthesize catalyst was able to synthesize platinum metallic particles from a chloroplatinic acid salt solution. In this research up until now it is observed that these platinum metallic particles are in fact active nano-sized catalytic particles and the catalyst EC activity is relative to the quantity of these platinum metallic particles. Also noted is the increase in smaller particles produced at ambient temperatures, and this parameter was explored even further as the reduction process was performed at sub ambient temperatures and the best results were achieved for samples A7, A8 and A9 where the reducing agent was formaldehyde and the reaction temperature was 4°C. When comparing the reducing agents, formaldehyde was chosen as it produced the highest EC activity at 0,5V (Ag/AgCl) compared to catalyst A2, where sample A2 was synthesized with formic acid as the reducing agent, was proven to be an effective reducing agent and formic acid has been proposed for use as a reducing in future research, mentioned later.

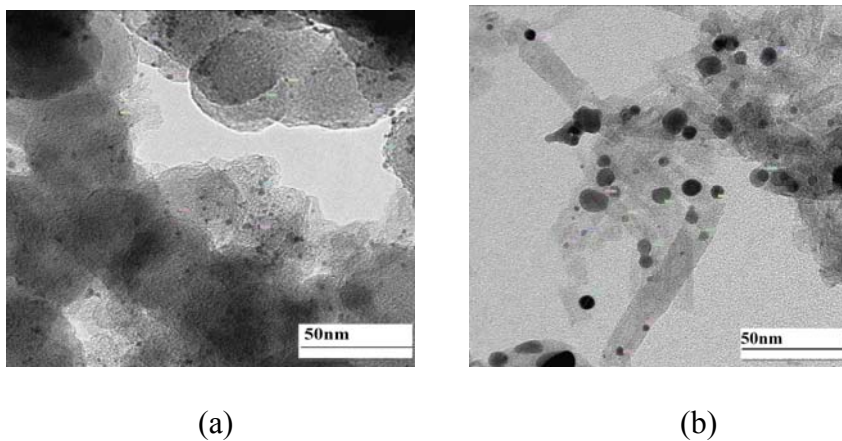


Fig. 4.4.2.5 TEM images of catalysts (a) A9, (b) A10

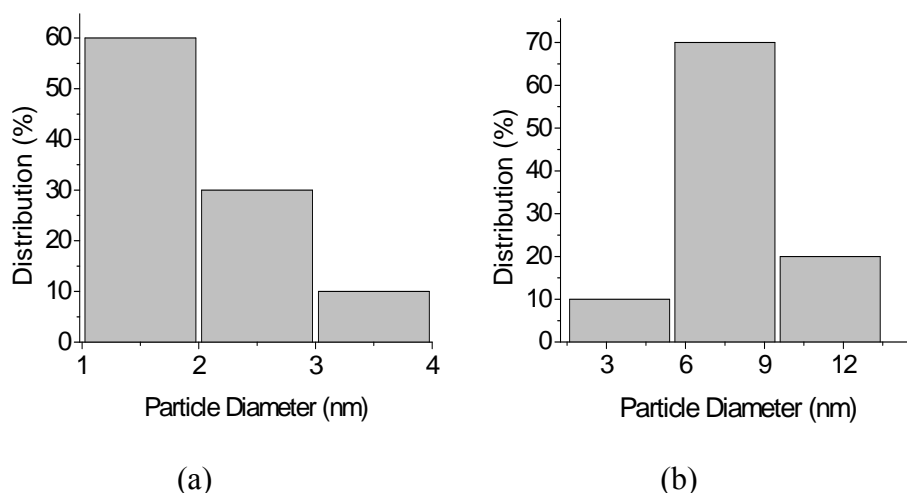


Fig. 4.4.2.6 Particle size distribution of catalysts (a) A9 and (b) A10

The particle size distribution graph Fig. 4.4.2.4 (d) shows 90% of catalyst A8's particles having diameters $< 3\text{nm}$'s. The TEM image Fig. 4.4.2.3 (d) shows nano-particles forming clusters and are moderately dispersed.

The introduction of the post reduction temperature of 80°C was significant with regards to the particle growth and formation and determining or used as an indicator that complete reduction had taken place, where at increased temperatures the particles growth rate was increases producing larger less EC active catalytic particles. In addition, the post reduction heating to 80°C aided in the removal of agents formed and added to control the pH. These impurities were heated along with the supported catalysts prior to the filtration process during the purification stage. This was evident in samples A7, where the reduction process was assumed to be completed, at 4°C , but as can be seen from fig. 4.4.2.4 (c) there was considerable particle growth at 80°C after reduction of 5 hours along with fewer particles compared to sample A8, fig. 4.4.2.4 (d). The purification step involving increasing the temperature which was clearly introduced too

soon, resulted in unreduced ions available in the reaction vessel forming larger catalytic particles covering or coating a smaller area of carbon support. In samples A8 and A9 the catalytic particles exhibited a particle size that was remarkably reduced to the range of $90\% < 3\text{nm}$ covering or coating a larger surface area. For samples A8 and A9 the post-reduction purification heating stage (temperature) was introduced after 18hours at 4°C after adding formaldehyde.

More than 90% of catalyst A10's particles were greater than 5,5nm in diameter. The lack of dispersion of the chloroplatinic acid could be due to agglomerations or entanglement thereof within the carbon nanotubes. The results and future treatments of MWCNTs will be discussed in chapter 5, 6 and 7.



4.4.3 Elemental Analysis by EDS

EDS was used to confirm the absence or presence of platinum on the carbon support.

The quantity was not referred to but is in accordance with the TEM observations.

Table 4.4.3.1 Results of the elemental analysis by EDS

Elemental Content	Catalyst									
	A1	A2	A3	A4	A5	A6	A7	A8	A9	A10
% Carbon	92,9	75,2	84,8	99,6	88,2	92,2	83,1	80,4	80,9	70,2
% Platinum	7,1	14,8	15,2	0,4	11,8	7,7	16,9	19,6	19,1	29,8

The EDS results, table 4.4.3.1, reflect the high quantity platinum formations as observed in the TEM analysis using the low temperature reduction methods where an abundance of platinum formed compared to lower levels of reduction as the temperature is increased. In all cases 20% Pt/C was aimed for.

The lowest level Pt formation, sample A1, was recorded for the high temperature hydrogen as the reducing agent reduction methods. The highest levels of platinum catalytic particle formation were recorded for the sub ambient temperature formaldehyde as reducing agent reduction methods.

4.4.4 Electrochemical Activity by Cyclic Voltammetric Analysis

The electrochemical (EC) activity was determined by cyclic voltammetric (CV) analysis of the different catalysts. By comparing the EC activity for each catalyst the reducing agents and other synthesis parameters can now be identified as effective contributors to synthesis routes. Table 4.4.4 the EC activity of the once-formed catalyst is analyzed in an acidic medium (base analysis), followed by the addition of 1M methanol which undergoes oxidation on the platinum surface as shown in the CV graphs below. The potential regions analyzed are -0,2 to 0,6V and -0,2 to 1,0V (vs. Ag/AgCl) and the scan rate used was 20mV/s.

The objective and application of the EC activity is mainly to determine the activity of the catalyst synthesized by different methods, and give an indication as to which method produces a catalyst with the highest EC activity at 0,5V (vs. Ag/AgCl), because it is at this potential that the direct methanol fuel operates optimally. The EC activity was used earlier in this chapter in relation with the characterization of each catalyst synthesized and as previously mentioned the EC activity was continuously referred to.

Table 4.4.4 compares the different catalysts, methods, EC activity and refers to the specific figure. The table indicates the activity status, this indication refers to the increase in current (I) as and when methanol is added. If the current increases from the base line the difference in current (between the black and red lines) is calculated at a specific potential, where the 2 potentials of interest as mentioned earlier were 0,5 or 0,6V (vs. Ag/AgCl),.

Table 4.4.4 Comparing the Electrochemical Activity by CV Analysis

Catalyst	Metal Support	EC Activity				
		T °C	I(A) (vs Ag/AgCl) 0,5V	I(A) (vs Ag/AgCl) 0,6V	EC Status	Reference Figures
A1	20%Pt Vulcan	20	$3,80 \times 10^{-6}$	$4,98 \times 10^{-6}$	Not Active	4.4.4.1
A1R1	20%Pt Vulcan	20	$5,79 \times 10^{-9}$	$8,0 \times 10^{-9}$	Not Active	4.4.4.2
A1R2	20%Pt Vulcan	20	$4,60 \times 10^{-7}$	$0,96 \times 10^{-6}$	Not Active	4.4.4.3
A2	20%Pt Vulcan	20	$4,25 \times 10^{-5}$	$1,75 \times 10^{-4}$	Active	4.4.4.4
A3	20%Pt Vulcan	20	$4,59 \times 10^{-5}$	$1,23 \times 10^{-4}$	Active	4.4.4.5
A4	20%Pt Vulcan	20	0,00	0,00	Not Active	4.4.4.6
A5	20%Pt MWNT	20	0,00	0,00	Not Active	4.4.4.7
A6	20%Pt Vulcan	20	$6,52 \times 10^{-7}$	$6,46 \times 10^{-7}$	Not Active	4.4.4.8
A7	20%Pt Vulcan	22	$1,02 \times 10^{-4}$	$1,57 \times 10^{-4}$	Active	4.4.4.9
A8	20%Pt Vulcan	22	$1,43 \times 10^{-4}$	$2,41 \times 10^{-4}$	Active	4.4.4.10
A9	20%Pt Vulcan	22	$1,13 \times 10^{-4}$	$2,29 \times 10^{-4}$	Active	4.4.4.11
A10	20%Pt MWNT	22	$1,93 \times 10^{-5}$	$2,29 \times 10^{-5}$	Not Active	4.4.4.12
JM	20%Pt Vulcan	22	$1,17 \times 10^{-4}$	$1,82 \times 10^{-4}$	Active	4.3.3

MWCNT (Multiwalled carbon nanotubes); I (Current); TP (Temperature program); T (Temperature); EC (Electrochemical); RT (Reduction time); N/A (Not available)

In figure 4.4.4.1 the black lines indicate the potential vs. current scans without the methanol. The indicated scan area gives an indication of the surface area of the catalyst. Poor EC activity is associated with larger catalytic particles and small surface areas. The poisoning effect is a well studied phenomenon and to meet our objectives, the production of CO will be kept to a minimum. To enable the minimizing of CO formation, the number of scans will be limited to a maximum of 2.

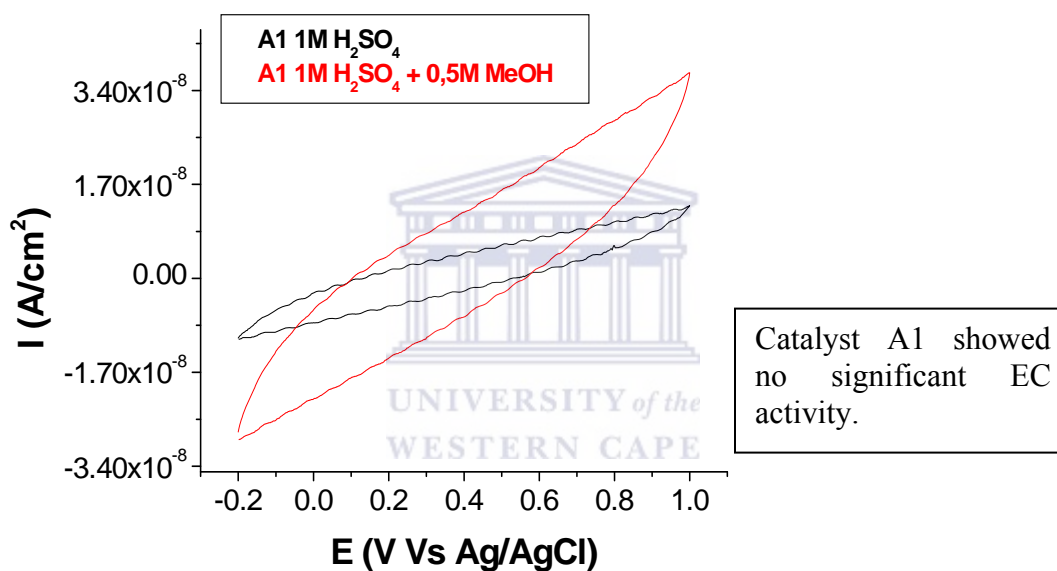


Fig. 4.4.4.1 CV of catalyst A1 at 1,0V vs. Ag/AgCl

The scan indicates very low EC activity in the region of $1,75 \times 10^{-8} \text{ A/cm}^2$ at 0,5V (vs. Ag/AgCl). The actual EC activity was the difference between the base line (Black line) without methanol and after methanol addition (Red line) calculated at $3,80 \times 10^{-6} \text{ A/cm}^2$ and this poor performance after the addition of 0,5M methanol can be attributed to inadequate amounts of catalytic particles formed during the synthesis process, the lack of dispersion and the formation of large particle comprising of sizes.

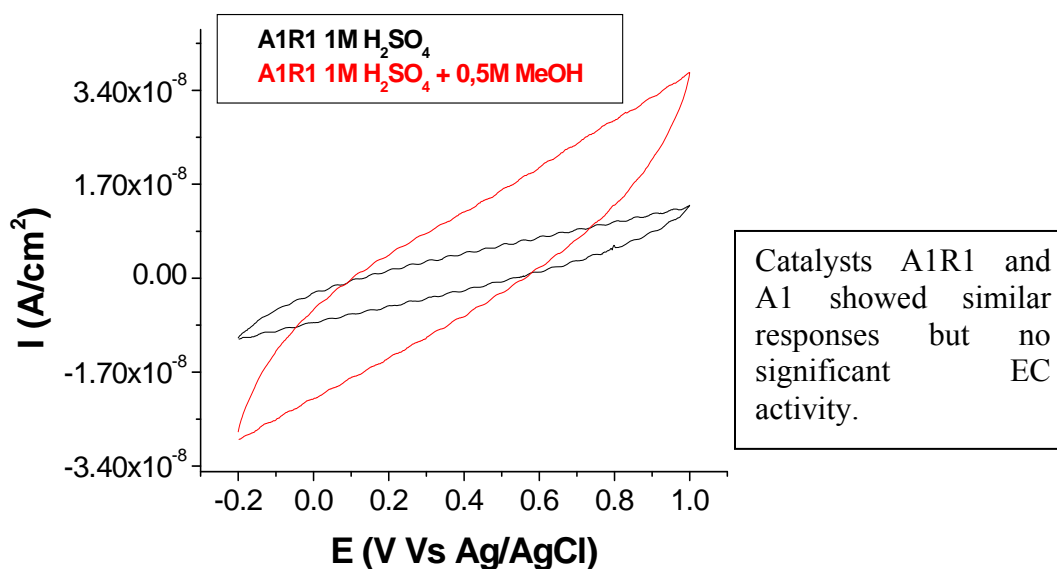


Fig. 4.4.4.2 CV of catalyst A1R1 at 1,0V vs. Ag/AgCl

The poor activity continued with the catalyst A1R1, fig. 4.4.4.2 showing minimal activity for this catalyst produced at 900°C with hydrogen as the reducing agent. The activity at 0,5V (vs. Ag/AgCl) was calculated at $5,79 \times 10^{-9} \text{ A/cm}^2$.

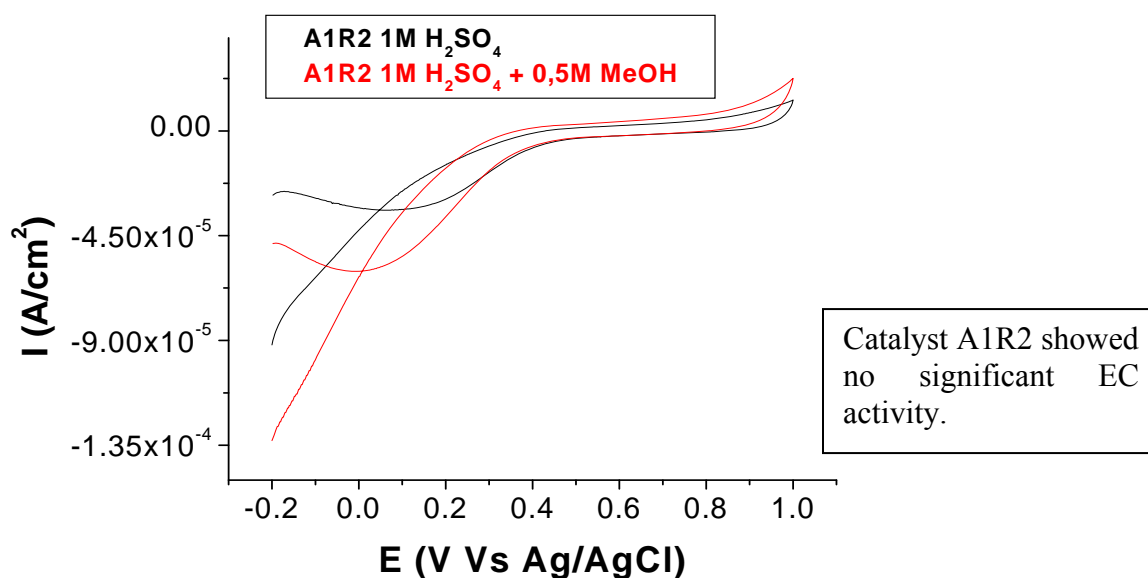


Fig. 4.4.4.3 CV of catalyst A1R2 at 1,0V vs. Ag/AgCl

There was a 99,7% decrease in EC activity from 650 to 900°C and 78,4% from 650 to 700°C. The 78,4% drop in EC activity proved that the high temperature methods used in this research continuously produced low EC activity catalyst. This was evident once again for catalyst A1R2, fig. 4.4.4.3.

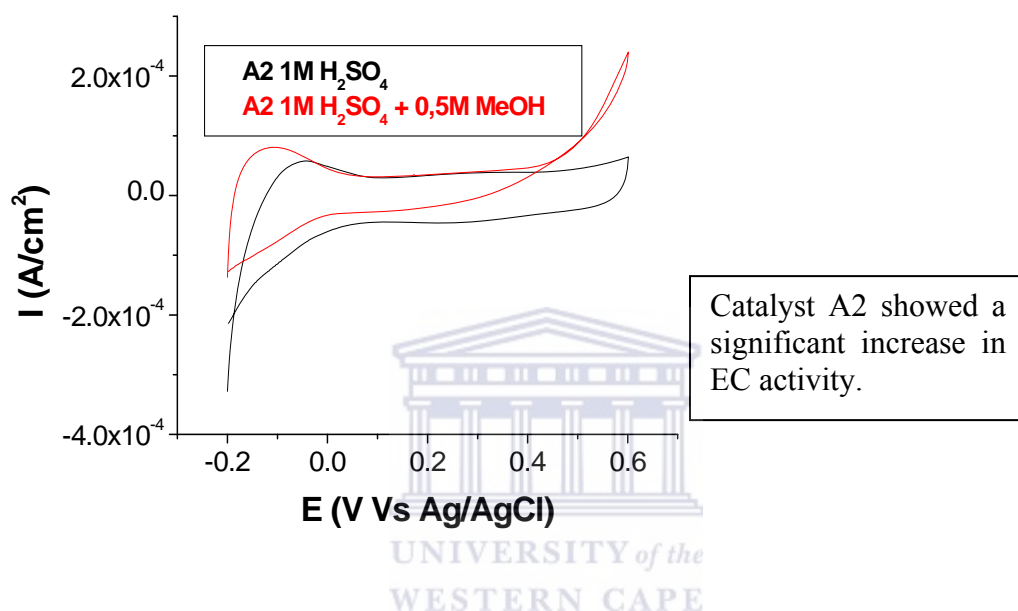


Fig. 4.4.4.4 CV of catalyst A2 at 0,6V vs. Ag/AgCl.

Catalyst A2 produced at 22°C using formic acid as the reducing agent showed early signs in the scan figure 4.4.4.4 of an increased active surface area in the potential region -0,2 to -0,5V (vs. Ag/AgCl) due to the hydrogen adsorption - desorption. An EC activity-plateau is observed at around 0,0 to 0,45V (vs. Ag/AgCl), for both the base line (Black) and methanol oxidation (Red) scans which starts to incline at approximately 0,5V (vs. Ag/AgCl). The activity in this region of 0,5 to 0,6V (vs. Ag/AgCl) the activity in this region is suitable for the fuel cell operations and applications as noted earlier in the literature review. The forward methanol oxidation scan (Red) showed a narrowing of

the curve area during the reverse scan compared to the base line methanol free scan (Black).

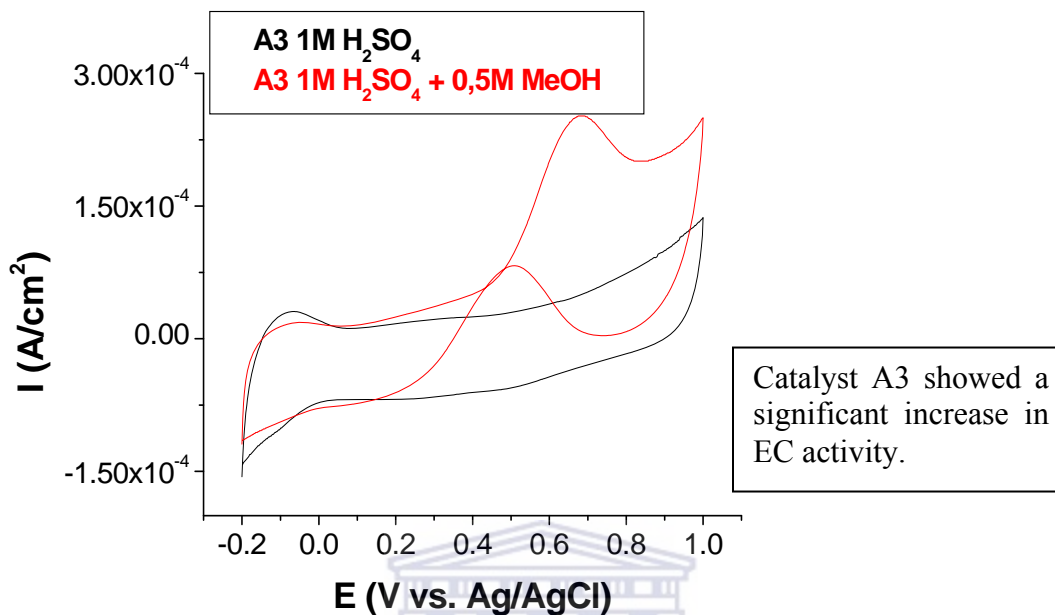


Fig. 4.4.4.5 CV of catalyst A3 at 1,0V vs. Ag/AgCl

Catalyst A3 figure 4.4.4.5 synthesized by the formaldehyde reducing agent route at 22°C, did not show any early signs of increases in current (Red) in the -0,2 to -0,1V (Ag/AgCl) region compared to the base line scan (Black) due to the hydrogen adsorption - desorption. These hydrogen adsorption - desorption peaks region is usually associated with acid mediums. A similar EC activity-plateau observed for catalyst A2, in figure 4.4.4.4, was observed at around 0,0 to 0,45V (vs. Ag/AgCl), for both the base line (Black) and methanol oxidation (Red) scans which starts to incline at approximately 0,5V (vs. Ag/AgCl). The scans maximum potential was extended to 1,0V (vs. Ag/AgCl) for catalyst A3 as seen in figure 4.4.4.5 to gather data for later applications as this reducing agent namely formaldehyde would be further explored in later chapters. In later chapters and the within the objectivity scope of this research, attempts will be made to reduce the

CO poisoning effect where the reverse scan would be free from the reduced activity effects of oxide formations and blocked catalytic sites. The difference in activity was calculated at 4% between catalysts A2 and A3, with the formaldehyde synthesized catalyst A3 proving to be slightly more active at lower potentials i.e. 0,5V (vs. Ag/AgCl). However catalyst A2 showed early signs of activity at even lower potentials, but this was overlooked due to the fact that this peak was also present in the methanol absent base line scan. Formic acid was proving to be a formidable reducing agent but due to the slight advantage formaldehyde exhibited by producing a catalyst with activity only 4% higher than that of the formic acid route synthesized catalyst A2, a decision based on the fuel cell efficiency and capability at the potential of 0,5V (vs. Ag/AgCl), formaldehyde was chosen to be used in sub ambient temperature catalysts preparation methods as will be seen for catalyst A7, A8, A9 and A10, in an attempt to produce a more active catalyst with similar activity to that of the JM commercially available catalyst.

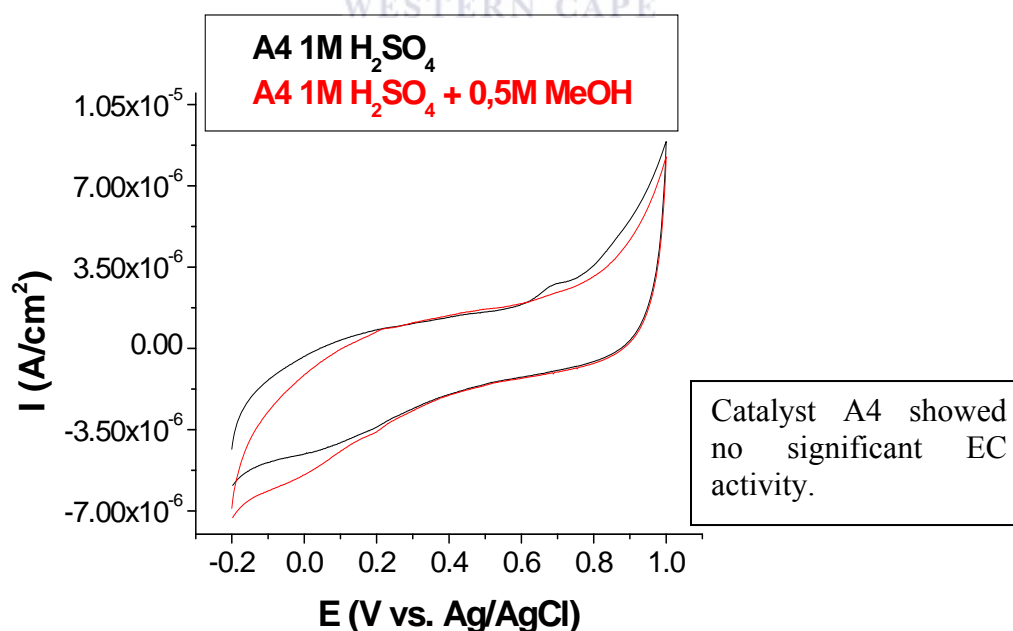


Fig. 4.4.4.6 CV of catalyst A4, 1,0V vs. Ag/AgCl.

There was very little or no difference at anticipated potential (V) regions of activity after the addition of methanol to the EC test cell. This was evidently the result as shown in figure 4.4.4.6 for catalyst A4. The base line scan with out methanol (Black) was very similar that of the scan with 0,5M methanol (Red). Hydrogen as a reducing agent at lower temperatures, 22°C, proved less effective than at higher temperatures in excess of 400°C.

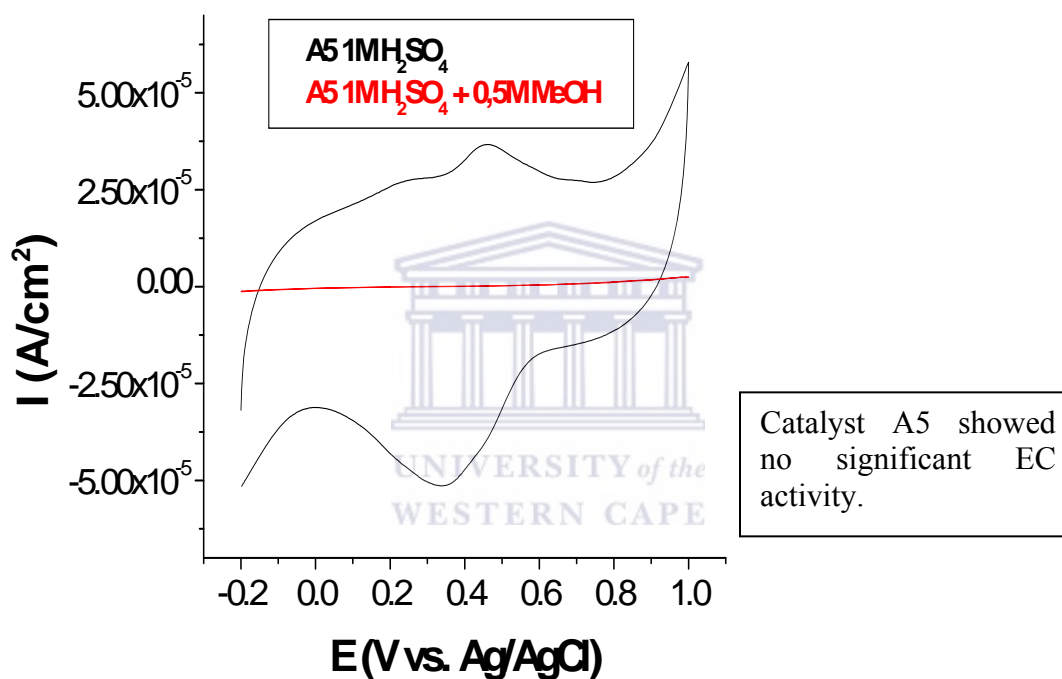


Fig. 4.4.4.7 CV of catalyst A5 at 1,0V vs. Ag/AgCl

Catalyst A5 figure 4.4.4.7 was compared to catalyst A10 figure where both catalysts were prepared on the MWCNT supports. The differences between the two catalysts were the reducing agents and post reduction procedures and treatments during the purification stages, depicting the influence these procedures could have considering the vast difference in the resulting EC activity. The formic acid reducing capability has been

suggested in the thesis concluding proposal as future research work. Previously it has been shown that formic acid is possibly equally effective as a reducing agent compared to that of formaldehyde, therefore post reduction procedures and treatments during the purification stage will be taken into account and used when preparing the next phase of catalysts, A7, A8 and A9. MWCNT supports will be used as supports again in chapters 5, 6 and 7, where these supports will be subjected to a series of pretreatments prior to use.

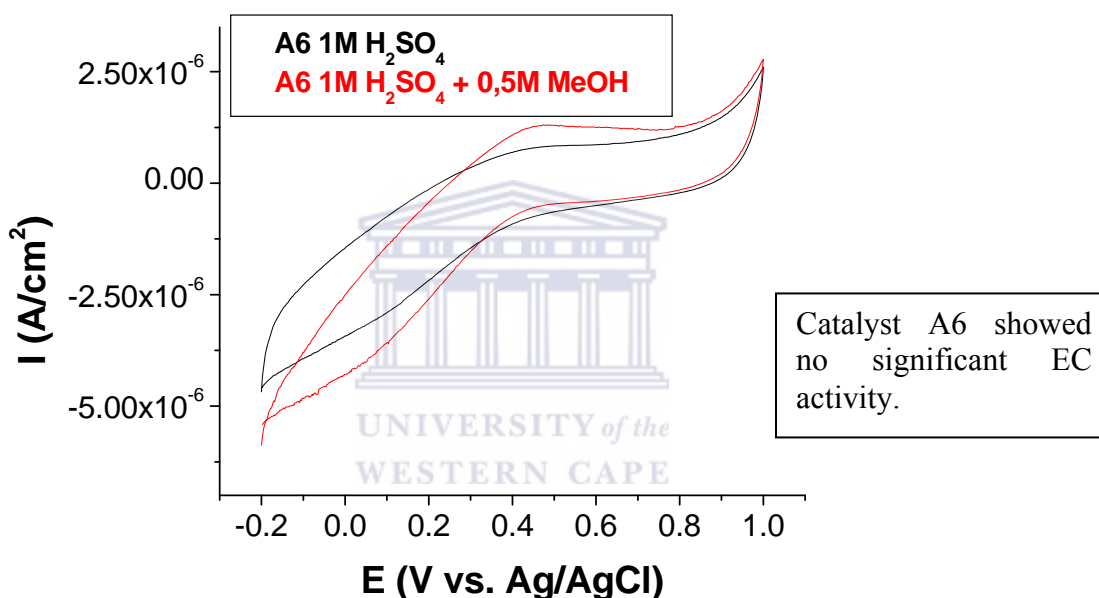


Fig. 4.4.4.8 CV of catalyst A6 at 1,0V vs. Ag/AgCl

Figure 4.4.4.8 shows once again that the hydrogen as a reducing agent was not successful. For the preparation of catalyst A6 the reducing temperature used was at 4°C, and with no real evidence to support future success with hydrogen as a reducing agent, there will no longer be any catalyst preparation using this reducing agent. Future preparations of catalysts involving hydrogen as a reducing agent may be proposed as a possible avenue for future research, however using organic chemical dispersants may be too costly to

remove during the purification stages, and which may also lower the activity of the catalyst.

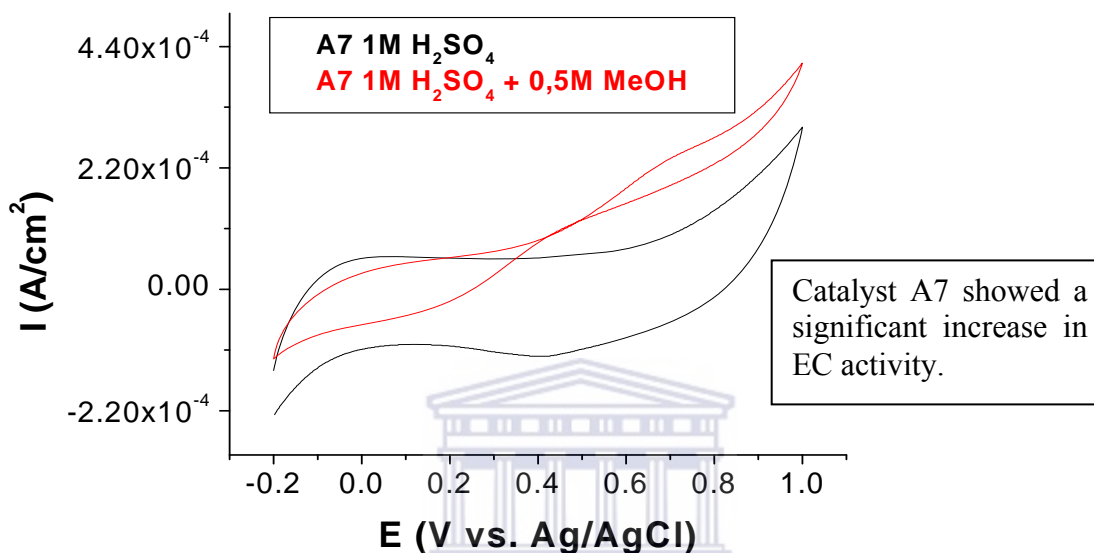


Fig. 4.4.4.9 CV of catalyst, A7 at 1,0V vs. Ag/AgCl

The area under the curve is normally calculated and used as an indication of the surface area available for EC activity. The hydrogen adsorption-desorption region in the potential region -0,2 to 0,1V (vs. Ag/AgCl) in acid medium. Previously in this chapter it was already established that the nano-sized catalytic particles for catalyst A7 does have a larger surface area compared to catalysts synthesized by other synthesis routes mentioned in this research. The potential region of interest was 0,45 to 0,6V (vs. Ag/AgCl), that is associated with the methanol oxidation peak.

A similar EC activity-plateau observed for catalyst A7 as that of A3, as in figure 4.4.4.4, was observed at around 0,0 to 0,45V (vs. Ag/AgCl), for both the base line (Black) and methanol oxidation (Red) scans which starts to incline at approximately 0,5V (vs. Ag/AgCl). The scans maximum potential was extended to 1,0V (vs. Ag/AgCl) for catalyst A7 as seen in figure 4.4.4.9 to gather data for later applications as this reducing agent namely formaldehyde would be further explored in later chapters.

Figure 4.4.4.9 shows the significant increase in activity in the potential region of interest being 0,45 to 0,6V (vs. Ag/AgCl), as mentioned before that is associated with the methanol oxidation peak. The activity is measured by calculating the difference between the base line scan (Black) and the methanol oxidation scan (Red). There was a 38% increase in EC activity at the 0,5V (vs. Ag/AgCl) potential for catalyst A7 from catalyst A3 compared at the same potential (refer to tables 4.5.1 and 4.5.2). The differences in the catalysts preparation and method development was that the reduction took place at 4°C instead of 22°C for catalysts A7 and A3 respectively, the core difference being the introduction of a post reduction heating cycle as part of the purification stage (refer to table 4.5.2).

The parameters and supporting information to the heating cycle was discussed earlier in this chapter, under the heading Synthesis Parameters.

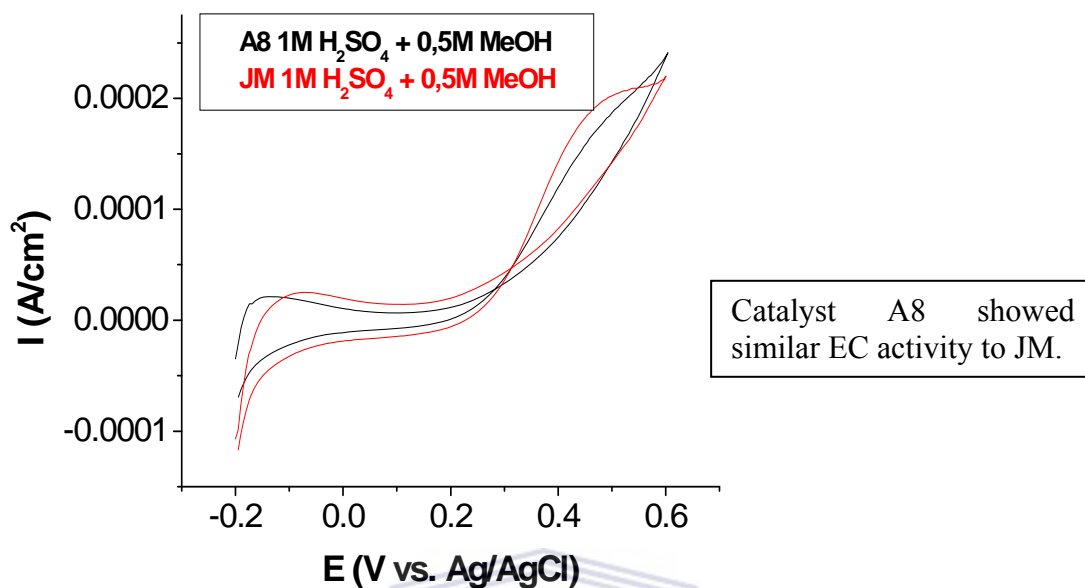


Fig. 4.4.4.10 CV of catalyst, A8, and JM 20% at 0,6V Vs Ag/AgCl

The post reduction heating cycle was previously shown to perform a bi-functional task of aiding in the removal of impurities during filtration and indicating the depletion of platinum ions available for reduction signaling the completion of the reduction process. The increased temperature would cause the formation of larger catalytic particles. The formation of larger catalytic particles was minimized during the synthesis of catalyst A7 by lowering the reduction temperature during formulation which had a significant effect on the EC activity. The catalyst synthesis method for A8, figure 4.4.4.10, incorporated a step to prevent the formation of particles in the region of 20 % > 3nm as observed for catalyst A7. Catalyst A8 was prepared with an increased reduction time period of 18 hours at 4°C (refer to table 4.5.2). A difference in the particle size distribution was then observed with a narrower distribution range of 90% < 3nm. Figure 4.4.4.10 shows the

success the method had achieved in producing an EC active catalyst, further supported with a comparison scan against a well respected commercially available JM catalyst.

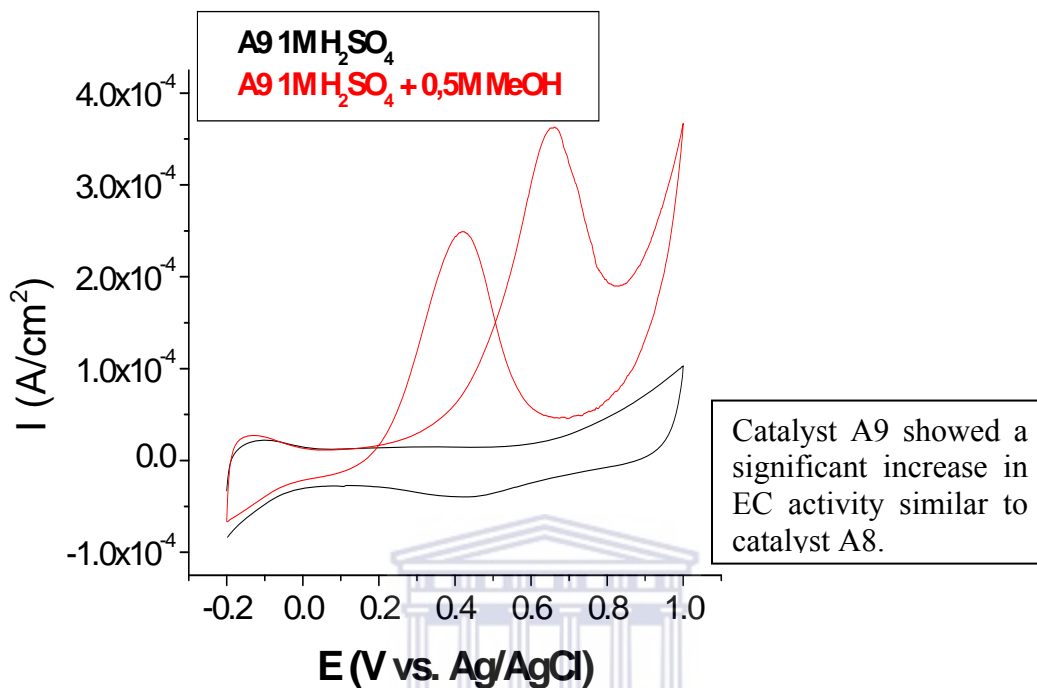


Fig. 4.4.4.11 CV of catalyst, A9 at 1,0V vs. Ag/AgCl

Catalysts A8 (figure 4.4.4.10) and A9 (figure 4.4.4.11), were synthesized using similar preparation methods. As can be seen in figure 4.4.4.11, the scanning potential range was increased to 1,0V (Ag/AgCl). The forward methanol oxidation scan scan (Red) starting from -0,2V starts to incline from approximately 0,2V and peaks at around 0,4V (vs. Ag/AgCl). The early incline was interpreted as EC activity occurring earlier than the other catalysts EC activity CV scans synthesized at higher temperatures. Although catalysts A3, figure 4.4.4.5, also showed an early increase in activity, there was no visible peak during the reverse scan in the 0,65V (vs. Ag/AgCl) potential scan region as observed for catalyst A9 (Figure 4.4.4.11). The peak in the reverse scan at 0,65V (vs.

Ag/AgCl) can be attributed to an oxide formation during the forward scan. The post-reduction temperature of 80°C may also be responsible. This electrochemical chemical reaction and resulting peak formation at 0,65V (vs. Ag/AgCl) has however not adversely influenced the EC activity of catalyst A9.

There was a 17% increase in EC activity from catalyst A7 to A8 and from catalyst A7 to A9 on each occasion. Considering catalysts A8 and A9 were synthesized via the same synthesis route this was expected and confirms the methods reproducibility. Table 4.5.2 gives a summary of catalysts synthesized, critical or limiting parameters, resulting particle size distributions and corresponding EC activities. All catalysts mentioned up until now (ie. Catalysts A1-A9) were prepared on Vulcan supports.

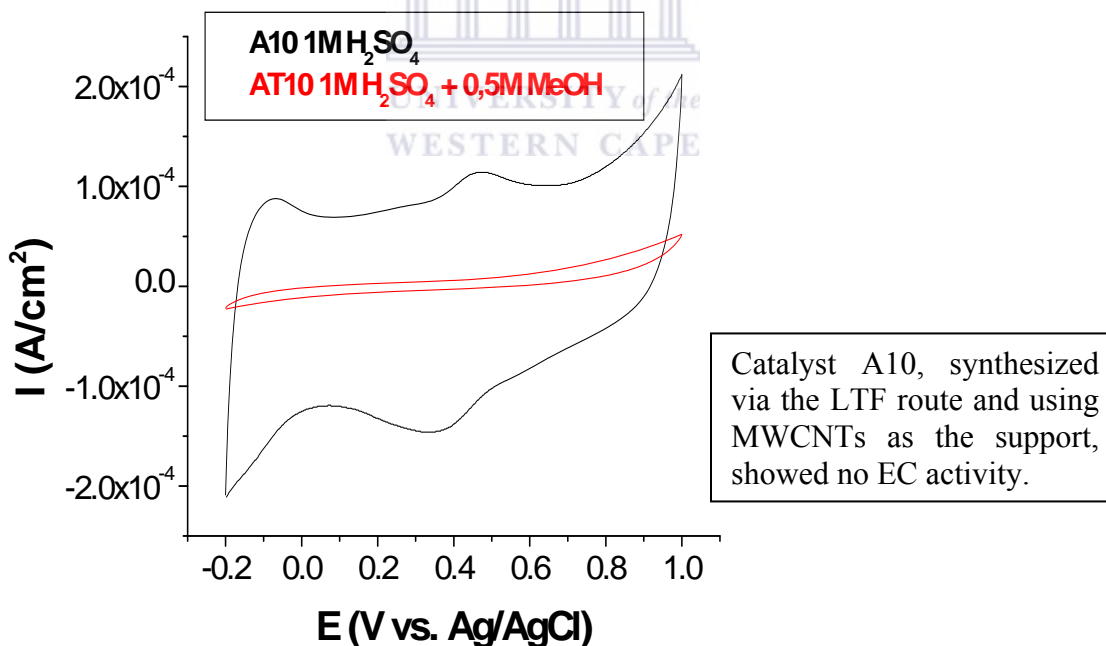


Fig. 4.4.4.12 CV of catalyst A10 at 1,0V vs. Ag/AgCl

Figure 4.4.4.12 shows the poor EC performance and activity during a potential scan from -0,2 to 1,0V (Ag/AgCl). The MWCNT supports were used as a support for catalyst A5.

Those comments apply here as well with regards to pre- and post-reduction procedures and treatments during the purification stages. The MWCNT pretreatments will be explored in chapters 5, 6 and 7. During the CV testing of catalysts supported on MWCNT it was noted that the catalyst did not adhere to the carbon surface when the conventional electrode preparation methods were used. In chapters 5, 6 and 7 a gel preparation will be used and this allowed for better adhesion of catalysts prepared on MWCNT supports, to the electrode.

The major similarity between the methods used thus far was the chemical form in which the platinum species arrived at the growth surface being the carbon support, and the major difference was the catalytic particle growth rate at the carbon support surface's atomic structure which influenced the formation of the nano-sized catalytic particles. The resulting surface atomic structure depended in turn on the growth temperature, which was varied and the relative concentration of the platinum species in the reaction vessel which remained constant for all catalyst preparations.

4.5 Discussion

The initial investigation explored a wide range of possible synthesis parameters as mentioned in Table 4.5.1. The most promising parameters with respect to EC and particle size were further investigated and optimized as shown in Table 4.5.2.

Table 4.5.1 Summary table comparing the different reducing agents and temperatures

Catalyst	Metal Support	Synthesis Parameters			EC Activity		
		TP °C	RA	Vol. ml	T °C	I(A) (vs. Ag/AgCl) 0,5V	I(A) (vs. Ag/AgCl) 0,6V
A1	Pt Vulcan	650	H ₂	150	20	3,80x10 ⁻⁶	4,98x10 ⁻⁶
A1R1	Pt Vulcan	900	H ₂	150	20	5,79x10 ⁻⁹	8,0x10 ⁻⁹
A1R2	Pt Vulcan	700	H ₂	150	20	4,60x10 ⁻⁷	0,96x10 ⁻⁶
A2	Pt Vulcan	22	FA	150	20	4,25x10 ⁻⁵	1,75x10 ⁻⁴
A3	Pt Vulcan	22	F	150	20	4,59x10 ⁻⁵	1,23x10 ⁻⁴
A4	Pt Vulcan	22	H ₂	150	20	0,00	0,00
A5	Pt MWNT	4	FA	150	20	0,00	0,00
A6	Pt Vulcan	4	H ₂	150	20	6,52x10 ⁻⁷	6,46x10 ⁻⁷

FA (Formic acid); RA (Reducing agent); F (40% Formaldehyde); TP (Temperature programme); T (Temperature); H₂ (Hydrogen); EC (Electrochemical); I (Current); MWNT(Multiwalled carbon Nano-tubes)

As will be seen in table 4.5.2, formaldehyde was chosen as the reducing agent for further investigation. Although formic acid produced activity similar to that of formaldehyde, the formaldehyde catalyst A3's activity was slightly higher at lower potentials of 0,5V (vs. Ag/AgCl). The parameters investigated included lower temperatures, reduction

times, sonication times, and MWCNT (Multi-walled Carbon Nano-tubes) as an alternative support.

Table 4.5.2 Summary table using Formaldehyde as the reducing agent

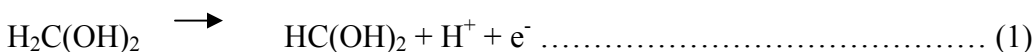
Catalyst	Metal Support	ACPS	Synthesis Parameters				EC Activity Analysis		
			RT hr	TP °C	RA	Vol. ml	T °C	I(A) (Vs Ag/AgCl) 0,5V	I(A) (Vs Ag/AgCl) 0,6V
A7	Pt Vulcan	80%>3nm 10%<4nm	5	4-80	F	150	22	1,02x10 ⁻⁴	1,57x10 ⁻⁴
A8	Pt Vulcan	90%<3nm	18	4-80	F	150	22	1,43x10 ⁻⁴	2,41x10 ⁻⁴
A9	Pt Vulcan	90%<3nm	18	4-80	F	150	22	1,41x10 ⁻⁴	2,39x10 ⁻⁴
A10	Pt MWNT	90%>3nm	18	4-80	F	150	22	1,93x10 ⁻⁵	2.29x10 ⁻⁵
JM	Pt Vulcan	80%<3nm	N/A	N/A	N/A	N/A	22	1,17x10 ⁻⁴	1,82x10 ⁻⁴

ACPS (Average catalyst particle size); RA (Reducing agent); F (40% Formaldehyde); I (Current); TP (Temperature program); T (Temperature); EC (Electrochemical); RT (Reduction time); N/A (Not available); MWCNT (Multi-walled Carbon Nano-tubes)

The surface morphology of the grains of the sample was examined on a transmission electron microscope (TEM). The TEM micrographs (section 4.4.2) of combustion derived samples show that the powder products are voluminous and porous. As a result of high temperature during the combustion process and partial sintering, agglomerated circular shaped primary and secondary metallic particles were formed. The voids in the combustion derived powders can be attributed to large amount of gases evolved during the combustion reaction of high temperature treatments. Upon calcinations of the sample, the size of primary particle increases which resulted in decrease in surface area of the sample as expected and it is confirmed by previous surface area measurements [427] and there was low EC catalytic activity observed here. The larger particles and reduced surface areas (samples A1-A4; table 4.5.1) were in turn associated with the low

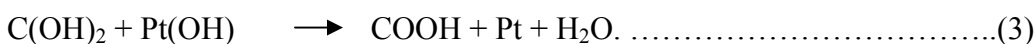
electrochemical activities. The formation of Pt/C catalytic particles at high temperatures produced catalysts with low electrochemical activity, table 4.5.1 and those synthesized at sub ambient temperatures produced high surface area catalysts with high electrochemical activity. In all cases where low or no activity was recorded the particle size distributions were in the region of 80-90% > 4nm and amount of platinum was less than 15%.

Regarding the mechanism for the Pt reduction and formaldehyde as reducing agent; formaldehyde proved to be a successful reducing agent, at sub-ambient temperatures thus requiring and reacting in minimal energy containing environments. The temperature at which formaldehyde was introduced was at 4°C, the temperature was maintained at 4°C for the duration of the reduction process. In an attempt to explain the formaldehyde oxidation mechanism reference [417] will be made to the cyclic voltammetry curve for Pt in 0.1 M HCHO (formaldehyde) + 1 M HClO₄ (perchloric acid), together with and more importantly the curve obtained in the base electrolyte 1M NaOH, since the reduction processes in this thesis were performed in a basic medium (pH=12-14). The general features of this voltammogram are similar to the voltammogram for Pt in HCOOH (formic acid) + 0.5 M sulfuric acid [414]. In each case three peaks occur in the anodic scan, though in the case of formaldehyde the first peak occurs at 0.7 V vs RHE instead of at 0.5 V vs RHE as for formic acid. This peak is attributed to a simple charge transfer step:

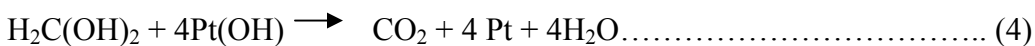


where HC(OH)₂ represents an adsorbed radical occupying a single site on the substrate. The first anodic peak is followed by a “passive” region (as opposed to an “inhibitive” region in the case of formic acid) before the onset of the second oxidation peak.

In the second anodic peak, the strongly adsorbed intermediates of the type COH are removed from the substrate by oxidation reactions such as



With the removal of the strongly adsorbed intermediates, more Pt(OH) sites were created and solution-phase formaldehyde was oxidized sequentially to give the following overall stoichiometry:



A drop in the current was observed in the second anodic peak, it was not clear whether the decrease in current after the second anodic peak was due to the formation of inactive PtO [415] or due to self-poisoning of the formaldehyde oxidation reaction by some sort of secondary disproportionation reaction [416]. However oxidation of formaldehyde does not totally cease after the second anodic peak, as in the case of formic acid. At around 1.1 V the current increases rather abruptly and this increase was attributed to the reaction of a PtO(O)_{ads} species with formaldehyde. At 1.2 V the potential scan was reversed.

The pH control was found to be essential to promote the reduction process. In a basic medium, as observed above and utilized in the in-house catalyst synthesis methods, formation of the of Pt(OH) intermediate to the formation of the Pt metal, was essential. In contrast to the findings of this research, the importance of the hydroxide ion and the pH dependence of formaldehyde oxidation were examined [417] and the findings indicated that the formaldehyde oxidation reaction is independent of hydroxide ion concentration in the solution. However this research attempts to distinguish between the

oxidation of formaldehyde and reduction of platinum mechanisms, where the platinum reduction mechanism possibly includes the –OH group as an intermediate function and the electrons were supplied by the oxidation of formaldehyde mechanism.

With reduction temperatures well in the sub-ambient region, the energy available in the system controlling the particle size producing a high surface area catalyst with particles size distributions in the range of 80% < 3nm, highlights another important aspect of surface energetics other than surface energies is the surface energy ratio. From previous findings [418], energetics were found to play a critical role in determining the shapes of nano-particles or nano-wires as these structures would prefer to minimize the total surface energy and stay in local minima. Especially when the size of the structure is big enough to ignore the effects coming from edges and vertices, the local minima could be identified by the Wulff construction based on the surface energy ratio, which had less uncertainty than the values of the individual surface energies, as previously found [418].

The XRD results obtained in section 4.4.1 indicate face-centered cubic (fcc) platinum structures were evidently characterizing the in-house catalysts. Considering the low energy levels available and the formation of ordered fcc structures for the in-house catalysts during synthesis, a possible explanation could be associated with the embedded-atom method (EAM) stemming from the density functional theory (DFT) [419,420] and mathematically equivalent methods that have been successfully applied to the bulk fcc metals [421,422], and have been pushed beyond the bulk environment to pursue this direction for the application of metals, surfaces and nanoparticles [423,424].

The formation of the nano-sized in-house catalytic particles relative to the embedded atom method consideration could be given to two driving forces in the EAM, assuming there is a non-linear nature of the bond strength. One is the coordination number

dependence resulting from the fact that atoms with a lower coordination number have higher bonding strength due to localized charge distribution. Another analogy that could be a driving force is structural dependence resulting from the fact that an ordered structure (symmetric or periodic) when compared to disordered structures, is likely to have lower bonding energy due to resonance stabilization [418].

In the following chapters the reduction temperatures will be controlled and adjusted as the need arises as certain metal types were observed to reduce readily at temperatures where other metals failed to reduce at all. As reflected earlier in the literature review the correct combination of different metals will be an important concept as multi-metallic catalysts are claimed by many to be the answer in resolving the CO poisoning issue where DMFCs are concerned. The catalyst supports explored include that of Vulcan and MWCNTs where catalysts A5 and A10 synthesized on MWCNTs as a support showed very poor electrochemical activity possibly due to surface impurities, entanglement and lack of dispersion along with insufficient metal particle formation from solution. In future chapters MWCNTs will be pretreated to remove impurities and improve dispersion prior to future use.

The most promising method identified in this chapter to produce active nano-sized catalytic Pt/C particles was that of pH controlled sub ambient temperatures with formaldehyde as the reducing agent. This method will be adopted in synthesizing the multi-metallic catalysts, discussed in future chapters 5-7. The motivation behind the multi-metallic catalysts synthesis will be discussed in chapter 5. The methods will be adjusted to accommodate different metal types.

Chapter 4- Monometallic catalysts

The concluding chapter will include the most effective methods identified during the course of this research.



CHAPTER 5

BIMETALLIC CATALYSTS

5.1 OBJECTIVES

- 5.1.1 To synthesize bimetallic catalysts for methanol oxidation.
- 5.1.2 To synthesize bimetallic catalysts with large electrochemically active surface areas.
- 5.1.3 To synthesize bimetallic catalysts with similar electrochemical activity to the commercially available JM catalysts.

5.2 INTRODUCTION

Bimetallic nanoparticles are of considerable interest from both scientific and technological points of view [317–321]. The bimetallic nanoparticles that are platinum based have a unique function as Fuel Cell catalysts, by functioning as CO removal and CO poisoning prevention catalysts. The mechanism of OH adsorption will be discussed further in sections 6.2 and 7.2. The electrical, optical and catalytic properties of nanoparticles can be tailored by changing composition, shape and size of the nanoparticles. For example, deposition of a second metal on the surface of monometallic nano-particles yields a novel property that cannot be obtained by the monometallic nano-particles. An important factor for controlling the shape and size of the nano-particles is their dispersion stability in synthesis. A number of techniques have been used for stabilizing the metallic nano-particles in solutions. In aqueous solution, polymeric stabilizers are very efficient dispersant, whereas long chain molecules such as alkanethiols are most commonly used in organic media [322–324]. Bi-functional stabilizers were employed by Liz-Marzan et al. [322] who proposed a two-step method to obtain gold Nano-particles with methoxy groups on their surfaces. They prepared gold

nano-particles by the “citrate route”, and subsequently replaced the citrate molecules on gold nano-particles with (3-aminopropyl)trimethoxysilane (APS). Buining et al. [325] prepared gold nanoparticles by the reduction of HAuCl_4 in the presence of bifunctional stabilizer, (3-mercaptopropyl)trimethoxysilane (MPS). A decrease in the molar ratio of $[\text{AuCl}_4^-]/[\text{MPS}]$ decreased the particle diameter in the range of 1–5 nm. Stabilizers to avoid particle aggregation have also been used in the synthesis of Pt–Ru bimetallic nanoparticles and have received considerable attention because of their high catalytic activity toward methanol oxidation in the direct methanol fuel cell (DMFC). To control the nanoparticle size affecting catalytic activity, Paulus et al. used organometallic compounds as both stabilizer and reducing agent in the synthesis of Pt–Ru nanoparticles [326]. The use of organometallic compound in toluene could prepare Pt–Ru nanoparticles less than 2 nm. However, the method was complex and required a delicate control of operating conditions. A simple method was proposed by Wang and Hsing [327] who used a quaternary ammonium surfactant as a stabilizer during the reduction of Pt and Ru ions in the presence of carbon powder (Vulcan XC-72). Average sizes of Pt–Ru nanoparticles on carbon could be controlled by the synthesis temperature in the range of 2–3.5 nm. The present work proposes a synthetic method for Pt–Ru nanoparticles with a bifunctional stabilizer, (3-aminopropyl)-trimethoxysilane (APS). The use of the bifunctional stabilizer can both modify the surface of nanoparticle and control the Pt–Ru nanoparticle size. This method is a one-step process, in which platinum and ruthenium ions are simultaneously reduced by sodium borohydride in the presence of APS [327]. The present work examined size distributions of Pt–Ru nanoparticles prepared at low temperatures and high dispersant volumes to obtain narrow particle size distributions,

which can uniformly increase the catalytic activity in anodes for DMFC. The method is similar to that of the mono-metallic platinum preparation which was modified to accommodate a second metal.

5.3 SYNTHESIS PARAMETERS

Initially the synthesis method was similar to that of the monometallic catalysts. This method was adopted because it was successful whereby the mono-metallic catalysts synthesized by this method showed significant increases when compared to other catalyst synthesis methods used in chapter 4.

Table 5.3.1 Summary of the synthesis parameters

Catalysts	Metal Support	Synthesis Parameters			
		ST Min.	TP °C	RA	Vol. (ml)
B1	<u>Pt-Ru</u> Vulcan	10	4	F	150
B2	<u>Pt-Ru</u> Vulcan	10	4	F	150
B3	<u>Pt-Ru</u> Vulcan	18hr	60-4-60	F	150
B4	<u>Pt-Ru</u> Vulcan	10	60-4-95	F	150
B5	<u>Pt-Ru</u> MWCNT	10	45-55-4-60	F	150

ST (Ultra-Sonication time); RA (Reducing agent); F (40% Formaldehyde); MWCNT (Multiwalled carbon nanotubes); TP (Temperature programme)

The synthesis parameters were initially adopted from the mono-metallic catalysts preparation and development. The methods adopted for the bi-metallic catalysts were attempted with 2 salt precursors instead of 1 as in the situation with mono-metallic Pt/C

catalysts. The mono-metallic Pt/C catalyst method was modified to accommodate the addition of platinum and ruthenium salt precursors. The temperature reduction at 4°C will remain as the central operating temperature and conditions were varied to improve the ECA (Electrochemical activity) to produce high ECA catalyst. After a series of trial catalyst synthesis methods involving different temperatures there was a need to add a temperature programme (TP). The temperature program as will be seen will be a sequential ECA and characterization motivated temperature change where a previously trialed or new temperature will be kept constant for a specific period of time or changed to a different temperature after a specified time:

Stage 1: Pretreatment temperature

Stage 2: Reduction temperature

Stage 3: Post-reduction temperature

Therefore 60-4-60 °C would mean; the salt precursors and 0,5M HCl would be stirred for specified time period at 60 °C, followed by the addition of formaldehyde, reducing agent (RA), maintaining the entire process and solutions involved at 4 °C, and finally a post-reduction temperature treatment at 60 °C. The post- and pre-reduction temperatures were systematically changed influencing the dispersion, size regulation ie. after a character study of the catalytic particles and relative ECA.

5.4 RESULTS AND DISCUSSION

5.4.1 Structural Characterization by XRD

Shown in the following figures are, the characteristic diffraction peaks of the face centered cubic (fcc) Pt demonstrating that a successful reduction of Pt precursor to metallic form has been achieved. The diffraction peaks at about 39° and 46° are due to the Pt(1 1 1), and (2 0 0) plane, respectively, which represents the typical character of a crystalline Pt face, that is fcc. This indicates that the in-house-supported Pt catalysts are Pt (fcc) crystal structure [204-209].

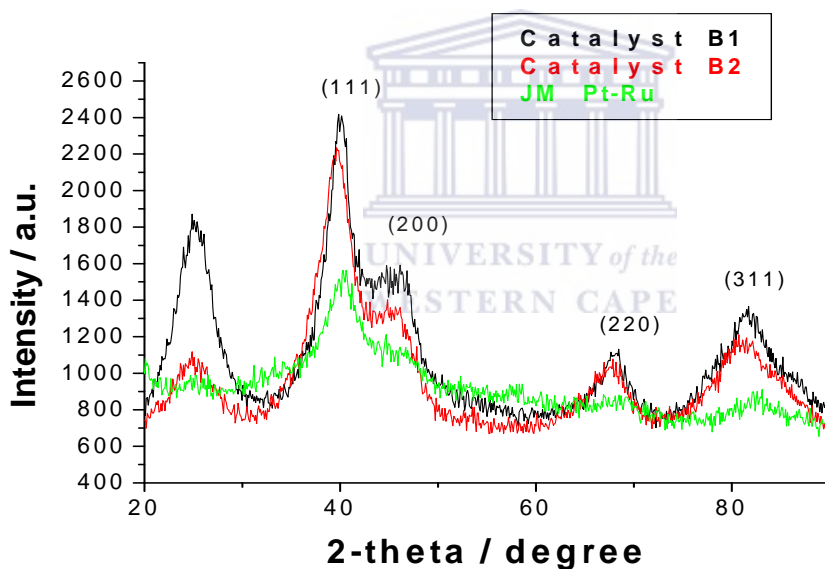


Fig. 5.4.1.1 XRD of catalysts B1, B2 and JM

Figure 5.4.1.1 shows the first of a series of methods used for the Pt-Ru / C catalysts preparation. The catalyst B1 shows similar well defined peaks at positions (111) and (311) as the commercially available JM catalyst. The JM catalyst was 20% Pt and 10% Ru composition on carbon, and all the bimetallic catalysts (B1-B5) were prepared with

the same atomic metal precursor composition and solution molarity concentration. The catalysts B1 and B2 preparation methods differ from one another by the sequence of precursor added to the reaction vessel. The preparation method of Catalyst B1 involved the simultaneous addition of both the platinum and ruthenium salt precursors. Whereas catalyst B2 involved the addition of platinum and ruthenium salt precursors individually and the sequence was controlled by allowing a specified time to pass before adding the second salt precursor. Catalysts B1 and the JM catalysts could share a similar atomic structure due to alloying of Pt-Ru and this could be a possible explanation for the peak shift to the right compared to catalyst B2.

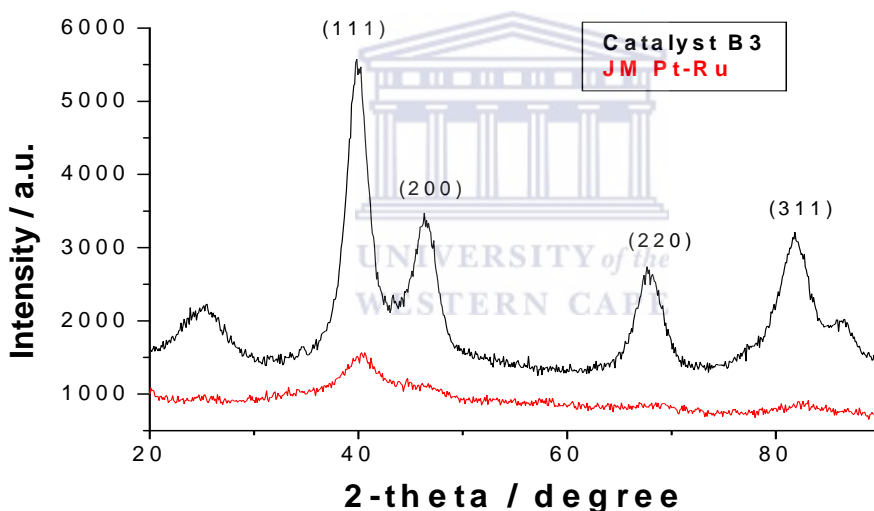


Fig. 5.4.1.2 XRD of catalysts B3 and JM

The simultaneous salt precursor addition gave similar peak positioning for catalyst B3 with regards to (111), (200), (220) and (311), to the JM catalyst, although the peak sizes were significantly different. There was clearly the peak profile platinum-ruthenium formation when compared to the JM spectrum profile.

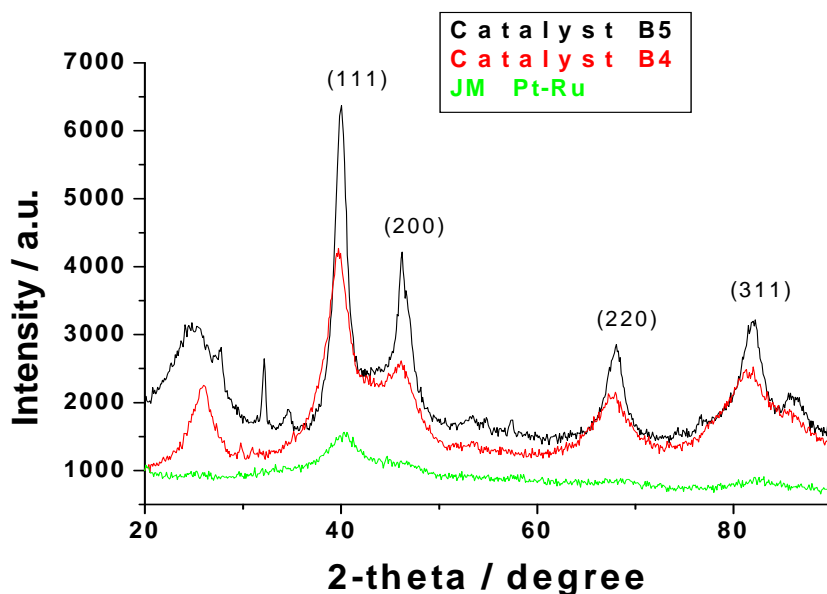


Fig. 5.4.1.3 XRD of catalysts B4, B5 and JM

Figure 5.4.1.3 shows the XRD peak spectrum and profile of catalysts B4 and B5 compared to the JM catalyst. Catalyst B5 shows the peaks shift to right similar to the JM. Catalyst B5 was prepared by the simultaneous salt precursor method to adopt the atomic structure similar to that of the JM catalyst. Catalysts prepared with methods involving individual addition of precursor salts do not match the peak positioning of the commercially available JM catalyst.

5.4.2 Morphological Characterization by TEM

Approximately 300 particles were assessed and counted per catalyst preparation. The particles were examined for closeness and dispersion rated as per method. The dispersion was related to the ECA activity and synthesis parameters. The methods were subsequently modified and this research was steered towards obtaining a highly active ECA catalyst.

Table 5.4.2.1 Catalysts APSD and depositing sequence

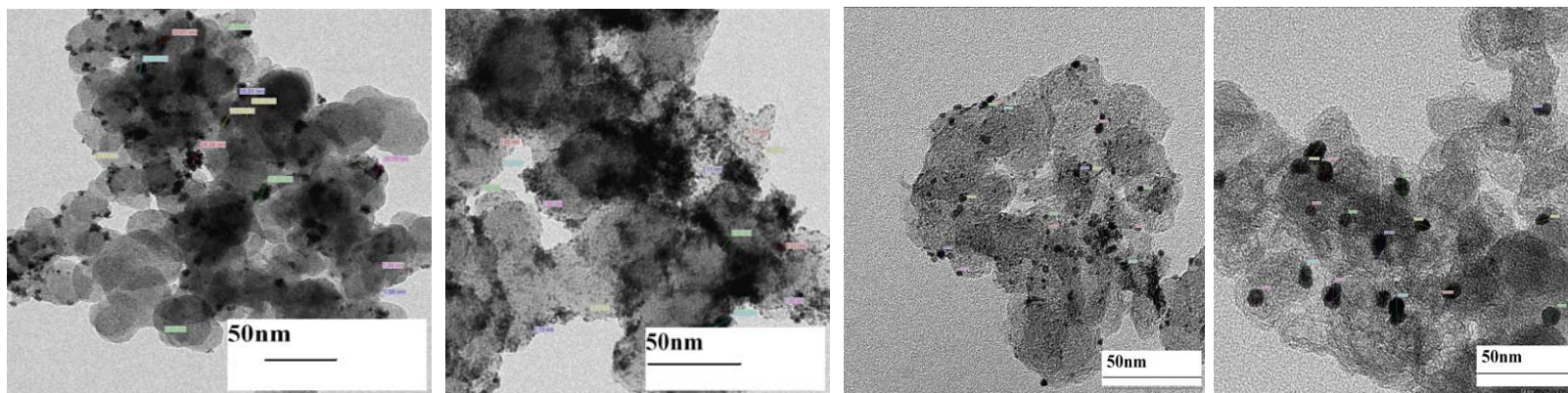
Catalyst	<u>Metals</u> Support	Deposit sequence	APSD nm	Reference figures	
				TEM	APSD
B1	<u>Pt-Ru</u> Vulcan	SD	5% <2,5nm	5.4.2.1(a)	5.4.2.2(a)
B2	<u>Pt-Ru</u> Vulcan	ID	30% <2,5nm	5.4.2.1(b)	5.4.2.2(b)
B3	<u>Pt-Ru</u> Vulcan	SD	3,5nm	5.4.2.1(c)	5.4.2.2(c)
B4	<u>Pt-Ru</u> Vulcan	ID	8,0nm	5.4.2.1(d)	5.4.2.2(d)
B5	<u>Pt-Ru</u> MWCNT	SD	50% <2,0nm 80% <3,0nm	5.4.2.3(a)	5.4.2.3(b)

APSD (Average catalyst particle size distribution); MWCNT (Multiwalled carbon nanotubes); ID (Individual deposition); SD (Simultaneous deposition)

The binary catalysts were prepared using various methods including simultaneous, individual deposition, reaction vessel design (not mentioned here) effective dispersion, longer sonication periods, temperature cycles and two different supports ie. Vulcan XC72 and multi-walled carbon nano-tubes.

The MWCNT will be once again explored here in this chapter and proven to be more effective (as will be seen in catalyst B5) than the Vulcan support mainly to support catalytic particles in producing well dispersed uniform high surface area electrochemically active catalysts with nano-sized particles in the range of less than 2nm. Table 5.4.2.1 shows the results of various parameter changes with regards to sequential precursor and temperature related formulations and their relative particles size distributions. The Vulcan support proved to be very effective compared to the MWCNT during the mono-metallic Pt/C catalyst synthesis (Chapter 4). The superior Vulcan support traits were further exploited to determine the optimum reaction conditions and synthesis parameters for bi-metallic Pt-Ru/C catalysts.





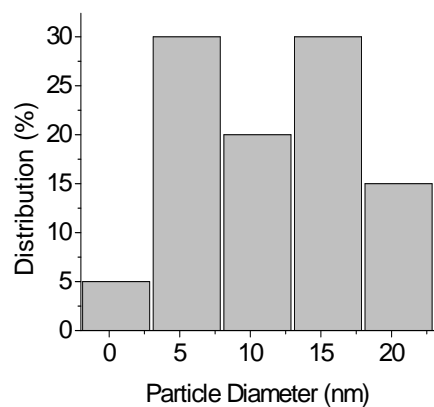
(a)

(b)

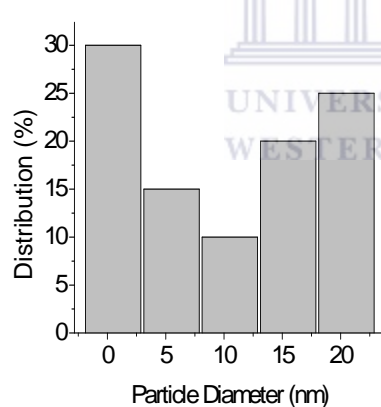
(c)

(d)

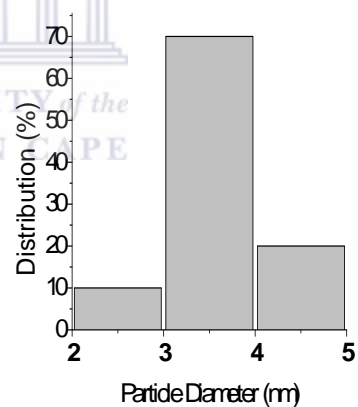
Fig. 5.4.2.1 TEM images of catalysts (a) B1, (b) B2, (c) B3, (d) B4



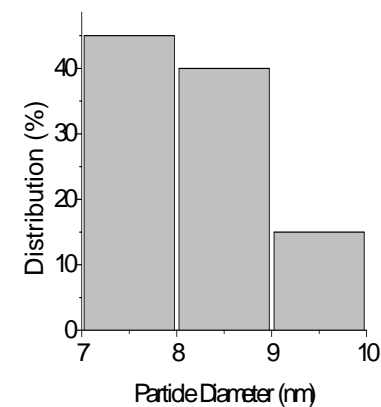
(a)



(b)



(c)



(d)

Fig. 5.4.2.2 Particle size distribution of catalysts (a) B1, (b) B2, (c) B3, (d) B4

Figure 4.5.2.1 (a) shows the particle formation of catalyst B1 on the Vulcan support. After ascertaining the particle size distribution the indication tended towards a particle range to be in the region of $5\% < 2,5\text{nm}$. With 95% of the particles $> 3\text{nm}$ exceeding the requirement previously established in this research for the formation of highly active catalytic particles, it can only be expected that the ECA would be moderate. Catalyst B1 was prepared by the simultaneous deposition method with no assistance from the pre reduction and post reduction temperature regulation.

Similarly, figure 4.5.2.2 shows catalyst B2, also prepared with no assistance from the pre reduction and post reduction temperature regulation. However catalyst B2 was prepared using the individual salt precursor method. The absence of the pre and post reduction temperature treatment regime was to prevent obscuring of the determination of the whether ruthenium would adversely affect the ECA of the catalysts if added together with the platinum precursor. The determination of the proximity effect would ascertain the effect of multi-metallic catalyst sequential preparation in relation to the structural advantages or disadvantages a multi-metallic catalyst may possess. The proximity of the ruthenium to platinum atomic layering had very little effect in lowering the ECA. Since the ruthenium was added second after the platinum salt precursor, it can be said that the close proximity of the ruthenium atomic layer does not adversely affect the ECA of the platinum sites with regards to the methanol oxidation.

Figure 5.4.2.1 (c) for catalyst B3 shows the sparsely embedded particles, greater than the optimum sized catalytic particles. The average particle size for 300 particles was $3,5\text{nm}$.

The method used was part of a series of temperature cycles with the introduction of the pre and post reduction temperatures. The method was repeated and the reduction time was changed to 10 hours (not indicated here), being sufficient, where during this time period a more effective quantity was deposited onto the carbon support. There was a 30% increase in ECA directly related to the increased catalytic quantity deposited and reduced particle size. The individual deposition approach was then used to optimize the temperature cycle, but the TEM image indicated a large particle size and insufficient dispersion, figure 5.4.2.1 (d).

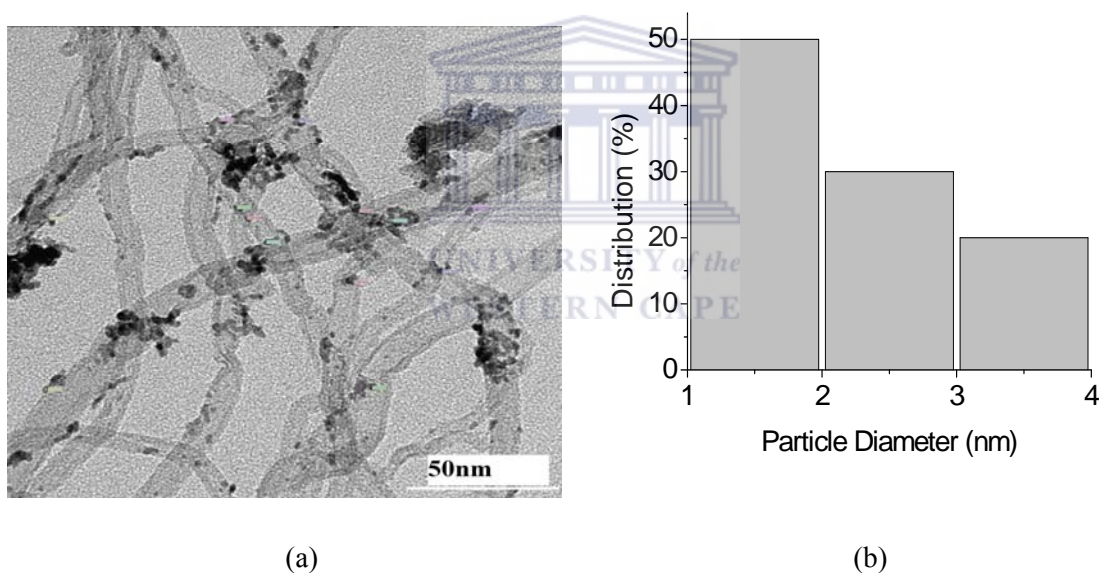


Fig. 5.4.2.2 Catalyst B5 (a) TEM image and (b) Particle size distribution

At first glance figure 5.4.2.2 seems to portray the particle size averaging around 5nm but upon closer inspection this was evidently reflecting the activity of the agglomeration of smaller particles and confirms that smaller particle activity is responsible for the significant increase in ECA.

In this chapter the MWCNT were pretreated as stated earlier using 50% HCl acid solution and hot (boiling) purified water, the washing the MWCNT in a series of cycles. The once washed MWCNT were filtered through a 0,45 micron membrane filter trapping the MWCNT, then heated to 400°C. This pretreatment enabled the successful deposition of catalytic particles as can be seen in figure 5.4.2.2 (a) below. Figure 5.4.2.2 (b) shows the particle size distribution, and the formation of areas with agglomeration of smaller particles in the region of 50% < 2nm.

The formation of high surface area catalytic particles on MWCNT will later show the significant increase in electrochemical catalytic activity at potentials 0,5 – 0,6V (Ag/AgCl) compared to the Vulcan supported catalysts of similar precursor and solutions of equivalent molarity.



5.4.3 Elemental Analysis by EDS

EDS was used to confirm the absence or presence of platinum and ruthenium on the carbon support. Table 5.4.3.1 gives a summary of the TDR (trend determining results) as many other variations in the temperature studies have been performed and not indicated here. The supports used were Vulcan and MWCNT, where the MWCNT proved easier to control with regards to the amount of metal at sub ambient temperatures.

Table 5.4.3.1 Results of the elemental analysis by EDS

Elemental Content	Catalysts				
	B1	B2	B3	B4	B5
% Carbon	79,1	70,4	63,2	76,1	67,8
% Platinum	18,4	23,3	29,8	17,6	25,9
% Ruthenium	2,5	6,3	7,0	6,3	6,3

The EDS results show that although there were instances where platinum was formed in quantities in excess of 20%, the physical properties relating to size, dispersion and particle growth were highlighted as limiting factors influencing the ECA. The pre and post reduction temperatures will prove significant in future applications as ternary and quaternary carbon supports. Pretreated MWCNT are more effective than Vulcan during temperature control and sequential deposition.

5.4.4 Electrochemical Activity determined by Cyclic Voltammetric Analysis

As in chapter 4, the electrochemical (EC) activity was determined by cyclic voltammetric (CV) analysis of the different catalysts. The reducing agents and other synthesis parameters can now be identified as effective synthesis routes when comparing the EC activity for each catalyst. In Table 5.3.3.1 the EC activity of the once-formed catalyst is analyzed in an acidic medium (base analysis), followed by the addition of 1M methanol

Table 5.4.4.1 Comparing the Electrochemical Activity by CV Analysis

	Metal Support	EC Activity				Reference Figures
		T °C	I(A) (vs. Ag/AgCl) 0,5V	I(A) (vs. Ag/AgCl) 0,6V	ECA Status	
B1	<u>20%Pt-10%Ru</u> Vulcan	20	$0,98 \times 10^{-4}$	$1,61 \times 10^{-4}$	Moderate	5.4.4.1
B2	<u>20%Pt-10%Ru</u> Vulcan	20	$3,47 \times 10^{-4}$	$3,92 \times 10^{-4}$	Moderate	5.4.4.2
B3	<u>20%Pt-10%Ru</u> Vulcan	20	$0,84 \times 10^{-4}$	$0,92 \times 10^{-4}$	Moderate	5.4.4.3
B4	<u>20%Pt-10%Ru</u> Vulcan	20	0,00	0,00	Low	5.4.4.4
B5	<u>20%Pt-10%Ru</u> MWCNT	20	$1,21 \times 10^{-3}$	$1,01 \times 10^{-3}$	High	5.4.4.5
JM	<u>20%Pt-10%Ru</u> Vulcan	20	$1,31 \times 10^{-3}$	$1,14 \times 10^{-3}$	High	5.4.4.6

MWCNT (Multiwalled carbon nanotubes); D (Deposition); ID (Individual deposition); SD (Simultaneous deposition); ECA (Electrochemical Activity)

which undergoes oxidation on the platinum surface as shown in the CV graphs below. The potential regions analyzed are -0,2 to 0,6V and -0,2 to 1,0V (vs Ag/AgCl) and the scan rate used was 20mV/s.

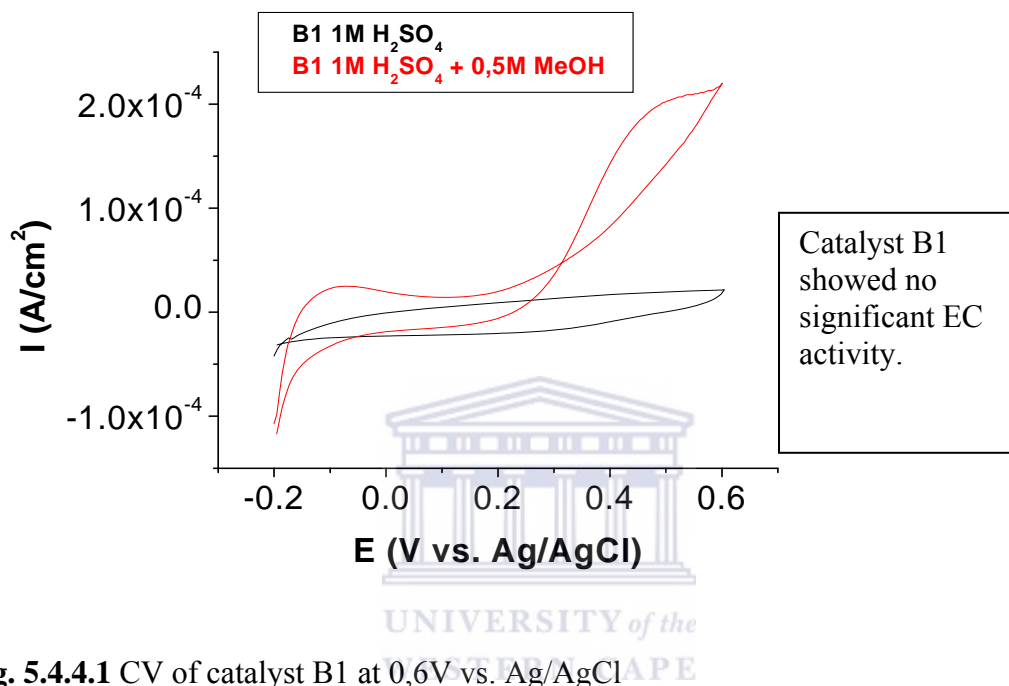


Fig. 5.4.4.1 CV of catalyst B1 at 0,6V vs. Ag/AgCl

Figure 5.4.4.1 shows moderate ECA activity with a particle size distribution including particles which are 5% < 2,5nm in diameter. The potential region of interest, which is 0,45 to 0,60V (Ag/AgCl) has been calculated from difference between the base run without methanol, acid medium (Black) and after methanol addition (Red) to be between 0,98 to 1,61x10⁻⁴ A/cm². As previously noted with the active mono-metallic catalysts (Chapter 5) there was an early increase in activity, after the addition of methanol (Red) between -0,2 to -0,1V (Ag/AgCl) with the plateau forming from 0,05 to 0,175 V (Ag/AgCl). The ECA increased significantly from 0,175 V (Ag/AgCl). The reverse

sweep was noted to have produced higher activity on its return. The forward and reverse scans meet at around 0,5V (Ag/AgCl). At this potential and the catalyst surface may be covered by an oxide from an irreversible reaction. Catalyst B1 was together with

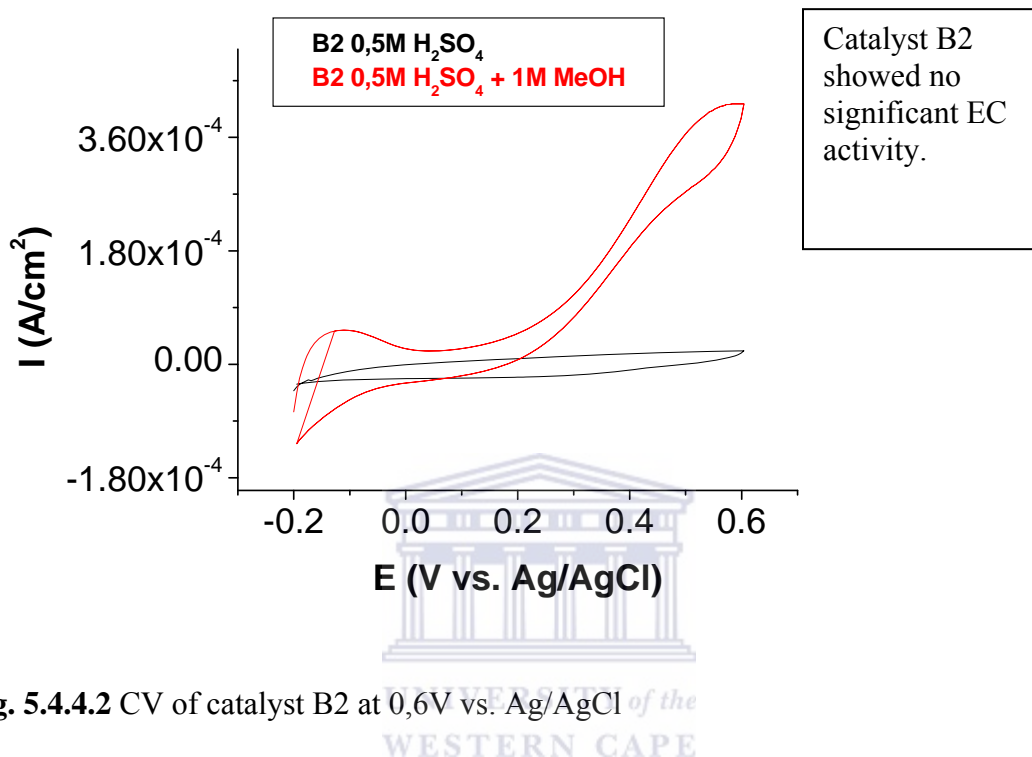


Fig. 5.4.4.2 CV of catalyst B2 at 0,6V vs. Ag/AgCl

catalyst B2, figure 5.4.4.2 rated as producing moderate levels of electrochemical activity. This rating was done compared to the most ECA catalysts synthesized including B5. Catalyst B2 did not have the possible irreversible oxide formation reaction at approximately 0,5V (Ag/AgCl). There was a considerable difference in particle size range for catalyst B2 compared to catalyst B1. Catalyst B2 had 30% of its particle size below 2,5nm whereas b1 had only 5%. Catalyst B2 also showed a 56% increase in ECA when compared to catalyst B1. Once again a direct relation between ECA and catalyst surface area was observed. The objective to obtain data relating simultaneous addition to

alloying and higher surface catalysts, was not fully achieved as in the case with catalyst B2 showing increased ECA and high surface area results compared to catalyst B1.

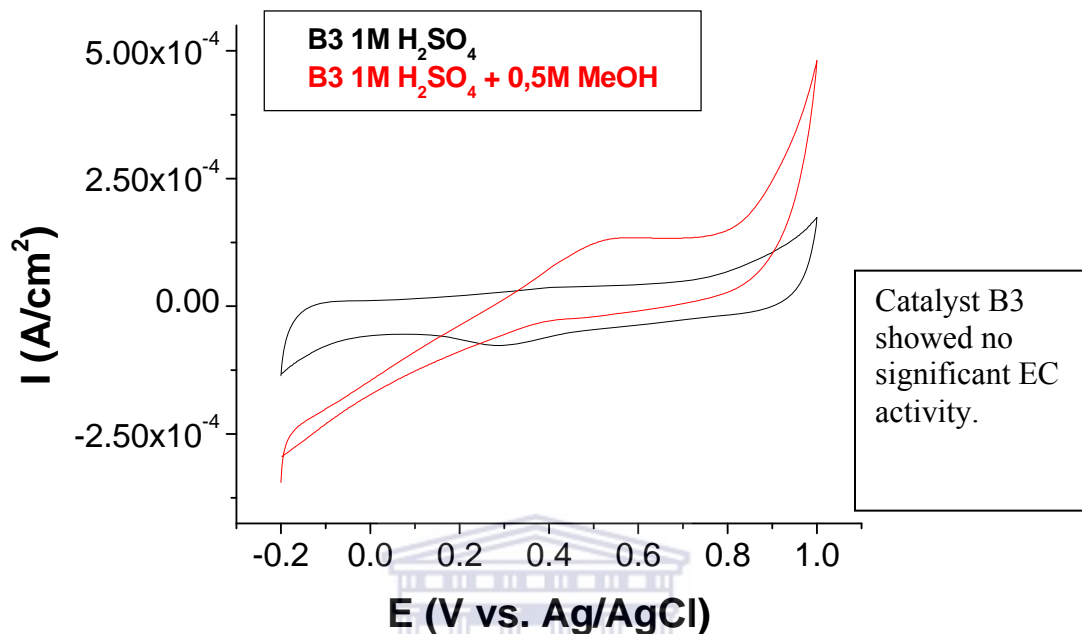


Fig. 5.4.4.3 CV of catalyst B3 at 1,0V vs. Ag/AgCl

From previous observations the simultaneous addition method where more than one salt precursor was added to the reaction vessel, the process was affected by the particle growth and nucleation rates which had to be taken into consideration. This was compounded by the increased concentration of metal ions. Catalyst B3 Figure 5.4.4.3 was a result of many trials concerning temperature variations during the pretreatment and post reduction stages. The complexity of the system metal was a combination of trying to synthesize nano-sized metal catalytic particles and still preserve the properties with respect to ECA. Compared to the scan of catalyst B1 there was a shift in the plateau region, to $0,5$ to $0,8$ V (Ag/AgCl) and there was a steady increase from the start of the

scan in the region -0,2 to -0,1V (Ag/AgCl). The most prominent difference also being the absence of the early ECA peak in the region -0,2 to -0,1V (Ag/AgCl) for catalyst B3.

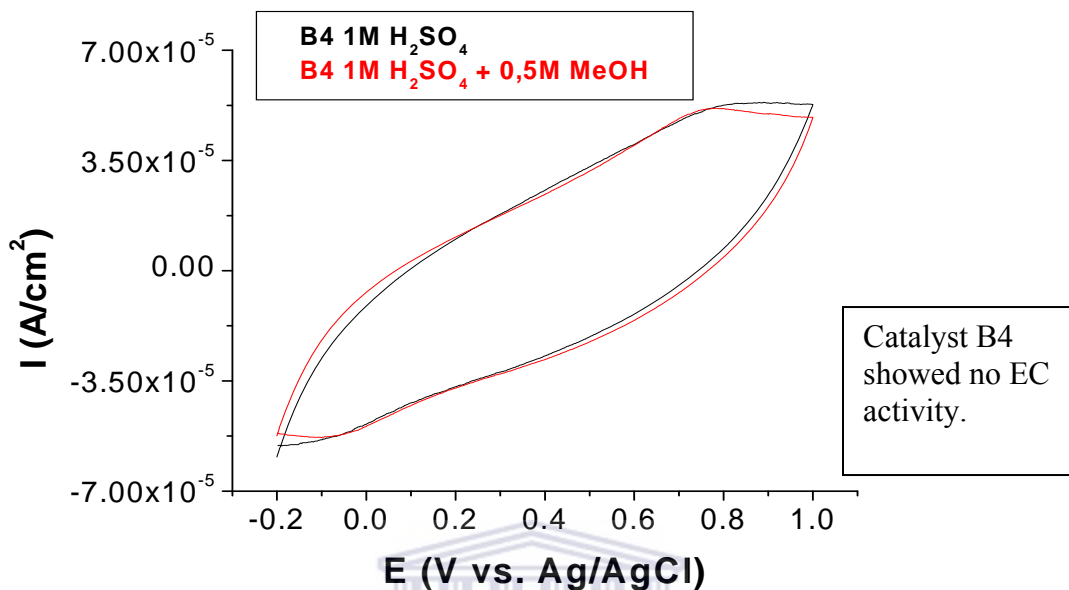


Fig. 5.4.4.4 CV of catalyst B4 at 1,0V vs. Ag/AgCl

Figure 5.4.4.4 shows a scan where the individual method differs from the individual method used for catalyst B2. The difference was the salt precursor solutions were added by 2ml volumes at a time and alternated between the two solutions. This procedure may have affected the atomic arrangement, not obvious in the XRD, where the ruthenium covered the platinum layers preventing the platinum from interacting with electrolyte during the cyclic voltammetric testing. Another postulation could stem from the generic nucleation stage where the ruthenium being less conductive forms at the base between the alloy and carbon support during this method.

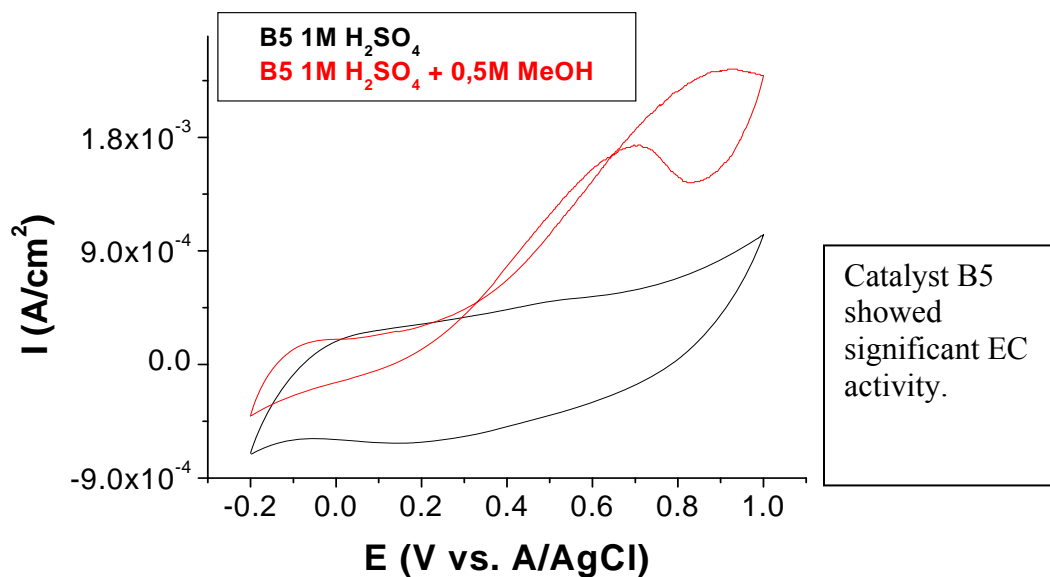


Fig. 5.4.4.5 CV of catalyst B5 at 1,0V vs. Ag/AgCl

MWCNT proved to be easier to manipulate after a series of pretreatments, by varying the different approaches to the deposition methods was useful as a very effective support. The MWCNT support responded to the temperature variations during the reduction and synthesis process. Catalyst B5, figure 5.4.4.5, showed a significant increase in activity compared to the catalysts prepared on Vulcan supports not mentioned as the activity was rated as moderate.

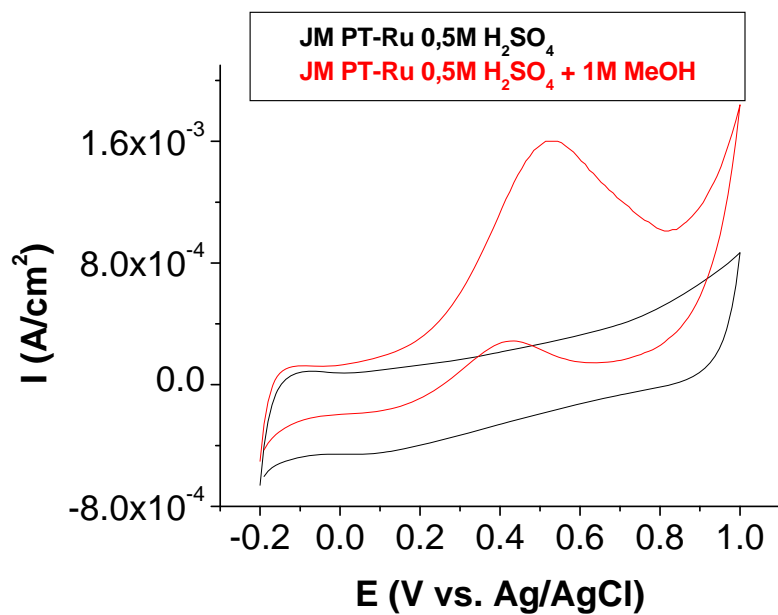
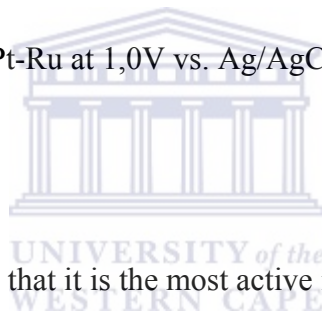


Fig. 5.4.4.6 CV of catalyst JM Pt-Ru at 1,0V vs. Ag/AgCl



Catalyst B5 has shown with CV that it is the most active in-house bimetallic catalyst, thus

CA was performed to determine the longevity thereof.

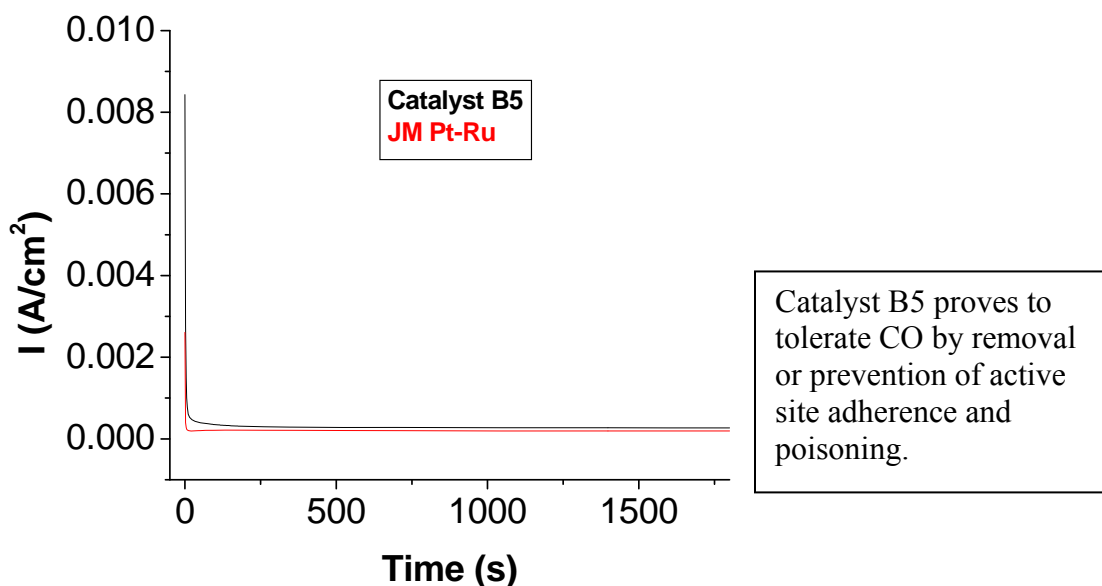


Fig. 5.4.4.7 CA of catalyst B5 at 0,3V vs. Ag/AgCl (1800 sec.)

To obtain a particle diameter less than 3nm for platinum-ruthenium, reduction is performed at temperatures below 5 °C, the temperature gradient and programme rapidly reduced platinum - ruthenium above 60 °C producing large particle diameters >3nm and resulting in lower electrochemical activity . The simultaneous reduction of platinum and ruthenium has temperature sensitive particle size ranges. At temperatures below 5°C, the platinum particle size diameter can be easily controlled to less than 2nm on pretreated MWCNT as compared to Vulcan. The pretreatment involved treating the commercial MWCNTs by filtration with 500ml HCl and boiling purified water (1:1) followed by heat treatment at 400°C in an inert atmosphere, N_2 .

Table 5.5.1 Summary table comparing the different reducing agents, temperatures and EC activities of the bimetallic catalysts

Catalyst	Metal Support	D	ACPS nm	Synthesis Parameters				EC Activity		
				ST Min	TP °C	RA	Vol. (L)	°C	I(A) (vs. Ag/AgCl) 0,5V MeOH	I(A) (vs. Ag/AgCl) 0,6V MeOH
B1	Pt-Ru Vulcan	SD	5% <2,5	10	4	F	0,15	20	$0,98 \times 10^{-4}$	$1,61 \times 10^{-4}$
B2	Pt-Ru Vulcan	ID	30% <2,5	10	4	F	0,15	20	$3,47 \times 10^{-4}$	$3,92 \times 10^{-4}$
B3	Pt-Ru Vulcan	SD	3,5	18h	60-4-60	F	0,15	20	$0,84 \times 10^{-4}$	$0,92 \times 10^{-4}$
B4	Pt-Ru Vulcan	ID	8,0	10	60-4-95	F	0,15	20	0,00	0,00
B5	Pt-Ru MWCNT	SD	50% <2,0 80% <3,0	10	45-4-60	F	0,15	20	$1,21 \times 10^{-3}$	1.01×10^{-3}

ACPS (Average catalyst particle size); ST (Sonication time); RA (Reducing agent); F (40% Formaldehyde); SBH (NaBH₄); MWCNT (Multiwalled carbon nanotubes); D (Deposition); ID (Individual deposition); SD (Simultaneous deposition); TP (Temperature program)

Using formaldehyde as the reducing agent complete reduction of platinum can be achieved using a heating cycle, heating for 5 hours at 40-45°C to ensure dispersion, followed by the addition of the reducing agent and stirring for 5 hours below 5°C, and finally heating for 1 hour at 60°C. With this exceptionally higher surface area, this catalyst produces exceptionally high activity with a ruthenium alloy, Table 5.5.1.

The voltammogram fig. 5.4.4.6 (Black line) shown was obtained prior to adsorption of the CO monolayer and the upper potential limit was extended to 1.0V. The voltammogram obtained after 2 cycles (black line) is almost without any outstanding peaks, characterised by a relatively large capacitive current. A small peak between -0.15 and -0.1V is observed on the positive forward sweep associated with hydrogen desorption from Pt sites and at more positive potentials the increase in current is

attributed to the formation of an oxide layer which is removed in the negative going sweep at potentials below 0.6V. In addition, with respect to the ruthenium stability, the capacitance decreases with the increased number of cycles, indicating a decrease in the amount of hydrous ruthenium oxide in the electrode structure [394,395]. The changes in the voltammograms observed occurred gradually during the cycling and were easily noticeable in the voltammograms. The possibility of ruthenium electrode degradation was supported by previously reported studies of a series of various preparation methods prepared catalysts with varying Ru coverage [396,397-400], support the conclusion that the changes observed correspond to an increase of the platinum and decrease of the ruthenium character of the surface of the catalyst metal nano-particles upon cycling. The mechanism depending on the formation of an alloy can be ascribed to the particle size allowing the nano-sized particles to interact with the matrix where evidence suggesting the role of Ru in promotion of the oxidation of CO at Pt-Ru alloy surfaces by providing direct evidence of the presence of both Ru³⁺ and Ru⁴⁺ species at the surface of Pt-Ru catalyst particles in the potential region in which CO oxidation occurs. The Ru–O distance provides an indication of the average oxidation state of the Ru atoms. The as prepared material corresponded to Ru³⁺, whilst a mixture of Ru³⁺ and Ru⁴⁺ are present at 0.5V when the Ru atoms were incorporated into a Pt-Ru bimetallic surface alloy.

The formation of larger particles during synthesis procedures mentioned above, Table 5.5.1, was found to be directly related to the temperature and dispersion techniques. The electrochemical activity of these larger (95%>3nm) catalytic particles was adversely affected and possibly due to the interaction loss of adsorption energy for CO [?].

This voltammogram fig. 5.4.4.6 also indicates the activity towards methanol oxidation, (red line), relating favorably to the particle size ($80\% < 3\text{nm}$) trends and low temperature synthesis procedures.

The bimetallic catalyst showing the most promising performance, B5, during the CV testing was analysed for CO tolerance using chronoamperometry observed in fig.5.4.4.7. This technique was performed at room temperature, at 0.3V and for 30minutes. The mechanism by which the promotion effect of ruthenium in improving the CO tolerance of Pt anode catalysts occurs was described by Watanabe and Motoo [390] as bifunctional, with Ru supplying oxygen species at lower potentials that facilitate the removal of adsorbed CO from the active Pt sites, by the activation of water to form OH, as well as decreasing the strength of the Pt–CO bond via a perturbation of electronic properties of the Pt atoms, a ligand effect. Considerable effort has gone into further understanding of the details of this mechanism and several excellent reviews are available that summarise the findings [390-393].

The CO tolerance observed in the CA analysis of B5 can be attributed to the effectiveness of the Pt-Ru-CO bonds formed during the sub ambient temperature synthesis. The Pt–Ru-CO bond may be explained from a binding energy point of view. Pt atoms and step atoms of small Pt clusters bind CO more strongly than Ru(0 0 1) does. In contrast, at bigger, more compact Pt islands with straight steps the binding energy of CO at Pt–Ru steps is lower than on Ru(0 0 1). This attraction of CO to Ru on well annealed surfaces might be one reason why PtRu bimetallic anodes show an enhanced CO tolerance in the

direct methanol fuel cell. In a simple bifunctional approach this effect would not be expected because Pt(1 1 1) and Ru(0 0 1) have similar CO binding energies [426].

The EDX and TEM results confirm the presences and formation of ruthenium metallic nano-particles and the XRD results confirmed an ordered growth formation at sub ambient temperatures. The energy available in the system, considering a temperature gradient was developed which was motivated by observations relating to dispersion and agglomeration formation, needed to be taken into account. It was decided that a pre-reduction temperature higher than the reduction temperature be introduced that was sufficient to allow precursor solubility and dispersion of ionic species with the carbon support. The bimetallic reduction would then follow and allowed to occur at temperatures below 5°C; therefore the energetics of the system should be taken into account. The epitaxial growth of one metal on another is determined not only by surface energy considerations but by the kinetics of the growing film as well. The system is generally far from thermodynamic equilibrium. However, a local equilibrium will be established in the surface region which will reflect the energetics of the system. The surface energy of the Pt(1 0 0) was recorded at 2.734 Jm^{-2} (1 electron volt = $1.60217646 \times 10^{-19}$ joules) [425].

In future chapters 6 and 7 attempts will be made to add non-noble metals to increase the mass activity of the Pt-Ru catalysts.

CHAPTER 6

TERNARY CATALYSTS

6.1 OBJECTIVES

- 6.1.1 To synthesize ternary catalysts for methanol oxidation.
- 6.1.2 To synthesize ternary catalysts with large electrochemically active surface areas.
- 6.1.3 To synthesize ternary catalysts using the simultaneous depositing method with similar electrochemical activity to JM catalysts.

6.2 INTRODUCTION

The development of new electro-catalyst materials, with significantly lower affinity for carbon monoxide, is essential in the further advancement of polymer electrolyte membrane fuel cell (PEMFC) technology. An ideal catalyst for the anode would be fully tolerant to CO poisoning, while maintaining its activity for the oxidation of methanol. Platinum, the most active material for the hydrogen oxidation reaction, is unfortunately extremely susceptible to CO. It is well established that bimetallic systems, with Pt as one of the components, can give substantial tolerance to the presence of CO in the fuel stream. One known example is that of PtRu, where enhanced tolerance could be ascribed to a decrease in CO binding energy on platinum due to electronic substrate effects [328], and to the oxidation of chemisorbed CO being catalyzed at low potentials by the activation of H₂O [329]. The latter is due to the facile formation of the oxygen containing species, in the form of adsorbed hydroxyl species (OH_{ads}), on oxophilic ruthenium. Water induced oxide formation has been attributed to metals situated in the early transition series and a high water dissociation capability has been predicted for these [330]. Quite recently, a two to threefold enhancement of CO tolerance in a PEM fuel cell was reported to be

exhibited by carbon supported alloy nano-crystalline PtMo (4:1)/C, as compared to PtRu/C [331, 332]. The increased CO tolerance was related to the ability of PtMo to promote the CO oxidation process at very low electrode potentials. This was attributed to oxygen transfer from Mo oxyhydroxide species with only the OH species of the oxyhydroxide states (predominantly MoO(OH)₂) being reactive with adsorbed CO [333, 334]. Since this reactive state, due to its size, has the potential of reducing the availability of adjacent Pt sites for molecular hydrogen dissociation, a PtMo catalyst with an atomic ratio of 4:1 was shown to give the best performance. Additionally, the formation of a molybdenum hydrogen bronze HyMoOx that could be formed by the ‘spillover’ of hydrogen from Pt sites to Mo, has been suggested as a possible explanation for enhanced catalytic activity towards CO [335]. There has also been an effort to improve the behavior of the PtRu binary catalyst by incorporation of a third metal exhibiting facile oxide formation characteristics. In the case of PtRuMo, promising results were attained for PEMFC operation on hydrogen [336, 337] or reformat gas [338, 339]. The inclusion of W was also found to be beneficial [339], while partial substitution of Ru in PtRu by Cr, Zr, or Nb, resulted in a decrease in activity for H₂ oxidation in the presence of 10 or 100 ppm CO [340]. In this chapter ternary catalyst formulation of one of Fe, Co and PtRu, supported on high-surface area carbon, were prepared and tested with CV and the most active combinatorial methanol oxidation catalyst for their applicability as CO tolerant anode electro-catalysts in the PEMFC will be done via CA.

6.3 SYNTHESIS PARAMETERS

In this chapter in relation to the synthesis parameters, the concepts adopted are from the binary synthesis method that were further refined with more focus on the temperature programme (TP) to accommodate the third metal in ternary catalyst synthesis:

Stage 1: Pretreatment temperature

Stage 2: Reduction temperature

Stage 3: Post-reduction temperature

Therefore 40-4-40 °C would mean; the salt precursors and 0,5M HCl would be stirred for specified time period at 40 °C, followed by the addition of formaldehyde, reducing agent

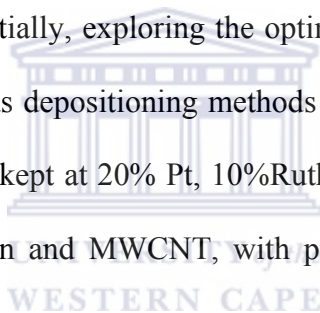
Table 6.3.1 Summary of the synthesis parameters for the Ternary Catalysts

Catalysts	Metals Support	Synthesis Parameters				
		Depositing sequence	ST min	Temp. Prog.	RA	Vol. ml
C1	<u>Pt/Ru/Co</u> Vulcan	SD	10	40-4-95	F	150
C2	<u>Pt/Ru/Co</u> Vulcan	ID	10	40-4-95	F	150
C3	<u>Pt/Ru/Fe</u> Vulcan	ID	10	40-4-95	F	150
C4	<u>Pt/Ru/Fe</u> MWNT	ID	10	40-4-95	F	150
C5	<u>Pt/Ru/Fe</u> MWNT	SD	1hr	40-4-40	F	150
JM	<u>Pt/Ru</u> Vulcan	N/A	N/A	N/A	N/A	N/A

APS (Average catalyst particle size); ST (Sonication time); RA (Reducing agent); F (40% Formaldehyde); SBH (NaBH₄); MWCNT (Multiwalled carbon nanotubes); D (Deposition); ID (Individual deposition); SD (Simultaneous deposition); N/A (Not available)

(RA), maintaining the entire process and solutions involved at 4 °C, and finally a post-reduction temperature treatment at 40 °C. Controlling the post reduction temperature proved essential in controlling the particle size.

The challenge of reducing or preventing the CO poisoning effect continued by adding 3 metals on to carbon supports involves the maintenance of the ECA with relative input from supporting properties of the catalyst including the particle size, dispersion and controlling the growth rate. This becomes even more challenging when four metals are deposited onto the carbon supports. The 4 metal interaction during preparation will be discussed in section 7.2. For the ternary catalysts Pt-Ru-M (M = Co or Fe) combinations are once again prepared sequentially, exploring the optimum metal deposition sequence. The individual and simultaneous deposition methods will be investigated again. The precursor salt solutions will be kept at 20% Pt, 10% Ruthenium and 10% Iron or Cobalt. The supports used were Vulcan and MWCNT, with pretreatments and post reduction temperature



6.4 RESULTS AND DISCUSSION

6.4.1 Structural Characterization by XRD

As for the binary catalysts, the following figures show the characteristic diffraction peaks of the face centered cubic (fcc) Pt demonstrating that a successful reduction of Pt precursor to metallic form has been achieved. The diffraction peaks at about 39° and 46° are due to the Pt(1 1 1), and (2 0 0) plane, respectively, which represents the typical character of a crystalline Pt face, that is fcc. This indicates that the in-house-supported Pt catalysts are Pt (fcc) crystal structure [204-209].

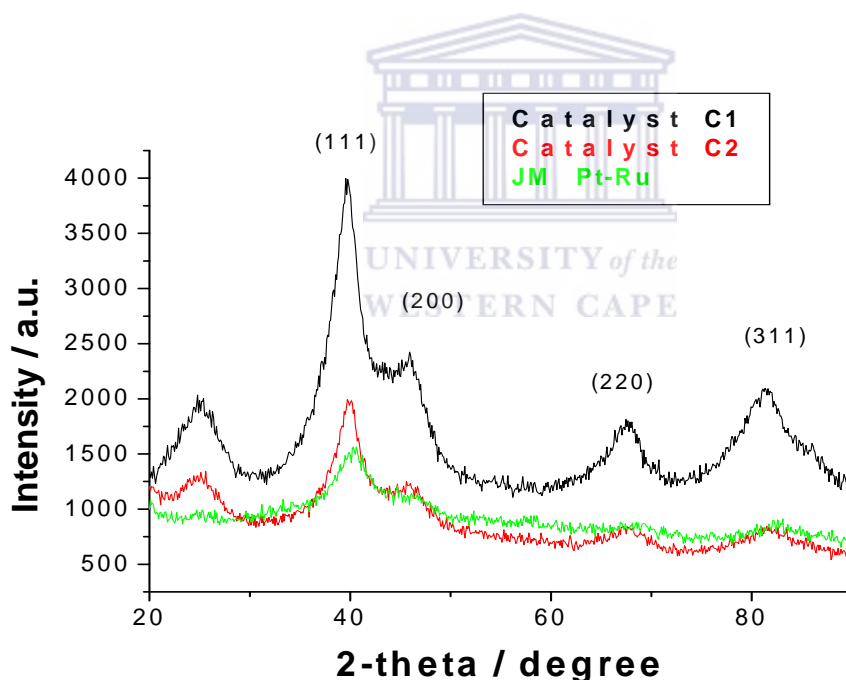


Fig. 6.4.1.1 XRD of catalysts (a) C1, C2 and JM

At peak position (111) catalyst C2 shifted to the right but not in line with the JM catalyst. The JM catalyst is in fact 20% Pt and 10% Ru whereas catalyst C1 and C2 are Pt-Ru-Co (20% Pt, 10% Ruthenium and 10% Iron or Cobalt). The addition of cobalt has

differentiated the XRD spectrums with regards to peak prominence where the (200), (220) and (311). These three peaks are not as well defined for catalyst C2 as they are for catalyst C1. This could be attributed the platinum layer being covered by the ruthenium and cobalt layers. The JM alloying clearly shows the platinum (111) shift when compared to all in house prepared multi-metallic catalysts.

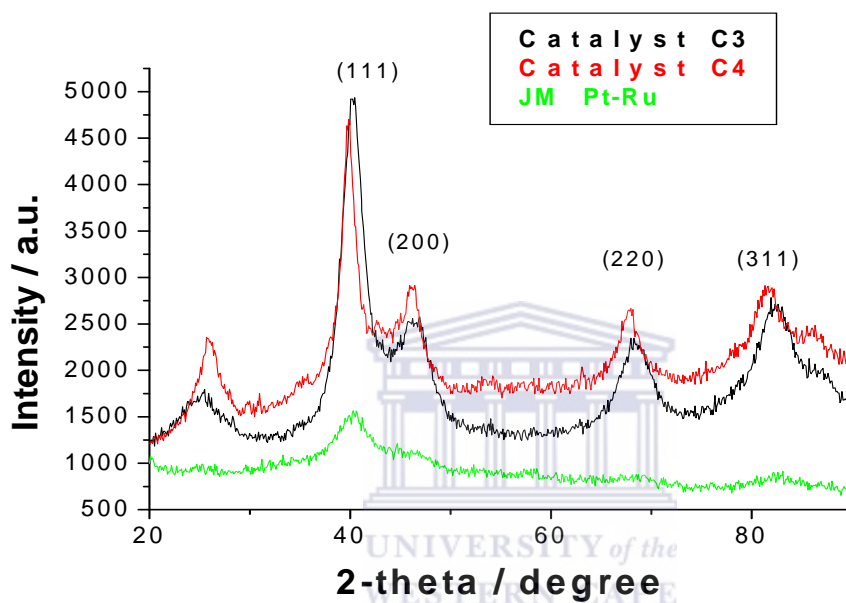


Fig. 6.4.1.2 XRD of catalysts (a) C3, C4 and JM

This intermediate shift at peak position (111) catalyst C3 shifted to the right but not in line with the JM catalyst once again. The JM catalyst was in fact 20% Pt and 10% Ru whereas catalyst C3 and C4 are Pt-Ru-Fe (20% Pt, 10% Ruthenium and 10% Iron). The iron atom structuring during layering and covering the platinum atoms depending on the sequence of deposition. Another concept or theory could be the interstitial placement of iron atoms in between the platinum atom structure where the foreign iron atoms and placement thereof may be changing the conventional platinum atomic layering and structure. The structure may be collapsing with smaller iron atoms causing a slight shift

to the right or in the case of cobalt, the shift may not be as pronounced. Ruthenium which is larger and the structural change to platinum would not be as major when compared to iron or cobalt; which then emphasizes another important factor being the rather increased quantity of ruthenium introduced into the reaction vessel as a salt precursor which then ionizes in solution would then be an effective structural deforming property. The uncertainty of the metallic bond formation cannot be explained by the electrovalence nor covalence and dative covalence where these theories are more useful in explaining the bonding between the metal to non-metal and non-metallic atoms. With reference to the metallic bonding it is assumed that each metal atom pools its valence electron and that these 'free' electrons 'cement' the positive ions together. The alloying of cobalt and iron generally form strong final products. But this is usually the case at high temperatures. The insertion of foreign atoms into the metal structure could be weakening the final inclusive atomic structure and calcinations at temperatures above 500°C may be carried out to reinforce the structure. This has been proposed for future research. For the immediate purpose and research objective the focus was on obtaining the high ECA and high surface area catalyst with minimum or no CO poisoning of active sites. The surface area was established to be related to nano-sized catalytic particles and the following section 6.4.2 will give a brief description of the various in house catalysts produced by means of TEM .

The XRD pattern for C5 was similar for C4, therefore C5s XRD pattern was not included here.

6.4.2 Morphological Characterization by TEM

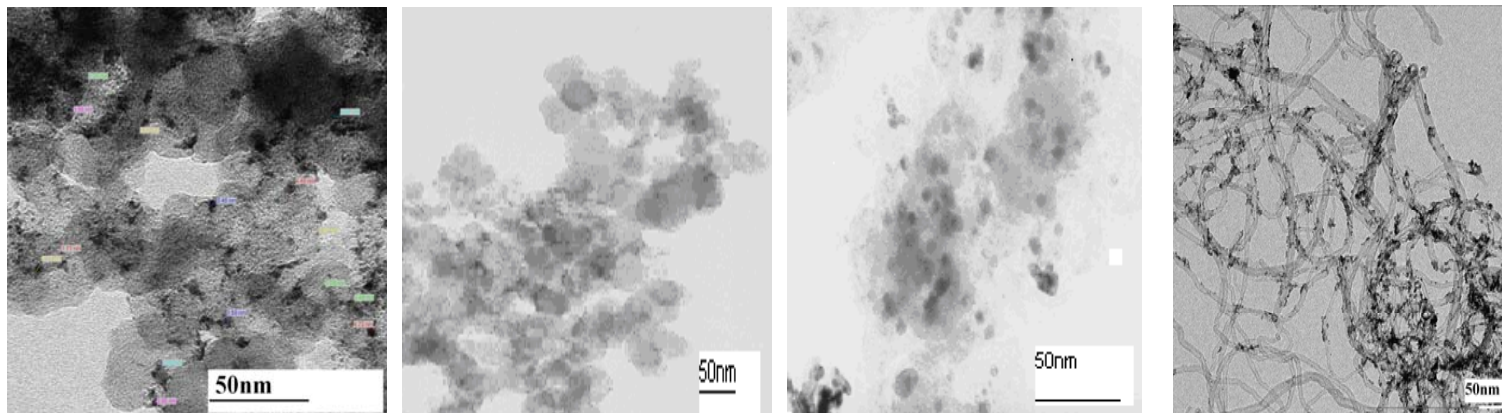
The ternary catalysts were prepared using various methods including simultaneous, individual deposition, increased volume for effective dispersion, longer sonication periods, temperature cycles and two different supports ie. Vulcan XC72 and multi-walled carbon nano-tubes, to produce well dispersed uniform high surface area electrochemically active catalysts nano-particle sizes of less than 2nm.

Table 6.4.2.1 Catalyst APSD and depositing sequence

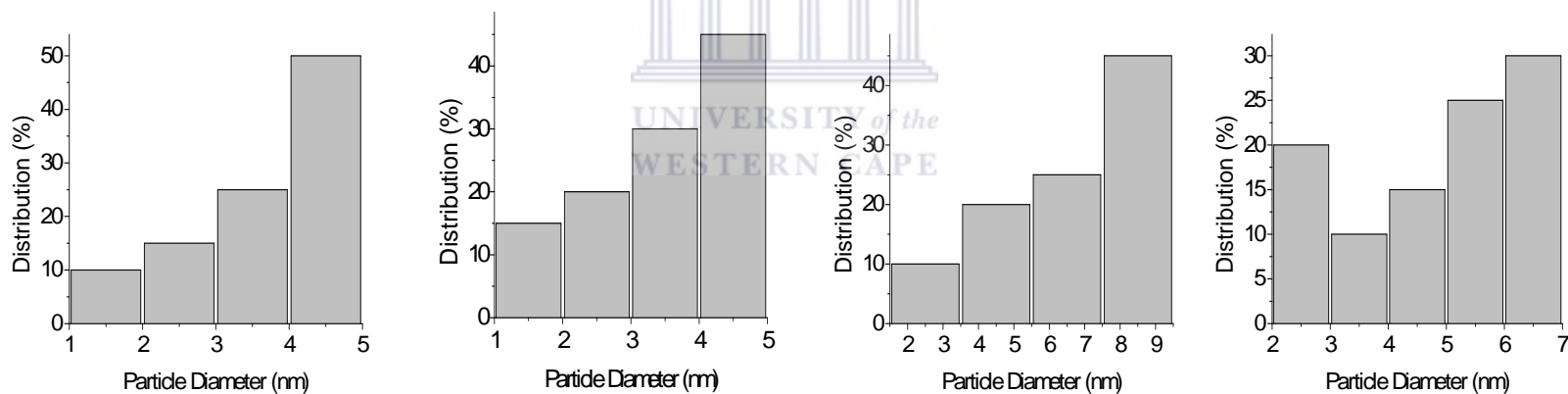
Catalyst	<u>Metals</u> <u>Support</u>	Depositing sequence	APSD nm	Reference figures	
				TEM	APSD
C1	<u>Pt/Ru/Co</u> Vulcan	SD	35%<3nm	6.3.2.1(a)	6.3.2.2(a)
C2	<u>Pt/Ru/Co</u> Vulcan	ID	35%<3nm	6.3.2.1(b)	6.3.2.2(b)
C3	<u>Pt/Ru/Fe</u> Vulcan	ID	10%<3nm	6.3.2.1(c)	6.3.2.2(c)
C4	<u>Pt/Ru/Fe</u> MWNT	ID	20%<3nm	6.3.2.1(d)	6.3.2.2(d)
C5	<u>Pt/Ru/Fe</u> MWNT	SD	80%<3nm	6.3.2.3(a)	6.3.2.3(b)

APSD (Average catalyst particle size distribution); MWCNT (Multiwalled carbon nanotubes); ID (Individual deposition); SD (Simultaneous deposition)

The particle size varied for the different in house catalysts as can be seen in table 6.4.2.1, and from past results the significance of the particle size in relation to ECA can now be observed at around 3nm and less. As noted in previous chapters that in this <3nm particle size region the ECA increases as the particle size is reduced.



(a) (b) (c) (d)
Fig. 6.4.2.1 TEM images of catalysts (a) C1, (b) C2, (c) C3, (d) C4



(a) (b) (c) (d)
Fig. 6.4.2.2 Particle size distribution of catalysts (a) C1, (b) C2, (c) C3, (d) C4

Cobalt has 2 oxidation states +2 and +3, where +2 is the most stable oxidation state of cobalt in solution. The formation of nano-sized particles was focused on the ability of the metals to bond forming alloys. It is in this state the Co (II) is reduced to Co and Fe(II) to Fe where the nucleation is simultaneously induced at sub ambient temperatures after the ions were subjected to a series of pretreatment conditions to find the most optimum reduction environment. The formation of the metal onto the supports Pt-C, Ru-C, Co-C or Fe-C under the low energy systems conditions were not confirmed in this research however increased temperatures after reduction did form larger particles, owed to possible fusion of smaller particles and increased growth rate. The catalytic particles formed could well be unbounded to the carbon support, be it Vulcan or MWCNT. The formation of catalytic particles whether bonded or unbounded to the carbon support has taken place and is active enough when compared to the commercially available JM catalyst. As viewed in figure 6.4.2.1 the agglomerations of small particles do not affect the overall electrochemical activity of the ternary catalyst C4. The fusion of these particles will how ever affect the surface area of the catalyst by producing lower activity. With larger quantities of ions in solution and valence states competing for the electrons in order to assume the metallic form the formation or the particle growth rate could escalate if the free energy available in the system is not controlled. The images or figure 6.4.2.1 show the eventual optimized nano-size particle formation on the MWCNT, 6.4.2.1 (d) of 3 different metals formed simultaneously.

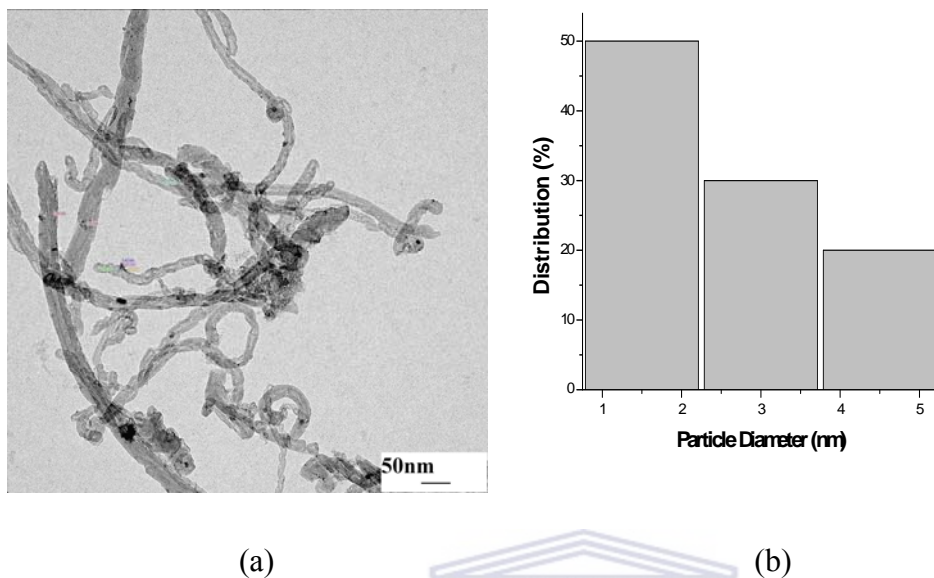


Fig. 6.4.2.3 Catalyst C5 (a) TEM image and (b) Particle size distribution

From the image 6.4.2.3, it can be seen that the MWCNT have not been fully occupied. There is ample space between agglomerations and this observation promotes the support as very capable if one were to add more metal and this shows that the surface area is large enough to accommodate more quantities of metal or catalyst deposits. With 80% of the particles formed on this support being in the region of less than 3nm, thus far this catalyst has been the most electrochemically active.

The ternary catalyst supported on MWCNT showed the significant improvement in ECA possibly due to the large quantities of nano-sized catalytic particles produced with the introduction of other metals to enhance the catalysts ability to reduce CO poisoning. The comparison of this, catalyst C5, to the other in house ternary catalysts produced thus far will be discussed in section 6.4.4.

6.4.3 Elemental Analysis by EDS

EDS was used to confirm the absence or presence of platinum, iron, cobalt and ruthenium on the carbon support.

Table 6.4.3.1 Results of the elemental analysis by EDS

Elemental Content	Catalysts				
	C1	C2	C3	C4	C5
% Carbon	70,2	70,0	67,2	65,7	64,4
% Platinum	26,3	26,0	27,6	22,1	22,4
% Ruthenium	2,0	2,3	1,9	7,3	8,1
% Iron	-	-	3,3	4,9	5,1
% Cobalt	1,5	1,7	-	-	-

Table 6.4.3.1 gives an indication as to the amount of metal formed on each catalyst support. The changes in pre and post reduction temperatures have played a critical role in ensuring complete and partial reduction of the expected quantity metal to be deposited. The EDS confirms a low cobalt formation referring to catalysts C1 and C2 during the sub ambient temperature reduction stage. Increased cobalt quantity formations were formed

at high temperatures above 40°C much to the detriment of the ECA and noticeably the formation of particles in excess of 4nm. Catalysts containing iron continued to show promise as the ECA increased with further additions of Fe to the catalyst metal composition. Unexpectedly the amount of iron deposited on MWCNT increased when the post reduction temperature was decreased to 40°C. This was not observed for the Vulcan supported catalyst when the reduction temperature was lowered to 40°C not shown here. As observed for the bimetallic catalysts, the individual deposition of metals produced catalysts with higher ECA compared to those produced during simultaneous deposition on Vulcan supports. The pretreatment somehow encouraged small particle synthesis during reduction and the MWCNT surface became more receptive for these nano-sized particles.



6.4.4 Electrochemical Activity by Cyclic Voltammetric Analysis

As in chapters 4 & 5, the electrochemical (EC) activity was determined by cyclic voltammetric (CV) analysis of the different catalysts. The reducing agents and other synthesis parameters can now be identified as contributors to effective synthesis routes when comparing the EC activity for each catalyst.

Table 6.4.4.1 Comparing Catalyst Electrochemical Activity by CV Analysis

Catalyst	<u>Metal Support</u>	EC Activity				Reference Figures
		T °C	I(A) (vs Ag/AgCl) 0,5V	I(A) (vs Ag/AgCl) 0,6V	ECA Status	
C1	<u>20%Pt/Ru/Co</u> Vulcan	20	$9,96 \times 10^{-5}$	$1,37 \times 10^{-4}$	Low	6.4.4.1
C2	<u>20%Pt/Ru/Co</u> Vulcan	20	$2,40 \times 10^{-4}$	$3,34 \times 10^{-4}$	Moderate	6.4.4.2
C3	<u>20%Pt/Ru/Fe</u> Vulcan	20	$1,54 \times 10^{-4}$	$2,23 \times 10^{-4}$	Moderate	6.4.4.3
C4	<u>20%Pt/Ru/Fe</u> MWCNT	20	$2,90 \times 10^{-4}$	$4,45 \times 10^{-4}$	Moderate	6.4.4.4
C5	<u>20%Pt/Ru/Fe</u> MWCNT	20	$1,00 \times 10^{-3}$	$1,25 \times 10^{-3}$	High	6.4.4.5
JM	<u>20%Pt/Ru</u> Vulcan	20	$1,31 \times 10^{-3}$	$1,14 \times 10^{-3}$	High	5.3.3.6

MWCNT (Multiwalled carbon nanotubes); ECA (Electrochemical Activity); I (Current); T (Temperature)

In table 6.4.4.1 the EC activity of the once formed catalyst is analyzed in an acidic medium (base analysis), followed by the addition of 1M methanol which undergoes oxidation on the platinum surface as shown in the CV graphs below. The potential

regions analyzed are -0,2 to 0,6V and -0,2 to 1,0V (vs. Ag/AgCl) and the scan rate used was 20mV/s.

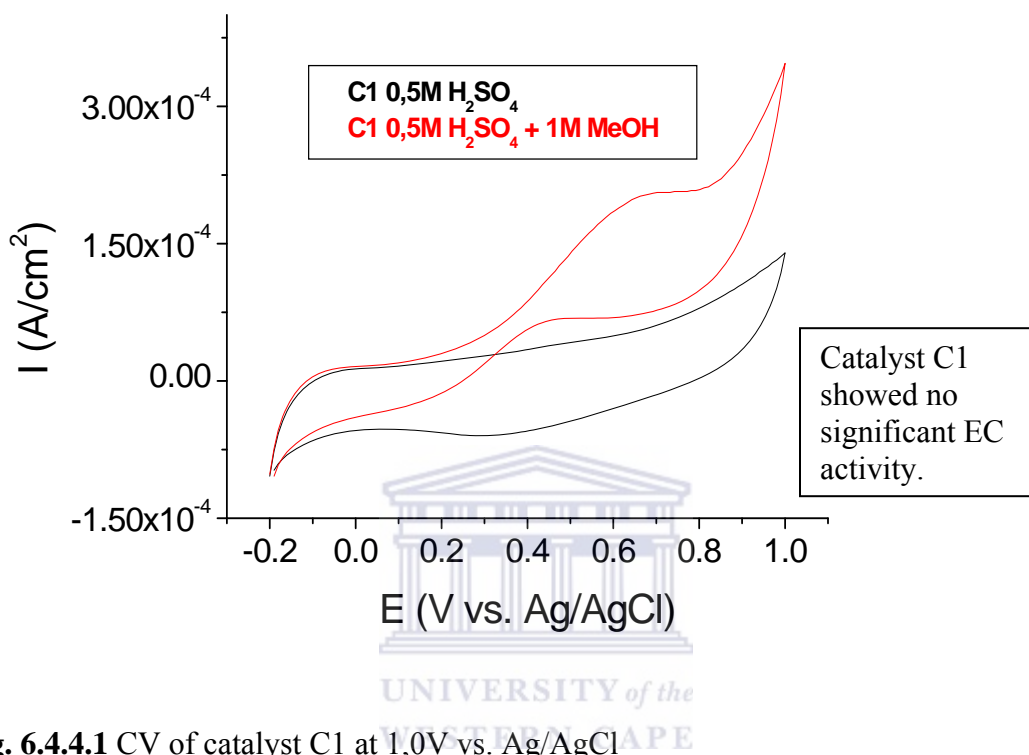


Fig. 6.4.4.1 CV of catalyst C1 at 1,0V vs. Ag/AgCl

Figure 6.4.4.1 showed 3 increases within 3 different potential regions in activity during the forward methanol oxidation scan. The first peak was in the region of -0,1V (Ag/AgCl), the second peaks at around 0,65V (Ag/AgCl) and the third approximately 1,0V (Ag/AgCl). The peak of interest was the one peaking around 0,65V (Ag/AgCl), where the peak started its incline at approximately 0,1V (Ag/AgCl). The activity status was regarded as low when compared to the other in-house ternary catalysts. The ECA was calculated as the difference between the base (Black) forward scan and the methanol oxidation forward scan (Red) at potentials 0,5 and 0,6V (Ag/AgCl).

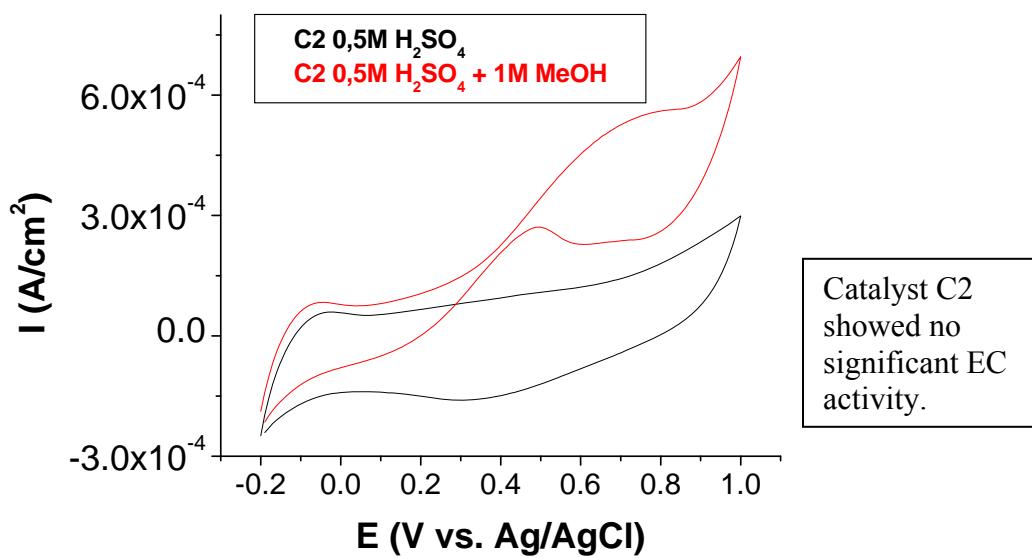


Fig. 6.4.4.2 CV of catalyst C2 at 1,0V vs. Ag/AgCl

Catalyst C2 shown in figure 6.4.4.2 similar to C1 showed 3 increases within 3 different potential regions in activity during the forward methanol oxidation scan. The first peak was in the region of -0,1V (Ag/AgCl), the second peaks at around 0,7V (Ag/AgCl) and the third approximately 1,0V (Ag/AgCl). However there was a peak shift to during formation at slightly increased potentials compared to catalyst C1. The peak of interest once again was the one peaking around 0,7V (Ag/AgCl), where for this particular peak the peak started its incline at approximately 0,1V (Ag/AgCl). The activity status was regarded as moderate when compared to the other in-house ternary catalysts. There was a 41% increase in ECA when compared to catalyst C1. In both instances the particle size distribution was in the region of 65% > 3nm mostly due to an attempt to reduce the third metal, cobalt at increased temperatures of 95°C.

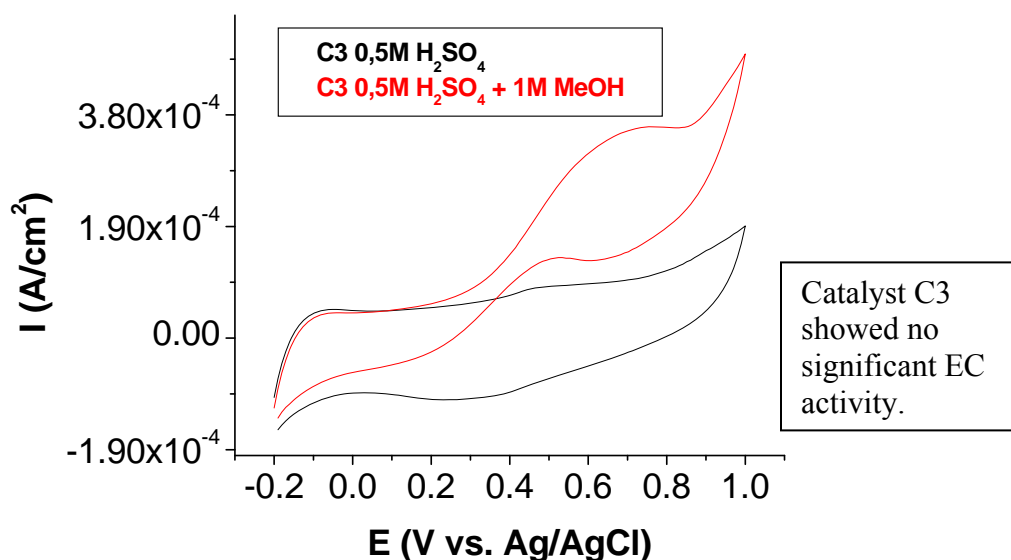


Fig. 6.4.4.3 CV of catalyst C3 at 1,0V vs. Ag/AgCl

Catalyst C3 prepared by the individual deposition method showed the increase in activity with 2 different metal contents, ie. Co vs. Fe as the third metal (Pt-Ru-M where M=Co or Fe). Catalyst C3 (Pt-Ru-Fe) figure 6.4.4.3 showed a 22% increase in ECA compared to catalyst C2 (Pt-Ru-Co) at a potential of 0,5V (Ag/AgCl).

The activity of increased mass related Pt formation and consequent increased ECA is observed at the methanol oxidation peak region 0,4 to 0,65V (Ag/AgCl) region (Red). The base line (black) once again indicating the hydrogen adsorption / desorption peaks in the region -0,2 to 01V (Ag/AgCl). This observation as mentioned earlier could indicate the formation of well developed Pt crystal faces. The Pt oxide possible oxidation peak (Red) as stated and predicted earlier in the literature review increased progressively with the decrease in particle size, resulting in an increase in surface area relationship earlier

established, as result of the OH adsorption strength. The oxide reduction peak in the 0,35V (Ag/AgCl) potential region, with reference to the base scan in the acidic medium 0,5M H₂SO₄ (Black), was present and will be compared to the catalysts C4 and C5 ECA scans later.

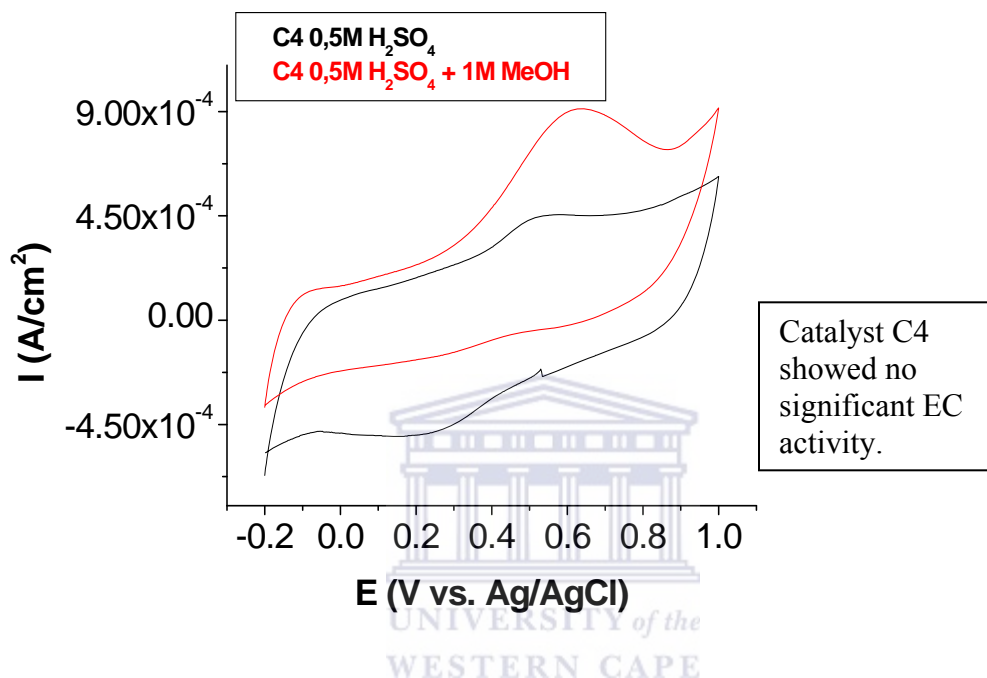


Fig. 6.4.4.4 CV of catalyst C4 at 1,0V vs. Ag/AgCl

Catalyst C4 was prepared on MWCNT where as the other ternary in house catalysts mentioned up until now (C1, C2, and C3) were prepared on Vulcan supports. C4 MWCNT supported catalysts ECA shown in figure 6.4.4.4 exhibits similar ECA scan profiles to C1, C2 and C3 with regards to the 3 increases within 3 different potential regions in activity during the forward methanol oxidation scan (Red). The first peak was in the region of $-0,1\text{V}$ (Ag/AgCl), the second peaks at around $0,6\text{V}$ (Ag/AgCl) where a noticeable shift to the negative had taken place and the third peaked at approximately

1,0V (Ag/AgCl). The second peak shift to the negative could be indicating the difference in activity to favour the methanol oxidation reaction at lower potentials for catalyst C4. However there was a peak not visible in the ECA scan for catalyst C4 during formation at slightly increased potentials compared to catalyst C3. The potential region where the peak, possibly the oxidation of the Pt oxide peak, appeared for catalyst C3 and not C4 was 0,5V (Ag/AgCl) during the reverse methanol oxidation scan (Red). The peak of interest once again was the one peaking around 0,6V (Ag/AgCl), the methanol oxidation peak (Red) where its ECA in this potential region signifies its suitability as Fuel cell catalyst, started its incline at approximately -0,1V (Ag/AgCl) also notably this was lower than the other ternary catalysts ECA scans with a slight increase in the area where hydrogen desorption would normally be associated with acidic mediums.. The activity status was regarded as moderate when compared to the other in-house ternary catalysts. There was a 31% increase in ECA for catalyst C4 when compared to catalyst C3. In the instance of catalyst C3 the particle size distribution was in the region of 90% > 3nm mostly and C4 was characterized with a particles size distribution of 80% >3nm due to an attempt to reduce the third metal, iron, at increased temperatures of 95°C. Never the less the catalyst with the most number of catalytic particles smaller than 3nm in size, as in the case with catalyst C4, exhibited a significant increase in ECA again.

The increase activity of subsequent increased mass related Pt formation is observed at the methanol oxidation peak region 0,4 to 0,65V (Ag/AgCl) region. The base line (black) once again indicating the hydrogen adsorption / desorption peaks in the region -0,2 to 01V (Ag/AgCl). This as mentioned earlier could indicate the formation of well developed Pt crystal faces. The Pt oxide reduction peak (Black) as stated and predicted

earlier in the literature review shifted progressively negative to 0,25V (Ag/AgCl) potential region with the decrease in particle size and increase in surface area relationship earlier established, as a result of the increase in OH adsorption strength.

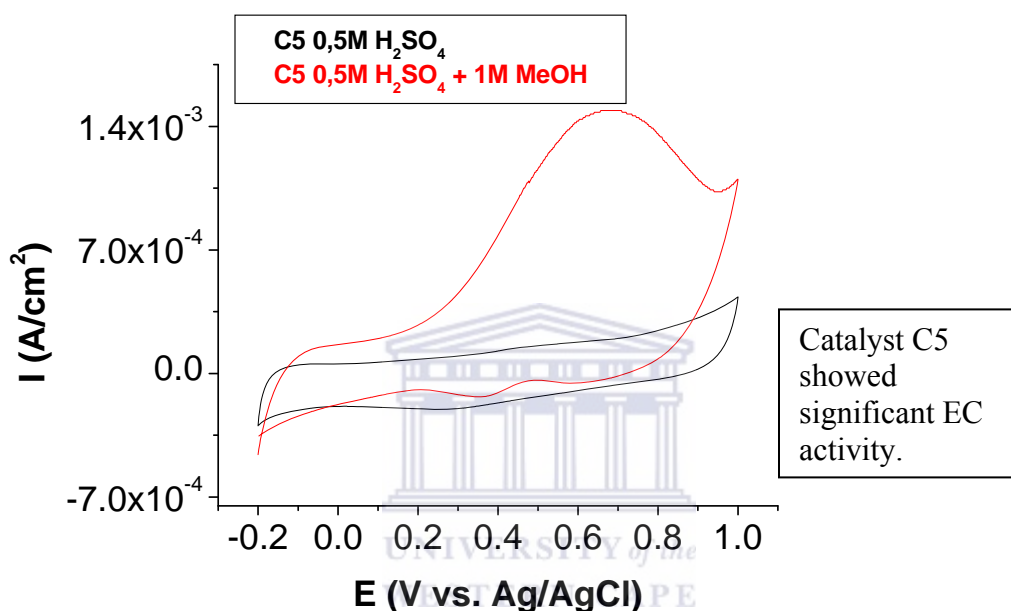


Fig. 6.4.4.5 CV of catalyst C5 at 1,0V vs. Ag/AgCl

There was a significant increase in activity with regards to the forward methanol oxidation (Red) scan for catalyst C5, figure 6.4.4.5, and an increase of more than 50% at 0,5V (Ag/AgCl) potential region with regards to the ECA. The characteristic plateau region starts at approximately -0,1 and ends at 0,05V (Ag/AgCl), where at 0,1V there was an increase in activity however there was in addition a steady increase from 0,2V onwards until 0,6V (Ag/AgCl). The steady increase can be explained as the superior

electrochemical activity during methanol oxidation with minimum interference from CO poisoning. Another plateau region is observed between 0,6 and 0,7V (Ag/AgCl). There are evidently 2 peaks in the reverse scan at potentials 0,5 and 0,2V (Ag/AgCl) possibly due to the redox reactions of oxide and CO formations. This reaction will be further assisted by the OH adsorption strength. As previously noted, the base scan (Black) peak shift for the peak now at potential 0,2V (Ag/AgCl) (previously at 0,25 (Ag/AgCl) for catalyst C4) further to the negative, for catalyst C5 as this shift previously indicated a significant increase in surface area due to an increase in smaller catalytic particles and the increased mass of Pt formed with this method.

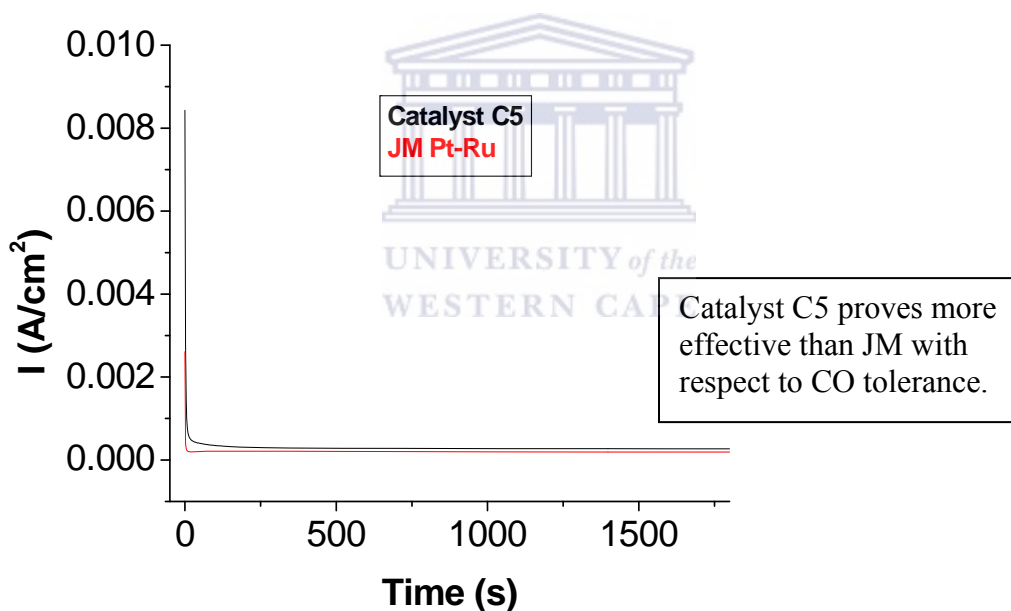


Fig. 6.4.4.6 CA of catalyst C5 and JM at 0,3V vs. Ag/AgCl

Once again the high mass activity of catalyst C5 was present by observing the shift in the platinum oxide reduction peak to the negative, giving an indication of the superiority of the catalyst as a potential direct methanol fuel cell catalyst and more significantly the

catalysts OH adsorption strength is directly related to the catalysts ability to prevent, reduce and overcome CO poisoning (as previously noted CO is a by product of methanol oxidation and can severely reduce the catalysts ability to produce power at low potentials other wise required to ensure the economical viability of the DMFC). To further advance the support of a CO tolerant catalyst, the catalyst, C5, was subjected to the chronoamperometric analysis to ascertain the endurance capability of the catalyst during methanol oxidation. Figure 6.4.4.6 shows the CO tolerance of this ternary catalyst and how it compares to the superior JM commercially available catalyst. After 30minutes the in-house ternary catalyst shows a slight advantage where the current increase is concerned with a 20%Pt-8%Ru-5%Fe composition on MWCNT. The introduction of larger quantities of non-precious metals can be further explored in future research, also mentioned later.



A summary table 6.5.1.1 and short summary of the characterization and ECA results to reflect the success and failures of the research with regards to ternary catalysts, their preparation and application will be given as the resulting improved electrochemical activity during the cyclic voltammetric analysis was characterized by particles <3nm diameter size particles and low level agglomerations. By lowering the post-reduction temperature further agglomerations and catalyst surface coatings were possibly prevented which would alternatively been formed at increased temperatures. Tabulated in Table 6.5.1.1 is the relationship between the different supports, reduction temperatures, particle size and EC activities.

Table 6.5.1.1 Summary table comparing the different supports, reduction temperatures, particle size and EC activities of the ternary catalysts

C	<u>Metals Support</u>	D	APS nm	Synthesis Parameters				EC Activity		
				ST min	TP °C	R A	Vol. ml	T °C	E (Vs Ag/AgCl) 0,5V	E (Vs Ag/AgCl) 0,6V
C1	<u>Pt/Ru/Co</u> Vulcan	SD	35%<3nm	10	40-4-95	F	150	20	$9,96 \times 10^{-5}$	$1,37 \times 10^{-4}$
C2	<u>Pt/Ru/Co</u> Vulcan	ID	35%<3nm	10	40-4-95	F	150	20	$2,40 \times 10^{-4}$	$3,34 \times 10^{-4}$
C3	<u>Pt/Ru/Fe</u> Vulcan	ID	10%<3nm	10	40-4-95	F	150	20	$1,54 \times 10^{-4}$	$2,23 \times 10^{-4}$
C4	<u>Pt/Ru/Fe</u> MWNT	ID	20%<3nm	10	40-4-95	F	150	20	$2,90 \times 10^{-4}$	$4,45 \times 10^{-4}$
C5	<u>Pt/Ru/Fe</u> MWNT	SD	80%<3nm	10	40-4-40	F	150	20	$1,00 \times 10^{-3}$	$1,25 \times 10^{-3}$
JM	<u>Pt/Ru</u> Vulcan	N/A	80%<3nm	N/A	N/A	N/A	N/A	20	$1,31 \times 10^{-3}$	$1,14 \times 10^{-3}$

APS (Average catalyst particle size); ST (Sonication time); RA (Reducing agent); F (40% Formaldehyde); MWCNT (Multiwalled carbon nanotubes); ID (Individual deposition); SD (Simultaneous deposition); EC (Electrochemical); N/A (Not available); TP (Temperature program); C (Catalyst)

Fe proved to be the most effective third metal for enhancing the electrochemical activity.

The particle size distribution, 80% < 3nm, was once again an important characteristic, by significantly increasing the surface area and assisting in lowering the poisoning effect of CO on Platinum electrochemically active catalytic sites. The significantly higher catalytic activity has been attributed to a thin platinum layer covering the alloy in addition to an electronic effect due to Fe on Pt, as previously reported by Watanabe and co-workers [389]. Temperature program during synthesis, 40-0-40°C, allowed the formation of uniform and well dispersed nano-sized catalytic particles. The pH and stirring rate were controlled at each stage and step during the synthesis procedure.

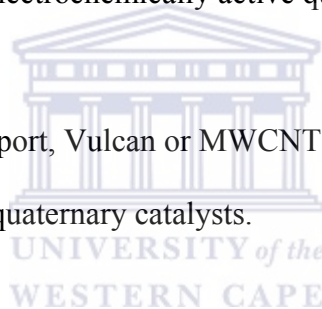
Catalyst C5 had been clearly identified as the most active ternary catalyst; therefore it was chosen for CA testing, performed in 1M methanol, at 0.3V and for 30minutes, Fig. 6.4.4.6, compares the CO tolerance of the commercially available catalyst and the in-house, C5, catalyst. The commercially available JM catalyst (20%Pt-Ru/C) is noted for its excellent catalytic activity and ability to with stand, tolerate and counter poisoning as an anode catalyst. The CA analysis showed comparable and a slightly better performance by C5, possibly due to the Fe assistance in the CO removal, an increased number of catalytic sites, due to higher distribution of nano-sized particles and 10% increase in metallic particles. Fe is a cost effective possible third metal and was effectively processed during the reduction process without additional equipment and reagents other than NaBH₄. With an objective to lower the cost, other catalysts such as metal oxides, metal porphyrins, and metal alloys have been pursued in the literature over the years, but their electro-catalytic activities are generally less than that of pure platinum [386-388]. In order to pursue a method of catalyst formation with a higher mass activity than ternary catalysts and incorporate non-noble metals to simultaneously reduce the cost of the catalyst, an attempt will be made in chapter 7 to achieve these objectives by using 4 different metals to synthesize high ECA quaternary catalysts.

CHAPTER 7

QUATERNARY CATALYSTS

7.1 OBJECTIVES

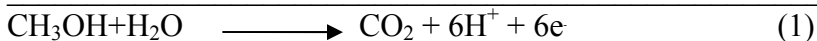
1. To synthesize quaternary catalysts for methanol oxidation.
2. To synthesize quaternary catalysts with large electrochemically active surface areas.
3. To synthesize quaternary catalysts using the simultaneous deposition method with similar electrochemical activity to JM catalysts.
4. To determine the most electrochemically active quaternary catalysts for methanol oxidation.
5. To determine which support, Vulcan or MWCNT, would be appropriate as the most active support for quaternary catalysts.



7.2 INTRODUCTION

To understand the need for multi-metallic catalysts, the motivation for these catalysts need to be understood first. The ternary catalysts produced thus far have shown significant advances towards promoting the release of the CO at Pt sites shown during the CA experiments and analysis. This was observed at 0,3V (Ag/AgCl), and with the advent of quaternary catalysts the focus will be to introduce increased quantities of non-noble metals but maintain the ECA of the catalyst. This will be critical in reducing the costs of these platinum based catalysts.

One of the factors limiting the practical development of direct methanol fuel cells (DMFCs) is the poor performance of Pt alloy catalysts that perform the anode reaction 1:



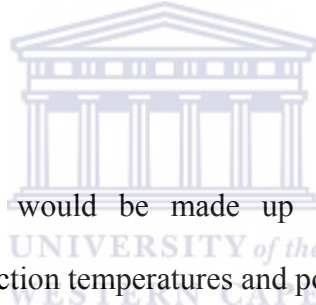
Although the oxidation of methanol is rapid on clean Pt, CO appears as an intermediate in the reaction and poisons the surface [341]. The turnover of catalytic sites involves oxidation of CO to CO₂, using oxygen atoms supplied by water. Pt does not adsorb H₂O at potentials negative of about 0.4 V vs RHE. Pure Pt anodes are therefore relatively poor catalysts for reaction 1. Alloys of Pt with more oxophilic elements have been investigated for many years as methanol electro-oxidation catalysts [342]. The superior performance of binary catalysts (Pt-Sn, Pt-Re, Pt-Mo, and Pt-Ru [343-348]) relative to Pt has been ascribed to two effects [349, 350]. In the bi-functional model, the oxophilic metal is thought to provide sites for water adsorption. In the ligand effect or electronic model, the role of the alloying element is to modify the electronic properties of Pt by contributing d-electron density. Beden et al. have proposed a detailed mechanism for the oxidation of methanol at Pt electrodes [351]. The sequence of reactions 2-5 below, in which M represents an alloying component or promoter metal, is based on their mechanism as modified for alloys by Frelink and co-workers [352]:



The best choice of alloying element(s) for an anode electro-catalyst depends on which step in this reaction sequence is rate limiting. Oxophilic additives will directly affect the rates of reactions 4 and 5 and, indirectly through electronic effects, [352-354] the rates of reactions 2 and 3 [355, 356]. Most studies in this area have considered reactions 4 and 5 as the rate-determining steps under different conditions and have focused, for reasons of simplicity, on binary Pt alloys. Recently, the author presenting this paper investigated the simultaneous addition of two oxophilic alloying elements (Ru and Os) to Pt. Os is more oxophilic than Ru but significantly less soluble in face-centered cubic (fcc) Pt. The best catalytic performance was therefore found at ternary compositions near the Os solubility limit [357]. To explore more complex compositions, the author presenting this paper subsequently developed a rapid combinatorial screening method for ternary and quaternary alloy catalysts [358]. In this thesis I will attempt to find the most EC active quaternary metal combinations, characterize and analyze the best catalyst/s for CO tolerance via CA. The metals used will be platinum, ruthenium, molybdenum, chromium, iron and cobalt.

7.2 SYNTHESIS PARAMETERS

Seven catalyst categories (D1 to D7) will encompass the optimization of the ternary catalysts synthesis methods by further refinement of the synthesis parameters to produce quaternary catalysts exhibiting a significant increase in the ECA. Each category refers to a metal combination of catalyst differentiated by support in cases of similar metal combinations. Each category will reflect the most active catalyst synthesized after a sequential and methodical trial of temperatures, metal combinations, reducing agents and supports. The best results with regards to ECA and simplicity in relation to being economically viable and possible at lab scale will be mentioned in table 7.2.1.



A temperature program (TP) would be made up of temperature stages namely, pretreatment temperatures, reduction temperatures and post-reduction temperature stages.

Stage 1: Pretreatment temperature

Stage 2: Reduction temperature

Stage 3: Post-reduction temperature

Therefore 40-4-40 °C would mean; the salt precursors and 0,5M HCl would be stirred for specified time period at 40 °C, followed by the addition of formaldehyde, reducing agent (RA), maintaining the entire process and solutions involved at 4 °C, and finally a post-reduction temperature treatment at 40 °C. Controlling the post reduction temperature proved essential in controlling the particle size in previous chapters.

The different metal combinations required a series of pretreatments as observed with the binary and ternary systems and certain metal formations were not part of a shared temperature system.

Table 7.2.1 Summary of the synthesis parameters for the Quaternary Catalysts

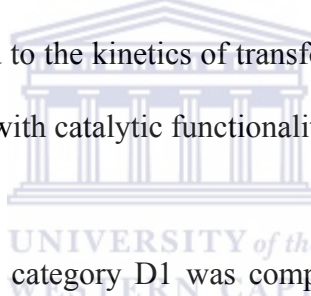
Catalyst Category	Metals Support	Synthesis Parameters				
		Depositing Sequence	ST min	TP	RA	Vol. ml
D1	<u>Pt/Ru/Co/Cr</u> Vulcan	ID	10	40-4-40	F	150
D2	<u>Pt/Ru/Mo/Fe</u> Vulcan	SD	10	40-4-40	F- SBH	150
D3	<u>Pt/Ru/Co/Fe</u> Vulcan	SD	10	40-4-40	F- SBH	150
D4	<u>Pt/Ru/Mo/Cr</u> Vulcan	SD	10	40-4-40	F- SBH	150
D5	<u>Pt/Ru/Co/Fe</u> MWCNT	SD	10	40-4-40	F- SBH	150
D6	<u>Pt/Ru/Mo/Cr</u> MWCNT	SD	10	40-4-40	F- SBH	150
D7	<u>Pt/Ru/Mo/Fe</u> MWCNT	SD	10	40-4-40	F- SBH	150
JM	<u>Pt-Ru</u> Vulcan	N/A	N/A	N/A	N/A	N/A

ST (Sonication time); RA (Reducing agent); F (40% Formaldehyde); SBH (NaBH₄); MWCNT (Multiwalled carbon nanotubes); D (Deposition); ID (Individual deposition); SD (Simultaneous deposition); N/A (Not available)

With the introduction of 4 metal salt precursors into a solution, the solution may now be viewed as a more saturated solution prior to crystallization compared to the monometallic, bimetallic and ternary solutions prior to crystallization and subsequent reduction to form metal. Here the reducing agent strength of formaldehyde has been tested and proved to

be sufficient, referring to the EDS results in managing to form 4 different metal types simultaneously on a carbon support.

In previous chapters the different metal combinations trials have laid the foundation for this, the quaternary type of multi-metallic quaternary synthesis from a solution containing salt precursors of various metals and the reducing agents. As previously noted, the formation of metallic particles are governed by specific properties unique to each metal which were characterized by TEM, CV, CA and XRD and the common properties were identified and explored aiming to reduce different metal ions simultaneously from a common solution. The synthesis processes adopted in this chapter for quaternary catalysts are also closely related to the kinetics of transformation of ions in solution to be engineered into metal particles with catalytic functionalities on carbon supports.



The most active catalysts from category D1 was composed of Pt/Ru/Co/Cr on Vulcan support. The precursor solution was subjected to a series of pretreatments at temperatures controlled around 40°C. The formaldehyde reduction took place at temperatures averaging 4°C. The post reduction purification stage was performed at 40°C.

The most active catalyst from category D2 was composed of Pt/Ru/Fe/Mo on Vulcan support. The salt precursors were added simultaneously whereas catalyst D1 involved the individual deposition method. The precursor solution was subjected to a series of

pretreatments at temperatures controlled around 40°C. The formaldehyde reduction took place at temperatures averaging 4°C.

The most active catalysts from categories D3 and D5 were composed of Pt/Ru/Co/Fe on Vulcan and MWCNT supports respectively. The precursor solutions were subjected to a series of pretreatments at temperatures controlled around 40°C. The precursors were added simultaneously. The reducing agents were formaldehyde and NaBH₄ where reduction took place at temperatures averaging 4°C.

The most active catalysts from categories D4 and D6 were composed of Pt/Ru/Mo/Cr on Vulcan and MWCNT supports respectively. The salt precursors were added simultaneously. The precursor solution was subjected to a series of pretreatments at temperatures controlled around 40°C. The reducing agents were formaldehyde and NaBH₄ where reduction took place at temperatures averaging 4°C.

The most active catalysts from categories D2 and D7 were composed of Pt/Ru/Mo/Cr on Vulcan and MWCNT supports respectively. The salt precursors were added simultaneously. The precursor solution was subjected to a series of pretreatments at temperatures controlled around 40°C. The reducing agents were formaldehyde and NaBH₄ where reduction took place at temperatures averaging 4°C.

7.4 RESULTS AND DISCUSSION

7.4.1 Structural Characterization by XRD

As for the binary and ternary catalysts, the following figures show the characteristic diffraction peaks of the face centered cubic (fcc) Pt demonstrating that a successful reduction of Pt precursor to metallic form has been achieved.

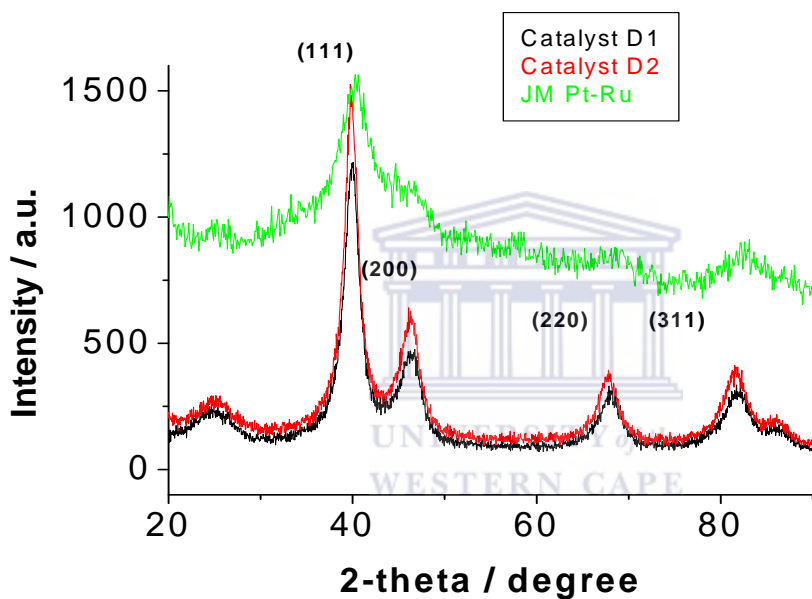


Fig. 7.4.1.1 XRD of catalysts D1, D2 and JM

The diffraction peaks at about 39° and 46° are due to the Pt(1 1 1), and (2 0 0) plane, respectively, which represents the typical character of a crystalline Pt, that is fcc[204-209]. This indicates that the in-house-supported Pt catalysts are Pt (fcc) crystal structure.

Figure 7.4.1.1 shows the successful formation of fcc Pt crystallization structures. The EDS results will later confirm the possible formation of solubilized ruthenium, cobalt, chromium and iron for catalysts D1 and D2.

The Pt/Ru/Co/Cr and Pt/Ru/Fe/Mo structures for catalysts D1 and D2 respectively stem from the crystal nucleus with their own structural properties. These properties of the crystal nucleus are a function of its surface energy, its dimensions and the energy of adhesion to the carbon support.

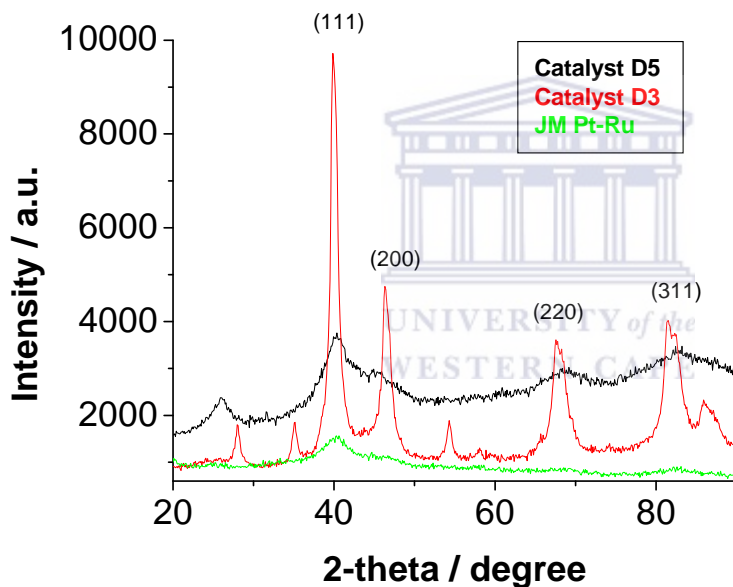


Fig. 7.4.1.2 XRD of catalysts D5, D3 and JM

The particle growth was of significance as 4 metals having different reducing requirements and forming crystals in different planes, sizes and shapes depending on the amount of energy is available in the system. Figure 7.4.1.2 also showed a similar XRD peak profile of catalysts D5, D3 and JM with the diffraction peaks at about 39° and 46° are due to the Pt(1 1 1), and (2 0 0) plane, respectively, which represents the typical

character of a crystalline Pt, that is fcc[204-209]. This indicates that the in-house-supported Pt catalysts are Pt (fcc) crystal structure. However catalysts D5 showed a shift in the spectrum peaks in-line with the JM spectrum possibly due to the alloying of metals. This could also indicate that some degree of solubility of certain metals into the Pt fcc structure has taken place or could be confirmed.

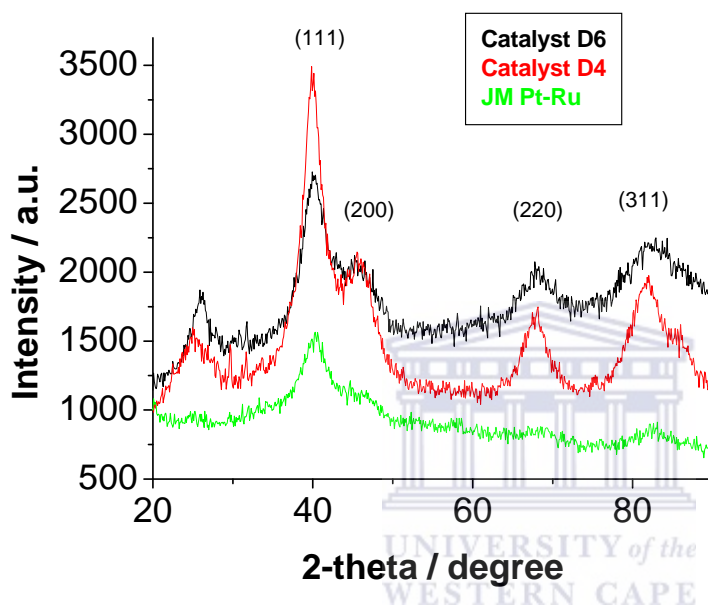
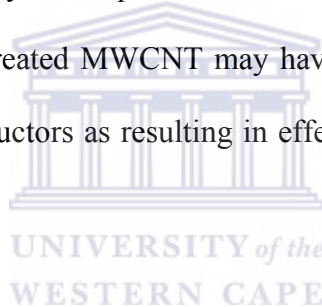


Fig. 7.4.1.3 XRD of catalysts D4, D6 and JM

The XRD pattern for catalyst D7 was similar to that of catalyst D6, therefore it was not necessary to include catalyst D7's XRD pattern here. The alloying of metals within catalyst D4, Pt/Ru/Mo/Cr, was not anticipated as the metal precursor addition was done individually, but a shift once again in the XRD peak profiles for catalysts D6 and D7 composed of Pt/Ru/Mo/Cr and Pt/Ru/Mo/Fe respectively were in line with the JM catalyst could confirm possible alloying. The alloying could be an overlap from the nuclei stages promoting the close packing of atoms during growth and crystallization.

The crystallization and formation can be explained as taking place or initiating at a suitable value of excess energy when nuclei are formed on the support surface. The nuclei have to be large enough to stabilize and avoid spontaneous decomposition on high energy surfaces. This is true for high energy surfaces, but in the case of carbon in sub ambient temperatures this growth or formation of small nuclei may proliferate under these low energy conditions. The lack of energy in the system may prevent spontaneous and further growth resulting in nano-sized catalytic particles. With the increase in temperature during the post reduction temperature energy transferred to the support surfaces could cause the already small particles formed to break up into even smaller particles.. The success of pre-treated MWCNT may have been owed to this property of excellent heat and energy conductors as resulting in effective supports for nano-sized Pt and alloyed particles.



7.4.2 Morphological Characterization by TEM

The quaternary catalysts were prepared using various methods including simultaneous, individual deposition, increased volume for effective dispersion, longer sonication periods, temperature cycles and two different supports ie. Vulcan XC72 and multi-walled carbon nano-tubes, to produce well dispersed uniform high surface area electrochemically active catalysts nano-particle sizes of less than 2nm.

Table 7.4.2.1 Catalyst APSD and deposition sequence for the Quaternary Catalysts

Catalysts	Metals Support	Depositing sequence	APSD	Reference figures	
				TEM	APSD
D1	Pt/Ru/Co/Cr Vulcan	SD	40%<3nm	7.4.2.1(a)	7.4.2.2(a)
D2	Pt/Ru/Fe/Mo Vulcan	ID	50%<5nm	7.4.2.1(b)	7.4.2.2(b)
D3	Pt/Ru/Co/Fe Vulcan	SD	85%>5nm	7.4.2.1(c)	7.4.2.2(c)
D4	Pt/Ru/Mo/Cr Vulcan	ID	100%<5nm	7.4.2.1(d)	7.4.2.2(d)
D5	Pt/Ru/Co/Fe MWCNT	SD	0%<3nm 80%>5nm	7.4.2.3(a)	7.4.2.4(a)
D6	Pt/Ru/Mo/Cr MWCNT	SD	0%<3nm 95%>5nm	7.4.2.3(b)	7.4.2.4(b)
D7	Pt/Ru/Mo/Fe MWCNT	SD	50%<2nm 80%<3nm	7.4.2.3(c)	7.4.2.4(c)

APSD (Average catalyst particle size distribution); MWCNT (Multiwalled carbon nanotubes); ID (Individual deposition); SD (Simultaneous deposition)

Table 7.4.2.1 gives an overview of the catalysts average particle size distribution, deposition sequence and support.

Figure 7.4.2.1 (a) shows the particle formation of catalyst D1 on the Vulcan (XC 72) support. After determining the particle size distribution the particle size distribution indication tended towards a particle range to be in the region of 40% < 3nm. With 60%

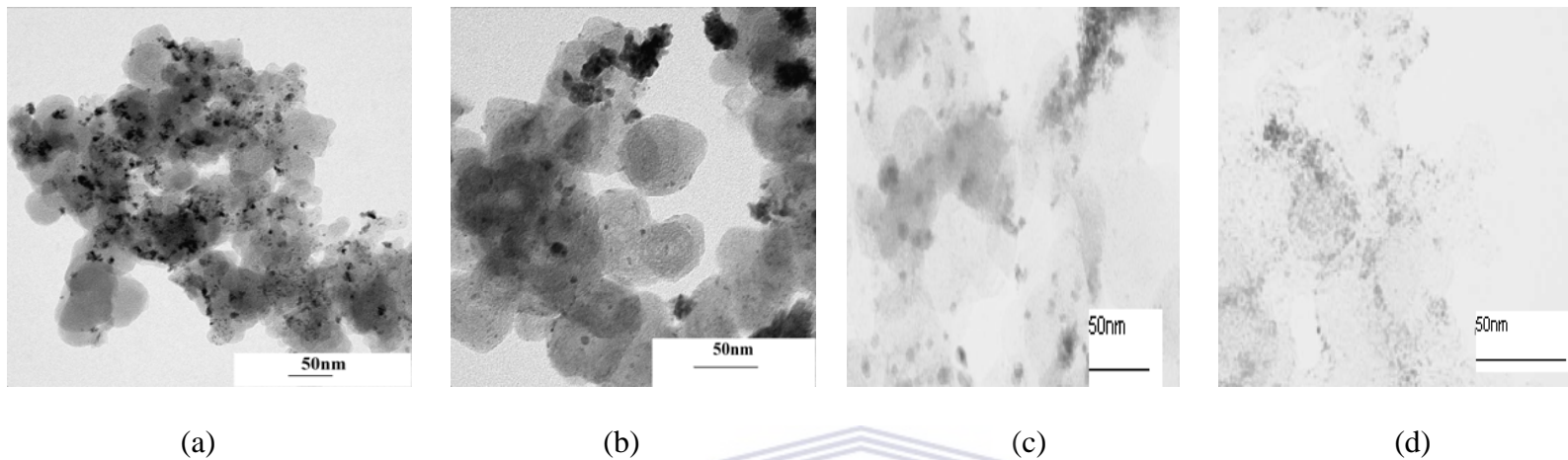


Fig. 7.4.2.1 TEM images of catalysts (a) D1, (b) D2, (c) D3, (d) D4

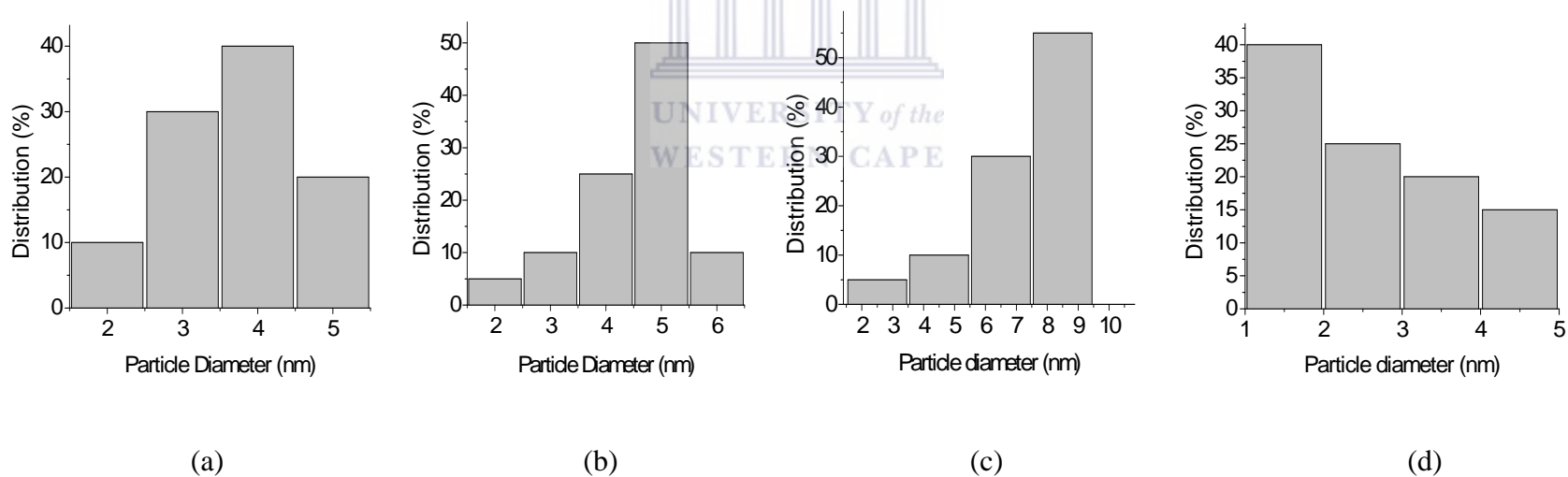


Fig. 7.4.2.2 Particle size distribution of catalysts (a) D1, (b) D2, (c) D3, (d) D4

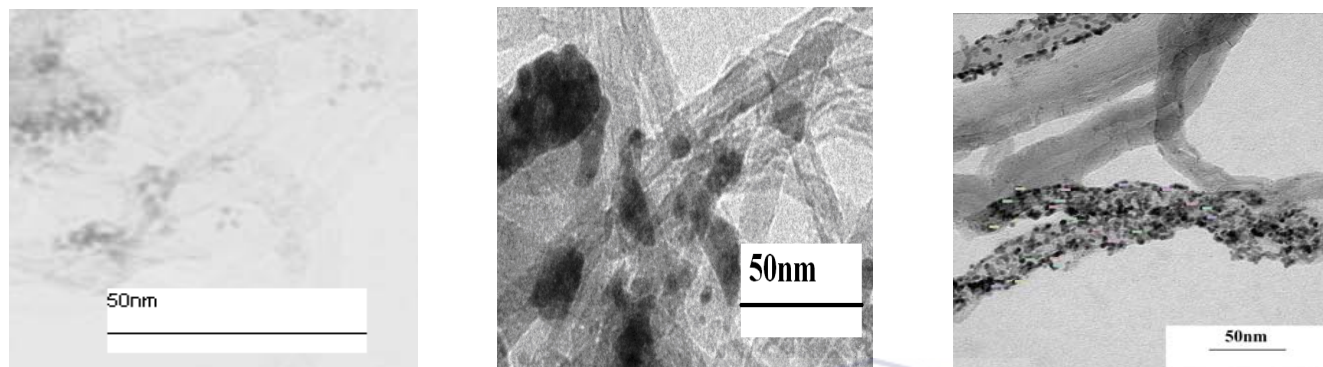


Fig. 7.4.2.3 TEM images of catalysts (a) D5, (b) D6, (c) D7

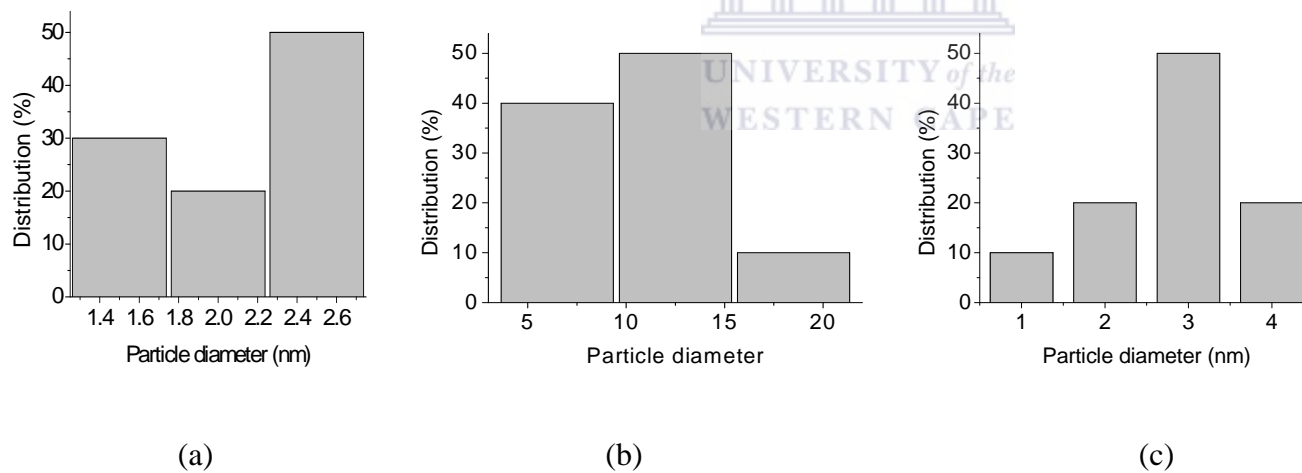


Fig. 7.4.2.4 Particle size distribution of catalysts (a) D5, (b) D6, (c) D7

of the particles $> 3\text{nm}$ exceeding the requirement previously established in this research for the formation of highly active catalytic particles, it can only be expected that the ECA would be moderate. Catalyst D1 was prepared by the simultaneous deposition method with assistance from the pre reduction and post reduction temperature regulation.

Similarly, figure 7.4.2.1 shows catalyst D2, also prepared with assistance from the pre reduction and post reduction temperature regulation. However catalyst D2 was prepared using the individual salt precursor method. The incorporation of the pre and post reduction temperature treatment regime was used to determine the Fe/Mo/Ru would adversely affect the ECA of the catalysts if added together with the platinum precursor. The particle size distribution for catalyst D2 was 15% $< 3\text{nm}$ and with only 15% of its particles conforming to the previously determine critical parameter for significant ECA this catalyst was further pursued with changing the support and sequential deposition mode to produce a much improved ECA catalyst D7. As mentioned earlier the structural advantages or disadvantages a multi-metallic catalyst may possess may be explained by the determination of the proximity effect would ascertain the effect of multi-metallic catalyst sequential preparation in relation to the proximity of the Pt/Ru/Mo/Fe atomic layering had very little effect in lowering the ECA for catalyst D7. The platinum with its 20% Pt atomic presence in solution may have formed the most nucleation sites on the



carbon support or onto an already formed monolayer. During the growth to atom stage and subsequent layering may have introduced the atoms of other metal salts (Ru/Mo/Fe) during this growth process. The formation of subsequent layers may have occurred in the way of forming other single nucleus which then spread undisturbed over the entire face or by formation of other nuclei before the face was completely enveloped or covered, referred to as multinuclear multilayer deposition, and during this process may have also introduced atoms and nuclei of other metals.

Figure 7.4.2.1 (c) for catalyst D3 shows the sparsely embedded particles, with sizes greater than the optimum sized catalytic particles previously determined to be around 3nm. The average particle size distribution for 300 particles was 85% > 5nm. The method used was part of a series of temperature cycles with the introduction of the pre and post reduction temperatures. The method was repeated and the reduction deposition procedure was changed to simultaneous and there was no change to the catalyst profile with regards to the characterization or ECA. The support was changed to MWCNT under similar synthesis parameters producing catalyst D5. Catalyst D5 characterized by TEM and its corresponding image shown in figure 7.4.2.4 (b), gave an equally poor characteristic of an under performing broad particle size distribution and low ECA catalyst.

7.4.3 Elemental Analysis by EDS

EDS was used to confirm the absence or presence of platinum, iron, cobalt, ruthenium, molybdenum and chromium on the carbon support. The weight % values were accepted and should be viewed as an approximation and not the accurate amount of metal deposited onto the carbon support.

Table 7.4.3.1 Results of the elemental analysis by EDS of the different categories of Quaternary catalysts

Elemental Content	Catalyst Categories						
	D1	D2	D3	D4	D5	D6	D7
% Carbon	66,6	60,5	54,5	66,5	86,4	79,2	63,9
% Platinum	23,4	27,9	33,3	20,4	6,7	5,9	22,6
% Ruthenium	7,6	5,5	10,5	7,5	4,5	7,7	7,1
% Iron	-	2,6	1,2	-	2,1	-	2,4
% Cobalt	0,3	-	0,5	-	0,3	-	-
% Molybdenum	-	3,5	-	2,4	-	5,2	4,0
% Chromium	2,1	-	-	3,2	-	2,0	-

Table 7.4.3.1 gives the metal quantities formed after the deposition reactions. Platinum was formed at a nominal 20% in most cases except for catalysts D5 and D6. The amount of Ruthenium formed was above 7% except for catalysts D2 and D5 which were below 6%. After a series of temperature adjustments and modifications to the reaction conditions Iron, Cobalt, Molybdenum and Chromium were introduced as the third and

fourth metals. The changes in reaction conditions to accommodate the properties of each metal were discussed earlier in the chapter namely synthesis parameters. Iron was consistent in the 2% region of formation. This metal quantity deposited for the quaternary catalysts was less than the ternary catalysts where the iron deposition was averaging approximately 4%.

The sites for cobalt nucleation initiation may not have been subjunctive enough to allow for the initial nucleation to proceed as the formation of cobalt metal was minimal, and the formation was some how limited to less than 1% in all instances where the quaternary reduction including cobalt from its salt precursor was attempted. The cobalt catalysts were not as active in its methanol oxidation capability possibly due the low levels of formation later confirmed in the ECA scans. The cobalt metal formation may require higher temperatures as observed in the ternary catalysts where higher post reduction temperatures were attempted, however the energy increase may have accelerated the nucleation and subsequent growth rate resulting in large particle formation, ie. greater than 3nm. The unique tendency of cobalt to form complexes and resulting oxides may have reduced its ability to react with and form alloys with the other metals.

7.4.4 Electrochemical Activity by Cyclic Voltammetric Analysis

As in chapters 4, 5 and 6, the electrochemical (EC) activity was determined by cyclic voltammetric (CV) analysis of the different category of catalysts. The reducing agents and other synthesis parameters can now be identified as contributors to effective synthesis routes when comparing the electrochemical activity of each catalyst. Tabulated here, in table 7.4.4.1, are the best catalysts from each category.

Table 7.4.4.1 Comparing the Quaternary Catalysts Electrochemical Activity by CV Analysis

Catalyst Category	Metal Support	EC Activity				Reference Figures
		T °C	I(A) (vs. Ag/AgCl) 0,5V	I(A) (vs. Ag/AgCl) 0,6V	ECA Status	
D1	<u>Pt/Ru/Co/Cr</u> Vulcan	20	$1,45 \times 10^{-4}$	$2,27 \times 10^{-4}$	Low	7.4.4.1
D2	<u>Pt/Ru/Fe/Mo</u> Vulcan	20	$7,87 \times 10^{-4}$	$1,44 \times 10^{-3}$	Low	7.4.4.2
D3	<u>Pt/Ru/Co/Fe</u> Vulcan	20	$3,32 \times 10^{-3}$	$3,22 \times 10^{-3}$	Moderate	7.4.4.3
D4	<u>Pt/Ru/Mo/Cr</u> Vulcan	20	$7,94 \times 10^{-4}$	$1,06 \times 10^{-3}$	Low	7.4.4.4
D5	<u>Pt/Ru/Co/Fe</u> MWCNT	20	$2,22 \times 10^{-3}$	$2,82 \times 10^{-3}$	Moderate	7.4.4.5
D6	<u>Pt/Ru/Mo/Cr</u> MWCNT	20	$2,27 \times 10^{-3}$	$1,59 \times 10^{-3}$	Moderate	7.4.4.6
D7	<u>Pt/Ru/Mo/Fe</u> MWCNT	20	$6,02 \times 10^{-3}$	$8,33 \times 10^{-3}$	High	7.4.4.7
JM	<u>Pt/Ru</u> Vulcan	20	$1,31 \times 10^{-3}$	$1,14 \times 10^{-3}$	Moderate	5.4.4.6

ACPS (Average catalyst particle size); MWCNT (Multiwalled carbon nanotubes); EC (Electrochemical); N/A (Not available)

In Table 7.4.4.1 the EC activity of the once-formed catalyst is analyzed in an acidic medium (base analysis), followed by the addition of 1M methanol which undergoes

oxidation on the platinum surface as shown in the CV graphs below. The potential regions analyzed are -0,2 to 0,6V and -0,2 to 1,0V (vs. Ag/AgCl) and the scan rate used was 20mV/s.

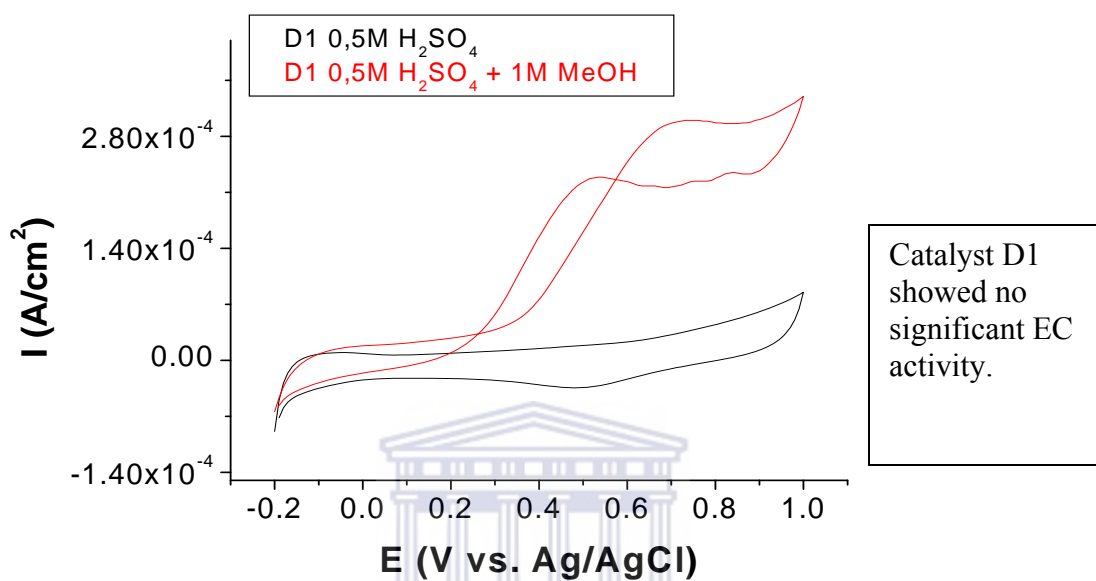


Fig. 7.4.4.1 CV of catalyst D1 at 1,0V vs. Ag/AgCl

The ECA scan for catalyst D1 (Pt/Ru/Co/Cr) / Vulcan XC72 in Figure 7.4.4.1 showed 3 increases within 3 different potential regions in activity during the forward methanol oxidation scan (Red) similar to the ternary catalysts during early stages of method development. The first peak was in the region of -0,1V (Ag/AgCl), the second peaks at around 0,45V (Ag/AgCl) and the third approximately 1,0V (Ag/AgCl). There was a 4th peak at 0,65V (Ag/AgCl) that was formed during the reverse scan (Red) and exhibited a much higher activity, a notable 22% increase in current was recorded, than that at potential 0,45V (Ag/AgCl). This peak could be the result of the oxidation reaction of an oxide formed during the forward scan of transition metal complexes with Co and Cr.

However the peaks of interest in relation to further Fuel cell applications, to be performed in chapter 8 with the most active ECA catalysts, were the ones peaking around 0,45V and 0,65V (Ag/AgCl) in the forward and reverse (Red) methanol oxidation scans. The 0,45V (Ag/AgCl) peak started its incline at approximately 0,1V (Ag/AgCl). Two irreversible reactions and possible oxide products formed during the redox reaction at potentials 0,25V and 0,55V (Ag/AgCl). These could be once again oxides or complexes formed with the transition metals cobalt and chromium, to be discussed later in this chapter. The ECA status was regarded as low when compared to the other in-house quaternary catalysts.

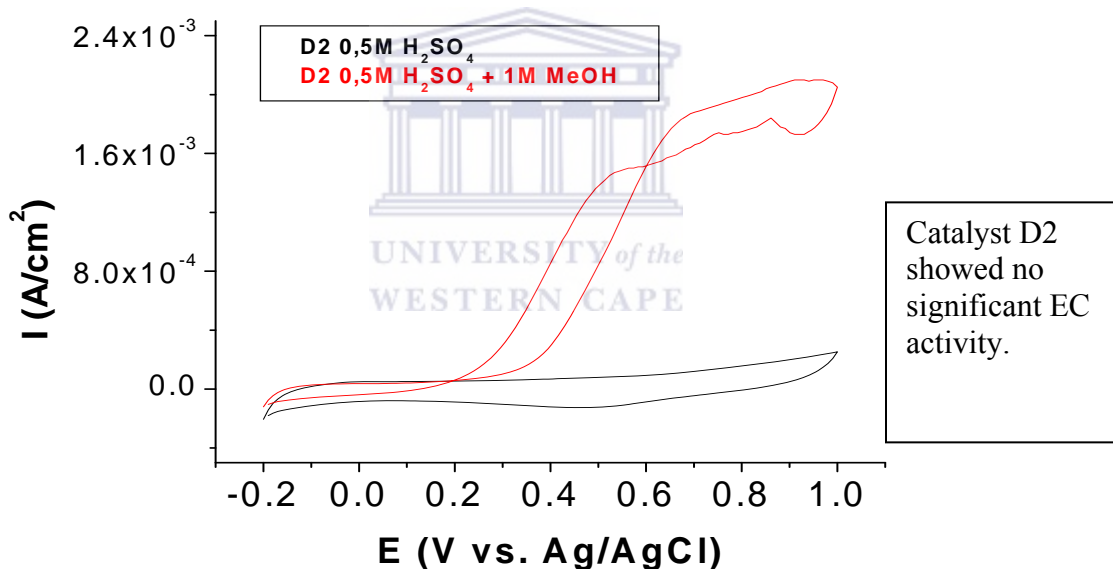


Fig. 7.4.4.2 CV of catalyst D2 at 1,0V vs. Ag/AgCl

The ECA was calculated as the difference between the base (Black) forward scan and the methanol oxidation forward scan (Red) at potentials 0,5 and 0,6V (Ag/AgCl).

For catalyst D1, figure 7.4.4.1, the base scan (Black) indicated the oxide or surface products reduction peak at potential 0,5V (Ag/AgCl) in the acidic medium (0,5M H₂SO₄). Slight elevations in peaks in the -0,2 to 0,1V potential region references the hydrogen desorption and comparison will be made to the other catalyst scan with varying amounts of metal deposits and different supports if significant differences are fourth coming.

The ECA scan for catalyst D2 (Pt/Ru/Fe/Mo) / Vulcan XC72 in Figure 7.4.4.2 showed 3 increases similar to catalyst D1 within 3 different potential regions in activity during the forward methanol oxidation scan (Red) similar to the ternary catalysts during early stages of method development. The first peak was in the region of -0,1V (Ag/AgCl), the second peaks at around 0,45V (Ag/AgCl) and the third approximately 0,65V (Ag/AgCl). The difference being was that the peak at 0,65V (Ag/AgCl) was formed during the reverse scan and exhibits a much higher activity, a notable 29% increase in current was recorded, than that at potential 0,45V (Ag/AgCl). This metal combination was assumed to be partially the reason for the increase in activity and will be looked at again in catalyst D7 with a modified MWCNT support. The peaks of interest in relation to the future Fuel cell application, were the ones peaking around 0,45V and 0,65V (Ag/AgCl) in the forward (Red) and reverse methanol oxidation scans. The 0,45V (Ag/AgCl) peak started its incline at approximately 0,1V (Ag/AgCl). As for D1 the two irreversible reactions and possible oxide products formed during the redox reaction at potentials 0,25V and 0,55V (Ag/AgCl) were present once more for D2 Pt/Ru/Fe/Mo metal combination catalyst. These could be oxides or complexes formed with the transition metals iron and molybdenum, however the ECA for catalyst D2 was 69 and 73% higher at potentials 0,5

and 0,6V (Ag/AgCl) respectively than that of catalyst D1. Although The ECA was higher than that of catalyst D1 the ECA status was regarded as low when compared to the other in-house quaternary catalysts. The ECA was calculated as the difference between the base (Black) forward scan and the methanol oxidation forward scan (Red) at potentials 0,5 and 0,6V (Ag/AgCl).

The base scan (Black) indicated the oxide or surface products reduction peak at potential 0,5V (Ag/AgCl) in the acidic medium (0,5M H₂SO₄). As for catalyst D1 slight elevations in peaks denoting ECA in the -0,2 to 0,1V potential region referenced the hydrogen desorption and comparison will be made to the other catalysts scans with varying amounts of metal deposits and on different supports to determine if there is significantly different peak profiles in that region.

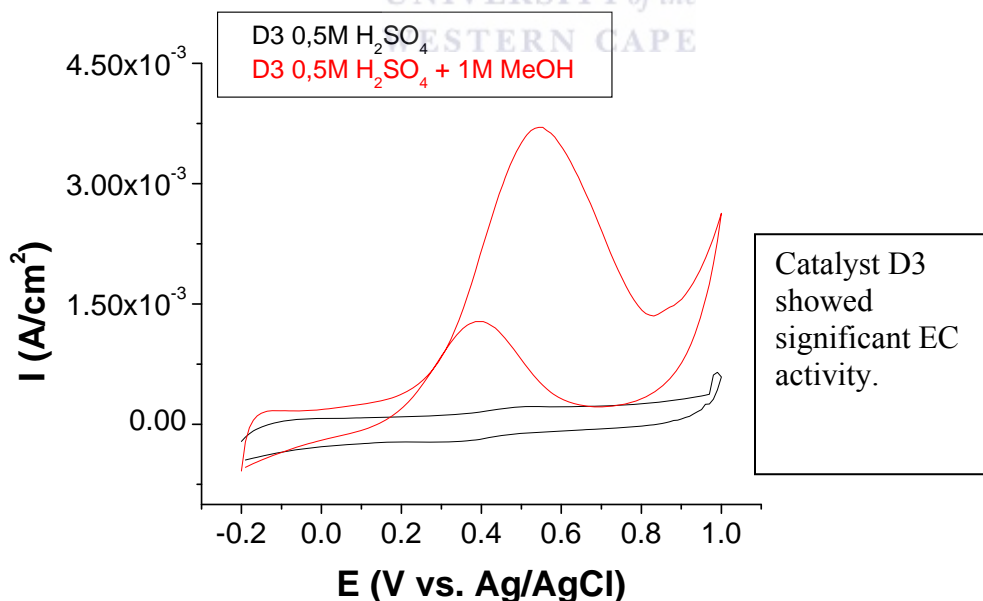


Fig. 7.4.4.3 CV of catalyst D3 at 1,0V vs. Ag/AgCl

The significant Pt oxide reduction peak scans showed in the above figures (Black) in an acidic electrolyte solution i.e. 0,5M H₂SO₄ has been previously discussed in relation to the OH adsorption strength was a partial mechanism of water adsorption and as previously mentioned in the literature review this mechanisms role in the removal of CO by CO₂ formation, where this peak shift (Black) to the negative signified that catalysts D2 (figure 7.4.4.2; Black) and D3 (figure 7.4.4.3; Black) are more CO tolerant catalysts than catalyst D1. The negative shift is also dependant on the decrease of the particle size [255].

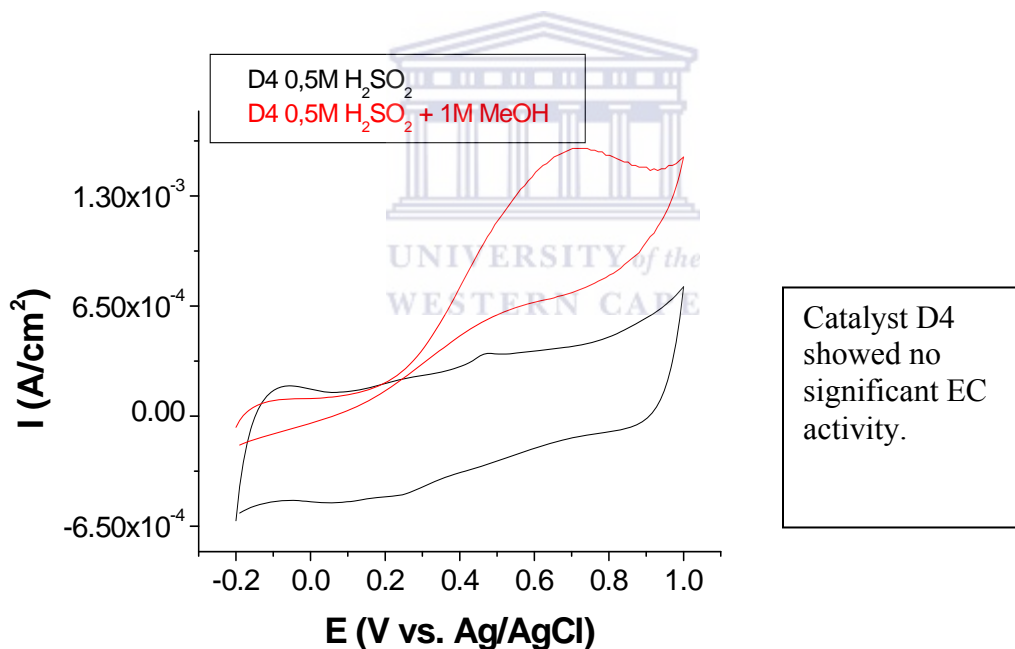


Fig. 7.4.4.4 CV of catalyst D4 at 1,0V vs. Ag/AgCl

The agglomerations of small particles, as observed in the TEM images for catalyst D2 and D3, have possibly contributed to the increased mass activity of the decreased particles size. The agglomerations are proving to be actual masses of smaller nano-sized

particles which act favourably towards producing a catalyst hub where each catalytic particle acts as an individual entity providing a high surface area for catalytic ECA.

The ECA scan for catalyst D3 (Pt/Ru/Fe/Co) / Vulcan XC72 in Figure 7.4.4.3 showed 3 increases in ECA similar to catalysts D4 (Figure 7.4.4.4) and D5 (Figure 7.4.4.5) within 3 different potential regions in activity during the forward methanol oxidation scan (Red) similar to the ternary catalysts during early stages of method development. There is also a notable fourth increase in the reverse scan (Red) at the potential 0,4V (Ag/AgCl) which is uniquely large in catalyst D3. This possible oxide oxidation peak at potential 0,4V (Ag/AgCl) cannot be readily associated to the metal combination as it is absent in catalyst D5s ECA scan with a matching Pt/Ru/Fe/Co metal combination.

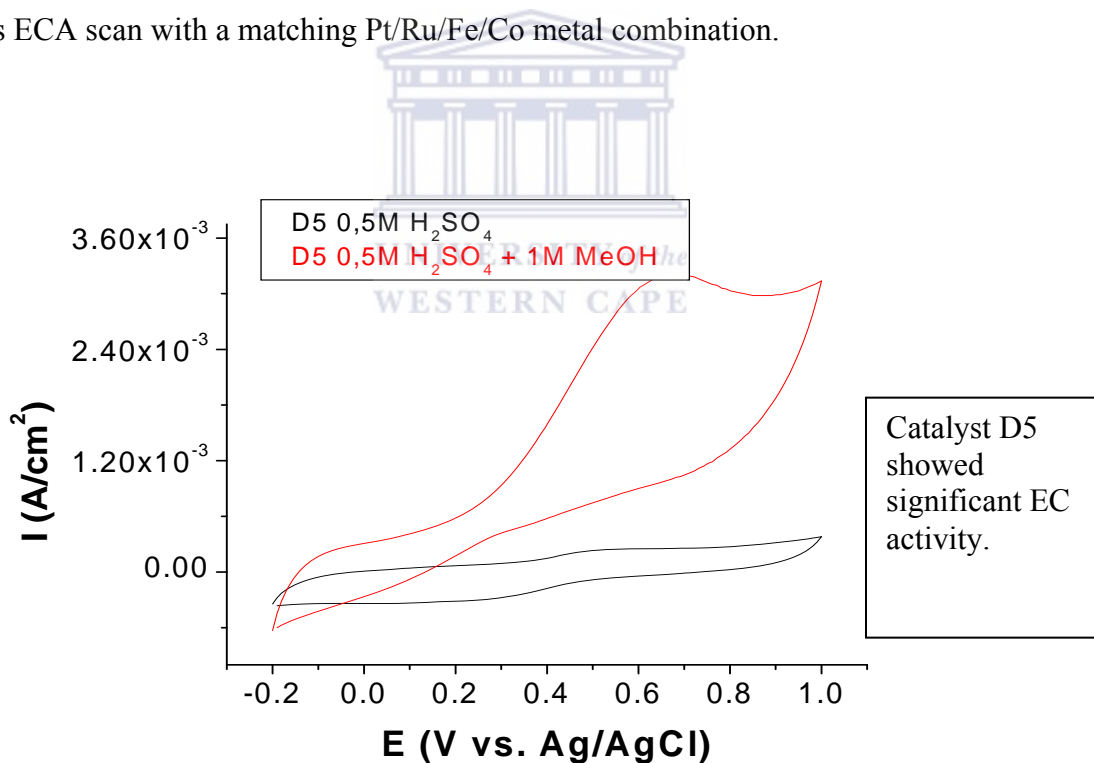


Fig. 7.4.4.5 CV of catalyst D5 at 1,0V vs. Ag/AgCl

For catalysts D3, D4 and D5 the first of the 3 inclining forward scan peaks was in the region of -0,1V (Ag/AgCl), the second peaks at around 0,45V (Ag/AgCl) and the third approximately 0,65V (Ag/AgCl). The difference in scan profile took place at the peak potential region of 0,3V (Ag/AgCl). At this potential there was an increase in the difference of ECA between the forward and reverse scan from catalyst D3 to D5 where D5 had the largest difference and D5 was prepared on MWCNT with the same metal combination as catalyst D3 prepared on Vulcan XC72 carbon support.

There is actually no difference in ECA for catalyst D3's forward and reverse scan at potential 0,3V (Ag/AgCl) as they meet during the scan indicating the formation of a irreversible possible oxide formation. The support can be seen as playing a role in incorporating atoms of different metals to give the required alloy properties into crystal positions which could play a role in preventing oxide formations and catalyst poisoning.

As for D1 the two irreversible reactions and possible oxide products formed during the redox reaction at potentials 0,25V and 0,55V (Ag/AgCl) were not present for catalysts D4 (Figure 7.4.4.4) and D5 (Figure 7.4.4.5) however catalyst D3 (Figure 7.4.4.3) Pt/Ru/Fe/Co metal combination did show an irreversible reaction at potential 0,25V (Ag/AgCl). These could be once again oxides or complexes formed but with the transition metals iron and cobalt functioning as individual atoms or in an alloyed form. The ECAs for catalysts D3, and D5 were similar and averaged $3,3 \times 10^{-3} \text{ A/cm}^2$ at 0,5V (Ag/AgCl). This average constituted a 61% increase in ECA at potential 0,5V (Ag/AgCl) when compared to that of catalyst D4. Although the ECA was higher than that of catalyst D4 the ECA status was still regarded as moderate when compared to that of catalyst D7

an in-house quaternary catalyst discussed later. The ECA once again was calculated as the difference between the base (Black) forward scan and the methanol oxidation forward scan (Red) at potentials 0,5 and 0,6V (Ag/AgCl) where indicated.

Catalysts D4 and D6 shared the identical atomic metal make and preparation method of simultaneous salt precursor addition to the reaction vessel. The difference was that catalyst D6 was prepared on MWCNT and catalyst D4 was prepared on Vulcan XC72 support. The ECA scan for catalyst D4 with out methanol i.e. in acid medium (0,5M H₂SO₄) in figure 7.4.4.4 (Black) shows the typical ECA surface area of the platinum

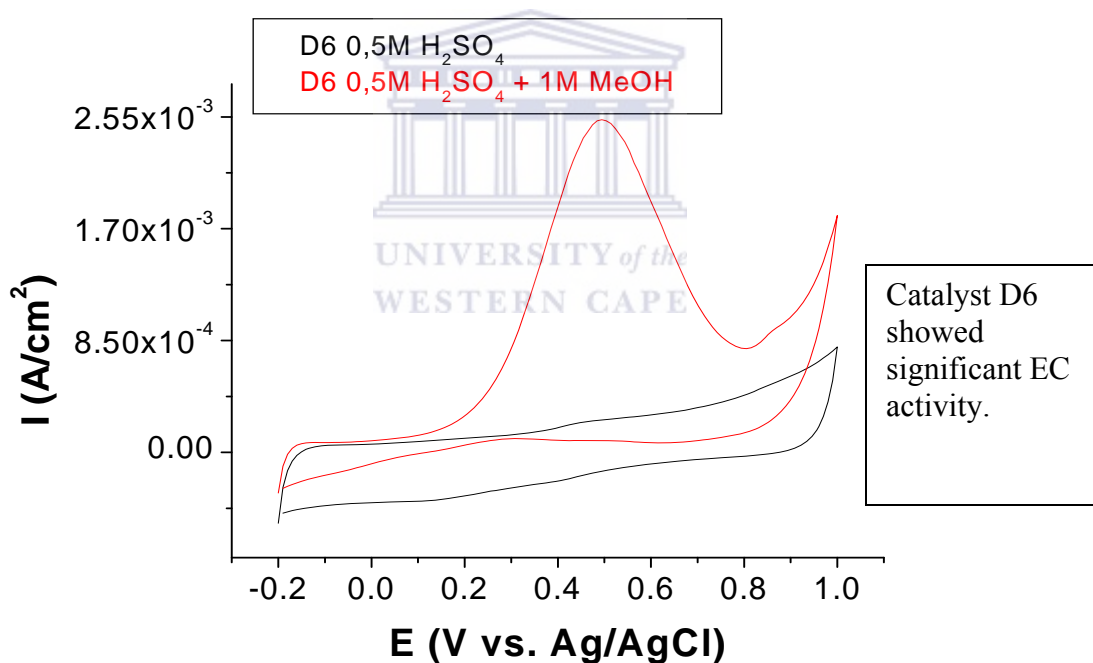


Fig. 7.4.4.6 CV of catalyst D6 at 1,0V vs. Ag/AgCl

catalyst. Present but not as clearly defined as scans of a pure platinum electrode are the hydrogen adsorption – desorption areas, as well as the oxide formation and reduction

areas. In figure 7.4.4.4 (Black) the shift to the negative in the base scan indicates the catalyst possess the potential to be a CO tolerant catalyst.

The ECA scan for catalyst D6 (Pt/Ru/Mo/Cr) / MWCNT in Figure 7.4.4.6 similar to the other quaternary scans for catalysts D3, D4 and D5 showed 3 increases within 3 different potential regions in activity during the forward methanol oxidation scan (Red) similar to the ternary catalysts during early stages of method development and quaternary catalysts depending on the metal combinations. The first peak was in the region of -0,1V (Ag/AgCl), the second peaks at around 0,5V (Ag/AgCl) and the third approximately 1,0V (Ag/AgCl). The difference between D6 and the other catalysts was that catalysts D6's inclining methanol oxidation peak, peaked at 0,5V (Ag/AgCl) formed during the forward scan and exhibits a much higher activity where as catalysts D3, D4 and D5 ECA's peaked at ~0,65V (Ag/AgCl), with a clear shift to the lower potential could indicate D6 is a more suitable Fuel cell catalyst. However apart from the shift to the lower potentials, the difference in activities when comparing catalysts D6 to D5 and D3 were not convincing enough to suggest that D6 will be a suitable catalyst above catalysts D6 to D5 and D3 without analyzing the ECA and performance results. There was only a 1% increase in ECA recorded as the difference between catalysts D5 and D6 at potential 0,5V (Ag/AgCl) and when comparing the maximum peak ECA for catalysts D5 and D6 there was a 11% increase in favour of catalyst D5. The metal combinations Co/Fe and Mo/Cr did not appear to affect the ECA enough to allow a direct comparison between the metal combinations and ECA, but once again the carbon supports did in fact suggest a

relative comparison as D6 and D4 were prepared on MWCNT and Vulcan XC72 respectively. Catalyst D6 showed a 48% increase in ECA compared to catalyst D4, prepared under similar conditions with the identical metal combination i.e. Pt/Ru/Mo/Cr. The activity of the catalysts may not be as successful in the Fuel cell itself during the actual application. Therefore to avoid the unnecessary trial and errors associated with Fuel cell testing this research first clearly identified a very ECA catalyst D7 and focused on the peaks of interest in relation to the future Fuel cell applications, and those were the ones peaking around 0,45V and 0,65V (Ag/AgCl) in the forward and reverse (Red) methanol oxidation scans. The 0,6V (Ag/AgCl) peak started its incline at approximately 0,1V (Ag/AgCl).

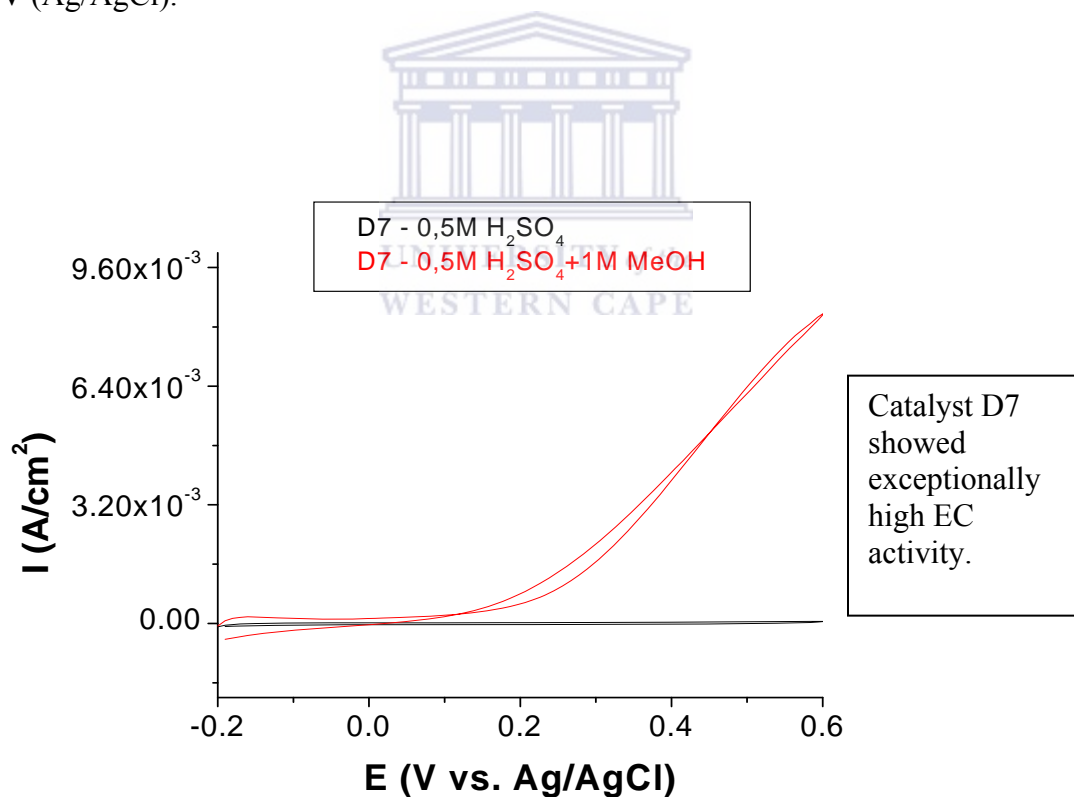


Fig. 7.4.4.7 CV of catalyst D7 at 0.6V vs. Ag/AgCl

With reference to figure 7.4.4.7 showing catalyst D7 there was the reappearance of the two irreversible reactions and possible oxide products formed during the redox reaction at potentials 0,25V and 0,55V (Ag/AgCl). These reactions and subsequent products could be attributed to oxides or complexes formed with the transition metals molybdenum and iron. The ECA status was regarded as high when compared to the other in-house quaternary catalysts. The ECA as before was calculated as the difference between the base (Black) forward scan and the methanol oxidation forward scan (Red) at potentials 0,5 and 0,6V (Ag/AgCl).

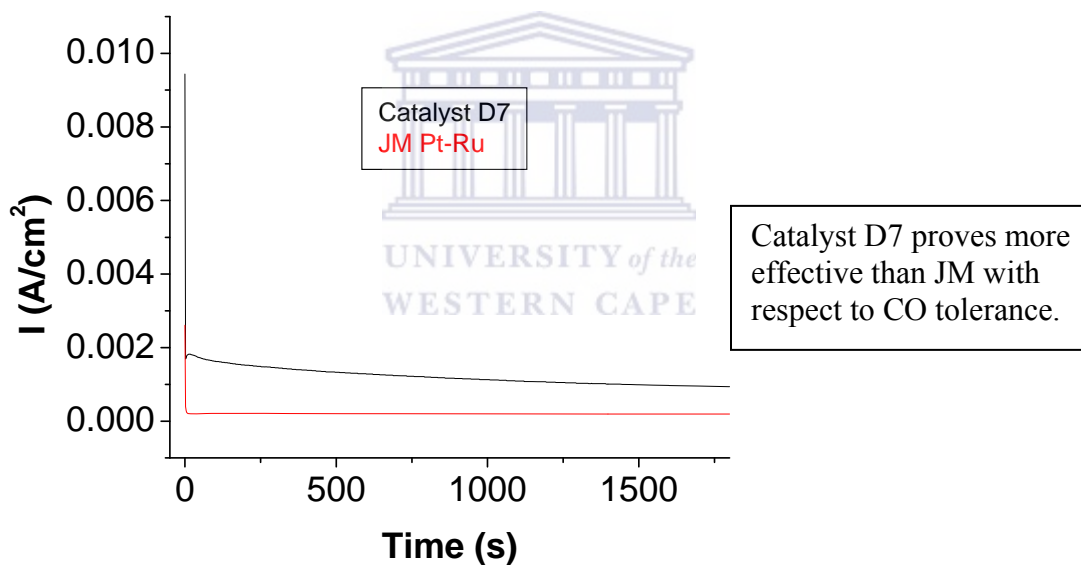
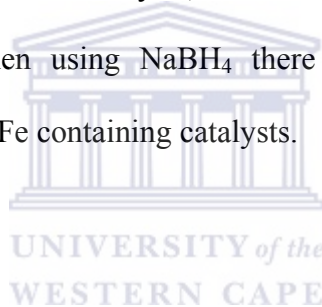


Fig. 7.4.4.8 CA of catalyst D7 at 0.3V vs. Ag/AgCl

Catalyst D7 has been clearly identified as the most active quaternary catalyst; therefore chronoamperometry (CA), Fig. 7.4.4.8, to determine CO tolerance. The CA was performed in 1M methanol at 0,3V (Ag/AgCl). This research was performed towards finding a suitably active quaternary catalyst was tabled and the relationships between the

different supports, reduction temperatures, particle sizes and EC activities are summarized in table 7.5.1. The obvious differences from the TEM images were the increased numbers of pocket formations of agglomerated nano-sized particles for the quaternary catalysts. The particle size distributions were not easily determined due to the high mass of metal particles formed from 4 salt precursors therefore much of the particle size distributions had to be assessed from previous bimetallic and ternary particles size distribution and ECA relationships. Improved electrochemical activity during the cyclic voltammetric analysis was characterized by particles <2nm diameter size particles and low level agglomerations. Although there was poor dispersion or less reduction than compared to the Vulcan supported catalysts, the MWCNT catalysts had comparable electrochemical activity. When using NaBH_4 there was a significant increase in electrochemical activity for the Fe containing catalysts.



The various metal combinations were responsible for the changes in the initiation of forward methanol oxidations peaks, and for the formation of complexes or oxides that were either product of reversible or irreversible reactions depending on the metal combinations. The metal combinations in addition to the support type affected the ECA of the catalysts allowing for increases of up to 50% at times. As previously stated in the literature review MWCNT possess unique electronic and structural characteristics that were observed to exhibit better performance during methanol oxidation reactions when compared to other carbon supported catalysts prepared under identical conditions.

Chapter 7 - Quaternary catalysts

To model the selective growth process, the chemistry (rate constants and other physical parameters such as site density and bulk diffusion coefficients) on the exposed window regions is the same as for un-patterned growth. The nucleation was a random process which was amplified by the varying temperature and support which either aided or resulted in absence of nucleation and subsequent growth.

Table 7.5.1 Summary table comparing the different reducing agents and temperatures and EC activities of the quaternary catalysts

	<u>Metals Support</u>	<u>D</u>	<u>APS</u> nm	<u>Synthesis Parameters</u>				<u>EC Activity</u>		
				<u>ST</u> Min	<u>TP</u> °C	<u>RA</u>	<u>Vol.</u> ml	°C	<u>I</u> (Vs Ag/AgCl) 0,5V MeOH	<u>I</u> (Vs Ag/AgCl) 0,6V MeOH
D1	<u>Pt/Ru/Co/Cr</u> Vulcan	ID	40%<3nm	10	40-0-40	F	150	20	$1,45 \times 10^{-4}$	$2,27 \times 10^{-4}$
D2	<u>Pt/Ru/Fe/Mo</u> Vulcan	SD		10	40-0-40	F- SBH	150	20	$7,87 \times 10^{-4}$	$1,44 \times 10^{-3}$
D3	<u>Pt/Ru/Co/Fe</u> Vulcan	SD	85%>5nm	10	40-0-40	F- SBH	150	20	$3,32 \times 10^{-3}$	$3,22 \times 10^{-3}$
D4	<u>Pt/Ru/Mo/Cr</u> Vulcan	SD	100%<5nm	10	40-0-40	F- SBH	150	20	$7,94 \times 10^{-4}$	$1,06 \times 10^{-3}$
D5	<u>Pt/Ru/Co/Fe</u> MWCNT	SD	0%<3nm 80%>5nm	10	40-0-40	F- SBH	150	20	$2,22 \times 10^{-3}$	$2,82 \times 10^{-3}$
D6	<u>Pt/Ru/Mo/Cr</u> MWCNT	SD	0%<3nm 95%>5nm	10	40-0-40	F- SBH	150	20	$2,27 \times 10^{-3}$	$1,59 \times 10^{-3}$
D7	<u>Pt/Ru/Mo/Fe</u> MWCNT	SD	50%<2nm 80%<3nm	10	40-0-40	F- SBH	150	20	$6,02 \times 10^{-3}$	$8,33 \times 10^{-3}$
JM	<u>Pt/Ru</u> Vulcan	N/A	50%<3nm 80%<4nm	N/A	N/A	N/A	N/A	20	$1,31 \times 10^{-3}$	$1,14 \times 10^{-3}$

APS (Average catalyst particle size); ST (Sonication time); RA (Reducing agent); F (40% Formaldehyde); SBH (NaBH₄); MWCNT (Multiwalled carbon nanotubes); D (Deposition); ID (Individual deposition); SD (Simultaneous deposition); EC (Electrochemical); N/A (Not available)

The quaternary crystal structure relies on theories supporting the addition of atoms to crystal structures. These ad-atoms allow for the understanding towards the alloying

process or surface formation of atoms on the outer structure of the crystal as these atoms are not the same i.e. 4 different types of atoms are expected in a quaternary metal crystal structure.

Their arrangement depended somewhat on the energies of formation, radii, forces of attraction, repulsion etc. Crystal structures contain many faults, and this number increases with temperature. This disorder was minimized by working at sub-ambient temperatures yet the disorder was welcomed to some degree with the interstitial incorporation of foreign atoms into ordered structures to give the alloy a multi functional cohesiveness. The platinum atoms arrangement was intact to a large degree allowing the ad atoms to function as CO removal and prevention. The introduction of atoms such as cobalt was not greater than 2%, this metal requires a super saturated solution of the cobalt precursor salt to overcome the forces acting against its introduction into the platinum structure.

Previous studies at temperatures above 200K were performed by three different temperature regions allowing preparation of nanometer-sized structures:

- (1) Formation of monatomic Fe chains occurs between 250 K and 500 K.
- (2) The best order of a Fe ML as judged from the He reflectivity is obtained around $T = 400$ K.
- (3) The FePt mixing remains restricted to the surface layer if Fe is evaporated between 500 K and 550 K.

Due to this behavior we assume that the first Fe layer grows in a pseudomorphic fashion on the Pt terrace although the atomically resolved structure on the terrace could not be assessed due to the large size of the step repeat unit and the small atomic corrugation.

The behavior is, however, induced by kinetics rather than by the balance of free surface and strain energies which are the important parameters in regular Stranski–Krastanov (SK) SK growth. This clearly indicates that the Fe diffusion barrier is much higher on the Fe covered surface than on the Pt substrate resulting in a reduction of step decoration in the second Fe layer and favoring island nucleation on the terraces. Although helium scattering has no explicit chemical

The rate controlling process was the oxidation of hydroxide ions or water molecules on the surface of the electrode in order to remove surface oxides and CO. This was enabled by producing more electrochemically active sites by increasing the surface area of the catalyst. The electrochemically active surface area was increased by increasing the number of nano-sized metal particles i.e. $< 3\text{nm}$. The catalyst mass activity was enhanced by increasing the amount of metal deposited onto the support without increasing the cost by the introduction of non-noble metals this increased the mass activity without increasing the platinum content. The introduction of non-noble metals increased the rate of oxidation of hydroxide ions or water molecules on the surface of the electrode in order to remove surface oxides and CO by increasing the mass activity of the catalysts. Few of the various metals combinations did not affect the activity of hydrogen or methanol oxidation and these unique combinations, mentioned earlier, have shown promise as being part of an electrochemical catalytic system that is CO tolerant.

CHAPTER 8

FUEL CELL APPLICATION AND TESTING

8.1 OBJECTIVES

- 8.1.1 To determine the optimum parameters for the MEA construction.
- 8.1.2 To determine the optimum parameters for the Fuel Cell operation.
- 8.1.3 To use the in-house catalysts in the MEA construction.
- 8.1.4 To compare the performance of the in-house catalysts to that of the commercially available catalyst.

8.2 INTRODUCTION AND LITERATURE REVIEW

8.2.1 Background

The fuel cell is mainly constituted of five components: anode backing layer, anode catalyst layer, proton exchange membrane, cathode catalyst layer and cathode backing layer. The heart of the fuel cell is the MEA. In this Chapter, the backing and catalyst layers and the influence of operating conditions on cell performance (temperature, pressure, gas flow rate, etc.) are investigated. Nafion[®] 117 a commercially available proton conductor was used as the membrane. The catalyst used was the commercially available JM Pt/Ru. Once the optimum conditions are identified an application of the in-house catalyst into the DMFC's MEA was made. These in-house catalysts were chosen after a series of quantification and characterization tests ultimately showing the highest performance.

8.2.2 PEMFC electrode preparation: Influence of the solvent composition and evaporation rate on the catalytic layer microstructure

A series of parameters affecting the catalytic layer microstructure in polymer exchange fuel cell electrodes have been evaluated. The deposition of the catalytic layer in the gas diffusion support is shown to depend not only on the ink deposition method but also on the characteristics of the solvent used to disperse both the catalyst and the Nafion ionomer. The solvent viscosity and its dielectric constant are two important factors to control for the catalytic ink preparation. In particular, the solvent dielectric constant is shown to be directly related to the electrode performance in single cell tests.

In order to determine the effect of the catalytic ink composition on the electro-active layer microstructure, a series of solvent mixtures composed of up to three compounds were tested. For the preparation of a solvent of suitable characteristics to disperse the catalyst, a number of single compounds were selected according to their physicochemical properties, which are compiled in Table 8.2.2.1. Liquids with high dielectric constants, above 10, are known to form a perfect Nafion solution, while solvents with dielectric constants below 3 lead to the formation of precipitates [401]. Ideally, it would be preferable using solvents with intermediate values for obtaining a Nafion colloidal solution, which provides a porous and uniform network without large polymer aggregates. The different texture adopted by Nafion depending on the solvent used becomes clear from the analysis

of SEM micrographs of gas diffusion supports that were impregnated with solutions of the ionomer dispersed in different organic compounds. [401] presents these images in

comparison with the carbon cloth support before its impregnation with Nafion. The physical properties of the used solvent not only influence the degree of dissolution of the ionomer, but also the porosity, distribution, coverage and adherence of the Nafion layer over the carbon cloth support. High dielectric constant alcohols (such as ethanol) lead to the formation of a high density Nafion film, which mainly covers the upper fibres of the carbon support without penetrating in the cloth. On the contrary, impregnation of the ionomer with a low dielectric constant solvent, such as butyl-acetate [402], results in a porous and less uniform structure, which is better distributed among the gas diffuser. However, the deposition process of the ink requires a compromise between the dielectric constant and other physical properties, such as the viscosity, the boiling point

Table 8.2.2.1 Physical properties of the single solvents used for inks preparation

Solvent	Dielectric Constant	Viscosity (298K) (cP)	Boiling Point (K)
Water	78.0	0.89	373
Ethanol	24.3	1.22	352
Isopropyl Alcohol	18.3	2.27	356
Butyl-Acetate	5.0	0.69	400
Glycerine	42.5	1400	563 (Boils with decomposition)

and the carbon wet capacity of the solvent. Butyl-acetate has been selected as one of the candidates for the composition of these mixtures because of its low dielectric constant. However, its high volatility and low viscosity make necessary to use other compounds to improve the properties of the ink solvent. Glycerine has been also selected as component for solvent mixtures because of its high viscosity, which allows maintaining a stable suspension during the ink deposition process.

Table 8.2.2.2 Experimental values of dielectric constants and viscosity obtained for binary and ternary mixtures of solvents with glycerine.

Solvent	Dielectric constant	Viscosity (cP)
Butyl-acetate:glycerine (85:15)	Not determined, unstable solution	Not determined, unstable solution
Ethanol:glycerine (85:15)	25.9	2.02
Isopropyl-alcohol:glycerine (85:15)	20.0	3.75
Water:glycerine (85:15)	74.9	1.40
Ethanol:butyl-acetate:glycerine (45:40:15)	16.5	2.80

The added amount has been reduced to a minimum in the mixtures to avoid increasing too much the dielectric constant value and the boiling temperature for solvent removal. It must be taken into account that the catalyst density influences the solvent viscosity requirements. The higher the catalyst metal loading for a given support, the higher the glycerine content required to maintain the catalyst in suspension. By considering the use of carbon blacks, the minimum amount of glycerine in the ethanol solvent to prepare a stable suspension of a bare Vulcan XC72 support was determined to be 5 wt.%. However, this percentage must be progressively increased for catalytic inks in order to maintain an

acceptable stability. Minimum concentrations of glycerine of up to a 15 wt.% are required when preparing inks with 20 wt.% Pt/Vulcan XC72 catalyst. On the other hand, both ethanol and isopropyl-alcohol could be also considered in principle suitable media for the suspension as main components of the solvent mixture and in contrast with water, which has an extremely high dielectric constant. Table 8.2.2.2 presents the composition of some representative binary mixtures of solvents and their physico-chemical properties, such as their dielectric constant value and viscosity. The dielectric constants of the prepared binary mixtures ranged from 20 to 75, with viscosity values between 1.4 and 3.8 cP (Table 8.2.2.2). It must be noted the low miscibility between butyl-acetate and glycerine, which did not allow obtaining a single phase as required for suitable ink impregnation. The other above mentioned solvents were used for the preparation of inks, which were sprayed on the carbon cloth. The ink deposition process and the morphology of the catalytic layers formed were observed to be greatly influenced by the solvents evaporation rate. Electrodes prepared from the water:glycerine mixture were constituted by a highly dense catalytic layer of low porosity, which contrasts with that formed from the ethanol:glycerine mixture. This latter electrode showed a thinner and more uniformly distributed catalytic layer that covered completely and individually the carbon fibres. The electrode prepared from the ink dispersed in the isopropyl-alcohol:glycerine mixture is the result of an intermediate situation. According to their physical properties, both isopropyl-alcohol and ethanol were considered initially good candidates as base components of the solvent mixtures. Furthermore, the higher viscosity and the slightly lower dielectric constant of the isopropyl-alcohol:glycerine mixture were even more favourable for the catalytic layer properties. However, the observation of the deposited

catalytic layer reveals a better wetting ability of the fibres in the case of the ethanol–glycerine mixture.

Typically water–glycerine solutions have been applied for thin film methods of deposition of the electrode catalytic layer as in the procedure in the Wilson’s patent in 1993 [403]. However, this kind of solvents yields highly dense films, which do not allow an effective dispersion of the catalyst. The effect of glycerine content in the catalytic ink was studied by Chun et al. [404], who found that high glycerine contents (above 25%) resulted in a high significant drop of performance, specially at high current densities, which the attributed to a contact area reduction between catalyst and Nafion. In order to reduce more the dielectric constant value of the ink solvent, ternary mixtures based in ethanol, butyl-acetate and glycerine were tested. The best results were obtained for a mixture whose percentages in weight of the single components were 45:40:15, respectively (Table 8.2.2.2). The dielectric constant measured for this solvent was 16.5, with a viscosity of 2.80 cP at 298 K. The structure of the Nafion film deposited over a carbon cloth using this mixture and a comparison among the Nafion coverage obtained with this ternary mixture and those resulting from its solution in single component solvents showed a large improvement in the distribution and homogeneity of the ionomer film. It must be stressed the importance of the ink drying process throughout the deposition. When compared the morphology of two electrodes prepared from a ternary ethanol:butyl-acetate:glycerine ink with and without instantaneous evaporation of the solvents and the airbrushing period, the accumulation of ink on the surface of the gas diffuser support at room temperature gives place to a thick and continuous catalyst layer that remains in the space among fibres when it is finally dried to remove the solvents.

Although the catalyst is uniformly distributed in the layer formed without heating, this structure increases the mass transfer resistance, makes more difficult the gas diffusion through the electrode and reduces the contact between the catalytic layer and the carbon cloth support. This problem is even aggravated when high boiling point components are present in the ink. The structure of the formed catalytic layer and its distribution can be largely improved by the instantaneous removal of solvents during the airbrushing process. An infrared source coupled to the airbrushing automated device is responsible of the heating over the gas diffusion support at temperatures close to 473 K. This fast drying produces a uniform coverage of the single fibres with the ink leaving a free space among them that improves the gas diffusion throughout the electrode. A detail of the covered fibres and their granular and porous microstructure included granules of about 0.1 micro.m size and a regular porous structure can be differentiated in the catalytic layer. The distribution of catalyst and ionomer at the nanometric scale was verified by TEM where Nafion structures could not be differentiated from catalyst particles, although energy dispersive X-ray analysis revealed the presence of the ionomer throughout the overall examined zone. The Pt/F and Pt/S ratios were obtained from EDAX analysis of the catalytic layer at different magnifications in the SEM, which yielded averaged values of 0.08 and 1.80, respectively. The theoretical ratios calculated from the nominal content of Pt and ionomer in the catalytic layer were determined to be: $Pt/F = 0.10$ and $Pt/S = 1.54$. The good agreement between experimental and theoretical values indicates a good dispersion of ionomer and catalyst throughout the electrode. The deviation of the Pt/F ratio to a lower value as compared to the theoretical one, and in contrast to that of Pt/S (slightly higher than the theoretical ratio), can be attributed to the water-proof treatment

of the carbon cloth support with PTFE. A mapping of the samples in the scanning electron microscope revealed in them a highly homogeneous distribution of Nafion and catalyst in the cloth fibres according to the quantitative analysis of the elements F, S and Pt. With the aim of verifying the complete removal of solvents from the inks and confirming the stability of the Nafion ionomer, the ink was analysed by FTIR in transmission mode after heating at different temperatures. The FTIR spectrum of the Nafion ionomer heated at 493K was identical to that obtained after drying at ambient temperature, which indicates no alteration of its molecular structure. Four main features at 1220, 1155, 1057 and 980 cm^{-1} were detected in the region from 1350 to 850 cm^{-1} , corresponding to the asymmetric and symmetric vibration of CF_2 , symmetric stretch of HSO^{3-} and C–F symmetric stretch in the $\text{CF}_2\text{--CF--CF}_3$ group respectively. A series of spectra was also obtained from the ink prepared from the ternary mixture of solvents in order to check the removal of each one of them from the catalytic layer. Butyl-acetate was easily removed at ambient temperature and no IR features corresponding to this compound were found in the spectra. Ethanol was detected in the ink at temperatures up to 353K showing the main absorption bands in the region near ca. 3478 cm^{-1} due to the OH group stretch vibration and at 2953, 2918, 2867 and 2844 cm^{-1} corresponding to the asymmetric and symmetric stretch of the CH_3 and CH_2 groups respectively. Somewhat higher temperatures were needed to eliminate glycerine residues from the ink. The glycerine characteristic bands at wave numbers between 1300 and 850 cm^{-1} (peaks at ca. 1108, 1040, 991, 922 and 852 cm^{-1}) decreased drastically at temperatures around 383K indicating practically complete glycerine removal from the catalytic layer. Infrared absorption bands remaining in the ink spectrum after heating at 438K are mainly due to

Nafion [405]. The performance of the electrodes prepared from inks dispersed in binary mixtures of solvents were also compared with that obtained from the ternary mixture of solvents (ethanol:butyl-acetate:glycerine). For identical Nafion content and Pt loading in the electrode, the efficiency of the cell increases as the solvent constant dielectric constant becomes reduced: water:glycerine < ethanol:glycerine < isopropylalcohol:glycerine < ethanol:butyl-acetate:glycerine. The better performance of the electrodes prepared from inks of lower dielectric constant solvents was evidenced in terms of higher voltage and power density for a given current density. This variation was represented as a function of the solvent dielectric constant. The observed trend indicates the close correlation between the ink physico-chemical properties and the microstructure of the electrodes, which is finally manifested in terms of performance. The effect of the preparation method of the inks on the performance of PEMFC electrodes were recently pointed out by Shin et al. [406] using as solvents butyl-acetate and isopropyl-alcohol. Ink solvents with suitable properties for the formation of fine colloidal dispersions of Nafion favour the deposition of catalytic layers of porous structure for reducing mass transfer resistance and providing good ionomer dispersion for enhanced proton conductivity. These two characteristics are key issues for the preparation of high-performance electrodes.

8.2.3 Preparation and performance of novel MEA with multi catalyst layer structure for PEFC by magnetron sputter deposition technique

Sputter deposition is widely used for integrated circuit manufacturing and has been investigated for the preparation of more effective fuel cell electrodes for more than a decade. The main problem encountered in this technique is how to increase the contact area. Expanding the two dimensional thin film structure of the sputter Pt catalyst layer to a three-dimensional reaction zone provides a feasible solution. This study proposes a novel catalyst layer structure composed of multi two-dimensional active layers. This structure is obtained by depositing a Pt layer by magnetron sputter deposition method on a Nafion–carbon ink layer alternatively in order to attain the required three-dimensional reaction zone. SEM, X-ray, EDS and EPMA analysis were used to characterize microstructures, chemical composition and distributions for the obtained electrocatalyst layers. The correlation of microstructures and operation parameters, such as operating pressure and sputtering time, relating to the electrode performance was investigated. The MEAs consist of a Nafion 117 membrane and a commercial electrocatalyst (20% Pt/C from E-TEK) on cathode side. Results show that three layers of Pt sputter-deposited on the gas diffusion layer provides better performance (324.4 mA/cm^2 at 0.6 V) than sputtering one Pt layer in the same loading, with an activity of 3244 A/g at 0.6 V for ultra-low loading (0.10 mg/cm^2). It demonstrates that the three-dimensional reaction zone causes the effective improvement of performance.

Changing the bias voltage, Pt target current, operating pressure and sputtering time to understand the correlations between the electrode performances and sputter deposition process parameters. Based on our preliminary experimental results, the existence of bias

voltage during the sputtering process might cause the deposited Pt layer to become a dense structure. However, the deposited porous Pt catalyst layer is desired to provide the largest reaction surface area. The bias voltage is thus not applied throughout all the sputtering process. Prior to depositing the Pt layer on the carbon layer, the current needed for drawing forth the Pt plasma was examined. It was noted that the Pt plasma could be obtained at a Pt target current of 0.25 A. This target current is used for all the process. The Pt loading is significantly influenced by both the operating pressure and sputtering time. The higher operating pressure leads to a larger depositing. The EDS results of

Table 8.2.3 Anode activity. EAS area and Pt percentage of prepared MEAs

Sample code	Activity at 0.6V (A/mg Pt)	EAS area (m ² /g Pt)	Pt percentage (%)
1L-B	2.072	80.02	15-16
3L-A	5.047	83.12	4-5
3L-B	3.244	84.14	6-7
3L-C	2.979	84.95	8-9

Table 8.2.4 Process parameters and resulting Pt loadings

Sample code	Process parameters				Pt loading (mg cm ⁻²)	Deposition rate (mgs ⁻¹ cm ⁻²)
	Bias Voltage (V)	Pt target current (A)	Pressure (torr)	Sputtering time (s)		
SP-A	0	0.25	6x10 ⁻³	30	0.065	2.16x10 ⁻³
SP-B	0	0.25	2x10 ⁻²	30	0.112	3.73x10 ⁻³
SP-C	0	0.25	6x10 ⁻³	60	0.130	2.16x10 ⁻³
SP-D	0	0.25	2x10 ⁻²	60	0.227	3.73x10 ⁻³
SP-E	0	0.25	6x10 ⁻³	470	1.024	2.18x10 ⁻³

sample SP-E shown in revealed that the surface of this sample is almost covered by a dense Pt layer. This indicated that a longer sputtering time might obtain a dense and thickened deposited Pt layer. By comparing the results of SEM and EDS for SP-D and SP-E samples, it is apparently inferred that the high operating pressure and short sputtering time are favorable to forming a deposited Pt layer with large porosity. MEAs were operated at 25 °C cell temperature under ambient pressure. The anode catalyst activity is defined as the currents (A) produced by unit mass of electro-catalyst based on the anode loading. The results reveal that the highest anode loading (1.024 mg/cm²) exhibits the best cell performance, while the lower anode loading, i.e. 0.112 mg/cm² (SPB) possesses the highest anode catalyst activity. It can be assumed that the deposited Pt layer must have the porosity, thickness and loading in an appropriate amount in order to gain the highest cell performance and catalyst activity. Among them, the process parameters for the SP-B sample are the best choice. Therefore, we adopt those conditions for SP-B sample to prepare the multi catalyst Pt layer for the studied anode. The anode for 3L-B sample is obtained by depositing a Pt layer by magnetron sputter deposition method on a Nafion–carbon ink layer alternatively three times. The accumulated sputtering time is 30 s. On the other hand, the anodes for both 3L-A and 3L-C samples are also applied with the same approach as in the anode for 3L-B sample. However, the accumulated sputtering time is 18 and 42 s, respectively. The anode for 1L-B sample is obtained by depositing only one Pt layer on a Nafion–carbon ink layer at a sputtering time of 30 s. The cathodes for all MEAs are prepared by the screen-printing method and the loadings are around 0.30 mg/cm². SEM, Xray and EPMA analysis were used to

characterize microstructures, phases and chemical composition for the obtained electrocatalyst layers. 3L-B sample presents no distinctly different layers between carbon and deposited Pt layer, but it is likely to observe a nano Pt layer on the carbon particles in the picture with a zoom of 200,000 times. The grazing incident X-ray diffraction (GID) method is applied to characterize the thin layer on the carbon particles. The characteristic peaks of Pt element [407] are clearly observed at the 2θ of 39.5° and 79.1° . These two peaks exhibit a broaden shape and a relative low intensity. When changed the X-ray incident angle to 2° and 3° the obtained diffraction patterns were the same as that of previous images. When subtracted, the diffraction spectrum for incident angle of 1° from that of the incident angle of 2° and/or 3° , it showed no peak at the spectrum. This indicated that the thin layer on the particles was the Pt layer with a thickness smaller than 50 nm [408,409]. To reinforce this statement, a piece of single crystal silicon wafer with a smooth surface is placed on the same holder with the same sputtering conditions to the GDLs for a sputtering time of 2 min. The resultant Pt/SiO₂ stack is subjected to cross-sectional view SEM imaging to verify the sputter deposited film thickness. The resultant thickness is approximately 70 nm. Therefore, the sputtering thickness increase rate is around 35 nm/min. On the basis of this data, we could infer the thickness of each deposited Pt layer to be around 5.8 nm for the anode of 3L-B sample. Consequently, the thickness of each deposited Pt layer for the anode of 3L-A and 3L-C samples are expected to be 3.5 and 8.2 nm, respectively. For 1L-B sample, the expected thickness of deposited one Pt layer on the uncatalyzed electrode is 17.5 nm. Note that due to the higher roughness of carbon layer than that of single crystal silicon wafer, the actual thickness of deposited Pt layer on the carbon layer is less than the one on the silicon

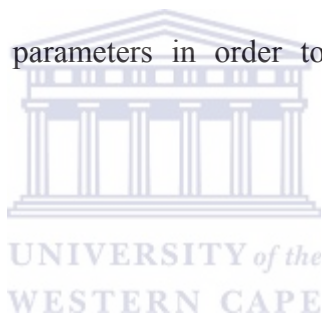
wafer. EPMA analysis is used to examine the composition percentage of Pt and carbon elements on the surface. The results listed in table 8.2.3. show that the anode Pt percentage for both 3L-B and 1L-B samples is almost the same (~16%) in the catalyst layer. The sequence of cell performance is 3L-CN3L-BN3LAN1L-B, indicating cell performance increases with the increasing anode Pt loading. It is worthy to note that the 0.15 mg/cm² anode loading could lead to the current density of 447.2 mA/cm² at 0.6 V. The 3L-B sample presents a higher current density of 117.2 mA/cm² than that of 1L-B sample at 0.6 V. On the other hand, the magnitude sequence of anode catalyst activity for various anode loadings was different from those of the cell performance. The sequence was 3L-AN3L-BN3L-CN1L-B, indicating the anode catalyst activity decreases with the increasing anode loading. The 3L-B sample shows better activity than the 1L-B sample, which contains single Pt layer (Table 8.2.3). The above results reveal that the 3L-B sample exhibits the higher cell performance and utilization efficiency of anode catalyst, while the 1L-B sample with single Pt layer on the anode owns the lowest cell performance and utilization efficiency of anode catalyst. The electro-active surface (EAS) area of our proposed anode is measured using the cyclic voltammetric method and the representative CV profiles. Data for EAS area (m²/g Pt) are listed in Table 8.2.3. Cyclic voltammetric studies from 0.0 to 0.4 V provide information on the hydrogen adsorption and desorption which occurs on the platinum surface. The region from 0.4 to 0.5 V is regarded as the doublelayer region [410]. To evaluate the Pt surface area, the current densities of hydrogen adsorption and desorption were integrated separately and referred to a charge of 210 μC/cm², which corresponds to a mono-layer of hydrogen adsorption on the Pt surface [411]. Apparently, the 3L-C, 3L-B and 3L-A samples have a larger

integrated area than the 1L-B sample. The platinum loading for 3L-B sample is almost the same as that of the 1L-B sample (0.108 mg/cm^2 versus 0.117 mg/cm^2), and thus the true reactive surface area is actually larger, i.e. $84.14 \text{ m}^2/\text{g Pt}$ versus $80.02 \text{ m}^2/\text{g Pt}$, respectively. The anode catalyst activities listed in Table 8.2.2 show the same inference. Although 3L-C sample showed the largest integrated area, however it has the highest platinum loading (0.153 mg/cm^2) thus the EAS area was $84.95 \text{ m}^2/\text{g Pt}$. The EAS areas for all three samples with layer wise Pt catalyst layers structure were larger than that of the E-TEK product ($81.67 \text{ m}^2/\text{g Pt}$) [412].

Comparing the 3L-B and 1L-B two samples, it showed that these two samples possess the identical loading as well as the preparation process and conditions. For the comparison of accumulated thickness, the thickness of Pt layer for 3L-B sample was the same as that of 1L-B sample. The only difference between them was thus the catalyst layer structure. The above results obviously indicated that the catalyst layer with multi nano Pt layer structure enhances the cell performance and utilization efficiency of catalyst. According to the electrode reaction kinetics, the active surface area in the catalyst layer was the key factor to influence the reaction rate. Further suggestion by Haug et al. [413] indicated that the active surface area in the catalyst layer must compose of continuous three-phase of Pt, Nafion and carbon necessary for an active catalyst. Therefore, the improvement was attributed to the higher EAS area provided by the proposed catalyst layer structure. Possible explanation was that the possible reaction area for the ultra low Pt loading with higher EAS area was a similar three-dimensional reaction zone created by the multi nano Pt layer with the assistance of the hot pressing procedure. This three-dimensional reaction zone comprises of a continuous three-phase interface region similar to that proposed by

Haug et al. [413]. Note that the MEA from this literature review had a cell performance exceeding that of similar catalyst layer structure on the GDL proposed by Haug et al. [413]. This is because the application of an appropriate amount of the Nafion solution using the brushing method to each sputtered Pt layer that produces the completely continuous three-phase interface was made. This improved the utilization efficiency of catalyst as well as the overall electrochemical reaction rate, and thus the cell performance. In order to support the above inference, the cell temperature (T_c) and backing pressure (P_b) were changed to observe the change of performance for these two samples 3L-B and 1L-B samples with varying cell temperature and backing pressures, respectively. For the 3L-B sample, the current density is 191.6 mA/cm^2 (at 0.6 V) at the cell temperature of $40 \text{ }^\circ\text{C}$ under ambient pressure. The current density increased to 293.8 mA/cm^2 as the cell temperature increased to $65 \text{ }^\circ\text{C}$, and increases to 324.4 mA/cm^2 when the applied backing pressure reached 100 kPa . By contrast, the current density for the 1L-B sample was only 85.3 mA/cm^2 (at 0.6 V) at the cell temperature of $40 \text{ }^\circ\text{C}$ under ambient pressure. While the cell temperature increased to $65 \text{ }^\circ\text{C}$, the current density increased to 174.6 mA/cm^2 . Further increasing of the backing pressure to 100 kPa caused the current density to increase to 207.2 mA/cm^2 . Comparing the current density at $40 \text{ }^\circ\text{C}$, $65 \text{ }^\circ\text{C}$ and with 100 kPa backing pressure at $65 \text{ }^\circ\text{C}$ between these two samples, it was discovered that the current density for the multi Pt layer structure was always higher than that of the single Pt layer up to 106.0 mA/cm^2 . This result further confirms the inference that multi nano Pt catalyst layer structure extends the reaction area to a continuous three-dimensional reaction zone improving the overall electrochemical reaction rate.

The nano catalyst electrode presented with the high performance and ultra low Pt loading was prepared here by the magnetron sputter deposition techniques. The effective enhancement of performance was attributed to the combination of nano catalyst and the multi Pt catalyst layer structure designed to provide the three-dimensional reaction zone as well as the completely continuous three-phase interface. These improve the intrinsic disadvantage of the two-dimensional coating by sputtering technique. The improvement of overall electrochemical reaction rate enhances the utilization efficiency of catalyst as well as the cell performance. On the other hand, the cell performance is correlated with the process parameter, especially the bias voltage, operating pressure and sputtering time. The electrode with high performance and catalyst activity can be obtained by appropriately selected process parameters in order to achieve the required catalyst porosity, thickness and loading.



8.3 SYNTHESIS AND EXPERIMENTAL PARAMETERS

8.3.1 Catalytic Ink Composition

The catalytic ink preparation involved weighing 0.21 g of the catalyst was in water under magnetic stirring, followed by the addition of 0.71 g of Nafion[®] solution (5 wt.%, 1100 EW, Aldrich) administered drop wise. Thereafter the solvents were added and stirred for 24 hours. The ink was sprayed onto the backing layer (carbon cloth or carbon paper) to the desired catalyst loading using an air brush. The solvents investigated in this study are IPA and BAc, and referred to hereafter as the solution and colloidal methods, respectively. 20%Pt-10%Ru on Carbon (Alfa Aesar) was used as the anode catalyst, whereas 40% Pt on carbon (Alfa Aesar) was used for the cathode. The sprayed backing layer was kept at room temperature for 24 hours, and then dried at 110°C for 1 hour prior to MEA preparation.

The MEA was prepared by the hot pressing procedure as follows: Nafion[®] solution (5 wt.%, 1100 EW, Aldrich) was brushed on one side of the electrode, dried for 30 minutes at room temperature and 1 hour at 80°C in an air oven. The electrodes (backing layer and the catalyst layer) were placed on both sides of a treated Nafion[®] 117 membrane, then the MEA was sandwiched between non-stick Teflon[®] and placed on a hot press for periods ranging from 2-5 min, at temperatures ranging from 100 - 160°C and pressures ranging from 500 – 1500 psi.

Different Nafion[®] percentages (dry weight) were used in the ink preparations ranging from 7% to 40%. The prepared inks were spread on a glassy carbon electrode and dried before use. The catalytic activity (methanol oxidation) was evaluated with cyclic

voltammetry (CV) using a conventional three-electrode system - a Pt basket as counter electrode and a saturated calomel electrode (SCE) as reference electrode. The prepared electrodes were dipped in 1M H₂SO₄/ 1M methanol and scanned in the region of 0-1.5 V at a rate of 20 mV s⁻¹.

It was discovered that 3:1 catalyst to Nafion[®] ratio represents the optimal concentration, which is roughly 14%. The presence of Nafion[®] in the catalyst layer enhanced the conductivity, thus extending the three-phase zone (i.e. increasing catalyst utilization). Furthermore, it was suggested by Chu et al. [359] that Nafion[®] content in the catalyst site affects the kinetics of methanol electro-oxidation by providing the protonic sites, which could promote CO oxidation.

When BAc was used as a solvent, a more viscous ink was formed compared to the ink formed with IPA. The ultrasonic bath proved more effective in an attempt to disperse the catalytic inks followed by magnetic stirring. The inks formed were spread on the backing layer by using a Pasteur pipette or air brushing, depending on the viscosity of the catalytic inks. The hand held air brush gun which was clamped in a standard position to ensure the process could be repeated under similar conditions with reproducible results. The solution method using IPA as the solvent produced the higher performance to the colloidal method using BAc. In the colloidal method the ink formed was thick, and the catalyst layer with this type of ink is thicker than the catalyst layer produced with IPA with similar catalyst loading. Therefore, the mass transfer resistance of methanol is increased in the catalyst layer, thus decreasing cell performance. This was obtained using carbon cloth E-TEK type “A” with 20 % PTFE content, a methanol flow rate 1 ml/min,

an air flow rate 1 l/min, a catalyst loading of 2 mg/cm^2 for both anode and cathode, a cell temperature 80°C , and atmospheric pressure for anode and cathode.

8.3.2 Backing Layers

Different backing layers were investigated for the DMFC mode. All of them are commercially available materials, including E-TEK carbon cloth type “A”, Toray TGP H 120 carbon paper, Electrochem carbon paper and Lydall GDL (gas diffusion layer). The cloth weaves of E-TEK produces a series of relatively large openings, approximately 50 to 100 μm in size. Carbon paper (Toray TGP H 120 and Electrochem) have a structure with a pore size between 20-50 μm , but a large portion of blocked passages. Lydall GDL (Lyflex C494) has very little opening area with most of the surface consisting of blocked passages.

1. ETEK, type “A”, 20% PTFE
2. Lydall Lyflex C494 GDL, 10%PTFE
3. Toray TGP H120, 20% PTFE
4. Electrochem. Carbon Paper, 35% PTFE

The PTFE mat area has small openings compared to the bare Toray paper. The open channels presumably act as liquid flow channels, while the PTFE mat acts predominantly as gas flow channels. Increasing the PTFE content reduces the number of open channels, which negatively influences liquid flow.

1. Toray TGP H120, 0% PTFE
2. Toray TGP H120, 20% PTFE
3. Toray TGP H120, 60% PTFE

The optimal PTFE content is around 20%, where liquid and gas (CO_2) flow are in separated channels. With a bare TGP H 120 paper (0% PTFE) there are no channels for CO_2 evolution, whereas with high PTFE loading (60%), the liquid channels were blocked. Furthermore, at high PTFE loading there was conductivity loss within the electrode, therefore, the cell performance was affected by significant electrical losses.

The cell performances with carbon cloth were much better than with carbon paper, which was attributed to the nature of the backing layers. In the visualization studies [360], it was found that in the case of carbon paper, large CO_2 slugs (groups of bubbles) were formed with a size of 0.8-1.8 mm, and these bubbles tend to attach themselves to the surface of the paper. The CO_2 bubbles formed remain attached at the point of generation and accumulate. After 3 minutes these bubbles completely block the channels resulting in a deterioration of cell performance. In the case of the carbon cloth, the CO_2 bubbles are relatively small (0.6-0.8 mm) and which have a tendency to coalesce and form bubble agglomerates. Since the carbon cloth has lower friction characteristics, bubbles tend to attach to the flow channels. This property of carbon cloth is advantageous, allowing the surface to be relatively clear and free from bubbles. The carbon cloth surface properties were superior resulting in a better cell performance due to the enhanced gas management in the cell.

8.3.4 Influence of Operating Parameters on Cell Performance

The operating parameters, namely, cell temperature, cathode pressure, air flow rate, etc. affect cell performance. Since a temperature range of 100 - 160°C was used in MEA preparation, where temperatures above 130°C is the glass transition temperature of Nafion[®], where it will lose water, thereby significantly reducing its characteristic ion conductivity ability, the MEA must be conditioned to restore the water in Nafion[®], prior to evaluating cell performance. The conditioning of the MEA was investigated by circulating methanol in the anode side at 80°C at open circuit potential for several hours. 72 hours were necessary to restore water (fully hydrated) to the membrane. After 72 hours, the cell performances were constant. This was conducted with E-TEK type “A” carbon cloth, 20 % PTFE as a backing layer, a 1 ml/min methanol flow rate, a 1 l/min air cathode flow rate, cell temperature 80°C and with anode and cathode at atmospheric pressure. An alternative moisturizing technique employed was not as time consuming it involved heating the MEA in water for 30 min at 80°C before connection in the cell.

The MEA moisturized at 80°C before connection to the cell gave better results than moisturizing in the cell for 8 hours. However, heating the MEA in water, is not a good way of moisturizing, since Nafion[®] polymer (Nafion[®] 117) when soaked in water loses its flat appearance seemingly bending out of shape. This deformation of the polymer is not predicted, and will de-laminate the electrodes from the membrane, which leads to a decrease in cell efficiency. This method can be used efficiently if an appropriate holder is used during moisturizing.

Increasing the catalyst loading will increase the thickness of the electrode. Therefore, the cell performance will suffer from mass transport limitations. With a thick electrode, methanol cannot enter the entire electrode structure, whereas CO₂ cannot escape from the electrode.

The influence of temperature on cell performance was investigated. Two factors were identified: firstly, an increasing temperature will increase membrane conductivity, thus reducing ohmic losses, and secondly enhance methanol oxidation. The best performances were obtained with a temperature of 80°C. This temperature is optimal for Nafion[®] 117. However, at 90°C, the cell performance starts to deteriorate, due to membrane dehydration, where the membrane starts to lose water, thereby increasing resistance. The methanol flow rate was 1 ml/min, air flow rate 1 l/min, catalyst loading 2 mg/cm² and atmospheric pressure for both anode and cathode.

The influence of cathode air flow rate was investigated with a cell constituted of E-TEK carbon cloth type “A” with 20% PTFE, IPA as the ink solvent, and the following cell operating parameters: methanol flow rate 1 ml/min, cell temperature 80°C, catalyst loading around 2 mg/cm² and atmospheric pressure for anode and cathode.

Equipment Validation

In addition to the routine testing and analysis, a series of validation tests were performed on the test equipment.

The test equipment and components were validated prior to use. The objective of the validation was to ensure that the equipment was operating at a level of confidence that the equipment was operating under a state of control. The minimum / maximum operating ranges were validated, of the temperatures, air pressures, water pressures and flow rates. The parameters assessed were the most appropriate challenge conditions, effective ranges of critical parameters and worst case scenarios.



8.4 RESULTS AND DISCUSSION

The results of the parameters challenged during the preparation of the Catalytic Ink (CI), MEA and Fuel Cell Operating conditions will be discussed. Once these parameters had been identified, they will be adhered to when fabricating the MEAs consisting of the in-house catalysts. The electrodes for the MEA will be prepared using the most active in-house catalysts identified in the previous chapters and Nafion 117 will be used as the proton conducting membrane. The catalytic activity will be compared against that of the commercially available catalyst, incorporated into the MEA fabricated under similar conditions.

8.4.1 Solvents

BAC as a solvent, produced an ink that was thick and an ultrasonic bath was used instead of magnetic stirring to disperse the catalytic ink content. The applicators used to spread the catalytic ink on the backing layer were plastic origin and stainless steel. Figure 8.1.1 shows the cell performance with the solvents, namely IPA and BAC. The solution method using IPA as the solvent produced the higher performance to the colloidal method using BAC. In the colloidal method the ink formed was thick, and the catalyst layer with this type of ink is thicker than the catalyst layer produced with IPA with similar catalyst loading. Therefore, the mass transfer resistance of methanol is increased in the catalyst layer, thus decreasing cell performance. Figure 4.1.1 was obtained by using carbon cloth E-TEK type “A” with 20 % PTFE content, a methanol flow rate 1 ml/min, an air flow rate 1 l/min, a catalyst loading of 2 mg/cm^2 for both anode and cathode, a cell temperature 80°C , and atmospheric pressure for anode and cathode.

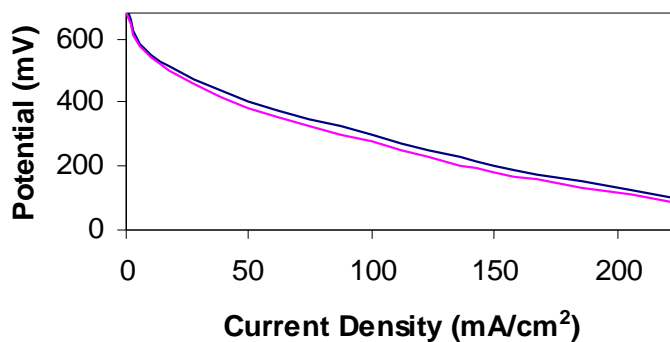


Fig. 8.1.1 Solvent use in CI preparation, blue: IPA and pink: Butyl Acetate

8.4.2 MEA Preparation

For the MEA parameter optimization, the Nafion electrolyte membrane, a commercial membrane produced by the DuPont Company, has been used as a high proton conductivity electrolyte for PEMFC. The electro-catalyst used to determine and optimize the parameters was the commercially available JM (20% Pt). Once these optimum parameters are identified the most active in-house catalyst, previously identified, will be tested in an MEA preparation. The optimization of the MEA structure cannot only reduce the electrical potential drop or resistance within the cell but can also provide good contact at the three-phase region [362-365]. Several researchers have performed research on materials and cell assembling techniques to decrease these resistances [366-371]. The activity of the electro-catalyst can also be enhanced by decreasing the active metal crystal size, which requires an efficient preparation method that can distribute the smaller amount of active metal uniformly over the support [365,372-377]. This directly

influences the activation of reactant gases reacting on the electrodes. One way to promote good contact within the three-phase region that can enhance the cell performance is through the hot-pressing process [362,365,378–382]. The hot-pressing technique has been used to fabricate MEA, and various conditions for hot pressing have been employed by researchers [362,363,383,378,384].

The full factorial design of experiment is a method widely used to determine the minimum number of experimental sets required and also to obtain the influence of parameters on the output or response of the process studied. In this work, three main MEA hot-pressing parameters, i.e. pressure, time and temperature were systematically studied. The full factorial analysis described in Montgomery [385] was the main analytical method used to find the significance of parameters. Here, optimum conditions for the hot-pressing process were determined making reference to the full factorial analysis described by Montgomery [385].

8.4.3 Time and Pressure effect on MEA preparation

A major loss in the MEA performance may be attributed to ohmic loss due to both the electrical resistance of the electrodes and the ionic resistance at the interface and in the electrolyte. Compressive pressure and temperature in the MEA fabrication process are two significant parameters affecting the ionic resistance at the interface. The conductive layers of the MEAs fabricated at high hot-pressing temperature and pressure were hard to observe, unlike those fabricated at low temperature and pressure. The conducting layer plays an important role in passing ions created at the electrode surface to the electrolyte

membrane. The drop in cell performance was due to the loss of the conducting layer. The above results show the trend and the effect of hot-pressing parameters on the cell performance at the low and high ends of the parameters. Since a short hot-pressing time was more preferable than a high value, the hot-pressing time was further reduced from 2 min to 1 min at 1500 psi and 100 °C condition. From Fig. 8.2.1, the MEA fabricated at 1500 psi and 100 °C for 2 min gave the best performance (highest power density of 72mWcm^{-2}). The shorter hot-pressing time of 1 min was not suitable since the short hot-pressing time is insufficient to soften the electrodes and the electrolyte membrane, so the electrode cannot penetrate sufficiently into the electrolyte membrane.

As a result, the hot-pressing time of 1 min MEA might not have enough active area for reaction. However, a long hot-pressing time could cause low-porosity in the gas diffusion layer and the electrode. Thus a hot-pressing time of 2 min was the most appropriate and was used for the next study. Here the purpose of using full factorial analysis was to identify key parameters for the hot-pressing process. However, the only significant parameter found was temperature, while others were equally less significant.

Further investigation of the suitable temperature and pressure was conducted by selecting the conditions at the average values between the low and high levels. Hot-pressing conditions at the pressure of 1000 psi for both 100 and 160 °C with 2 min of hot-pressing time were additionally tested. Then a comparison of the performance of the cells prepared under the three compressive pressures at 100 and 160 °C is illustrated in Fig. 8.2.2. The 1000 psi for an MEA was found to be the best hot-pressing pressure for both low and high hot-pressing temperatures.

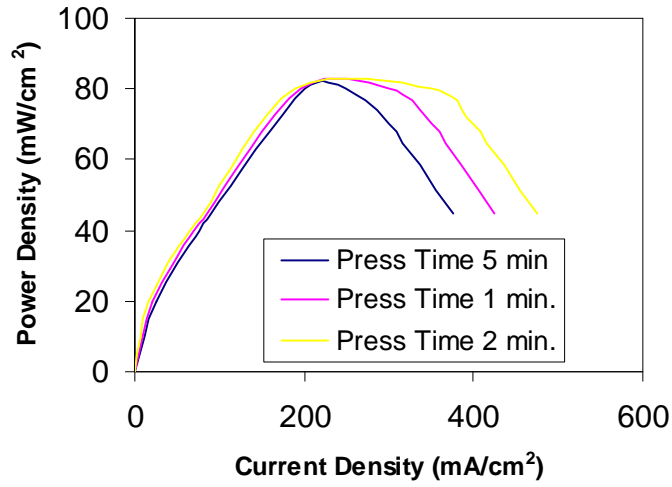


Fig. 8.2.1 Effect of hot pressing time on power density curves of MEAs fabricated at 1500psi and 100°C

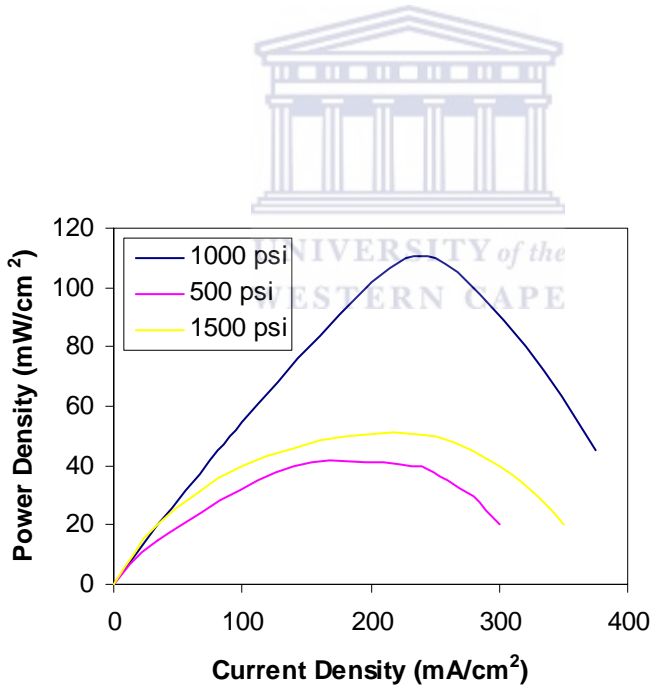


Fig. 8.2.2 Effect of hot pressing pressure on power density curves of MEAs fabricated at 100°C.

8.4.4 Temperature Effect on MEA preparation

After the suitable pressure was selected, the effect of hot-pressing temperature was investigated, and the results are shown in Fig. 8.2.3. Three MEAs, prepared at a pressure of 1000 psi and a 2 min hot-pressing time while using temperatures of 100, 130 and 160 °C, produced similar power outputs to the previous runs. The most suitable hot-pressing temperature found was 100 °C. The most effective MEA hot-pressing conditions, was found to be 1000 psi, 100 °C and 2 min.

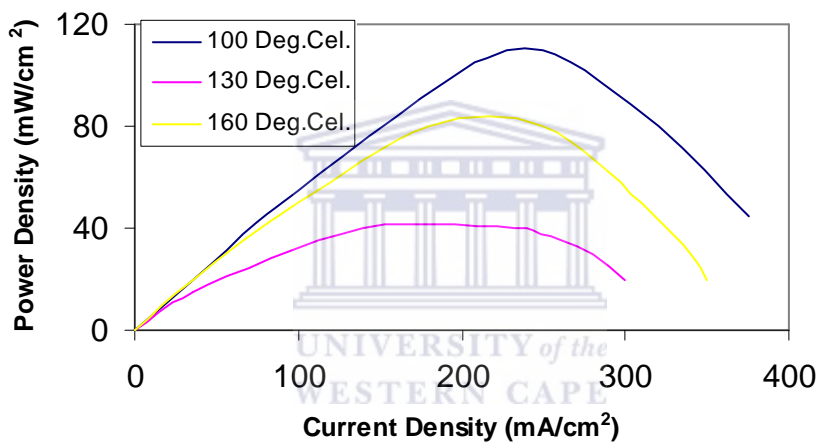


Fig. 8.2.3 Optimization of hot-pressing temperature on polarization of MEAs fabricated under 1000 psi for 2 min.

8.4.5 Cathode Air-Oxygen Feed Determination

After identifying the parameters which may be critical in producing a suitable MEA, the cathode air and oxygen optimum pressure was determined.

Figure 8.2.3.2 shows the influence of cathode pressure on cell performance. As can be seen, increasing the cathode pressure increased cell performance. Usually high performance cells are obtained with a cathode pressure of 2 bar. Increasing the cathode cell pressure will increase the cell performance as was demonstrated by Ren *et al.* [361] where an air pressure of 3 bar and an oxygen pressure of 5 bar were used. Figure 8.2.3.2 was obtained using a cell constituted of Toray TGP H 120 paper with 20% PTFE, IPA as the catalytic ink solvent, and the following cell operating parameters: methanol flow rate 1 ml/min, cell temperature 80°C, catalyst loading around 2 mg/cm² for anode and cathode, and atmospheric pressure for the anode and cathode was changed using a needle valve at the exhaust.

Figure 8.2.3.1 shows cell performance with air and oxygen. The cell operating parameters were as follows: E-TEK carbon cloth type “A” with 20% PTFE, IPA as the ink solvent, a methanol flow rate 1 ml/min, cathode gas flow rate 1 l/min, cell temperature 80°C, catalyst loading around 2 mg/cm² for anode and cathode, and atmospheric pressure for the anode and cathode.

As can be seen, using oxygen is an attractive way to maximize the power output due to the minimizing of ORR losses. Furthermore, the mass transfer resistance at the cathode is increased when using air, due to the presence of a blanket of nitrogen. However, from an

operational point of view, using neat oxygen is not practical and air fed cathodes is the most realistic option for terrestrial applications.

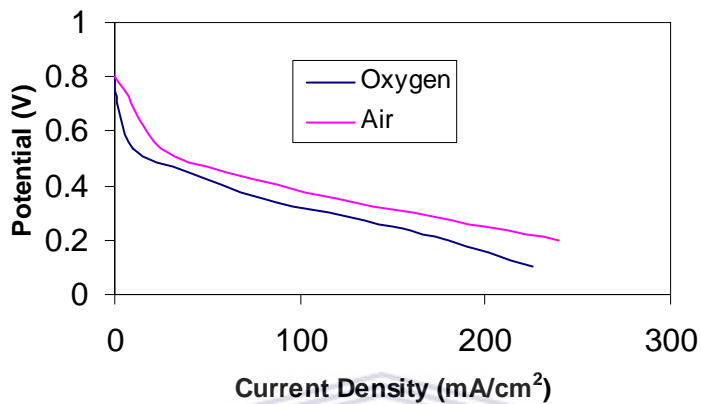


Fig.8.2.3.1 The effect on current density using different cathode feeds

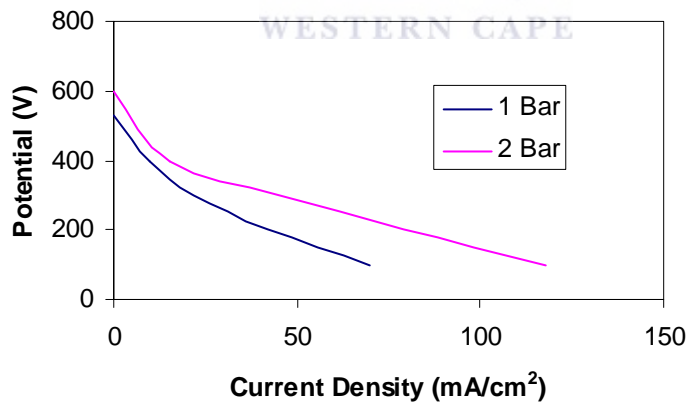


Fig.8.2.3.2 Influence of air cathode pressure on cell performance at 80°C, Nafion 117 as the membrane

8.4.6 MEA Performance: In-house Catalysts vs. Commercial Catalysts

Since the PEMFC performance of all MEAs made in our laboratory was found to be relatively low compared to the recent published values, the reliability of the hot-pressing process and cell testing was then verified. The best hot-pressing conditions obtained (1000 psi, 100 °C and 2 min) were utilized to fabricate an MEA with Pt loading of 0.5 mg cm⁻², the same loading of a commercial MEA. The performances of the in-house and that of the commercial MEA were found to be similar where the performance of the in-house MEA was slightly higher than that of the commercial one. This result confirms that a condition of 1000 psi, 100 °C and 2 min was the most suitable hot-pressing condition for MEA fabrication for PEMFC.

In addition, these optimum conditions were applied to fabricate MEAs consisting of the same Pt loading for in-house as well as the commercial catalyst. The parameters were similar for the hot-pressing process and cell testing.

The MEAs were prepared using the following catalysts:

1. Quaternary catalyst consisting of Platinum, Ruthenium, Molybdenum and Iron.
2. Ternary catalyst consisting of Platinum, Ruthenium and Iron.
3. Bi-metallic catalyst consisting of Platinum and Ruthenium.
4. Commercially available catalyst consisting of Platinum and Ruthenium.

The catalysts (Quaternary, Ternary and Bi-metallic) were previously identified as the best performing catalysts, in each category, during methanol oxidation studies using an electrochemical 3-electrode test cell (Chapters 4-7).

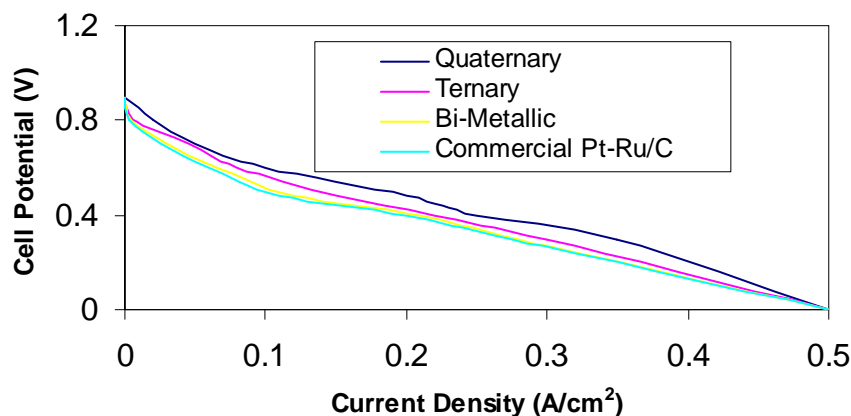


Fig. 8.3.1 Polarization curves for in-house and commercial catalyst containing MEAs at 80°C under atmospheric pressure.

As with the cyclic voltammetric analysis, the polarization curves fig. 8.3.1, are in agreement with the activity and catalytic performances. The quaternary catalyst containing MEA produced the highest energy output for the potential range investigated, 0-1.0V, followed by the ternary and bi-metallic catalysts containing MEAs. The performance of the commercially available catalyst was in the range of the in-house bi-metallic and ternary catalysts containing MEAs. In the current density range of 0.08 – 0.13A/cm² the ternary MEA performed slightly higher with respect to the current density, compared to the rest of the MEAs. It can also be noted that although there was a steady decline by the ternary catalyst containing MEA, there was a noticeable drop in performance by the remaining 3 MEAs in this region. The Quaternary catalyst containing MEA had slight increases in performance in the current density regions of 0.1-0.25 and 0.25-0.48 A/cm².

CHAPTER 9

CONCLUSIONS AND RECOMMENDATIONS FOR FUTURE RESEARCH

Different approaches were used to prepare the Pt/C catalyst. High temperatures proved to be very effective in effecting a fast but uncontrollable catalytic particle growth rate. Sub ambient temperatures proved to be the most effective when controlling the particle size and maintaining the particle size distribution to be as narrow as possible. Formaldehyde, formic acid and hydrogen were reducing agents that were examined in addition to varying other synthesis procedures as can be seen in chapter 4. These parameters were summarized in tables 4.5.1 and 4.5.2. The methods producing the most effective ECA catalysts in chapter 4 were continuously advanced and explored in chapters 5,6 and 7. The most effective ECA catalysts were defined and characterized by well dispersed, having a narrow particle size distribution and subsequent high surface area of nano-sized catalytic particles. After a series of trials including different catalyst preparation methods the most effective method from chapter 4 producing the most active ECA catalyst was used in the bi-metallic catalyst preparation. The mono-metallic catalysts are generally regarded as cathode catalysts and do not possess the properties allowing them to prevent or remove CO from poisoning the platinum active sites. Therefore the methods developed in chapter 4 allowed the core structure of platinum (fcc) to be formed and these methods were even further developed in chapters 5 to 7 where this core structure of platinum was formed with interstitial inclusions of non-noble metal atoms, possessing OH adsorption properties to enhance or facilitate water oxidation and subsequent CO

removal adsorbed onto platinum atoms. In chapters 5 to 7 the interstitial inclusions of non-noble metal atoms were strategically placed within the platinum structure with its added function mentioned above simultaneously allowing the catalyst to be an effective ECA catalyst for methanol oxidation. In effect the platinum oxidizes the methanol, the second, third and fourth metals function as CO removal entities and the multi-metallic collective function in a mass activity with a significantly increased number of active sites to perform these functions as high surface area nano-sized catalytic particles.

The catalytic ability of ruthenium proved invaluable as the second metal in the bi-metallic catalyst performance. After analyzing the characterization and ECA results for bi-metallic (Pt/Ru) catalysts the overall conclusion and findings were synonymous with that of the monometallic catalyst (Pt/C). Like the monometallic catalyst the most effective and ECA catalysts were the ones characterized by well dispersed, having a narrow particle size distribution and subsequent high surface areas. These methods were then used to pave the way for the numerous trials to establish the synthesis procedures for the most ECA multi-metallic catalysts (Ternary and Quaternary catalysts).

The most active catalysts were distinguished as catalysts C5 (Ternary) and D7 (Quaternary) were in each category those showing the highest ECA. The electrochemical activity (ECA) was established as the current density $I(\text{A}/\text{cm}^2)$, and recorded (Chapters 6 and 7) as $1,00 \times 10^{-3}(\text{A}/\text{cm}^2)$ and $6,023 \times 10^{-3}(\text{A}/\text{cm}^2)$ for the ternary and quaternary catalysts respectively. The order of magnitude with regards to the ECA for the best catalyst in each category was: $D7 > C5 > B5 > A8$ (See below)

Quaternary Catalyst **D7** (Pt/Ru/Fe/Mo)/MWCNT > Ternary Catalyst **C5** (Pt/Ru/Fe)/MWCNT > Bi-metallic Catalyst **B5** (Pt/Ru)/MWCNT > Mono-metallic Catalyst **A8** (Pt/Vulcan XC72).

9.1 Mono-metallic catalysts

- 9.1.1 Formaldehyde proved to be the best reducing agents by producing the most EC active catalyst, A8, for methanol oxidation followed by formic acid, catalyst A2. (Refer to table 4.5.1).
- 9.1.2 At temperatures below 22 °C catalysts formed with formaldehyde as the reducing agent are the most electrochemically active. (Table 4.5.2)
- 9.1.3 Temperature programmes including low temperature formaldehyde catalysts (LTF catalysts) are able to produce nano- sized particles in the range 1,5 to 3nm's. (Table 4.5.2) therefore does possess a larger electrochemically active surface area with respect to its formation of nano-sized particles and narrow particle size distribution.
- 9.1.4 The LTF catalysts supported on Vulcan XC72 have similar electrochemical activity to commercially available JM catalysts.

9.2 Bimetallic catalysts

- 9.2.1 The bimetallic catalyst B5 synthesized can be used for methanol oxidation as it proved effective in the removal of CO. (refer to table 5.5.1)
- 9.2.2 Catalyst B5, synthesized via the variable-temperature programmed method does possess a larger electrochemically active surface area with respect

to its formation of nano-sized particles and narrow particle size distribution.

9.2.3 Catalyst B5 showed significantly higher electrochemical activity compared to the JM catalysts.

9.2.4 B5 has properties such as CO tolerance which allowed the catalyst to perform slightly more effectively than the JM catalyst during the chronological amperometrical (CA) analysis (Fig. 5.4.4.6).

9.2.5 Pretreated MWCNT proved to be the most EC active support for the binary catalyst compared to Vulcan XC72. (Refer 5.5.1)

9.3 Ternary catalysts

9.3.1 The ternary catalyst C5 proved to be the most effective ternary catalyst for methanol oxidation (Refer to table 6.5.1.1).

9.3.2 Catalyst C5 possess a large electrochemically active surface area with respect to its narrow particle size distribution and increased mass activity (Refer to table 6.5.1.1).

9.3.3 The ternary catalyst C5 showed similar electrochemical activity to JM catalysts and has properties which allow the catalyst to perform better during the chronological amperometrical (CA) analysis (fig. 6.4.4.6).

9.3.4 MWCNT proved to be the most EC active support for the ternary catalyst compared to Vulcan XC72 (Refer to table 6.5.1.1).

9.4 Quaternary catalysts

9.4.1 The quaternary catalyst D7 synthesized can be used for methanol oxidation.

- 9.4.2 The quaternary catalyst D7 does possess a large electrochemically active surface area with respect to its narrow particle size distribution.
- 9.4.3 The quaternary catalyst D7 showed significantly higher electrochemical activity to the JM catalyst and has properties which allow the catalyst to perform better during the chronological amperometrical analysis.
- 9.4.4 MWCNT has proven to be the most active and effective quaternary catalyst support.
- 9.4.5 NaBH_4 as a reducing agent has proven effective producing high EC activity for Fe containing catalysts by maintaining the prerequisite particle size of $< 3\text{nm}$.



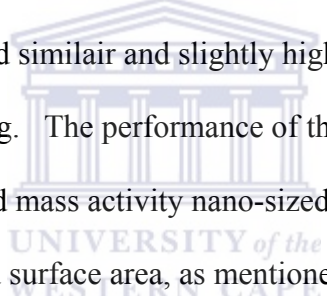
9.5 Fuel Cell Application and Testing

- 9.5.1 The significance or importance of hot-pressing parameters on PEMFC performance was observed. The suitable or suggested condition to hot-press MEAs for PEMFCs was achieved by using a design of experiment method. An analysis of the three main hot-pressing parameters to fabricate MEA for PEMFC supports temperature as the most significant parameter, followed by pressure, time–temperature interaction and pressure–time–temperature interaction. The analysis of the three-phase region confirmed that the unsuitable hot-pressing conditions caused a thinning of the conductive layer and a deep embedding of catalyst into the electrolyte membrane. In the range of parameters studied, the MEA prepared at a hot-pressing condition of 1000

- psi, 100 °C and 2 min resulted in the highest power density of PEMFC.
- 9.5.2 Nafion® provides the necessary conductivity to the electrodes, thus enhancing catalyst utilization by extending the three-phase zone. A 14 wt.% Nafion® content in the electrode, which corresponds to a ratio of 3:1 (catalyst to Nafion®) was found to be optimal.
- 9.5.3 The characteristic composition of the catalytic depends on the solvent. IPA ($\epsilon = 18.30$) formed a diluted suspension, while BAc ($\epsilon = 5.01$) formed highly dense colloidal agglomerations. Cell performance was found to be better with solution ink than with colloidal ink, due to the high electrode resistance.
- 9.5.4 From the commercially available backing layers tested in this study, E-TEK type “A” was found to be the most suited for DMFC application. The CO₂ bubbles attached to the Toray TGP H 120 carbon paper, forming agglomerates of bubbles which blocked the electrode. Electrochem and Lydall Lyflex were the least suited for DMFC application due to the high PTFE loading and the high friction in the former and cathode flooding in the latter. To avoid a two-phase flow, CO₂ bubbles moving counter-currently to liquid methanol, PTFE needs to be added to the electrode. A concentration of 20% was found to be optimal to create discrete paths for CO₂ to move out from the electrode.
- 9.5.5 During the MEA fabrication process the membrane was subject to drying. Therefore, after fabrication and prior to cell testing, water must be restored to the membrane. Circulating water through the anode cell for 72 hours was found to be the most adequate way to restore water, thus high performance can be achieved.

The temperature when increased to 80°C, enhanced cell performance due to the increased membrane conductivity and methanol oxidation. However, above 80°C cell performance starts to deteriorate due to membrane dehydration.

9.5.6 Increasing the cathode pressure enhanced cell performance. However, from a DMFC application point of view, high pressure is not a realistic option. Pure oxygen at the cathode produces better results than air, but for DMFC commercialization, air at the cathode is the most desirable. The optimal operating conditions were found to be: 1 ml/min methanol flow rate, 1 l/min cathode flow rate and it is preferable to preheat the methanol before entering the cell. Carbon cloth proved to be the most suitable backing layer for DMFC application. The in-house catalysts showed similar and slightly higher performances at times during the fuel cell testing. The performance of the in-house catalyst can be attributed to the increased mass activity nano-sized particles in the region of 2nm, and subsequent increased surface area, as mentioned earlier.

The logo of the University of the Western Cape is centered in the background of the text. It features a classical building facade with a pediment and columns, with the text 'UNIVERSITY of the WESTERN CAPE' overlaid in a light blue color.

RECOMMENDATIONS FOR FUTURE WORK

1. The metal concentrations used previously in this research were in support of mass activity with an increased number of active sites where as in future the concentrations of the metal combinations could be varied and the optimum ratio could be determined.
2. Use an inert synthesis atmosphere, ie. Ar or N₂ to determine the influence oxide formation has on the ECA and if the quantity of oxides can be prevented and controlled. The use of inert gases and the structural effect inert gases would have on the crystallization, lattice structures and alloying processes could be examined.
3. Use formic acid as a reducing agent at sub-ambient temperatures. Determine the effect formic acid would have on the reduction of metals (noble and non-noble). The formation of by products and impurities during formaldehyde and formic acid reduction by IR or GC-MS and how does this affect the ECA of the catalysts.
4. Determine the crystal growth variations using different stirring speeds, volumes and shapes of reactor vessels.
5. Study the surface morphology of the supports and explore the modified MWCNT.
6. Use BET to determine the actual surface area of the catalysts synthesized.
7. Perform CO-Stripping CV electrochemical analysis on the catalysts synthesized.
8. Improve the existing purification techniques employed in this research.
9. Explore crystal growth at temperatures lower than the sub-ambient temperature of 4°C used, and determine if nuclei formation can be accomplished at even lower surface energies.

REFERENCES

- [1] E.S. Goodstein, Economics and Environment, Upper Saddle River, NJ, Prentice Hall, 1999
- [2] M.G.L. Santarelli, M. Cali, A. Bertonasco, Energy Conversion and Management 44 (2003) 2353-2370
- [3] L. Carrette, K.A. Friedrich, U. Stimming, Fuel Cells 1 (2001) 5-39
- [4] K.V. Kordesch and G.R. Simader, Chem. Rev. 95 (1995) 191-207
- [5] J.W. Raadschelders and T. Jansen, J. Power Sources 96 (2001) 160-166
- [6] D.M. Bernardi, M.W. Verbrugge, AIChE Journal 37 (8) (1991) 1151-1163
- [7] S.J. Shin, J.K. Lee, H.-Y. Ha, S.-A. Hong, H.-S. Chun, I.-H. Oh, J. Power Sources 106 (2002) 146-152
- [8] M. Uchida, Y. Aoyama, N. Eda, A. Ohta, J. Electrochem. Soc. 142 (1995) 463-468
- [9] J.S. Yi and T.V. Nguyen, J. Electrochem. Soc. 146 (1999) 38-45
- [10] D. Chu and R. Jiang, J. Power Sources 80 (1999) 226-234
- [11] R.W. Glazebrook, J. Power Sources 7 (1982) 215-256
- [12] M.J. Schatter, in Fuel Cells, G.J. Young (Ed.), Vol. 2, Reinhold, New York, 1983, p. 290
- [13] K. Tamura, T. Tsukui, T. Kamo, T. Kudo, Hitachi Hyoron 66 (1984) 135-138
- [14] K.R. Williams, An Introduction to Fuel Cells, Elsevier, 1966, p. 152
- [15] C. Lamy, E.M. Belgsir, J.-M. Léger, J. Appl. Electrochem. 31 (2001) 799-809
- [16] K. Kordesch and G. Simader, Fuel cells and their Applications, VCH, Weinheim, 1996
- [17] J.N. Murray and P.G. Grimes, in Fuel Cells, American Institute of Chemical

References

- Engineers, New York, 1963, p. 57
- [18] L.K. Verma, *J. Power Sources* 86 (2000) 464-468
- [19] M. Mench, S. Boslet, S. Thynell, J. Scott, C.Y. Wang, in *Direct Methanol Fuel Cells*, S. Narayanan, T. Zawodzinski, S. Gottesfeld (Eds.), PV 2001-4, The Electrochemical Society Proceeding Series, Pennington, NJ, 2001, p. 241
- [20] J. Larminie and A. Dicks, *Fuel Cell Systems Explained*, Wiley, Chichester, 2000
- [21] J.-M. Léger, *J. Appl. Electrochem.* 31 (2001) 767-771
- [22] Z. Qi and A. Kaufman, *J. Power Sources* 110 (2002) 177-185
- [23] K. Scott, W.M. Taama, P. Argyropoulos, *J. Appl. Electrochem.* 28 (1998) 1389-1397
- [24] D. Chu and S. Gilman, *J. Electrochem. Soc.* 141 (1994) 1770-1773
- [25] A. Argyropoulos, K. Scott, W.M. Taama, *J. Appl. Electrochem.* 29 (1999) 661-669
- [26] S. Surampudi, S.R. Narayanan, E. Vamos, H. Frank, G. Halpert, A. LaConti, J. Kosek, G.K. Surya Prakash, G.A. Olah, *J. Power Sources* 47 (1994) 377- 385
- [27] M. Hogarth, P. Christensen, A. Hamnett, A. Shukla, *J. Power Sources* 69 (1997) 113-124
- [28] C. Lim and C.Y. Wang, *J. Power Sources* 113 (2003) 145-150
- [29] M.P. Hogarth and T.R. Ralph, *Platinum Metals Rev.* 46 (4) (2002) 146-164
- [30] P. Argyropoulos, K. Scott, W.M. Taama, *Electrochim. Acta* 44 (1999) 3575-3584
- [31] J. Nordlund, A. Roessler, G. Lindbergh, *J. Appl. Electrochem.* 32 (2002) 259-265

References

- [32] X. Ren and S. Gottesfeld, *J. Electrochem. Soc.* 148 (2001) A87-A93
- [33] J.C. Amphlett, B.A. Peppley, E. Halliop, A. Sadiq, *J. Power Sources* 96 (2001) 204-213
- [34] Z.H. Wang, C.Y. Wang, K.S. Chen, *J. Power Sources* 94 (2001) 40-50
- [35] S.R. Narayanan, A. Kindler, B. Jeffries-Nakamura, W. Chun, H. Frank, M. Smart, T.I. Valdez, S. Surampudi, G. Halpert, J. Kosek, C. Cropley, in *Proceedings of 11th Annual Battery Conference on Applications and Advances*, Long Beach, Calif., Jan. 9-12, 1996, p. 113-122
- [36] M.W. Mench and C.Y. Wang, *J. Electrochem. Soc.* 150 (2003) A79-A85
- [37] V.C.Y. Kong, F.R. Foulkes, D.W. Kirk, J.T. Hinatsu, *Int. J. Hydrogen Energy* 24 (1999) 665-675
- [38] V. Raman, in *fuel cell power for transportation*, J. Seaba, R. Stobart (Eds.), Society of Automotive Engineers, Vol. 4, Warrendale, PA, 1999, p. 2
- [39] R.G. Ding, G.Q. Lu, Z.F. Yan, M.A. Wilson, *J. Nano. Nanotechno.* 1 (2001) 7-19
- [40] F.L. Darkrim and D. Levesque, *J. Phys. Chem. B* 104 (2000) 6773-6776
- [41] F.L. Darkrim, P. Malbrunot, G.P. Tartaglia, *Int. J. Hydrogen Energy* 27 (2002) 193-202
- [42] A.C. Dillon, K.M. Jones, T.A. Bekkedahl, C.H. Kiang, D.S. Bethune, M.J. Heben, *Nature* 386 (1997) 377-379
- [43] A. Züttel, P. Sudan, Ph. Mauron, T. Kiyobayashi, Ch. Emmenegger, L. Schlapbach, *Int. J. Hydrogen Energy* 27 (2002) 203-212
- [44] S.M. Lee, J.H. Kim, H.H. Lee, P.S. Lee, J.Y. Lee, *J. Electrochem. Soc.* 149 (2002) A603-A606

References

- [45] V. Guther and A. Otto, *J. Alloys and Compounds* 293-295 (1999) 889-892
- [46] G. Sandrock and R.B. Bowman Jr., *J. Alloys and Compounds* 356-357 (2003) 794-799
- [47] J.M. Ogden, M.M. Steinbugler, T.G. Kreutz, *J. Power Sources* 79 (1999) 143-168
- [48] K. Ledjeff-Hey, V. Formanski, Th. Kalk, J. Roes, *J. Power Sources* 71 (1998) 199-207
- [49] C.E. Borroni-Bird, *J. Power Sources* 61 (1996) 33-48
- [50] EA Engineering, Science, and Technology, Inc. Report: "Methanol Refueling Station Costs", Prepared for the American Methanol Institute, February 1, 1999
- [51] K.-A. Adamson and P. Pearson, *J. Power Sources* 86 (2000) 548-555
- [52] K. Takahashi, N. Takezawa, H. Kobayashi, *Appl. Cat.* 2 (1982) 363-366
- [53] N. Takezawa, H. Kobayashi, Y. Kamegai, M. Shimokawabe, *Appl. Cat.* 3 (1982) 381-388
- [54] J.C. Amphlett, M.J. Evans, R.F. Mann, R.D. Weir, *Can. J. Chem. Eng.* 63 (1985) 605-611
- [55] C.J. Jiang, D.L. Trimm, M.S. Wainwright, N.W. Cant, *Appl. Cat. A* 93 (1993) 245-255
- [56] K. Kochloefl, L.H. Lunsford, J.B. Hansen, J.H. Sinfelt: in *Handbook of Heterogeneous Catalysis, Energy-Related Reactions*, G. Ertl, H. Knozinger, J. Weitkamp (Eds.), Volume 4, Wiley-VCH, Weinheim, 1997
- [57] B. Emonts, J.B. Hansen, S.L. Jørgensen, B. Höhlelein, R. Peters, *J. Power Sources* 71 (1998) 288-293
- [58] H.G. Duesterwald, B. Höhlelein, H. Kraut, J. Meusinger, R. Peters, U. Stimming,

References

- Chem. Eng. Technol. 20 (1997) 617-623
- [59] J.P. Breen and J.R.H. Ross, *Catalysis Today* 51 (1999) 521-533
- [60] M.L. Cubiero and J.L.G. Fierro, *J. Catalysis* 179 (1998) 150-162
- [61] S. Velu, K. Suzuki, T. Osaki, *Catal. Lett.* 62 (1999) 159-167
- [62] J. Agrell, K. Hsselbo, K. Jansson, S.G. Jaras, M. Boutonnet, *Appl. Catal. A* 211 (2001) 239-250
- [63] L. Ma, C. Jiang, A.A. Adesina, D.L. Trimm, M.S. Wainwright, *Chem. Eng. J.* 62 (1996) 103-111
- [64] N. Edwards, S.R. Ellis, J.C. Frost, S.E. Golunski, A.N.J. van Keulen, N.G. Lindewald, J.G. Reinkingh, *J. Power Sources* 71 (1998) 123-128
- [65] B. Höhlelin, M. Boe, J. Bøgild-Hansen, P. Bröckerhoff, G. Colmsan, B. Emonts, R. Menzer, E. Riedel, *J. Power Sources* 61 (1996) 143-147
- [66] P. Mizsey, E. Newson, T.-B. Truong, P. Hottinger, *Appl. Cat. A* 213 (2001) 233-237
- [67] F. Panik, *J. Power Sources* 71 (1998) 36-38
- [68] T. Ioannides and S. Neophytides, *J. Power Sources* 91 (2000) 150-156
- [69] J.C. Amphlett, R.F. Mann, B.A. Peppley, P.R. Roberge, A. Rodrigues, J.P. Salvador, *J. Power Sources* 71 (1998) 179-184
- [70] N. Fujiwara, K.A. Friedrich, U. Stimming, *J. Electroanal. Chem.* 472 (1999) 120-125
- [71] X. Gong, A. Bandis, A. Tao, G. Meresi, Y. Wang, P.T. Inglefield, A.A. Jones, W.-Y. Wen, *Polymer* 42 (2001) 6485-6492
- [72] W.J. Zhou, B. Zhou, W.Z. Li, Z.H. Zhou, S.Q. Song, G.Q. Sun, Q. Xin, S.

References

- Douvartzides, M. Goula, P. Tsiakaras, J. Power Sources 126 (2004) 16-22
- [73] A.S, Aricò, P.Creti, P.L. Antonucci, V. Antonucci, Electrochem. Solid State Lett. 1 (1998) 66-68
- [74] J. Wang, S. Wasmus, R.F. Savinell, J. Electrochem. Soc. 142 (1995) 4218-4224
- [75] H. Cnobloch, D. Gröppel, H. Kohlmüller, D. Kuhl, H. Poppa, G. Siemsen, Progr. Batteries & Solar Cells 4 (1982) 225-229
- [76] C. Lamy, Electrochim. Acta 29 (1984) 1581-1588
- [77] E. Peled, V. Livshits, T. Duvdevani, J. Power Sources 106 (2002) 245-248
- [78] H. Cnobloch, H. Kohlmüller, 27th I.S.E. Meeting, Extended Abstract, Zurich, Sept., 1976, p. 282
- [79] Z. Qi and A. Kaufman, J. Power Sources 110 (2002) 65-72
- [80] Z. Qi and A. Kaufman, J. Power Sources 112 (2002) 121-129
- [81] Z. Qi and A. Kaufman, J. Power Sources 118 (2003) 54-60
- [82] Z.G. Qi, M. Hollett, A. Attia, A. Kaufman, Electrochem. Solid State Lett. 5 (2002) A129-A130
- [83] D. Cao and S.H. Bergens, J. Power Sources 124 (2003) 12-17
- [84] O. Savadogo and B. Xing, J. New Mater. Electrochem. Systems 3 (2000) 343-347
- [85] O. Savadogo and F.J. Rodriguez Varela, J. New Mater. Electrochem. Systems 4 (2001) 93-97
- [86] J.T. Wang, W.F. Lin, M. Weber, S. Wasmus, R.F. Savinell, Electrochim. Acta 43 (1998) 3821-3828
- [87] J.T. Müller, P.M. Urban, W.F. Hölderich, K.M. Colbow, J. Zhang, D.P.

References

- Wilkinson, J. *Electrochem. Soc.* 147 (11) (2000) 4058-4060
- [88] A. Hamnett, *Catalysis Today* 38 (1997) 445-457
- [89] R. Parsons and T.J. VanderNoot, *J. Electroanal. Chem.* 257 (1988) 9-45
- [90] R. Inada, K. Shimazu, H. Kita, *J. Electroanal. Chem.* 277 (1990) 315-326
- [91] T. Frelink, W. Visscher, J.A.R. van Veen, *Surf. Sci.* 335 (1995) 353-360
- [92] W. Vielstich and T. Iwasita, in *Handbook of Heterogeneous Catalysis*, G. Ertl, H. Knözinger, J. Weitkamp (Eds.), Vol. 4, Wiley, Chichester, 1997
- [93] S. Wasmus and A. Küver, *J. Electroanal. Chem.* 461 (1999) 14-31
- [94] B. Beden, J.-M. Léger, C. Lamy, in *Modern Aspects of Electrochemistry*, J. O'M. Bockris, B.E. Conway, R.E. White (Eds.), Vol. 22, Plenum Press, New York, 1992, p. 97-247
- [95] J.-M. Léger and C. Lamy, *Ber. Bunsenges. Phys. Chem.* 94 (1990) 1021-1025
- [96] A. Papoutsis, J.-M. Léger, C. Lamy, *J. Electroanal. Chem.* 359 (1993) 141-160
- [97] E. Herrero, K. Franaszczuk, A. Wieckowski, *J. Phys. Chem.* 98 (1994) 5074-5083
- [98] P.C. Biswas, Y. Nodasaka, M. Enyo, *J. Appl. Electrochem.* 26 (1996) 30-35
- [99] G.T. Burstein, C.J. Barnett, A.R. Kucernak, K.R. Williams, *Catalysis Today* 38 (1997) 425-437
- [100] W.-F. Lin, J.-T. Wang, R.F. Savinell, *J. Electrochem. Soc.* 144 (1997) 1917-1922
- [101] Y. Zhu, H. Uchida, T. Yajima, M. Watanabe, *Langmuir* 17 (2001) 146-154
- [102] P.A. Christensen, A. Hamnett, G.L. Troughton, *J. Electroanal. Chem.* 362 (1993) 207-218

References

- [103] D. Pletcher and V. Solis, *Electrochim. Acta* 27 (1982) 775-782
- [104] J. Sobkowski and A. Wieckowski, *J. Electroanal. Chem.* 41 (1973) 373-379
- [105] D.N. Upadhyay, V. Yegnaraman, G. Prabhakara Rao, *J. Power Sources* 36 (1991) 11-16
- [106] K. Yahikozawa, Y. Fujii, Y. Matsuda, K. Nishimura, Y. Takasu, *Electrochim. Acta* 36 (1991) 973-978
- [107] K. Kinoshita, *J. Electrochem. Soc.* 137 (1990) 845-848
- [108] Y. Takasu, Y. Fujii, Y. Matsuda, *Bull. Chem. Soc. Jpn.* 59 (1986) 3973-3974
- [109] P.A. Attwood, B.D. McNicol, R.T. Short, J.A. van Amstel, *J. Chem. Soc. Farad. Trans. I* 76 (1980) 2310-2321
- [110] B.D. McNicol, P.A. Attwood, R.T. Short, *J. Chem. Soc. Farad. Trans. I* 77 (1981) 2017-2028
- [111] B.J. Kennedy and A. Hamnett, *J. Electroanal. Chem.* 283 (1990) 271-285
- [112] J.B. Goodenough, A. Hamnett, B.J. Kennedy, S.A. Weeks, *Electrochim. Acta* 32 (1987) 1233-1238
- [113] L.D. Burke and J.K. Casey, *Ber. Bunsenges. Phys. Chem.* 94 (1990) 931-937
- [114] M. Watanabe, S. Saegusa, P. Stonehart, *J. Electroanal. Chem.* 271 (1989) 213-220
- [115] T. Frelink, W. Visscher, J.A.R. van Veen, *J. Electroanal. Chem.* 382 (1995) 65-72
- [116] R.A. Lampitt, L.P.L. Carrette, M.P. Hogarth, A.E. Russell, *J. Electroanal. Chem.* 460 (1999) 80-87
- [117] B. Beden, C. Lamy, A. Bewick, K. Kunitatsu, *J. Electroanal. Chem.* 121

References

- (1981) 343-347
- [118] W. Vielstich, P.A. Christensen, S.A. Weeks, A. Hamnett, *J. Electroanal. Chem.* 242 (1988) 327-333
- [119] P.A. Christensen, A. Hamnett, S.A. Weeks, *J. Electroanal. Chem.* 250 (1988) 127-142
- [120] T. Iwasita and W. Vielstich, *J. Electroanal. Chem.* 250 (1988) 451-456
- [121] K.J. Kunimatsu, *J. Electroanal. Chem.* 145 (1985) 219-224
- [122] B. Bedan, F. Hahn, S. Juanto, C. Lamy, J.-M. Léger, *J. Electroanal. Chem.* 225 (1987) 215-225
- [123] R.J. Nichols and A. Bewick, *Electrochim. Acta* 33 (1988) 1691-1694
- [124] T.D. Jarvi and E.M. Stuve, in *Electrocatalysis*, J. Lipkowski, P.N. Ross (Eds.), Wiley/VCH, New York, 1988, p.75
- [125] L.-W.H. Leung and M.J. Weaver, *Langmuir* 6 (1990) 323-333
- [126] N.M. Marković, H.A. Gasteiger, P.N. Ross Jr., X. Jiang, I. Villegas, M.J. Weaver, *Electrochim. Acta* 40 (1995) 91-98
- [127] T. Iwasita-Vielstich, in *Advances in Electrochemical Science and Engineering*, H. Gerischer, C.W. Tobias (Eds.), 1st edn., VCH, Weinheim, 1990, p. 127-170
- [128] M. Watanabe and S. Motoo, *J. Electroanal. Chem.* 60 (1975) 259-266
- [129] M.M.P. Janssen and J. Moolhuysen, *Electrochim. Acta* 21 (1976) 861-868
- [130] M. Watanabe, Y. Furuuchi, S. Motoo, *J. Electroanal. Chem.* 191 (1985) 367-375
- [131] S.A. Campbell and R. Parsons, *J. Chem. Soc. Farad. Trans.* 88 (1992) 833-841
- [132] Y.B. Vassiliev, V.S. Bagotzky, N.V. Osetrova, A.A. Mikhailova, *J. Electroanal.*

References

- Chem. 97 (1979) 63-76
- [133] B. Beden, F. Kadirgan, C. Lamy, J.-M. Léger, J. Electroanal. Chem. 127 (1981) 75-85
- [134] C.E. Lee, P.B. Tiege, Y. Xing, J. Nagendran, S.H. Bergens, J. Am. Chem. Soc. 119 (1997) 3543-3549
- [135] C.E. Lee and S.H. Bergens, J. Phys. Chem. B 102 (1998) 193-199
- [136] B. Beltowska-Brzezinska, J. Heitbaum, W. Vielstich, Electrochim. Acta 30 (1985) 1465-1471
- [137] M. Shibata and S. Motoo, J. Electroanal. Chem. 229 (1987) 385-394
- [138] A.B. Anderson, E. Grantscharova, S. Seong, J. Electrochem. Soc. 143 (1996) 2075-2082
- [139] A.S. Aricò, V. Antonucci, N. Giordano, A.K. Shukla, M.K. Ravikumar, A. Roy, S.R. Barman, D.D. Sarma, J. Power Sources 50 (1994) 295-309
- [140] A.K. Shukla, A.S. Aricò, K.M. El-Khatib, H. Kim, P.L. Antonucci, V. Antonucci, Applied Surface Science 137 (1999) 20-29
- [141] M.R. Andrew, J.S. Drury, B.D. McNicol, C. Pinnington, R.T. Short, J. Appl. Electrochem. 6 (1976) 99-106
- [142] A. Hamnett and B.J. Kennedy, Electrochim. Acta 33 (1988) 1613-1618
- [143] F. Kadirgan, B. Beden, J.-M. Léger, C. Lamy, J. Electroanal. Chem. 125 (1982) 89-103
- [144] V.B. Hughes and R. Miles, J. Electroanal. Chem. 145 (1983) 87-107
- [145] J.B. Goodenough, A. Hamnett, B.J. Kennedy, R. Manoharan, S.A. Weeks, J. Electroanal. Chem. 240 (1988) 133-145

References

- [146] M. Watanabe, M. Uchida, S. Motoo, *J. Electroanal. Chem.* 229 (1987) 395-406
- [147] M.A. Quiroz, I. Gonzalez, Y. Meas, E. Lamy-Pitara, J. Barbier, *Electrochim. Acta* 32 (1987) 289-291
- [148] H.A. Gasteiger, N. Marković, P.N. Ross, Jr., E. J. Cairns, *J. Phys. Chem.* 98 (1994) 617-625
- [149] A.B. Anderson and E. Grantscharova, *J. Phys. Chem.* 99 (1995) 9149-9154
- [150] G.A. Camara, M.J. Giz, V.A. Paganin, E.A. Ticianelli, *J. Electroanal. Chem.* 537 (2002) 21-29
- [151] H.N. Dinh, X. Ren, F.H. Garzon, P. Zelenay, S. Gottesfeld, *J. Electroanal. Chem.* 491 (2000) 222-233
- [152] A.S. Aricò, G. Monforte, E. Modica, P.L. Antonucci, V. Antonucci, *Electrochem. Commun.* 2 (2000) 466-470
- [153] A.S. Aricò, P. Cretì, E. Modica, G. Monforte, V. Baglio, V. Antonucci, *Electrochim. Acta* 45 (2000) 4319-4328
- [154] C.H. Lee, C.W. Lee, D.I. Kim, D.H. Jung, C.S. Kim, D.R. Shin, *J. Power Sources* 86 (2000) 478-481
- [155] H.M. Saffarian, R. Srinivasan, D. Chu, S. Gilman, *Electrochim. Acta* 44 (1998) 1447-1454
- [156] A. Hamnett, B.J. Kennedy, S.A. Weeks, *J. Electroanal. Chem.* 240 (1988) 349-353
- [157] A.K. Shukla, M.K. Ravikumar, A.S. Aricò, G. Candiano, V. Antonucci, N. Giordano, A. Hamnett, *J. Appl. Electrochem.* 25 (1995) 528-532
- [158] K. Lasch, L. Jörissen, J. Garche, *J. Power Sources* 84 (1999) 225-230

References

- [159] P.K. Shen, K.Y. Chen, A.C.C. Tseung, *J. Electrochem. Soc.* 141 (1994) 1758-1762
- [160] P.K. Shen and A.C.C. Tseung, *J. Electrochem. Soc.* 141 (1994) 3082-3090
- [161] K.Y. Chen, P.K. Shen, A.C.C. Tseung, *J. Electrochem. Soc.* 142 (1995) L54-L56
- [162] E.A. Meulenkamp, *J. Electrochem. Soc.* 144 (1997) 1664-1671
- [163] C.-H. Lee, C.-W. Lee, D.-H. Jung, C.-S. Kim, D.-R. Shin, *J. New Mater. Electrochem. Systems* 2 (1999) 125-129
- [164] B. Rajesh, V. Karthik, S. Karthikeyan, K.R. Thampi, J.-M. Bonard, B. Viswanathan, *Fuel* 81 (2002) 2177-2190
- [165] J. Wang, H. Nakajima, H. Kita, *J. Electroanal. Chem.* 250 (1988) 213-217
- [166] H. Kita, H. Nakajima, K. Shimazu, *J. Electroanal. Chem.* 248 (1988) 181-191
- [167] M. Uchida, Y. Aoyama, M. Tanabe, N. Yanagihara, N. Eda, A. Ohta, *J. Electrochem. Soc.* 142 (1995) 2572-2576
- [168] B.R. Rauche, F.R. McLarnon, E.J. Cairns, *J. Electrochem. Soc.* 142 (1995) 1073-1084
- [169] A.K. Shukla, P.A. Christensen, A. Hamnett, M.P. Hogarth, *J. Power Sources* 55 (1995) 87-91
- [170] L. Dubau, F. Hahn, C. Coutanceau, J.-M. Léger, C. Lamy, *J. Electroanal. Chem.* 554-555 (2003) 407-415
- [171] E. Ticianelli, J.G. Beery, M.T. Paffett, S. Gottesfeld, *J. Electroanal. Chem.* 258 (1989) 61-77
- [172] H.A. Gasteiger, N. Marković, P.N. Ross Jr., E.J. Cairns, *J. Phys. Chem.* 97

References

- (1993) 12020-12029
- [173] H.A. Gasteiger, N. Marković, P.N. Ross, E.J. Cairns, *J. Electrochem. Soc.* 141 (1994) 1795-1803
- [174] K. Wang, H.A. Gasteiger, N.M. Marković, P.N. Ross Jr., *Electrochim. Acta* 41 (1996) 2587-2593
- [175] G.L. Troughton and A. Hamnett, *Bull. Electrochem.* 7 (1991) 488-492
- [176] A. Aramata and M. Masuda, *J. Electrochem. Soc.* 138 (1991) 1949-1957
- [177] K.L. Ley, B. Liu, C. Pu, Q. Fan, N. Leyarovska, C. Segre, E.S. Smotkin, *J. Electrochem. Soc.* 144 (1997) 1543-1548
- [178] B. Gurau, R. Viswanathan, R. Liu, T.J. Lafrenz, K.L. Ley, E.S. Smotkin, E. Reddington, A. Sapienza, B.C. Chan, T.E. Mallouk, S. Sarangapani, *J. Phys. Chem. B* 102 (1998) 9997-10003
- [179] E. Reddington, A. Sapienza, B. Gurrau, R. Viswanathan, S. Sarangapani, E.S. Smotkin, T.E. Mallouk, *Science* 280 (1998) 1735-1737
- [180] C. He, H.R. Kunz, J.M. Fenton, *J. Electrochem. Soc.* 144 (1997) 970-979
- [181] M. Götz and H. Wendt, *Electrochim. Acta* 43 (1998) 3637-3644
- [182] W.C. Choi, J.D. Kim, S.I. Woo, *Catalysis Today* 74 (2002) 235-240
- [183] A.S. Aricò, Z. Poltarzewski, H. Kim, A. Morana, G. Giordano, V. Antonucci, *J. Power Sources* 55 (1995) 159-166
- [184] A.S. Aricò, P. Cretì, N. Giordano, V. Antonucci, P.L. Antonucci, A. Chuvilin, *J. Appl. Electrochem.* 26 (1996) 959-967
- [185] A.S. Aricò, P. Cretì, Z. Poltarzewski, R. Mantegna, H. Kim, N. Giordano, V. Antonucci, *Mater. Chem. Phys.* 47 (1997) 257-262

References

- [186] L. Liu, C. Pu, R. Viswanathan, Q. Fan, R. Liu, E.S. Smotkin, *Electrochim. Acta* 43 (1998) 3657-3663
- [187] H. Bönemann, R. Brinkmann, W. Brijoux, E. Dinjus, T. Jousen, B. Korall, *Angew. Chem.* 103 (1991) 1344-1346
- [188] T.J. Schmidt, M. Noeske, H.A. Gasteiger, R.J. Behm, P. Britz, W. Brijoux, H. Bönemann, *Langmuir* 14 (1997) 2591-2595
- [189] T.J. Schmidt, M. Noeske, H.A. Gasteiger, R.J. Behm, P. Britz, W. Brijoux, H. Bönemann, *J. Electrochem. Soc.* 145 (1998) 925-931
- [190] T.J. Schmidt, H.A. Gasteiger, R.J. Behm, *Electrochem. Commun.* 1 (1998) 1-4
- [191] H. Bönemann, R. Brinkmann, P. Britz, U. Endruschat, R. Mörtel, U. Paulus, G. Feldmeyer, T.J. Schmidt, H.A. Gasteiger, R.J. Behm, *J. New Mater. Electrochem. Systems* 3 (2000) 199-206
- [192] C. Roth, M. Götz, H. Fuess, in *Proceedings of the Workshop on Electrocatalysis in Indirect and Direct Methanol PEM Fuel Cell*, C. Lamy, H. Wendt (Eds.), 12-14 September, Portoroz, Slovenia, 1999, p.30
- [193] K. Lasch, L. Jörissen, J. Garche, in *Proceedings of the Workshop on Electrocatalysis in Indirect and Direct Methanol PEM Fuel Cell*, C. Lamy, H. Wendt (Eds.), 12-14 September, Portoroz, Slovenia, 1999, p.104
- [194] A.J. Dickinson, L.P.L. Carrette, J.A. Collins, K.A. Friedrich, U. Stimming, *Electrochim. Acta* 47 (2002) 3733-3739
- [195] Earnshaw, Greenwood. *Chemistry of the Elements*. 2nd Edition. Elsevier Butterworth-Heinemann. New York. 2005

References

- [197] G.F. Smith, J.L. Gring. “ The separation and Determination of the Alkali Metals using Perchloric and Chloroplatinic acid in the determination of small amounts of Potassium in the presence of large amounts of Sodium” *J.Am. Chem. Soc.* 55(10) 1933 3957-3961.
- [198] J.L. Speier, J.A. Webster, G.H. Barnes “The Addition of Silicon Hydrides to Olefinic Double Bonds. PartII. The Use of Group VIII Metals Catalysts” *J.Am. Chem. Soc.* 79(4) (1957) 974-979.
- [199] P.Rudnick, R.D. Cooke. The Preparation of Hydrochloroplatinic Acid by Means of Hydrogen Peroxide. *J.Am. Chem. Soc.* 39(4) (1917) 633-635.
- [200] A.E. Schweizer, G.T. Kerr. Thermal Decomposition of Hexachloroplatinic Acid. *Inorg. Chem.* 17(8) (1978) 2326-2327.
- [201] Holleman, Wiberg. *Inorganic Chemistry First Edition.* Acedemic Press. New York, 2001.
- [202] John C. Saam, John L. Speier. “The Addition of Silicon Hydrides to Olefinic Double Bonds. Part111. The Addition to Non-terminal Olefins in the presence of Chloroplatinic Acid” *J.Am. Chem. Soc.*,80 (1958) 4104.
- [203] L.N. Lewis, K.G Sy, G.L. Bryant, Jr. and P.E. Donahue. *Organometallics.* 10 (1991) 3750.
- [204] A. Sep´ulveda-Escribano, F. Coloma, F. Rodr´iguex-Reinoso, *Appl. Catal. A Gen.* 173 (1998) 247.
- [205] Y. Takasu, T. Kawaguchi, W. Sugimoto, Y. Murakami, *Electrochim. Acta* 48 (2003) 3861.
- [206] T. Frelink, W. Visscher, J.A.R. van Veen, *J. Electroanal. Chem.* 382

References

- (1995) 65.
- [207] R.W. Pekala, *J. Mater. Sci.* 24 (1989) 3221.
- [208] R.W. Pekala, S.T. Alviso, X. Lu, J. Gross, J. Fricke, *J. Non-Cryst. Solids* 188 (1995) 34.
- [209] J. Fricke, in: J. Fricke (Ed.), *Aerogels*, Springer-Verlag, New York, (1986) 2.
- [210] R.W. Pekala, J.C. Farmer, C.T. Alviso, T.D. Tran, S.T. Mayer, J.M. Miller, B. Dunn, *J. Non-Cryst. Solids* 225 (1998) 74.
- [211] S. Ye, A.K. Vijh, *Electrochem. Commun.* 5 (2003) 272.
- [212] K.-L. Yang, S. Yiacoumi, C. Tsouris, *J. Electroanal. Chem.* 540 (2003) 159.
- [213] S. Ye, A.K. Vijh, L.H. Dao, *J. Electrochem. Soc.* 143 (1996) L7.
- [214] S. Ye, A.K. Vijh, L.H. Dao, *J. Electrochem. Soc.* 143 (1997) 1734.
- [215] S. Ye, A.K. Vijh, L.H. Dao, *J. New Mater. Electrochem. Syst.* 1 (1998) 17.
- [216] H. Tamon, H. Ishizaka, T. Yamamoto, T. Suzuki, *Carbon* 37 (1999) 2049.
- [217] T. Yamamoto, T. Sigimoto, T. Suzuki, S.R. Mukai, H. Tamon, *Carbon* 40 (2002) 1345.
- [218] H. Tamon, H. Ishizaka, T. Yamamoto, T. Suzuki, *Carbon* 38 (2000) 1099.
- [219] T. Yamamoto, T. Nishimara, T. Suzuki, H. Tamon, *J. Non-Cryst. Solids* 288 (2001) 46.

References

- [220] B. Babić, B. Kalu – derović, Lj. Vračar, N. Krstajić, *Carbon* 42 (2004) 2617.
- [221] B. Babić, D. Đokić, N. Krstajić, *J. Serb. Chem. Soc.* 70 (2005) 21.
- [222] Z.H. Zhou, S.L. Wang, W.J. Zhou, G.X. Wang, L.H. Jiang, W.Z. Li, S.Q. Song, J.Q. Liu, G.Q. Sun, Q. Xin, *Chem. Commun.* 1 (2003) 393.
- [223] V. Radmilovic, T.J. Richardson, S.J. Chen, P.N. Ross, *J. Catal.* 232 (2005) 199.
- [224] A.J. Bard, L. Faulkner, *Electrochemical Methods, Fundamentals and Applications*, John Wiley & Sons, New York, 1981 (Chapter 8).
- [225] N.M. Markovic, B.N. Grgur, P.N. Ross, *J. Phys. Chem. B* 101 (1997) 5405.
- [226] T.J. Schmidt, P.N. Ross, N.M. Markovic, *J. Electroanal. Chem.* 524–525 (2002) 252.
- [227] V.S. Bagotzky, N.V. Osetrova, *J. Electroanal. Chem.* 43 (1973) 233.
- [228] J.W. Guo, T.S. Zhao, J. Prabhuram, C.W. Wong, *Electrochim. Acta* 50 (2005) 1973.
- [229] M. Umeda, M. Kokubo, M. Mohamedi, I. Uchida, *Electrochim. Acta* 48 (2003) 1367.
- [230] A.S. Arico, S. Srinivasan, V. Antonucci, *Fuel Cells* 1 (2001) 1.
- [231] S. Wasmus, A. Kuver, *J. Electroanal. Chem.* 461 (1999) 14.
- [232] M.-ki. Min, J. Cho, K. Cho, H. Kim, *Electrochim. Acta* 45 (2000) 4211.

References

- [233] K.Y. Chan, J. Ding, J. Ren, S. Cheng, K.Y. Tsang, *J. Mater. Chem.* 14 (2004) 505.
- [234] O.P. Yadav, A. Palmqvist, N. Cruise, K. Holmberg, *Colloids Surf. A: Physicochem. Eng. Aspects* 221 (2003) 131.
- [235] X. Zhang, K.-Y. Chan, *Chem. Mater.* 15 (2003) 451.
- [236] Z.L. Liu, X.Y. Liu, X. Su, J.Y. Lee, *J. Phys. Chem. B* 108 (2004) 8234.
- [237] Z.H. Zhou, S.L. Wang, W.J. Zhou, G.X. Wang, L.H. Jiang, W.Z. Li, S.Q. Song, J.G. Liu, G.Q. Sun, Q. Xin, *Langmuir* 3 (2003) 394.
- [238] W.X. Chen, J.Y. Lee, Z.L. Liu, *Chem. Commun.* 21 (2002) 2588.
- [239] H.G. Petrow, R.J. Allen, US Patent No. 4,044,193 (1977).
- [240] M. Watanabe, M. Uchida, S. Motoo, *J. Electroanal. Chem.* 229 (1987) 395.
- [241] C.R.K. Rao, D.C. Trivedi, *Coord. Chem. Rev.* 249 (2005) 613.
- [242] D.A. Stevens, J.R. Dahn, *J. Electrochem. Soc.* 150 (2003) A770.
- [243] D.N. Furlong, A. Launikonis, W.H.F. Sasse, *J. Chem. Soc., Faraday Trans.* 1 (1984) 571.
- [244] S. Ghannoum, Y. Xin, J. Jaber, L.I. Halaoui, *Langmuir* 19 (2003) 4804.
- [245] S.N. Pron'kin, G.A. Tsirlina, O.A. Petrii, S.Y. Vassiliev, *Electrochim. Acta* 46 (2001) 2343.
- [246] P.K. Shen, Z.Q. Tian, *Electrochim. Acta* 49 (2004) 3107.
- [247] J. Turkevich, G. Kim, *Science* 169 (1970) 873.
- [248] A. Harriman, G.R. Millward, P. Neta, M.C. Richoux, J.M. Thomas, *J. Phys. Chem.* 92 (1988) 1286.

References

- [249] X.W. Teng, H. Yang, *J. Am. Chem. Soc.* 125 (2003) 14559.
- [250] W. Li, W.J. Zhou, H.Q. Li, Z.H. Zhou, B. Zhou, G.Q. Sun, X. Qin, *Electrochim. Acta* 49 (2004) 1045.
- [251] Z.L. Liu, J.Y. Lee, W.X. Chen, M. Han, L.M. Gan, *Langmuir* 20 (2004) 181.
- [252] S.A. Lee, K.W. Park, J.H. Choi, B.K. Kwon, Y.E. Sung, *J. Electrochem. Soc.* 149 (2002) A1299.
- [253] R. Venkataraman, H.R. Kunz, J.M. Fenton, *J. Electrochem. Soc.* 150 (2003) A278.
- [254] M. Peuckert, F.P. Coenen, H.P. Bonzel, *Electrochim. Acta* 29 (1984) 1305.
- [255] S. Mukerjee, J. McBreen, *J. Electroanal. Chem.* 448 (1998) 163.
- [256] F. Maillard, M. Eikerling, O.V. Cherstiouk, S. Schreier, E. Savinova, U. Stimming, *Faraday Discuss.* 125 (2004) 357.
- [257] T.V. Frelink, W. Visscher, J.A.R. van Veen, *J. Electroanal. Chem.* 382 (1995) 65.
- [258] Y. Takasu, H. Itaya, T. Iwazaki, R. Miyoshi, T. Ohnuma, W. Sugimoto, Y. Murakami, *Chem. Commun.* 4 (2001) 341.
- [259] A. Hamnett, G. Troughton, *Chem. Ind.* 7 (1992) 480.
- [260] A.S. Arico, S. Srinivasan, V. Antonucci, *Fuel Cells* 2 (2001) 1.
- [261] W. Vielstich, *J. Braz. Chem. Soc.* 14 (2003) 503.
- [262] K.W. Park, J.H. Choi, B.K. Kwon, S.A. Lee, Y.E. Sung, H.Y. Ha, S.A. Hong, H. Kim, A. Wieckowski, *J. Phys. Chem. B* 106 (2002) 1869.
- [263] S.A. Lee, K.W. Park, J.H. Choi, B.K. Kwon, Y.E. Sung, *J. Electrochem. Soc.* 149

References

- (2002) 1299.
- [264] K.W. Park, K.S. Ahn, J.H. Choi, Y.C. Nah, Y.M. Kim, Y.E. Sung, *Appl. Phys. Lett.* 81 (2002) 907.
- [265] X.M. Ren, P. Zelenay, S. Thomas, J. Davey, S. Gottesfeld, *J. Power Sources* 86 (2000) 111.
- [266] B.D. McNicol, D.A.J. Rand, K.R. Williams, *J. Power Sources* 83 (1999) 15.
- [267] S. Wasmus, A. Kuver, *J. Electroanal. Chem.* 461 (1999) 14.
- [268] K. Kordesch, G. Simader, *Fuel Cells and their Applications*, VCH, Weinheim, Germany, 1996.
- [269] M. Watanabe, H. Igarashi, T. Fujino, *Electrochem.* 67 (1999) 1194.
- [270] T. Fujino, Thesis for M. Eng., Yamanashi University, 1996.
- [271] M. Watanabe, H. Igarashi, T. Fujino, in: *The 1997 Joint International Meeting of ECS and ISE, Meeting Abstract 97-2*, p. 1238.
- [272] T. Toda, H. Igarashi, H. Uchida, M. Watanabe, *J. Electrochem. Soc.* 146 (1999) 3750.
- [273] M. Watanabe, Y.M. Zhu, H. Uchida, *J. Phys. Chem. B* 104 (2000) 1762.
- [274] W.Z. Li, C.H. Liang, J.S. Qiu, H.Q. Li, W.J. Zhou, G.Q. Sun, Q. Xin, *React. Kinet. Catal. Lett.* 82 (2004) 2235.
- [275] T. Toda, H. Igarashi, M. Watanabe, *J. Electroanal. Chem.* 460 (1999) 258.
- [276] A.K. Shukla, R.K. Raman, N.A. Choudhury, K.R. Priolkar, P.R. Sarode, S. Emura, R. Kumashiro, *J. Electroanal. Chem.* 563 (2004) 181.
- [277] W.Z. Li, W.J. Zhou, H.Q. Li, Z.H. Zhou, B. Zhou, G.Q. Sun, Q. Xin, *Electrochim. Acta* 49 (2004) 1045.

References

- [278] C. Lamy, J.M. Leger, S. Srinivasan, *Mod. Aspects Electrochem.* 34 (2001) 73.
- [279] T. Matsumoto, T. Komatsu, K. Arai, T. Yamazaki, M. Kijima, H. Shimizu, Y. Takasawa, J. Nakamura, *Chem. Commun.* (2004) 840.
- [280] C. Bock, C. Paquet, M. Couillard, G.A. Botton, B.R. MacDougall, *J. Am. Chem. Soc.* 126 (2004) 8028.
- [281] Z. Liu, X.Y. Ling, X. Su, J.Y. Lee, *J. Phys. Chem. B* 108 (2004) 8234.
- [282] R.M. Baum, *Chem. Eng. News* 75 (1997) 39.
- [283] C. Bernard, J.M. Planeix, B. Valerie, *Appl. Catal. A* 173 (1998) 175.
- [284] J.M. Planeix, N. Coustel, B. Coq, V. Brotons, P.S. Kumbhar, R. Dutartre, P. Geneste, P. Bernier, P.M. Ajayan, *J. Am. Chem. Soc.* 116 (1994) 7935.
- [285] C.H. Liang, Z.L. Li, J.S. Qiu, C. Li, *J. Catal.* 211 (2002) 278.
- [286] W.Z. Li, C.H. Liang, W.J. Zhou, J.S. Qiu, Z.H. Zhou, G.Q. Sun, Q. Xin, *J. Phys. Chem. B* 107 (2003) 6292.
- [287] G. Wu, Y.S. Chen, B.Q. Xu, *Electrochem. Commun.* 7 (2005) 1237.
- [288] R.Q. Yu, L.W. Chen, Q.P. Liu, J.Y. Lin, K.L. Tan, S.C. Ng, H. Chan, G.Q. Xu, T.S. Andyhor, *Chem. Mater.* 10 (1998) 718.
- [289] N. Fujiwara, K. Yasuda, T. Ioroi, Z. Siroma, Y. Miyazaki, *Electrochim. Acta* 47 (2002) 4079.
- [290] D.R. Rolison, P.L. Hagans, K.E. Swider, J.W. Long, *Langmuir* 15 (1999) 774.
- [291] X. Zhang, K.Y. Chan, *Chem. Mater.* 15 (2003) 451.
- [292] B. Rajesh, K.R. Thampi, J.M. Bonard, N. Xanthopoulos, H.J. Mathieu, B. Viswanathan, *J. Phys. Chem. B* 107 (2003) 2701.
- [293] H.-G. Boyen, G. Kaestle, F. Weigl, B. Koslowski, C. Dietrich, P. Ziemann, J.P.

References

- Spatz, S. Riethmüller, C. Hartmann, M. Möller, G. Schmid, M.G. Garnier, P. Oelhafen, *science* 297 (2002) 1533–1536.
- [294] S.J. Riley, in: H. Haberland (Ed.), *Clusters of Atoms and Molecules II*, Springer Verlag, Berlin, 1994, p. 226.
- [295] S.J. Riley, E.K. Parks, *NATO ASI Ser. B* 15 (1987) 727.
- [296] D.M. Cox, K.C. Reichmann, D.J. Trevor, A.J. Kaldor, *Chem. Phys.* 88 (1) (1988) 111–119.
- [297] Y.H. Pan, K. Sohlberg, D.P. Ridge, *J. Am. Chem. Soc.* 113 (1991) 2406–2411.
- [298] P. Schnabel, M.P. Irion, K.G. Weil, *J. Phys. Chem.* 95 (1991) 9688–9694.
- [299] Z. Xu, F.-S. Xiao, S.K. Purnell, O. Alexeev, S. Kawi, S.E. Deutsch, B.C. Gates, *Nature* 372 (1994) 346–348.
- [300] M. Vaarkamp, J.T. Miller, F.S. Modica, G.S. Lane, D.C. Koningsberger, in: L. Guzzi et al. (Eds.), *Proceedings of the Tenth International Congress on Catalysis*, Elsevier, Amsterdam, 1993, pp. 809–820.
- [301] (a) K.F. Blurton, P. Greenburg, G.H. Oswin, D.R. Rutt, *J. Electrochem. Soc.* 119 (1972) 559;
- (b) L.J. Bergoli, *Electrochim. Acta* 23 (1978) 489;
- (c) M. Peukert, T. Yoneda, R.A. Dalla Betta, M. Boudart, *J. Electrochem. Soc.* 143 (1996) 944.
- [302] (a) K. Kinoshita, *J. Electrochem. Soc.* 137 (3) (1990) 845–848;
- (b) O. Antoine, Y. Bultelb, R. Durand, *J. Electroanal. Chem.* 499 (1)

- (2001) 85–94.
- [303] D. Thompsett, in: G. Hoogers (Ed.), *Fuel Cell Technology Handbook*, CRC Press, Boca Raton, 2003, pp. 6–15.
- [304] K.-W. Park, Y.-E. Sung, S. Han, Y. Yun, T. Hyeon, *J. Phys. Chem. B* 108 (2004) 939–944.
- [305] (a) J.R. Regalbuto, A. Navada, S. Shadid, M.L. Bricker, Q. Chen, *J. Catal.* 184 (1999) 335;
- (b) X. Hao, J.R. Regalbuto, *J. Colloid Interf. Sci.* 267 (2003) 259;
- (c) M. Schreier, J.R. Regalbuto, *J. Catal.* 255 (2004) 190.
- [306] J.T. Miller, M. Schreier, A.J. Kropf, J.R. Regalbuto, *J. Catal.* 255 (2004) 203.
- [307] X. Hao, L. Quach, J. Korah, W.A. Spieker, J.R. Regalbuto, *J. Mol. Catal. A: Chem.* 219 (2004) 97.
- [308] J. de Graaf, A.J. van Dillen, K.P. de Jong, D.C. Koningsberger, *J. Catal.* 203 (2001) 307.
- [309] (a) P. Gallezot, A. Alarcon-Diaz, J.-A. Dalmon, A.J. Renouprez, B. Imelik, *J. Catal.* 39 (1975) 334;
- (b) D. Exner, N. Jaeger, A. Kleine, G. Schulz-Ekloff, *J. Chem. Soc. Faraday Trans. I* 84 (11) (1988) 4097;
- (c) J.A. Rabo, V. Schomaker, P.E. Pickert, in: W.M.H. Sachtler (Ed.), *Proceedings of the Third International Congress Catalysis*, vol. 2, North-Holland, Amsterdam, 1965, p. 1264;
- (d) A.I. Serykh, O.P. Tkachenko, V.Yu. Borovkov, V.B. Kazansky,

References

- M. Beneke, N.I. Jaeger, G. Schulz-Ekloff, *Phys. Chem. Chem. Phys.* 2 (2000) 5647.
- [310] S. Jun, S.H. Joo, R. Ryoo, M. Kruk, M. Jaroniek, Z. Liu, T. Ohsuna, O. Terasaki, *J. Am. Chem. Soc.* 122 (2000) 10712.
- [311] S. Che, A.E. Garcia-Bennett, X. Liu, R.P. Hodgkins, P.A. Wright, D. Zhao, O. Terasaki, T. Tatsumi, *Angew. Chem., Int. Ed.* 42 (2003) 3930.
- [312] M. Kruk, M. Jaroniek, C.H. Ko, R. Ryoo, *Chem. Mater.* 12 (2000) 1961–1968.
- [313] A.B. Fuertes, *Micropor. Mesopor. Mater.* 67 (2004) 273.
- [314] Z. Ma, T. Kyotani, Z. Liu, O. Terasaki, A. Tomita, *Chem. Mater.* 13 (2001) 4413.
- [315] F. Su, J. Zeng, Y. Yu, L. Lv, J.Y. Lee, X.S. Zhao, *Carbon* 43 (2005) 2366–2373.
- [316] S.H. Joo, S.J. Choi, I. Oh, J. Kwak, Z. Liu, O. Terasaki, R. Ryoo, *Nature* 412 (2001) 169.
- [317] M. Wu, D. Chen, T. Huang, *Langmuir* 17 (2001) 3877.
- [318] I. Srnova-Sloufova, B. Vlckva, Z. Bastl, T.L. Hasslett, *Langmuir* 20 (2004) 3407.
- [319] A. Henglein, *J. Phys. Chem. B* 104 (2000) 2201.
- [320] M. Wu, L. Lai, *Colloid Surf. A* 204 (2004) 149.
- [321] S.K. Ghosh, M. Mandal, S. Kundu, S. Nath, T. Pal, *Appl. Catal. A* 268 (2004) 61.

References

- [322] L.M. Liz-Marzan, M. Giersig, P. Mulvaney, *Langmuir* 12 (1996) 4329.
- [323] M. Brust, M. Walker, D. Bethell, D.J. Schiffrin, R. Whyman, *J. Chem. Soc., Chem. Commun.* (1994) 801.
- [324] T. Yonezawa, K. Yasui, N. Kimizuka, *Langmuir* 17 (2001) 271.
- [325] P.A. Buining, B.M. Humbel, A.P. Philipse, A.J. Verkleij, *Langmuir* 13 (1997) 3921.
- [326] U.A. Paulus, U. Endruschat, G.J. Feldmeyer, T.J. Schmidt, H. Bonnemann, R.J. Behm, *J. Catal.* 195 (2000) 383.
- [327] X. Wang, I. Hsing, *Electrochim. Acta* 47 (2002) 2981.
- [328] M.T.M. Koper, T.E. Shubina, R.A. van Santen, *J. Phys. Chem.* 106 (2002) 686.
- [329] M. Watanabe, S. Motoo, *J. Electroanal. Chem.* 60 (1975) 267.
- [330] A.B. Anderson, E. Grantscharova, S. Seong, *J. Electrochem. Soc.* 143 (1996) 2075.
- [331] S. Mukerjee, S.J. Lee, E.A. Ticianelli, J. McBreen, B.N. Grgur, N.M. Markovic, P.N. Ross, J.R. Giallombardo, E.S. De Castro, *Electrochem. Solid State Lett.* 2 (1999) 12.
- [332] E.A. Ticianelli, S. Mukerjee, S.J. Lee, J. McBreen, J.R. Giallombardo, E.S. De Castro, in: S. Gottesfeld, T.F. Fuller (Eds.), *Proton Conducting Membrane Fuel Cells*, PV 98-27, The Electrochemical Society Proceedings Series, Pennington, NJ, 1999, p.162.
- [333] B.N. Grgur, N.M. Markovic, P.N. Ross, *J. Electrochem. Soc.* 146 (1999) 1613.
- [334] B.N. Grgur, N.M. Markovic, P.N. Ross, in: S. Gottesfeld, T.F. Fuller (Eds.), *Proton*

References

- Conducting Membrane Fuel Cells, PV 98-27, The Electrochemical Society Proceedings Series, Pennington, NJ, 1999, p. 176.
- [335] H. Zhang, Y. Wang, E.R. Fachini, C.R. Cabrera, *Electrochem. Solid-State Lett.* 2 (1999) 437.
- [336] A. Lima, C. Coutanceau, J.M. Le'ger, C. Lamy, *J. Appl. Electrochem.* 31 (2001) 379.
- [337] M. Götz, H. Wendt, *Electrochim. Acta* 43 (1998) 3637.
- [338] G.L. Holleck, D.M. Pasquariello, S.L. Clauson, in: S. Gottesfeld, T.F. Fuller (Eds.), *Proton Conducting Membrane Fuel Cells*, PV 98-27, The Electrochemical Society Proceedings Series, Pennington, NJ, 1999, p. 151.
- [339] E. Auer, A. Freund, T. Lehmann, K.A. Starz, R. Schwarz, U. Stenke, US Patent 6,007,934, 1999.
- [340] S. Mukherjee, J.L. Moran-Lopez, *Surf. Sci.* 189_/190 (1987) 1135.
- [341] Parsons, R.; VanderNoot, T. *J. Electroanal. Chem.* **1988**, 257, 9.
- [342] Koch, D. F. A. Australian Patent 46123, 1964.
- [343] Rauhe, B. R., Jr.; McLarnon, F. R.; Cairns, E. J. *J. Electrochem. Soc.* **1995**, 142, 1073.
- [344] Bockris, J. O'M.; Wroblowa, H. *J. Electroanal. Chem.* **1964**, 7, 428.
- [345] Ross, P. N. In *Proceedings of the Workshop on Direct Methanol-Air Fuel Cells*; Landgrebe, A. R., Sen, R. K., Eds.; The Electrochemical Society: Pennington, NJ, 1992; Vol. 92-14, p 51.
- [346] Frelink, T.; Visscher, W.; van Veen, J. A. R. *Electrochim. Acta*

References

- 1994**, 39, 1871.
- [347] Frelink, T.; Visscher, W.; Cox, A. P.; van Veen, J. A. R.
Electrochim. Acta **1995**, 40, 1537.
- [348] Haner, A. N.; Ross, P. N. *J. Phys. Chem.* **1991**, 95, 3740.
- [349] Bae, I. T.; Takeshi, S.; Scherson, D. A. *J. Electroanal. Chem.* **1991**,
297, 185.
- [350] Beden, B.; Leger, J.-M.; Lamy, C. In *Modern Aspects of Electrochemistry*;
Bockris, J. O'M, Conway, B. E., White, R. E., Eds.; Plenum
Press: New York, 1992; Vol. 22, pp 97-247.
- [351] Frelink, T.; Visscher, W.; van Veen, J. A. R. *Surf. Sci.* **1995**, 335,
353.
- [352] McBreen, J.; Mukerjee, S. *J. Electrochem. Soc.* **1995**, 142,
3399.
- [353] Iwasita, T.; Nart, F. C.; Vielstich, W. *Ber. Bunsen-Ges. Phys. Chem.*
1990, 94, 1030.
- [354] Anderson, A. B.; Grantscharova, E.; Seong, S. *J. Electrochem. Soc.*
1996, 143, 2075.
- [355] Sobkowski, J.; Franaszczak, K.; Piasecki, A. *J. Electroanal. Chem.*
1985, 196, 145.
- [356] Il'chenko, N. I.; Golodets, G. I. *J. Catal.* **1975**, 39, 73.
- [357] Ley, K. L.; Liu, R.; Pu, C.; Fan, Q.; Leyarovska, N.; Segre, C.;
Smotkin, E. S. *J. Electrochem. Soc.* **1997**, 144, 1543. (b) Liu, L.;
Viswanathan, R.; Liu, R.; Smotkin, E. S. *Electrochem. Solid State Lett.*

1998, *I*, 123.

- [358] Reddington, E.; Sapienza, A.; Gurau, B.; Viswanathan, R.; Sarangapani, S.; Smotkin, E. S.; Mallouk, T. E. *Science* **1998**, *280*, 1735.
- [359] Y.-H. Chu, Y. G. Shul, W.C. Choi, S. I. Woo, H.-S. Han, *J. Power Sources* **118** (2003) 334-341.
- [360] A. Argyropoulos, K. Scott, W.M. Taama, *J. Appl. Electrochem.* **29** (1999) 661-669.
- [361] X. Ren, M.S. Wilson, S. Gottesfeld, *J. Electrochem. Soc.* **143** (1996) L12-L15.
- [362] Swathirajan S, Mikhail YM. US Patent No. US 5316871, 1994. See also [/http://patft.uspto.gov/netacgi/srchnum.htm](http://patft.uspto.gov/netacgi/srchnum.htm).
- [363] Kong CS, Kim D, Lee HK, Shul YG, Lee TH. *J Power Sources* 2002;108:185–91.
- [364] Larminie J, Dicks A. *Fuel cell systems explained*. New York: Wiley; 2000. p. 45–119.
- [365] Mosdale R, Stevens A. *Solid State Ionics* 1993;61:251–5.
- [366] Hsu CH, Wan CC. *J Power Sources* 2003;115:268–73.
- [367] Antolini E, Passos RR, Ticianelli EA. *J Power Sources* 2002;109:477–82.
- [368] Song JM, Cha SY, Lee WM. *J Power Sources* 2001;94:78–84.
- [369] Moreira J, Sebastian PJ, Ocampo AL, Castellanos RH. In: Proceedings of the 2001 joint international meeting—the 20th meeting of the Electrochemical Society, Inc. and the 52nd annual meeting of the International Society of Electrochemistry, San Francisco, California, September 2–7, 2001.
- [370] Iyuke SE, Mohamad AB, Kadhum AAH, Daud WRW, Rachid C. *J Power Sources* 2003;114:195–202.

References

- [371] Wakizoe M, Velez OA, Srinivasan S. *Electrochim Acta* 1995;40:335–44.
- [372] Qi Z, Kaufman A. *J Power Sources* 2003;114:21–31.
- [373] Escudero MJ, Hontanon E, Schwartz S, Boutonnet M, Daza L. *J Power Sources* 2002;106:206–14.
- [374] Acres GJK, Frost JC, Hards GA, Potter RJ, Ralph TR, Thompsett D, et al. *Catalysis Today* 1997;38:393–400.
- [375] Escribano S, Aldebert P. *Solid State Ionics* 1995;77:318–23.
- [376] Havranek A, Klafki K, Wippermann K. ABA 2001–Reports.
- [377] Wilson MS, Valerio JA, Gottesfeld S. *Electrochim Acta* 1995;40:355–63.
- [378] Mehta V, Cooper JS. *J Power Sources* 2003;114:32–53.
- [379] Mennola T. Design and experimental characterization of polymer electrolyte membrane fuel cell, Master's thesis, Helsinki University of Technology, 2000. p. 1–92.
- [380] Paganin VA, Ticianelli EA, Gonzalez ER. In: Gottesfeld S, Halpert G, Landgrebe A, editors. *Proceedings of the first international symposium on proton conducting membrane fuel cells*, The Electrochemical Society Inc., Pennington, NJ, 1995. p. 102.
- [381] Frey Th, Linardi M. *Electrochim Acta* 2004;50:90–105.
- [382] Wei Z, Wang S, Yi B, Liu J, Chen L, Zhou W, et al. *J Power Sources* 2002;106:364–9.
- [383] Iyuke SE, Mohamad AB, Kadhum AAH, Daud WRW, Rachid C. *J Power Sources* 2003;114:195–202.
- [384] Gamburgzev S, Appleby AJ. *J Power Sources* 2002;107:5–12.

References

- [385] Montgomery DC. Design and analysis of experiments. 5th ed. New York: Wiley; 1997. p. 228–341.
- [386] M. Min, J. Cho, K. Cho and H. Kim, *Electrochim. Acta.*, **45**, 4211(2000).
- [387] H. Bonnemann, R. Brinkmann, P. Britz, U. Endruschat, R. Mortel, U.A. Paulus, G.J. Feldmeyer, T.J. Schmidt, H.A. Gasteiger and R.J. Behm, *J. New Mat. Electrochem. Sys.*, **3**, 199 (2000).
- [388] A.K. Shukla, M. Neergat, P. Bera, V. Jayaram and M.S. Hegde, *J. Electroanal. Chem.*, **504**, 111(2001).
- [389] T. Toda, H. Igarashi, M. Uchida, M. Watanabe, *J. Electrochem. Soc.* 146 (1999) 3750.
- [390] M. Watanabe, S. Motoo, *J. Electroanal. Chem.* 60 (1975) 267.
- [391] R. Parsons, T. Vandernoot, *J. Electroanal. Chem.* 257 (1988) 9.
- [392] A. Hamnett, in: A. Wieckowski (Ed.), *Interfacial Electrochemistry: Theory, Experiment, and Applications*, Marcel Dekker, New York, 1999, p. 843.
- [393] J.S. Spendelow, P.K. Babu, A. Wieckowski, *Curr. Opin. Solid State Mater. Sci.* 9 (2005) 37.
- [394] W. Dmowski, T. Egami, K.E. Swider-Lyons, C.T. Love, D.R. Rolison, *J. Phys. Chem. B* 106 (2002) 12677.
- [395] F. Scheiba, M. Scholz, L. Cao, R. Schafranek, C. Roth, C. Cremers, X. Qiu, U. Stimming, H. Fuess, *Fuel Cells* 6 (2006) 439.
- [396] E.M. Crabb, M.K. Ravikumar, D. Thompsett, M. Hurford, A. Rose, A.E. Russell, *Phys. Chem. Chem. Phys.* 6 (2004) 1792.
- [397] C.E. Lee, S.H. Bergens, *J. Phys. Chem. B* 102 (1998) 193.

References

- [398] W.F. Lin, M.S. Zei, M. Eiswirth, G. Ertl, T. Iwasita, W. Vielstich, *J. Phys. Chem. B* 103 (1999) 6869.
- [399] Z. Jusys, J. Kaiser, R.J. Behm, *Electrochim. Acta* 47 (2002) 3693.
- [400] C.L. Green, A. Kucernak, *J. Phys. Chem. B* 106 (2002) 11446.
- [401] S. Gamburgzev, A. Appleby, *J. Power Sources* 107 (2002) 5–12.
- [402] G. Sasikumar, J.W. Ihm, H. Ryu, *J. Power Sources* 132 (1–2) (2004) 11–17.
- [403] M.S. Wilson, Membrane Catalyst Layer for Fuel Cells, U.S. Patent No. 5.234.777 (1993).
- [404] Y.-G. Chun, C.-S. Kim, D.H. Peck, D.-R. Shin, *J. Power Sources* 71 (1998) 174–178.
- [405] Z. Liang, W. Chen, J. Liu, S. Wang, Z. Zhou, W. Li, G. Sun, Q. Xin, *J. Membr. Sci.* 233 (1–2) (2004) 39–44.
- [406] S.-J. Shin, J.-K. Lee, H.-Y. Ha, S.-A. Hong, H.-S. Chun, I.-H. Oh, *J. Power Sources* 106 (2002) 146–152.
- [407] N. Fujiwara, K. Yasuda, T. Ioroi, Z. Siroma, Y. Miyazaki, *Electrochim. Acta* 47 (2002) 4079.
- [408] B. Viswanathan, S. Sivasanker, A.V. Ramaswamy, *Catalysis: Principles and Applications*, 1st edn., Narosa Publishing House, New Delhi, 2002, p. 62.
- [409] C. Roth, N. Martz, H. Fuess, *Phys. Chem. Chem. Phys.* 3 (2001) 315.
- [410] R.L. Borup, N.E. Vanderborgh, *Electrochem. Soc. Proc.* 95-23 (1995) 167.
- [411] T. Biegler, D.A.J. Rand, R. Woods, *J. Electroanal. Chem.* 29 (1971) 269.
- [412] C.H. Hsu, C.C. Wan, *J. Power Sources* 115 (2003) 268.

References

- [413] A.T. Haug, R.E. White, J.W. Weidner, W. Huang, S. Shi, T. Stoner, N.Rana, J. Electrochem. Soc. 149 (2002) A280.
- [414] A. Capon and R. Parsons, "The Oxidation of Formic Acid on Noble Metal Electrodes, Part 11. Comparison of the Behavior of Pure Metals," J. Electroanal. Chem. 44, (1973) 239.
- [415] O.G. Tyunikova, N. B. Miller, A. A. Yakovleva, and V. I. Veselovski, "Mechanism of Formic Acid Electrooxidation at the Platinum Electrode in Acid Solution," Electrokhimiya 7, (1971) 690.
- [416] A. Capon and R. Parsons, "The Oxidation of Formic Acid on Noble Metal Electrodes, Part 111. Intermediates and Mechanism on Platinum Electrodes," J. Electroanal. Chem. 45, (1973) 205.
- [417] P. Bindra, J.M. Roldan and G.V. Arbach, Mechanisms of electroless metal plating: II. Decomposition of formaldehyde, IBM J. R& D Vol. 28 No. 6, Nov. (1984).
- [418] B. Lee, K. Cho, Extended embedded-atom method for platinum nanoparticles, Elsevier Science, (2005).
- [419] M. S. Daw and M. I. Baskes, Phys. Rev. B 29, (1984) 6443.
- [420] S. M. Foiles, M. I. Baskes, and M. S. Daw, Phys. Rev. B 33, (1986) 7983.
- [421] A. E. Carlsson, Solid State Physics, Academic Press, New York, 43 (1990) 771.
- [422] M. S. Daw, S. M. Foiles, and M. I. Baskes, Mater. Sci. Rep. 9, (1993) 251.
- [423] C. L. Cleveland, U. Landman, T. G. Schaaff, M. N. Shafiqullin, P. W. Stephens, and R. L. Whetten, Phys. Rev. Lett. 79, (1997) 1873; M. D. Wolf and U. Landman, J. Phys. Chem. A 102, (1998) 6129.
- [424] J. W. M. Frenken and P. Stolze, Phys. Rev. Lett. 82, (1999) 3500.

References

- [425] L. Vitos, A.V. Ruban, H.L. Skriver, J. Kollar, The surface energy of metals, *Surface Science* 411 (1998) 186.
- [426] A. Schlapka , U. K.Casberger, D. Menzel, P. Jakob, Vibrational spectroscopy of CO used as a local probe to study the surface morphology of Pt on Ru(001) in the submonolayer regime, *J. Surface Science* 502–503 (2002) 129–135.
- [427] B.M. Nagabhushana, R.P. Sreekanth Chakradhar, K.P. Ramesh, V. Prasad, C. Shivakumara, G.T. Chandrappa, Magnetoresistance studies on barium doped nanocrystalline manganite, *Journal of Alloys and Compounds* 450 (2008) 364–368.

